



UNIVERSITY OF NAIROBI

DEPARTMENT OF PHYSICS

**INVESTIGATION OF THE POINT-OF-USE WATER PURIFICATION EFFICACY OF
FABRICATED DIATOMACEOUS EARTH-BASED FILTER MEMBRANES WITH
STATIC MAGNETIC FIELD**

A THESIS FOR A DOCTORATE DEGREE IN PHYSICS

BY

SR. MARY TAABU SIMIYU

Reg. No: I80/52654/2018

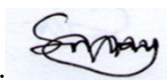
A Thesis Submitted in Fulfilment of the Requirements of the Degree of Doctor of Philosophy in
Physics of the University of Nairobi 2022

Declaration

I declare that this thesis is my original work and has not been submitted elsewhere for examination, award of degree, or publication. Where other people's work or my work has been used, this has properly been acknowledged and referenced in accordance with the University of Nairobi's requirements

Sr. Mary Taabu Simiyu

Department of Physics, University of Nairobi

Signed... 

Dated 27th June 2022.....

This thesis is submitted for examination with our approval as research supervisors

Prof. Francis Nyongesa

Prof Bernard O. Aduda

Dr. Zephania Birech

Department of Physics


Department of Physics

Department of Physics


University of Nairobi

University of Nairobi

University of Nairobi


Signed.....


Signed.....


Signed.....

Date 27/06/2022

Dated...27/06/2022.

Dated...27/06/2022.

Abstract

Waterborne diseases pose major challenges in developing countries. The World Health Organization estimates that 90.0% of the 2.3 million people who die annually due to waterborne diseases come from developing countries. At the same time fluorosis occurrence in the world's geological fluoride belts has left many people maimed due to drinking highly fluoridated water. This work is in two parts. The first part reports on the fabrication of diatomaceous earth (DE)-based water filter membranes whose mechanical strength was altered through the application of organic binders, and filtration characteristics using charcoal and carbon activated with molasses to improve the efficiency of the filters. The effect of the use of a static magnetic field in water purification was the second part investigated in this work. The ceramic membranes were fabricated from DE-powder and plant-based organic binders (*Abelmoschus esculentus*, *Basella alba*, *Corchorus olitorius*, and *Aloe vera*) in a ratio of 2:1 by mass. The dried samples were fired at 700.0 to 1150.0 °C and cooled at room temperature. A third of the fabricated membranes were soaked in molasses for 24.0 hours and heat-treated anaerobically for 2.0 hours at 600.0 °C then cooled to room temperature for 24.0 hours. The elemental analysis was carried out on binders, DE powder, molasses, and membranes using an x-ray fluorescence spectrometer. The x-ray diffraction pattern of DE powder and membrane was also determined. The three-point test was done using Universal Testing Instrument (Model EN 77065 7108CCN) 60000 N and the bulk density and the porosity were determined by the Archimedes' immersion technique. The fabricated membranes were then made to filter water contaminated with *Escherichia coli*, Rotavirus, and sodium fluoride. The second part reports on the efficiency of water purification using a 0.8 T static magnetic field from permanent magnets in defluoridation of sodium fluoride and purification of *E. coli* and Rotavirus. The water being purified was circulated at varying fluxes of 2.0 ml/s to 0.1 ml/s and ambient temperatures of 16.0 °C to 40.0 °C for 0.5 hours to 9.0 hours.

The results show that the DE had high content silica: DE-A had 87.5% silica content, DE-B had 89.6%, and waste had 79.0%. Other metallic oxides were in traces acceptable for the fabrication of membranes. The potter's clay comprised 50.0% silica, 28.8% Al_2O_3 , and 7.0% total flux content. The XRD of DE-A, DE-B, and DE-waste powder and membrane showed crystalline structures matching cristobalite, quartz, and wollastonite. The viscous binders were mostly characterized by metallic ions, carbohydrates proteins, and fats. All binders improved

the MOR of the membranes ranging from 33% to 175.0% increase. *Basella alba* was found to form membranes with the highest MOR, with a percentage increase of 175.1%, compared to the effect of the other binder. The diatomaceous membranes were stronger than the Potter's clay membranes. Carbon activating the membranes improved the mechanical strength but reduced their flow rates significantly. All the fabricated membranes passed the *Escherichia coli* test by recording >99.9% efficacy. The result of the Rotavirus in the Enzyme-linked immunoassay ELISA test showed that the membranes fabricated showed an efficiency of more than 88.5% of defluoridation and Rotavirus removal. The activated carbon had a bulk density of 450.0 kg/m³ and it improved the decontamination of water by around 10.0%. The activated carbon improved the modulus of rupture (MOR) of the DE-waste membrane by 47.8% and the average pore size of the active DE-waste membrane was 18.4 nm. The filtration process was found to be dependent on the contaminant's size, concentration, and pressure applied to the water during the filtration process. The use of normal pressure only yielded 88.7% and 48.5% in filtering Rotavirus, and NaF respectively. Carbon-activating the membranes improved the efficiency of removing Rotavirus and defluoridation by 9.7% and 8.6% respectively while applying a pressure of 50.0kPa reduced the efficiency of the carbon-activated membranes by 4.3% and 5.5% in NaF and Rotavirus respectively. The filtration results of the DE-based membranes fitted best the Complete Blocking and Standard Blocking Filtration models than the Cake and Intermediate blocking models.

It was further found that when ionized water was circulated under the static magnetic field for nine hours, its pH was lowered by 9.7% and that the flux of water in circulation did not affect the purification efficiency. The static magnetic field lowered the replication of *Escherichia. Coli* and Rotavirus by 9.8% and 7.1% respectively and 14.1% of defluoridation of water was also achieved. Thus, DE-waste together with molasses is good material in fabricating water membranes. The use of the magnetic field in water purification should be complemented by other methods for it to be effective.

TABLE OF CONTENTS

TABLE OF CONTENTS	iv
LIST OF TABLES	ix
LIST OF FIGURES.....	xi
LIST OF ABBREVIATIONS AND SYMBOLS.....	xix
CHAPTER ONE: INTRODUCTION	1
1.1 Scarcity of Water	1
1.2 Types of Water Contaminants	1
1.2.1 Fluoride Contaminant.....	2
1.2.2 Pathogens.....	3
1.3 Conventional Water Purification Methods	5
1.4 Diatomaceous Earth (DE).....	6
1.5 Activated Carbon	7
1.6 Magnetic Field.....	8
1.7 Problem Statement.....	9
1.8 Objectives	10
1.8.1 Aim	10
1.8.2 Specific Objectives	10
1.9 Justification.....	10
1.10 Significance	11
2 CHAPTER TWO: LITERATURE REVIEW.....	12
2.1 Approaches Used in Water Filtration	12
2.1.1 Microfiltration	12
2.1.2 Ultrafiltration	12
2.1.3 Reverse Osmosis	13
2.1.4 Nanofiltration	14
2.1.5 Forward Filtration.....	14
2.2 Ceramic Water Membranes	15
2.2.1 Mechanical Strength of Ceramic Water Membranes	16
2.2.2 Factors Affecting Water Filtration Efficiency.....	23

2.3	Filtration Models	27
2.4	Application of Magnetic Field in Water Purification.....	30
	2.4.1 Direct Actions on the Dissolved Ions and Water Molecules.....	31
	2.4.2 Magnetic Field Effects on Different Salt Solutions	31
	2.4.3 The Cluster Transformation	32
	2.4.4 Capillary Phenomena.....	33
3.	CHAPTER THREE: THEORETICAL BACKGROUND	35
3.1	Factors Affecting Strength of the Ceramic Membranes	35
	3.1.1 Clay Minerals	35
	3.1.2 Binders.....	36
	3.1.3 Drying Process.....	36
	3.1.4 Particle Size	39
	3.1.5 Firing Temperature	44
3.2	Relationship Between Porosity and Mechanical Strength.....	56
	3.2.1 Minimum Contact Area Model (MCA).....	56
	3.2.2 Stress Concentration Effects (SCE) Model	60
	3.2.3 Porosity-Density Relationship.....	63
3.3	Filtration Theory.....	64
	3.3.1 Type of Clay	64
	3.3.2 Adsorption	65
	3.3.3 Size Exclusion	66
3.4	Analytical Techniques	69
	3.4.1 X-ray Fluorescence.....	69
	3.4.2 X-ray diffraction	70
	3.4.3 Crystallinity	72
	3.4.4 Scanning Electron Microscope (SEM)	72
3.5	Concept of Magnetic Field Application	73
	3.5.1 Magnetization and Magnetic Field Susceptibility	73
	3.5.2 Magnetic Gradient	74

	3.5.3 Lorentz Force.....	75
	3.5.4 Magnetic memory.....	76
4.	CHAPTER FOUR: MATERIALS AND METHODS	77
4.1	Sourcing of Materials	77
	4.1.1 Diatomaceous Earth and Charcoal	77
	4.1.1 The Organic Binders and Molasses.....	77
4.2	Material Characterization	78
	4.2.1 Particle Size	78
	4.2.2 X-Ray Fluorescence Analysis	78
	4.2.3 X-ray Diffraction of Diatomaceous Earth Powder.....	79
4.3	Estimation of Organic and Inorganic Matter.....	80
	4.3.1 Reducing Sugars.....	80
	4.3.2 Fats	80
	4.3.3 Proteins (Kjeldahl Technique).....	81
	4.3.4 Viscosity.....	82
4.4	Fabrication of Green Ceramics Membranes.....	82
	4.4.1 Greenware Drying and Sintering.....	83
	4.4.2 Measuring the Physical Properties and Mechanical Properties.....	83
4.5	Microstructural Analysis	85
	4.5.1 XRF and XRD	85
	4.5.2 Microstructure and Morphology Determination	86
4.6	Filtration	87
	4.6.1 Flow Rate.....	87
	4.6.2 The Permeability of the Membrane.....	87
	4.6.3 Biological Analysis	88
	4.6.4 Aspect Ratio α	93
4.7	Magnetic Field Test.....	93
	4.7.1 <i>Escherichia Coli</i> Removal Test.....	93

4.5.1	Rotavirus Removal Test	94
4.5.2	Sodium Fluoride Removal Test.....	95
5.	CHAPTER FIVE: RESULTS AND DISCUSSIONS	96
5.1	Characterization of Raw Materials	96
5.1.1	Particle Size Distribution.....	96
5.1.2	X-Ray Fluorescence and Diffraction Composition of DE Raw Materials.....	97
5.1.3	X-Ray Diffraction Analysis.....	99
5.1.4	Characteristics of the Binders and Molasses	101
5.2	Physical Properties of the DE Greenware and Fired Membranes	104
5.2.1	Linear Drying Shrinkage	104
5.2.2	Linear Firing Shrinkage (LFS)	107
5.2.3	Bulk Density	109
5.3	Mechanical Properties	111
5.3.1	Modulus of Rupture (MOR) Green Samples.....	111
5.3.2	Modulus of Rupture (MOR) fired Samples.....	112
5.4	Effect of Charcoal on the Membranes Strength	118
5.5	Effect of the Organic Binders	119
5.6	Porosity-Mechanical Property Relationship.....	123
5.6.1	Porosity-Bulk Density Relationship	123
5.6.2	Effect of Pore Diameter on Bulk Density.....	126
5.6.3	Aspect Ratio	127
5.6.4	Comparison of the Experimental Data with the Minimum Contact Area and Stress Concentration Effects Models.....	128
5.7	Purification Efficiency.....	133
5.7.1	Flow Rate.....	133
5.7.2	Filtration Efficiency.....	136
5.7.3	Models	138
5.7.4	Blockage after Number of Runs	144

5.8	Purification Using Magnetic Fields	146
5.8.1	pH of Water	146
5.8.2	Effect of Time.....	147
5.8.3	Effect of Temperature.....	148
5.8.4	Effect of the Flow Rate of Water	149
5.8.5	Magnetic Field Purification Efficiency	150
CHAPTER SIX: CONCLUSION		152
8.	Acknowledgment.....	155
9.	REFERENCES	156

LIST OF TABLES

Table 0.1: Typical waterborne pathogens found, their causative agent, diseases, and their routes of transmission (Sila, 2019; Leclerc et al., 2002).....	3
Table 3.1: The models to predict the relationship between mechanical strength and porosity	63
Table 4.1: The setting for the Ball mill used in grinding charcoal diatomaceous earth.....	77
Table 4.2: The Specifications of the Energy Dispersive X-Ray Fluorescence Spectrometer for carrying out elemental analysis	79
Table 4.3: The parameters used in determining the viscosity of the binders extracted from the green leaves	82
Table 5.1: The descriptive statistics of particle size for DE-A, DE-B. DE-waste and charcoal powder	96
Table 5.2: The 2θ values at which peaks occurred for pure diatomaceous earth samples and diatomaceous waste with the interplanar distance and the crystals associated with them. (Cr - Cristobalite, Q – Quartz, and W - wollastonite).....	101
Table 5.3: The percentage of the elemental and organic content of molasses	103
Table 5.4: Firing temperature and the linear firing shrinkage of DE-waste membranes fabricated with 50% binders obtained from <i>Basella alba</i> , <i>Corchorus olitoris</i> , <i>Abelmoschus esculentus</i> , and <i>Aloe vera</i>	108
Table 5.5: The components of linear fits extracted from diatomaceous earth A models.....	124
Table 5.6: The y-intercept, gradient, and their inverse values as predicted by a linear fit of diatomaceous earth B membranes. The R-Squared and Pearson's are also shown.....	125
Table 5.7: The y-intercept, gradient, and their inverse values as predicted by a linear fit of diatomaceous earth waste membranes. The R-Squared and Pearson's are also shown	126
Table 5.8: Summary of the materials used together with calculated values of empirical parameters based on Equations 5.4 and 5.4 respectively	130

Table 5.9: The constants b and η obtained from MCA and SCE fit respectively. The R^2 values and Pearson's correlations are also shown	131
Table 5.10: The constants of MCA and SCE fit on experimental data of DE Waste sintered at 900 °C.....	132
Table 5.11: The fitting parameters of Complete Blocking, Cake Filtration, Intermediate Filtration, and Standard Filtration Models developed from water contaminated with E. coli, Rotavirus, and sodium fluoride	143
Table 5.12: The velocity of contaminated water and the effective percentage efficiency obtained when a 0.8 T magnetic field was used to purify the water	150

LIST OF FIGURES

Figure 2.1: Schematic showing the types of contaminants filtered by microfilters, ultrafilters, nano-filters, reverse osmosis filters, and forward filters	13
Figure 2.2: Plot of bulk density against sintering time in hours and particle size in μm of silica (Giesche, 1994; Giesche and Matijević, 1994)	17
Figure 2.3: The plot of compressive strength against fraction porosity of porous hydroxyapatite ceramics (Liu, 1997). The dimensions of different sizes of pore-forming material are given	19
Figure 2.4: Plot of apparent porosity and apparent density against firing temperature of membranes fabricated from kaolinite clay and sugarcane bagasse ash (Andrade et al., 2019).....	21
Figure 2.5: The plot of sintered density (g/cm^3) and porosity (vol.%) against sintering temperature ($^{\circ}\text{C}$) of diatomaceous earth monoliths (Akhtar et al., 2010).	22
Figure 2.6: The plot of compressive strength and sintered density against the firing temperature of diatomaceous earth monoliths (Akhtar et al., 2010)	23
Figure 2.7: The plot of flow rate against firing temperature of porous ceramic pots. B14, B19, B20, and B23 represent the different sample batches. (Soppe et al., 2015)	26
Figure 2.8 The plot of log reduction values (LRV) against firing temperature of filter pots. B19, B20, and B23 represent the different sample batches (Soppe et al., 2015)	26
Figure 2.9: Plot of permeability and average pore size against the temperature	27
Figure 3.1: A schematic representation of water subjected to different conditions of evaporation. RH, T_{air} , and T_{w} stand for the relative humidity, ambient temperature, and temperature of water respectively (Oummadi, 2019).....	37
Figure 3.2: A schematic representing evaporation in a porous material. RH, stand for T_{air} for the relative humidity, ambient temperature, and temperature of water respectively (Oummadi, 2019)	38

Figure 3.3: A schematic of a compact body showing particle coarsening and grain boundary formation (Kang, 2005)	42
Figure 3.4: A schematic showing the two sintering processes; solid-state sintering and liquid face sintering (Fang, 2010; Kang, 2005)	43
Figure 3.5: The equilibrium condition for surface energy (γ) and dihedral angle in solid-vapor (sl) and solid-liquid (sl) interfaces (Kang, 2005)	44
Figure 3.6: shows the initial stage of the sintering process. In (a) the particles are just touching each other and in (b) the necking process has been initiated and the contact area of the particles has increased up to 20%	46
Figure 3.7: Shows the neck area at the initial stage of sintering as the particles maintain the particle distance; the two particles have an equal radius before the necking process and each particle has a neck arch of x	47
Figure 3.8: The paths followed by the vacancy movement from the neck region to other parts of the particle (Fang, 2010)	48
Figure 3.9: A schematic showing the rate of shrinkage of a material undergoing an intermediate stage of sintering at two different firing temperatures T_1 and T_2 (Kang, 2005)	48
Figure 3.10: The pore with vertices 1, 2, 3, and 4 manifesting the viscous flow mechanism of linear shrinkage (Kang, 2005); γ stands for the surface energy, gb for grain boundary, and sv for solid-vapor with ϕ and λ as the dihedral angles.....	49
Figure 3.11: The intermediate stage of the sintering process that comprises polyhedral continuous solid phase and linear pores (Kang, 2005).....	50
Figure 3.12: The isolated pores in the final stage of sintering located on the polyhedral grain (Kang, 2005).....	51
Figure 3.13 Schematic showing the stress concentration at the crack tip as explained in Inglis theory and σ is the load the ceramic can hold without breaking	52

Figure 3.14: Shows the sample with thickness t_h under the strain of σ_s . In (a) the sample has no crack and sample (b) has a crack of length L_c	54
Figure 3.15: A Schematic diagram of a bend (three-point test) where L is the distance between two supporting loads, d is the diameter of the sample and F is the fracture load.....	55
Figure 3.16: A pore contained in a large isotropic material whose axis of rotation is Z and is tilted to z' with an angle ϕ (Andersson, 1996)	57
Figure 3.17: A porous ceramic material under tension with applied for W	60
Figure 3.18: Herman-Brede'e models; d_m : pore size of membrane filter, and d_p : the particle size of suspended material (Hatori and Suzuki, 2021; Iritani and Katagiri, 2016)	67
Figure 3.19: A Kossel diagram showing the K_α x-ray transition of the silicon atom. Other shells (M and L) are also shown (Halliday et al., 2001).....	70
Figure 3.20: Bragg's reflection under constructive interference. Ray P and Q strike two successive planes at a glazing angle θ (Ghoshal, 2007)	71
Figure 3.21: The schematic representation of the scanning Electronic Microscope.....	73
Figure 3.22: The arrangement of polar and nonpolar molecules in the presence and absence of the magnetic field (Zaidi et al., 2014)	74
Figure 3.23: A contaminant molecule with a negative charge q in water with a velocity v under the influence of force \vec{F}_B caused by a magnetic field \vec{B} (Puri and Babbar, 2010)...	76
Figure 4.1: The Energy Dispersive X-Ray Fluorescence Spectrometer used in elemental analysis of diatomaceous earth and the binder	86
Figure 4.2: The setup of the Denton Vacuum sputter coater at 100 milliTorr used for coating the samples.	87
Figure 4.3: The pure double and single strength MacConkey Broth Purple w/ BCP solution filtered by the fabricated membranes	88
Figure 4.4: Characteristic colonies of Escherichia coli incubated under Cystine-Lactose-Electrolyte-Deficient Agar for at least twenty- four hours.....	89

Figure 4.5: The schematic representation of the setup used to filter the contaminated water .	90
Figure 4.6: Image of MacConkey broth laced with filtered water from fabricated membranes and cultured for 24 hours to test the presence of Escherichia coli. The yellow color shows a positive result and the purple shows a negative result.	90
Figure 4.7: showing how the samples suspected to have E.coli were treated and the negative and positive result presentation	91
Figure 4.8: The Procedure for carrying out the ELISA Test for Rotavirus samples and the presentation of the results	92
Figure 4.9: The filtration set up in which the disc-shaped membranes were fitted in the cartridge connected to a syringe fitted with a pressure pump	93
Figure 4.10: The setup used to filter contaminated water across the 0.8 T magnetic field.....	94
Figure 5.1: The volume density and cumulative distribution frequency of volume density of particle sizes of DE-A, DE-B, DE-waste, and charcoal powder as measured by Malvern Panalytical Master Sizer 3000	97
Figure 5.2: The histogram of the elemental composition of the diatomaceous earth powder (DE-A, DE-B, and DE-waste) and Potters' Clay obtained from x-ray fluorescence spectroscopy	98
Figure 5.3: X-ray characteristic spectra of pure diatomaceous earth samples and diatomaceous earth waste	100
Figure 5.4: The percentage of elemental content (a) and organic matter (b) present in the binders extracted from Abelmoschus esculentus, Aloe vera, Basella alba, and Corchorus olitorius.....	101
Figure 5.5: Viscosity of the molasses and the extracted binders measured at room temperature of 22 °C. The symbols A.E, C.O, B.A, A.V, and D.W stand for Abelmoschus esculentus, Aloe vera, Basella alba, Corchorus olitorius, and distilled water respectively. (Distilled water was used as the reference since the plants were all boiled in distilled water).....	104

Figure 5.6: Variation of linear drying shrinkage with binder content in dried pure diatomaceous earth, the diatomaceous earth waste, and Potter's clay discs	105
Figure 5.7: The different scenarios of the interaction of the organic binder and the particles	107
Figure 5.8: Linear firing shrinkage of DE, DE-Waste, and Potter's clay membranes fabricated with <i>Basella alba</i> binder against firing temperature	109
Figure 5.9: The plot of bulk density against the binder concentration used in the fabrication of diatomaceous earth and Potter's clay green membranes	110
Figure 5.10: The plot of bulk density (Kg/m^3) against firing temperature of diatomaceous earth (DE-A, DE-B, and DE-waste), and Potter's clay fired at varying temperatures.....	111
Figure 5.11: A plot of the MOR of the green DE, DE-Waste, and Potter's clay samples against the binder concentration used in the fabrication	112
Figure 5.12: The relationship of MOR against firing temperature (700.0 °C to 1150.0 °C) of the membranes of diatomaceous earth (DE-A, DE-waste, Pure DE-B) and Potter's clay formed with different organic binders	114
Figure 5.13: Volume fraction porosity against sintering temperature of diatomaceous based pellets (DE-waste, DE-A, and DE-B) bound by different organic binders (<i>Basella alba</i> , <i>Aloe vera</i> , <i>Corchorus olitorius</i> , and <i>Abelmoschus esculentus</i>).....	115
Figure 5.14: The plot of MOR and porosity against firing temperature of DE-B membrane fabricated with <i>Basella alba</i>	116
Figure 5.15: The XRD pattern of DE-A (a), DE-B (b), and DE-waste (d) membranes for samples fabricated with <i>Basella alba</i> and fired at 750.0 °C, 800.0 °C, 900.0 °C, 950.0 °C, 1000.0 °C, and 1150.0 and (d) shows the plot crystallinity and grain size against firing temperature	117
Figure 5.16: The micrographs of DE-waste membranes fired at 750.0 °C, 800.0 °C, 850.0 °C, 900.0 °C, 1000.0 °C, and 1100.0 °C.....	118

Figure 5.17: Relationship of porosity against the content of charcoal in DE earth membranes with different organic binders and fired at a constant temperature of 900.0°C under air .	119
Figure 5.18: Average porosity of diatomaceous earth sand Potter’s clay samples against the binder percentage concentration at a constant temperature of 900.0 °C for DE-A, DE-B, DE-waste, and clay membranes	120
Figure 5.19: The variation of linear firing shrinkage (LFS) with the binder in pure diatomaceous earth samples and the waste membranes fired at 900.0 °C.....	121
Figure 5.20: Average modulus of rupture against binder concentration (Abelmoschus esculentus, Aloe vera, Basella alba, and Corchorus olitorius) of DE and Potter’s membranes fired at 900.0 °C	122
Figure 5.21: The percentage increase in strength (MOR) in DE-A, DE-B, DE-waste and Potter’s clay membranes fabricated with Abelmoschus esculentus, Aloe vera, Basella alba, and Corchorus olitorius	123
Figure 5.22: The linear fit and scatter plot of the relationship between bulk density and volume fraction porosity of diatomaceous earth A membranes fabricated with different binders	124
Figure 5.23: The linear fit and scatter plot of the relationship between bulk density and volume fraction porosity of diatomaceous earth B membranes fabricated with different binders	125
Figure 5.24: The linear fit and scatter plot of the relationship between bulk density and volume fraction porosity diatomaceous earth waste membranes fabricated with different binders	126
Figure 5.25: The relationship between bulk density and pore size of diatomaceous earth waste fabricated with Basella alba binder	127
Figure 5.26: The bar chart of the number of occurrences against the aspect ratio of membranes of porosities ϵ_p 0.12, 0.18, 0.22, 0.28 and the SEM image of DE-B membrane fired at 900.0 °C.....	128

Figure 5.27: The scatter plot relative strength of Pure DE A membranes sintered at not 900.0 °C against volume fraction porosity fitted with MCA and SCE models.....	129
Figure 5.28: The experimental data of relative strength against volume fraction porosity of DE-B membranes fitted with MCA and SCE models	131
Figure 5.29: The plots of relative strength against volume fraction fitted with MCA and SCE models. The membranes were sintered at 900.0 °C.	132
Figure 5.30: The plot of the volume of water filtered against the time taken to filter water for membranes fabricated with Basella alba and fired at 800.0 °C, 900.0 °C, 1000.0 °C, 1100.0, and 1150.0 ° C	133
Figure 5.31: The column chart showing the porosity of membranes from DE-A, DE-B, DE-waste, and clay fabricated with Basella alba and fired at 900.0 °C. In (a) the membranes are without carbon and in (b) the membranes are carbon activated	134
Figure 5.32: The plot of flow rates and volume of water against time. The water was contaminated with 10 ³ CFU/ml E.coli and filtered with DE-A, DE-B, DE-waste, and Potter’s clay membrane fabricated by Basella alba and fired at 900.0 °C	135
Figure 5.33: Micrograph of DE-A (a), DE-B (b), and DE-waste (c) membranes fired at 850.0 °C. The DE-A and DE-B membranes are characterized by diatomaceous structures but DE-waste lacks such structures	136
Figure 5.34: The bar chart of the percentage filtration efficiency of the 0.48 porosity membrane fabricated with DE-A DE-B, DE-waste, and clay combined with different binders: Abelmoschus esculentus, Aloe vera, and Basella alba in filtering water contaminated with E.coli, NaF, and Rotavirus.....	137
Figure 5.35: The models of complete blocking, standard blocking, intermediate blocking, and cake filtration are represented graphically using data derived from filtering water contaminated with E.coli, 10 ³ CFU/ml, 10 ³ viral particles, and 1.0 g/ml.....	140
Figure 5.36: The models of complete blocking, standard blocking, intermediate blocking, and cake filtration are represented graphically using data derived from filtering water contaminated with E. coli, 10 ³ CFU/ml.....	141

Figure 5.37: The models of complete blocking, standard blocking, intermediate blocking, and cake filtration are represented graphically using data derived from filtering water contaminated with Rotavirus, 10^3 viral particles/ml	142
Figure 5.38: The models of complete blocking, standard blocking, intermediate blocking, and cake filtration are represented graphically using data derived from filtering water contaminated with 5 mg/ml, Sodium fluoride solution	143
Figure 5.39: Plot of flow rate against the number of runs of DE-A, DE-B, DE-waste, and clay membranes fabricate with <i>Basella alba</i> and fired at 900.0 °C.....	145
Figure 5.40: The plot of flow rate against the number of runs for DE-A membranes fabricated with <i>Basella alba</i> and fired at 900.0 °C	146
Figure 5.41: The pH value of different water solutions circulated in the presence and absence of a 0.8 T static magnetic field at an ambient temperature of 24.0 °C.....	147
Figure 5.42 The replication curves of (a) <i>Escherichia coli</i> ,(b) and Rotavirus Pathogens in the presence and absence of the static magnetic field at an ambient temperature of 24.0 °C.	148
Figure 5.43 The variation of (a) <i>E.coli</i> concentration, (b)Rotavirus concentration, and (c) pH of NaF solutions under a 0.8 T magnetic field with the flow rate of 2.0 ml/s and varying temperature	149
Figure 5.44. The plot of the contaminants' purification efficiency against time used to purify the water in a static magnetic field at an ambient temperature of 24.0 °C.....	151

LIST OF ABBREVIATIONS AND SYMBOLS

AC	Activated carbon
a_o	Interparticle spacing
a_w	Water activity
C_σ	Crack size
C_c	Concentration
C_{co}	Initial concentration
C_{cf}	Final concentration
C_{crit}	Critical arch-length
C_{cslb}	Vapour concentration at solid-liquid boundary
C_{clb}	Vapour concentration at liquid boundary
CWF	Ceramic water filters
d	Interplanar spacing
d_p	Pore diameter
d_m	Contaminant size
d_{pat}	Particle size
D_s	Sample diameter
D_w	Diffusion coefficient
DE	Diatomaceous earth
DE-A	Kensil 90
DE-B	Kensil SSF
DE -waste	Diatomaceous earth waste
E	Electric field
E_g	Energy gained
E_l	Energy lost
$F_o(G)$	Shrinkage rate factor
G	Grain size
H	Height covered by the vapour layer
J	Flux
J_o	Initial flux
J_L	Liquid flux
J_D	Diffusion coefficient of moisture
k	Mass transfer coefficient

K_c	Blocking coefficient for the cake filtration model
K_b	Blocking coefficient for the complete blocking filtration model
K_i	Blocking coefficient for the intermediate blocking filtration model
K_I	Stress intensity factor
K_{IC}	Critical stress intensity factor
K_s	Blocking coefficient for the standard blocking filtration model
K_{sr}	Constant in of shrinkage before densification
K_{srd}	Constant in of shrinkage after densification
L	Length of fracture
L_c	The length of cake layer
L_f	Length of the fired ceramic/membrane
M_{sample}	Mass of sample
M_o	Original mass
M_1	1 st reading of mass
M_2	2 nd reading of mass
MF	Magnetic field
MOR	Modulus of rupture
MSA	Minimum Solid Area
M_t	Mass transfer
n_c	Critical number
P_d	Pore size
P_c	Contaminant size
P_{erm}	Permeability
P	Pressure
p	Radius of the tip of the crack
P_s	Saturated pressure
Pure DE-A	Kensil 90
Pure DE-B	Kensil SSF
P_{flat}	Pressure at the flat surface of the particle
q	Heat flux
R	The ideal gas constant
r	Pearson's correlation
RH	Relative humidity

S_R	Shrinkage
SCE	Stress Concentration Effects
SCS	Self Consistency Scheme
T	Temperature
T_{cd}	Thermal conductivity
t^n	Sintering time component
T_{air}	Ambient temperature of saturated sample
T_s	Temperature of the sample
T_w	Temperature of water
U_{elas}	Elastic energy stored in the material
U_o	Energy of the material before applying external load
V	Volume
V_A	Volume per unit area
V_{HCl}	Volume of HCl
$V_{HCl+sam}$	Volume of HCl plus volume of sample
V_{sample}	Volume of sample
V_{op}	Volume of the open pores of porous material
V_{max}	Maximum volume
V_p	Volume of bulk sample
U	Energy
U_o	Initial energy
U_{Tot}	Total energy
U_{elas}	Total elastic energy
W_{inti}	The initial total weight of the green sample
W	Sample weight (Sample under drying conditions)
W_d	Sample weight (Dried at 110.0 °C)
$W(t)$	Sample weight at time t
x	Particle neck arch as a result of extended length caused by sintering
X	Dry basis of green ceramic
X'	Wet basis of green ceramic
Z	Additional grain boundary
α_c	Resistance of cake filtration model
α_s	Resistance of standard blocking filtration model
α_b	Resistance of complete blocking filtration model

α_i	Resistance of intermediate blocking filtration model
σ_y	Young's modulus
σ_e	Elastic modulus
ε_p	Porosity
ε_{px}	The mean porosity in the volume Adx
μ	Viscosity
Γ	Solid-vapour surface
λ	Thermal conductivity
γ	Surface energy
γ_{sl}	Solid-liquid surface energy
γ_{gb}	The energy at the grain boundary
γ_{sv}	Solid-vapour surface energy
ϕ	Dihedral angle
ΔL	Change in length
ΔP	Change in pressure
σ	Modulus of rupture
σ_c	Critical stress
σ_E	Elastic modulus
σ_{max}	Maximum modulus of rupture
σ_{th}	Theoretical cohesive strength
ρ	Density of the porous material
ζ	Loading pattern

CHAPTER ONE: INTRODUCTION

1.1 Scarcity of Water

National Aeronautics and Space Administration, NASA, of the United States of America, has speculated that the third world war could be caused by the scarcity of water (Dolatyar and Gray, 2000). In as much as this may be seen as an exaggeration, some countries in sub-Saharan Africa have recently experienced tribal and border conflicts caused by the scarcity of or lack of access to water. The scarcity of potable water in the world has been exacerbated by climate change. Steckler *et al* (1999) predicted that by the first quarter of the twenty-first century, the amount of potable and clean water on earth would diminish whilst the human population, urbanization, and industrialization would be doubled (Seckler *et al.*, 1999). An increase in such factors as industrialization, population increase, and urbanization, requires the use of more water thereby putting stress on available potable water meant for human consumption. Furthermore, industrial waste, if not properly disposed of, contaminates the available potable water and the consumption of such polluted water is harmful to human life. It is estimated that around fifteen percent of the human population (7.9 billion) worldwide cannot access safe drinking water due to a lack of decent sanitation and affordable water purification systems (Momberg *et al.*, 2021; Montgomery and Elimelech, 2007). Ninety percent of the affected population comes from developing countries. Kenya is one of the developing countries that has been struggling with the burden of water stress and waterborne diseases.

According to the 2019 Kenyan National Census, approximately fifty-two million people are residing in Kenya. Forty-three percent of the Kenyan population (22 million) cannot access safe water and the majority of these are low-income earners living in rural and informal settlements in urban set-ups (Alaazi and Aganah, 2020; Silva *et al.*, 2020). Contamination of the scarce water (both surface and sub-surface) is another issue that has exposed the fast-growing population of Kenya to unsafe water. The aforementioned reasons have resulted in an almost yearly outbreak of cholera, dysentery, and other water-borne diseases among the poor urban and rural dwellers in Kenya (Bundi *et al.*, 2019). Different types of water contaminants are discussed in the following sections.

1.2 Types of Water Contaminants

There are several contaminants in water namely; physical, radiological, chemical, and biological, contaminants (Morton, 1997). The physical contaminants affect the physical

appearance of water and they comprise organic matter and sedimentation in water (Templeton *et al.*, 2009; Muncaster *et al.*, 1990). Radiological contaminants are chemicals with unstable atoms that emit radiations such as uranium (Peterson *et al.*, 2007; Blanchard *et al.*, 1985). Chemical contaminants introduce other molecules in water such as soluble salts, gases, and acids (Morton, 1997; Muncaster *et al.*, 1990). In Kenya, chemical pollution is mainly caused by the poor disposal of industrial wastes, agricultural inputs (fertilizers and pesticides), and the natural occurrence of some salts such as sodium fluoride. The chemical pollutants together with biological pollutants (mainly pathogens such as bacteria, protozoa, viruses, and helminths) account for 95.6% of the Kenyan water pollution (Sila, 2019).

1.2.1 Fluoride Contaminant

Fluoride is one of the major contaminants of groundwater, which the World Health Organisation classifies alongside arsenic and nitrates as posing danger to human health (Amini *et al.*, 2008; WHO, 2004). Elevated levels of fluoride in groundwater occur worldwide (Brahman *et al.*, 2013; Rafique *et al.*, 2009; Ncube and Schutte, 2005; Ncube and Schutte, 2004). Fluorides enter the groundwater through the dissolution of rocks containing fluorine-like minerals (Banks *et al.*, 1995). Such rocks include basalt, granite, shale, and syenite among others (Saxena and Ahmed, 2001). Apart from natural contamination of groundwater by the dissolution of fluoride-like rocks, another major source of this contaminant is industrial wastes from plants manufacturing glass (Fan and Li, 2013), semiconductors (Arno and Vermeulen, 2002), and beryllium mining plants (Thorat *et al.*, 2011). The fluoridation of water by the industries is worse than the natural fluoridation as it contaminates water with a high concentration of fluorides (thousands of mg/L) (Choubisa and Choubisa, 2016; Krook and Justus, 2006; Maylin and Krook, 1982; Krook and Maylin, 1979). The World Health Organization (WHO) predicts that at least 200 million people worldwide consume fluoridated water with levels beyond recommended levels of 1.5 mg/L (WHO, 2004). In humans, fluorides can be beneficial or harmful depending on the quantity of intake. Unfortunately, the human body only needs 1.5 mg/L of fluoride for its dental and bone-strengthening especially in infants (Harrison, 2005; Ysart *et al.*, 2000). On the other hand, too much intake of fluorides in water initially leads to fluorosis, and in advanced stages diseases like Alzheimer, arthritis, brain damage, brittle bones, cancer, infertility, osteoporosis, and thyroid disorder can set in (Harrison, 2005; Kauffman, 2005; Ysart *et al.*, 2000; Ripa, 1993; Murray and WHO, 1986). Fluorosis results in the mottling of teeth and severe cases of it

cause neurological damages and embrittled bones (Abdeljawad, 2019; Harrison, 2005; Baylink *et al.*, 1983). Some researchers have shown that excess fluorides in the human body can interfere with the metabolism rate and cause intestinal challenges (Jha *et al.*, 2011; Rich *et al.*, 1964; Rich and Ensinnck, 1961) and DNA (Zhou *et al.*, 2019). Intestinal mucous is what is used by fluorides to attack the intestines. The hydrochloric acid in the mucous interacts with the fluoride to form hydrofluoric acid which causes gastrointestinal irritation and if prolonged, this can lead to intestinal corrosion (Sondhi *et al.*, 1995; Nopakun *et al.*, 1989). Once the gastrointestinal irritation sets in other oxidative activities such as coagulation, glycolysis, neurotransmission, and phosphorylation also get interrupted. Furthermore, people with underlying kidney issues are more susceptible to fluoride poisoning because fluorides have been reported to cause kidney poisoning in adults and children (Xiong *et al.*, 2007; Cittanova *et al.*, 1996). Apart from the teeth and bone, fluoride is also known to accumulate at the pineal gland thereby interfering with brain functioning (Kalisinska *et al.*, 2014; Luke, 1997). Fluorides are also known to cause cancer-related complications in the bladder and thyroid (Lima *et al.*, 2007). It is due to the above health reasons that a lot of water purification systems have focused on removing fluoride contaminants. Research in diatomaceous earth by (Gitari *et al.*, 2020; Izuagie *et al.*, 2016a) and activated carbon (Getachew *et al.*, 2015) indicates that these materials can defluoridate water cheaply.

1.2.2 Pathogens

Pathogens are any microorganisms that can cause diseases. Most waterborne pathogens infect the gastrointestinal tract of humans and other animals. The inhabitation of these pathogens in the intestines serves as an adaptation that allows them to be transmitted into the water through animal feces (George *et al.*, 2001). Drinking water contaminated with such pathogens cause water-borne diseases both in humans and other animals. These pathogens also infect the skin lesions and respiratory tract and some affect the brain (Leclerc *et al.*, 2002). Water often gets contaminated with bacteria, helminths, protozoa, and viruses. These micro-organisms, upon ingestion by humans through drinking contaminated water, cause diarrhea diseases such as typhoid fever and cholera (Fayer, 2004; Taittet *et al.*, 2004). The causative agents of waterborne diseases and their transmission routes are summarized in (Table 1.1)

Table 0.1: Typical waterborne pathogens found, their causative agent, diseases, and their routes of transmission (Sila, 2019; Leclerc et al., 2002)

Type of causative agent	Causative agent	Common transmission route	Name of diseases
-------------------------	-----------------	---------------------------	------------------

Pathogen			
Bacterial	<i>Shigella</i> species	Human-stool- <i>Musca domestica</i> -food and water-human	Shigellosis
	<i>Salmonella typhi</i> and <i>paratyphi</i>	Human-stool-food and water-human	Typhoid fever
	<i>Vibrio cholerae</i>	Human-stool-food and water -human	Cholera
	<i>E. coli</i>	Human-stool-water-human	Acute Gastroenteritis
Viral	Hepatitis virus (A, and E)	Human-stool-food and water -human	Infectious hepatitis
	Poliovirus	Human-stool-water-human	Poliomyelitis
	Hepatitis E, Rotavirus	Human-stool-water-human	Acute Gastroenteritis
Protozoal	<i>Entamoeba histolytica</i>	Human-stool-food and water-human	Amebiasis
	<i>Giardia lamblia</i>	Human-stool-food and water-human	Giardiasis
Helminths	<i>Dracunculus medinensis</i>	Human-water-human	Dracunculiasis (Guinea worm)

Viruses present in water include; adenovirus, astrovirus, caliciviruses, enteroviruses (coxsackieviruses and polioviruses), hepatitis viruses (A and E), norovirus and rotavirus, (Organization, 2004). Viruses excreted through urine such as polyomaviruses and cytomegalovirus are also present in water (Cannon *et al.*, 2011). Viral infections are self-limiting in healthy persons and their effects are immense among the elderly, infants under the age of five, immune-compromised people, and expectant mothers. The said viruses are commonly associated with abdominal pains, diarrhea, fever, and vomiting caused by gastroenteritis. Waterborne virus-based diseases such as Rotavirus, just like any other waterborne disease, are higher in developing countries, despite the many water purification systems that exist in these regions. This is because the conventional water purification systems such as reverse osmosis (Pype *et al.*, 2016; Michen *et al.*, 2011; Adham *et al.*, 1998; Sorber *et al.*, 1971) and ultrafiltration (Yahya *et al.*, 1993; Sorber *et al.*, 1971) that can remove viruses from water are costly, hence, hardly used on large scale in the developing world. The porous ceramic water membranes that would have addressed this challenge are brittle and unable to purify viruses to recommended levels of >99.9%, due to their micro-sized pores that are much bigger than the nano-sized viruses. Thus, addressing the mechanical strength weakness nature of the ceramic membranes, reducing their pore, and increasing their surface area for pathogen adsorption would address the challenges of water filtration in developing countries. Research

by (Izuagie *et al.*, 2016a; Izuagie *et al.*, 2016b) shows that DE-based ceramic membranes have nanopores that are promising in viral and chemical water purification. Furthermore, there are prospects in improving the mechanical properties of the ceramics for water purification using plant-derived organic binders (Njogu *et al.*, 2008; Ogacho *et al.*, 2006; Aduda *et al.*, 1999).

1.3 Conventional Water Purification Methods

Water purification is the disinfection of water, which entails the elimination, either by physical removal, deactivation, or killing of the pathogens (Safarzadeh-Amiri *et al.*, 2011). Several chemicals such as chlorine have been used to successfully kill pathogens in water (Cutler and Miller, 2005). Table 1.2 gives a summary of the various chemicals and methods used in water disinfection, their advantages, and their disadvantages. Most of the methods can remove all pathogens except viruses and fluorides. Research in diatomaceous earth (Michenet *et al.*, 2012) and magnetic field (Fojt *et al.*, 2004) suggest that the above challenges can be overcome.

Table 0.2: Conventional methods used in water purification, including their advantages and disadvantages.

Method	Advantages	Disadvantages
Chlorination	<p>Effective in eradicating all water pathogens</p> <p>Used in both primary and secondary disinfection.</p> <p>Most of them are easier to handle</p>	<p>Chlorine gas is lethal even at low concentrations</p> <p>Leaves harmful by-products after disinfection</p> <p>It is very corrosive and should be handled with care</p> <p>It can easily decompose and should not be stored for more than one month.</p> <p>Has a strong odour</p>
Ozonation	<p>Its contact time is shorter than chlorination processes.</p> <p>Its dosage is also smaller than the chlorination process.</p> <p>Ozone alone does not directly produce harmful organic materials such as halogenated organic material</p>	<p>Ozone gas is unstable</p> <p>Ozone can only be generated on-site</p> <p>It is only used as a secondary disinfectant since it does not maintain enough residual in the water</p> <p>Expensive</p>

UV radiation	It does not produce toxic residuals It requires short contact times, and The equipment is easy to operate and maintain.	It does not eliminate pathogens such as <i>Cryptosporidium</i> cysts It cannot be used to remove turbidity in water High costs
Reverse Osmosis	It gets rid of most of the pathogens including viruses and chemicals No by-products	Water purified by reverse osmosis is demineralized and lacks essential minerals Demineralized water is acidic and affects the pH of the blood Some chemical contaminants such as chlorine and chloramines are not removed High costs due to use of electricity
Ultra-filtration	It gets rid of most of the pathogens including viruses and chemicals There are different semipermeable membranes to suit different needs No by-products	The challenge of fouling Costly but cheaper than reverse osmosis
Filtration	Efficient in eliminating bacteria, cysts, particles, and some viruses The filters can be cleaned Affordable and compatible	Ceramic filters alone are incapable of removing soluble chemical contaminants such as chlorine. Some types of filters suffer cracking and breakages They get clogged and demand replacement

1.4 Diatomaceous Earth (DE)

Diatomaceous earth (DE) is made of fossils of diatoms, a planktonic single-cell aquatic organism. When diatoms die, they get deposited on the shores of a water body and accumulate over time. During volcanic eruptions, such water bodies may die off leaving behind deposits of DE. Diatoms are made of natural silica (silicon dioxide) (Fulton, 2000a). There are two types of diatomaceous earth; freshwater and salty water diatomaceous depending on the source of the water body. In Kenya, freshwater diatomaceous earth is mined from the great Rift valley escarpments while the salty water DE is found in the coastal regions (Michenet *et al.*, 2011). The capability of diatomaceous earth to purify water was discovered by engineer Wilhelm Berkefeld who developed a candle filter from DE which was used successfully in 1892 to handle the cholera epidemic in Hamburg (Michenet *et al.*, 2011; Lynch *et al.*, 2006). Currently, DE has found its applicability in wine (Gergely *et al.*, 2003), fruit juice (Kilara and Van Buren, 1989), and paint (Boccardo, 1993) processing industries.

The current challenges in water purification using ceramic filters are viruses since most ceramic filters have micro-sized pores through which the viruses can easily pass resulting in virus-caused outbreaks. In Kenya, hepatitis E outbreaks were recorded in 2006, 2007, and 2012 respectively and there is no guarantee that this will not happen again (Ahmed *et al.*, 2013; Bird *et al.*, 2008). The only way to prevent the recurrence of such outbreaks is to come up with mechanisms that can remove viruses from the water accessible to the majority of the citizens. Currently, viruses can be eliminated from water using adsorption mechanisms where electrostatic forces facilitate the negatively charged virus to get adsorbed on the positively charged filter membrane (Attinti *et al.*, 2010; Gutierrez *et al.*, 2009; Wegmann *et al.*, 2008a; Wegmann *et al.*, 2008b). Diatomaceous earth (DE) can be used to make filter membranes with uniform nano-scale pores that will adsorb water pathogens due to the electrostatic, Van der Waals forces, and hydrophobic interactions (Fewtrell *et al.*, 2005). It has also been reported that the drinking water filters made from DE can remove up to 80.0% - 99.9% of the viruses (Michen *et al.*, 2011). Due to the coarse porosity present in diatomaceous earth, the flowrates of the filter are usually high with no pressure pumps unlike in reverse osmosis and ultra-filtration processes (Greenlee *et al.*, 2009). The use of silver nanoparticles is also not needed in DE-based membranes as the spear-like pore endings physically destroy the pathogens adsorbed on the membrane's surface.

1.5 Activated Carbon

Activated carbon, is a substance derived from carbonaceous organic material. It can be made using physical and chemical methods (Rivera-Utrilla *et al.*, 2011). In the physical method, a carbonaceous material such as charcoal is furnace-heated under controlled temperature and pressure. The carbonaceous material is changed to activated carbon by physical and thermal alterations in a furnace giving rise to a product with a network of submicroscopic pores and a large surface area per unit volume that allows adsorption of organic and inorganic materials on its surface (Haydar *et al.*, 2003). Under the use of chemicals, the carbonaceous material is treated with either a strong acid or a strong base to gain increased surface area for absorption of contaminants (Zhao *et al.*, 2005). Over the years, activated carbon has shown to be a good adsorbent of pathogens and has been employed in the removal of different pollutants from fluids. It can remove pathogens from gasses and liquids due to its huge surface area and high porosity (Rivera-Utrilla *et al.*, 2011). In water, activated carbon has been employed in decontaminating wastewater (Zhao *et al.*, 2005) and other contaminants such as dyes (Pereira

et al., 2003; Considine *et al.*, 2001), acids (Rivera-Utrilla and Sánchez-Polo, 2002), *p* nitrophenols (Haydar *et al.*, 2003) and metals like Cr III, Cr IV, Cd (Jia and Thomas, 2000; Bautista-Toledo *et al.*, 1994) and copper ions (Jia and Thomas, 2000). Activated carbon has also been used in studying the effect of ozone treatment in ammonia removal (Park and Jin, 2005). Fabricating carbon-activated DE-based ceramic would highly improve the adsorption properties of the membranes.

1.6 Magnetic Field

The magnetic treatment is a physical water treatment that averts the use of chemicals such as chlorine that form by-products in water considered harmful to human and aquatic environment life. A magnetic field can be employed in water treatment by circulating contaminated water through a dynamic or static magnetic field and it has been used in water treatment for almost two centuries now but its development has been hampered by negative criticism (Baker and Judd, 1996a). Though there have been controversial views over the performance of the magnetic treatment, their continuous increase in the market seems to point out the efficacy of water treatment using magnetic fields. Many assertions over the effects of magnetic fields (MFs) in water have been made especially in changing the physicochemical properties of water, surface tension, pH value, and chemical equilibria (Cai *et al.*, 2009; Morimitsu *et al.*, 2000).

Flowing and static water was tested by (Tombacz *et al.* 1991) using MF ranging from 0.1 T to 0.8 T and it was found that the effect of MF is best observed in flowing water. Similar results were observed by (Kobe *et al.*, 2001) when they used a magnetic flux density of 0.5 T to carry out their experiments. Chang and Weng (2006) on the other hand, showed that when water flows through a magnetic field of 1.0 T to 10.0 T the hydrogen bond gets enhanced by 34%. Similar findings were found by Hosoda *et al.* (2004). They attributed the hydrogen-bond strength enhancement to increased electron delocalization in the hydrogen-bonded molecules. It has also been observed by many researchers that magnetic induction increased with an increase in the exposure time while the flux of water exerts minimal influence (Knez and Pohar, 2005). There have also been reports of the magnetic field being used in scale reduction (Gabrielli *et al.*, 2001) of calcium carbonate (Fathi *et al.*, 2006a; Botello-Zubiate *et al.*, 2004; Kobe *et al.*, 2001; Herzog *et al.*, 1989) and calcium sulfate from water pipes (Gehr *et al.*, 1995).

Despite the many studies done on the effect of MF on water, there is limited research focused on its applicability to water purification. However, pathogens such as *Escherichia coli* (Ji *et al.*, 2009a; Fojt *et al.*, 2004), *Leclercia adecarboxylata*, and *Staphylococcus aureus* (Fojt *et al.*, 2004) have been investigated outside water and MF was reported to reduce their multiplication. However, the effect of microbe (in water) multiplication has not been investigated. It is for the aforementioned reasons that we investigate the application of a static magnetic field and a composite water filter (diatomaceous earth and activated carbon) in the development of an effective point-of-use water purification system.

In this work, we seek to improve the mechanical strength of diatomaceous-based ceramic water filter membrane using plant-based organic binders and investigate its filtration efficiency with and without carbon activation. The ability of static magnetic field in decontaminating water is also investigated using *E. coli*, Rotavirus, and sodium fluoride as the contaminants.

1.7 Problem Statement

There is a population bulge, large-scale industrial and agricultural usage of water, that has caused a scarcity of potable water on the planet earth. This is something the entire world is struggling with. In the developing world, the diminishing water supply is often contaminated and the World Health Organization estimates that at least 2.3 million people die annually from waterborne disease in the third world countries with most of the deaths comprising mainly infants (eighty percent). Because of these challenges a lot of research has been focusing on water purification systems. This has yielded effective water purification systems, which unfortunately are too costly for developing countries. The affordable porous ceramic water filters that could have solved these challenges in developing countries are ineffective in virus purification and are mechanically weak. The use of a static magnetic field which is equally cheap is not accepted due to limited literature on its use in water purification. There is, therefore, an urgent need of fabricating effective, affordable, and durable point-of-use water purifiers capable of eliminating pathogens and fluorides.

1.8 Objectives

1.8.1 Aim

This work aims to investigate the use of plant-derived organic binders in improving the mechanical strength of diatomaceous earth-based composite membranes, the membranes' point-of-use purification efficacy, and the use of static magnetic fields in the purification of virus-contaminated, and fluoridated water.

1.8.2 Specific Objectives

The specific objectives of the study are to:

1. Characterize the raw materials (diatomaceous earth, plant-derived organic binders, activated carbon) used in the fabrication of the point-of-use water filter membranes;
2. Undertake morphological studies of the fabricated water filter membranes and study the effects of the plant-derived organic binders and firing temperature on physiomechanical properties of the membranes;
3. Assess experimentally and through theoretical models the effectiveness of the membranes in filtering. *E. coli*, Rotavirus, and sodium fluoride (fluoridation) contaminants respectively;
4. Carry out a comparative study on diatomaceous earth-based and Potters' clay-based membranes;
5. Assess the effect of static magnetic field on the purification of *E. coli*, Rotavirus, and sodium fluoride.

1.9 Justification

Despite the great strides in the twentieth century, water-borne diseases remain a challenge in developing countries because of poor sanitation, improper disposal of industrial waste, and poverty. The more easily accessible ceramic water membranes are characterized by low mechanical strength, relatively large pores, and inefficient in virus filtration and defluoridation. Therefore, an affordable, portable, nanoporous, and mechanically strong point-of-use (POU) water purification system is needed. This work seeks to develop a water purification system based on a composite membrane fabricated from diatomaceous earth waste, molasses, and organic binders from local weeds. Its efficiency in the purification is

tested using contaminants in the absence of and in the presence of a 0.8 T static magnetic field.

1.10 Significance

Over the years, viruses, and fluoridation have presented challenges in water purification systems. This work seeks to develop a cheap composite water purification system that would be capable of removing most pathogens in water including viruses, and simultaneously address the fluoridation challenge. Hence contribute to the availing of adequate potable water to many people at the point of use; which is one of the Sustainable Development Goals (SDGs) (SDG number 6). This low-cost water treatment system will use local material; activated carbon, diatomaceous earth, and an organic binder to make a composite porous media.

CHAPTER TWO: LITERATURE REVIEW

2.1 Approaches Used in Water Filtration

Filtration approaches are processes used to remove contaminants from water by passing the water through a permeable membrane (Clark and Elmore, 2011; Bielefeldt *et al.*, 2009). Potable water is drawn from various sources such as rivers, freshwater lakes, wells, boreholes, rainwater storage tanks, and ponds but often contains contaminants. There are several approaches used in water filtration; ultrafiltration, nanofiltration, forward filtration, microfiltration, and reverse osmosis. These techniques remove most of the contaminants in water (Al-Bastaki, 2004; Campos *et al.*, 2002; Majewska-Nowak *et al.*, 2002). Filtration is contaminant-size dependent. Therefore the process depends on various factors such as the type of material used to fabricate the filtration membrane, pore structure and size, fabrication techniques, the driving force or pressure, and the type and concentration of contaminants.

2.1.1 Microfiltration

Microfiltration can be pressure-driven or use gravitational force and can filter contaminants of less than 0.2 μm (see Figure 2.1) (Werber *et al.*, 2016; Qu *et al.*, 2013). In waste treatment, microfiltration is used as the initial pre-treatment in preparation of more sensitive processes like ultrafiltration, reverse osmosis, nanofiltration, reverse osmosis ultrafiltration, and forward filtration to reduce fouling. However, microfiltration is incapable of removing viruses multivariate, and monovalent dissolved ions unless when combined with other techniques such as disinfection (Torkiet *et al.*, 2017). Examples of microfilters such as ceramics are discussed in Section 2.2.

2.1.2 Ultrafiltration

Ultrafiltration is a highly sensitive approach that can remove tiny contaminants such as viruses as demonstrated in Figure 2.1 (Qu *et al.*, 2014). Apart from its sensitivity ultrafiltration approach consumes relatively low energy as compared to reverse osmosis and removes macro-molecules, microorganisms, and suspended contaminants from water (Krüger *et al.*, 2016). Recently hybrid ultrafilters have been fabricated by impregnating hydrophilic materials onto a polymer surface to get a hydrophilic hybrid surface membrane. Some researchers such as (Mocanu *et al.*, 2017) used polysulfone and graphene nanoplatelets to fabricate a synthetic hybrid membrane for water treatment; others like (Zhang *et al.*, 2016) used wet-phase inversion and deposited zinc oxide on a one-sided soluble membrane

(Mocanu *et al.*, 2017). Igbinigun and colleagues, on the other hand, used UV-induced amination to modify the germanium oxide membrane which was 2.6 times better than the unmodified membrane in recovering flux in greywater because of its ability to resist organic fouling (Igbinigun *et al.*, 2016). However, ultrafiltration membranes are prone to clogging, high-cost regeneration and they are unable to remove dissolved contaminants in water (Zhang *et al.*, 2016).

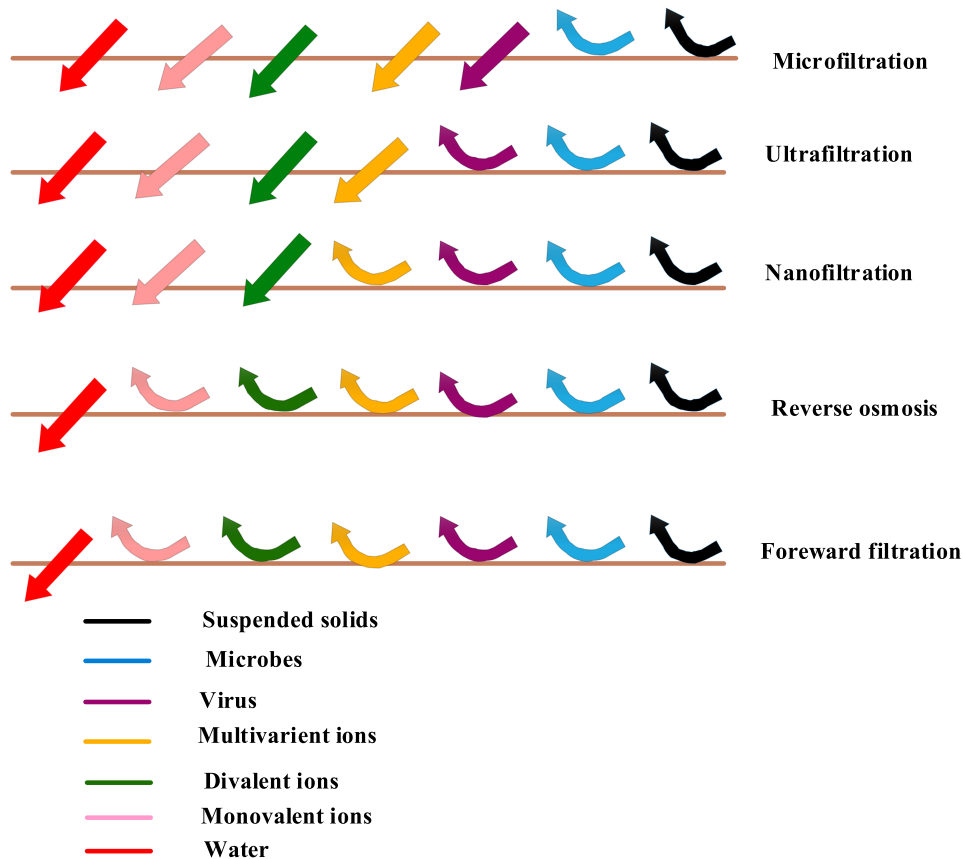


Figure 2.1: Schematic showing the types of contaminants filtered by microfilters, ultrafilters, nano-filters, reverse osmosis filters, and forward filters

2.1.3 Reverse Osmosis

Reverse osmosis membranes are highly sensitive membranes that remove all contaminants from water and only allow water molecules to pass through them (see Figure 2.1). Just like ultrafiltration, reverse osmosis uses pressure to overcome osmotic pressure which enables the membrane to remove dissolved contaminants and nano-sized particles. The pore structure of the reverse osmosis membrane is the main reason for its high effectiveness as it has smaller pores less than 1.0 nm capable of eliminating all bacteria, particles, and microorganisms

(Wood *et al.*, 2017). In their work on reverse osmosis membrane, Huang and others showed that effective antibacterial and hydrophilic membranes can be achieved using azide functionalized graphene oxide thereby giving rise to reduced fouling and high anti-bacterial sensitivity (Huang *et al.*, 2016). However, due to the extremely small pores of around 0.1 nm (Yan *et al.*, 2016), reverse osmosis membranes over-purify water by removing important ions in water. Other disadvantages include; the exorbitant cost of maintaining high pressure during filtration and fouling challenges. To avoid clogging of the membranes, pre-treatment is also required (Liu *et al.*, 2017).

2.1.4 Nanofiltration

Nanofiltration uses lower pressure than reverse osmosis and its pore size is around 0.001 μm (Otero *et al.*, 2008). The capability of nano-filters to remove divalent ions makes these membranes handy in water softening. However, research by (Yang *et al.*, 2017) on composite nanofiltration membranes shows that water filtered by composite membranes with hydrophilic surfaces gave rise to a purer water flux than nanofiltration membranes made from a pure polymer. The composite membrane was also characterized by high fouling resistance and dye rejection (Yang *et al.*, 2017). In another research on wastewater treatment in the textile industry, Xu and others showed high removal efficiency of dyes, heavy metals, and common salts (Xu *et al.*, 2015; Xu *et al.*, 2014). In similar research, (Lin and Juang, 2002) showed low salt rejection but high dye rejection by composite nanofiltration membranes. Unfortunately, soluble heavy metals are not removed by nanofiltration and it is also ineffective in purifying heavily polluted waters. For effective purification of heavily polluted water, pre-treatment procedures are required (Wang *et al.*, 2016) which further raises the costs.

2.1.5 Forward Filtration

Forward filtration is made up of a permeable membrane that allows the movement of contaminants from a low concentration region to a high concentration region (Ong *et al.*, 2017). Forward filtration is generally known for its high efficiency just like reverse osmosis because it is capable of removing monovalent microbes at a low rate of production of brine. The main drawback of forwarding filtration is the high cost of regeneration of the draw solution (Blandin *et al.*, 2016).

Most of the above filters; forward, nano, reverse osmosis, and ultrafilters are costly. This study will focus on microfiltration, particularly on low-cost ceramic membranes.

2.2 Ceramic Water Membranes

Ceramic water filters (CWFs) are examples of microfilters discussed in Section 2.1.1. CWFs are normally made from clay and sawdust or any other organic material that can easily burn off during firing. The raw materials used to fabricate the ceramic water filters are cheap and easily available and this makes their application handy. Moreover, the making of these ceramic filters does not require any long technical training and complicated procedures (Hunter, 2009). The World Health Organization recommends that household water membranes should filter at least 99.9% of *E. coli* from water (Fewtrell and Bartram, 2001). Several researchers have fabricated membranes that have achieved recommended levels (Yakub *et al.*, 2013; Van der Bruggen and Vandecasteele, 2003). Sobsey *et al.* (2008) confirmed that CWFs can remove *E. coli* from the water up to 99.9% but can only remove water viruses up to 95.0 % (Sobsey *et al.* 2008). Lantagne and colleagues showed that CWF can remove 10^4 CFU/ml of protozoa, and were capable of preventing diarrhea diseases (Lantagne *et al.*, 2010; Lantagne *et al.*, 2008). Thus, CWF would be best suited as a point-of-use household water treatment method in less developed countries (Hunter, 2009).

In a study carried out in three countries: Bolivia, Cambodia, and Colombia, CWFs were given to individuals in these countries and the results indicated a 50.0% decrease in diarrheal illnesses (Brown *et al.*, 2008; Clasen *et al.*, 2005; Clasen *et al.*, 2004). It has also been reported that incorporating hydroxyapatite or metal oxides in ceramic membranes improved their efficiency in filtering chemical and heavy metal contaminants (Yakub and Soboyejo, 2013). The same research by Yakub and Soboyejo (2013) reported a 93.7% efficiency in removing fluorides from contaminated water when the hydroxyapatite was incorporated in the ceramic, while Bhatnagar *et al.* (2011) reported a 97.5% removal efficiency of a similar contaminant. The improved efficiency was attributed to the substitution of hydroxyapatite with the metallic elements in the clay (Yakub and Soboyejo, 2013). The hydroxyapatite ($\text{Ca}_{10}(\text{PO}_4)_6(\text{OH})_2$) exchanges its phosphate ions with sodium or potassium ions during sintering forming more stable structures. Furthermore, hydroxyapatite is made up of nanosized crystallites with a large surface area ($100 \text{ m}^2/\text{g}$) that encourages the adsorption of contaminants (Verwilghen *et al.*, 2007).

Coating CWF with silver nanoparticles improves microbe removal efficiency from water (Halem *et al.*, 2009). However, the notion of improved microbe removal efficiency is not accepted among all researchers as some have reported no significant difference between plain

CWF and silver nanoparticle-coated CWF (Lucier *et al.*, 2017; Bielefeldt *et al.*, 2009). Lantagne and his colleagues reported that coliform removal was the same in plain CWF and silver nanoparticle-coated CWF (Lantagne *et al.*, 2010). The study by Laan *et al.* (2014) showed not much difference in *E. coli* log removal values (LRV) between the plain CWF (0.6 to 3.5 LRV) and silver nanoparticles coated CWF (0.5 to 3.1 LRV). Laan *et al.* (2014) also reported similar results with bacteriophages when plain CWF showed 0 to 1.4 LRV and silver nanoparticle-coated CWF showed 0.1 to 1.0 LRV. In another study using different thicknesses of silver nanoparticles, it was found that 0.003 mg/g and 0.3 mg/g of silver nanoparticles gave an insignificant difference in the microbe removal efficiency (Rayner *et al.*, 2013). However, it has been pointed out that different types of clay could have a major contribution to microbe removal efficiency (Rayner *et al.*, 2013). This implies more work on the filtering characteristics and microbe removable for domestic water needs to be done to show the efficiency of ceramic water filtration (CWF) without the use of silver nanoparticles.

2.2.1 Mechanical Strength of Ceramic Water Membranes

The mechanical strength of the porous ceramic membranes depends on factors like particle size pore-forming material and clay powder, additives like binders, membrane size, and sintering temperature (Ahmed, 2017; Lantagne *et al.*, 2010).

2.2.1.1 Particle Size

The particle size affects the agglomeration of the green ceramic, drying, sintering, and filtration efficiency of the porous ceramic. In this section, we focus on how particle size affects mechanical strength and filtration efficiency. A study by Soppe 2015 showed that clay powder with particles less than 10 μm resulted in a high mouldability of green ceramic when an adequate amount of water was added to it (Soppe *et al.*, 2015). Mono-sized powders produce dense, fine, uniform-grained ceramics (Ting and Lin, 1994a). Chappell *et al.* (1998) theoretically showed that particle-size distribution and time were crucial in the initial and intermediate stages of sintering (Chappell *et al.*, 1986). Silica was reported to show uniform controlled sphere-like particles when mixed in different solutions such as ammonia, ethanol, or water (Edelson and Glaeser, 1988). Increasing the monodispersed micro-sized particles by 2.0% intervals, perfect packing of the ceramic was achieved (Sacks and Tseng, 1984a; Sacks and Tseng, 1984b). These packings were used to develop different pore models based on their distribution, geometry, and orientation (Matijevic *et al.*, 1996). However, some questionable

results were obtained in developing the models. For instance, two regressions were found while plotting bulk density against sintering time. The first linear regression was a result of closing the pore channels of the small particles while the second regression was caused by closing large pore channels. Another explanation given for the questionable results was that there were not enough contact points for the packing density. That is, most of the particle material was not in contact with neighbouring particles. Thus, the sintering did not reach its maximum (Sacks and Tseng, 1984a; Sacks and Tseng, 1984b). Once the particles came in contact with the neighbouring particles the sintering process increased. Other researchers reported that the sintering time has a positive relationship with densification and increases with the square diameter of the silica particles as shown in Figure 2.2 (Giesche, 1994; Giesche and Matijević, 1994). However, Giesche and Matijević (1994) carried out the sintering in an open atmosphere where impurities could have interfered with the process which resulted in low silica density ranging from 1500 Kgcm⁻³ to 1900 Kgcm⁻³ instead of the theoretical value of 2200 Kgcm⁻³. The impurities have microorganisms that contain a hydroxyl group that introduces water vapor to the material being sintered (Giesche and Matijević, 1994). These findings have stimulated the production of approximately mono-sized powders and, also, elevated the studies on how narrow particle-size distribution is ideal (Coble and Kingery, 1956).

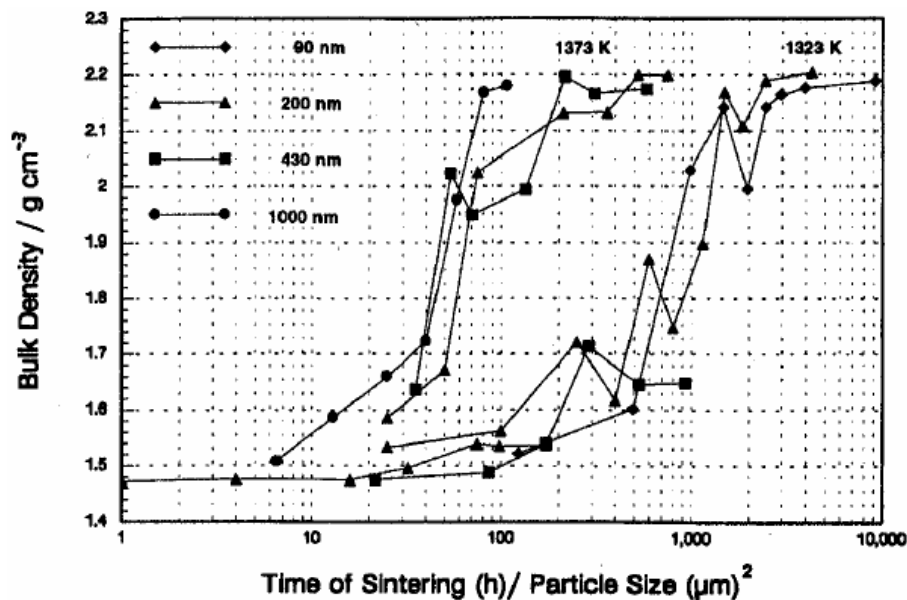


Figure 2.2: Plot of bulk density against sintering time in hours and particle size in μm of silica (Giesche, 1994; Giesche and Matijević, 1994)

Another work, (Coble, 1973), looked at the initial stage of sintering and developed the diffusion model that explained densification in this stage. The model explained diffusion at the lattice, and the grain boundary and predicted that with an introduction of interstitial particles, the sintering rate increased by 25.0% in binary mixtures. However, his prediction did not have an experimental backup and the particle-size distribution was not considered in the model. Thus, making it difficult to predict the powders' kinetics sintering behavior. Chappell et al., (1986) developed a model that explained densification in both the initial and intermediate stages of sintering. The model predicted a decrease in the rate of sintering with an increase in the distribution of particles at the initial and intermediate stages of sintering (Chappell *et al.*, 1986). The findings of Chappell and colleagues were contrary to the model of bimodal powders and Coble's model (Kwon and Messing, 1998; Ting and Lin, 1994a). And just like Coble's model Chappell's model also lacked experimental backup. Ting and Lin, (1994) later showed that finer powders increased the rate of sintering which was attributed to the high driving force generated by them. They further showed that densification depended on the particle-size distribution in all stages of sintering. They explained that before grain growth, the rate of densification increases with a decrease in particle-size distribution but once the grain growth takes place, densification decreases as particle-size distribution increases (Ting and Lin, 1994a). Their finding was further supported by their experimental work where they used alumina to study the effect of particle-size distribution on sintering (Ting and Lin, 1994b). Therefore it is important to consider the particle size of the ceramic powders and their distribution while fabricating mechanical viable porous ceramics.

2.2.1.2 Porosity

There is a need to balance between mechanical strength and porosity for any ceramic that is used as a water filter; the mechanical strength needs to be high enough to bear the weight of water meant for filtration, besides being able to withstand handling during installation and regeneration when this is done. The porosity of ceramic membrane is affected by so many factors among them is the type of clay and burn-out material among others. Rayner *et al* (2016) studied the effects of input materials on ceramic water filter efficacy for household drinking water treatment and showed that different clay powders formed ceramics with different densities. The ceramic density also varied according to the type of burnout material with membranes produced from rice husks being denser than membranes fabricated from sawdust. They also noted that density and porosity had a strong negative correlation (Rayner

et al., 2017). The burnout material is key in fabricating porous ceramics as it determines its porosity and its mechanical strength. There are many studies on porous ceramic materials used for load-bearing application and filtration fabricated from clay powder. Using hydroxyapatite porous ceramics, Huec *et al.*, (1995) investigated the effect of burn-out material on porosity and compressive strength and they noted that an increase in burn-out material increased porosity which corresponded with decreased compressive strength of hydroxyapatite porous ceramics. Similarly, Liu, (1997) using polyvinyl butyral as a burnout urgent in hydroxyapatite porous ceramics investigated the effect of pore size and porosity on the compressive strength and reported a range of pore diameter and porosity as 0.093 mm to 0.420 mm and 0.33% to 0.78% and respectively as shown in Figure 2.3. The study further showed materials with large pores were characterized by low compression strength while materials with smaller pores showed high compression strength (Liu, 1997).

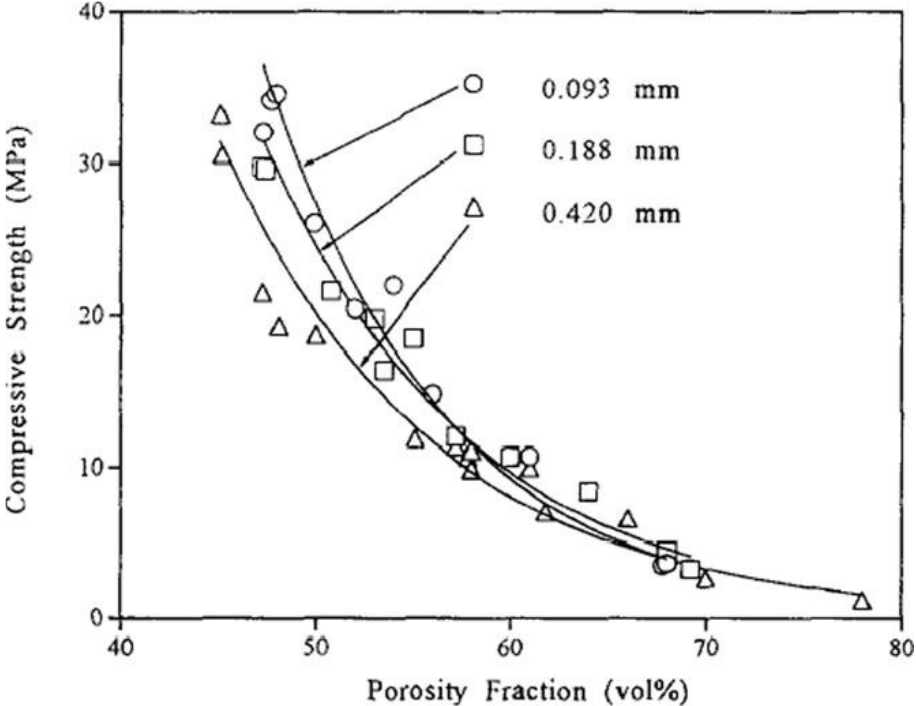


Figure 2.3: The plot of compressive strength against fraction porosity of porous hydroxyapatite ceramics (Liu, 1997). The dimensions of different sizes of pore-forming material are given

The porosity and compressive strength relationship had earlier been derived by Rice, (1996a) of the form.

$$\sigma = \sigma_o \exp(-b\varepsilon_p) \tag{2.1}$$

where σ was the compressive strength, ε_p was the fraction porosity, σ_o was the initial compressive strength of fully dense material and b was the constant associated with the pore shape. Most of the ceramic membranes discussed above have been fabricated from clay yet diatomaceous earth is a good material for the filtration (Gitari *et al.*, 2020; Gitari *et al.*, 2020; Izuagie *et al.*, 2016b; Izuagie *et al.*, 2016a; Bello *et al.*, 2014; Michen *et al.*, 2012; Wambu *et al.*, 2011; Akhtar *et al.*, 2010; Bhardwaj and Mirliss, 2005; Fulton, 2000b; Farrah *et al.*, 1991; Sanchis *et al.*, 1951). However, studies in water filtration using diatomaceous earth have used it as loose particles (Bello *et al.*, 2014; Bhardwaj and Mirliss, 2005; Fulton, 2000a; Farrah *et al.*, 1991) but when used as ceramic water filters their mechanical strength needs to be established. The few researchers who have fabricated ceramic membranes with this material did not consider incorporating a burn-out material in DE (Izuagie *et al.*, 2016b; Izuagie *et al.*, 2016a; Michen *et al.*, 2012; Michen *et al.*, 2011). Therefore, there is a need to assess the performance of ceramic water membranes fabricated with a burnout material.

2.2.1.3 Effect of Organic Binders

The use of organic additives can also improve the mechanical properties of porous membranes. In 1997 Baklouti and his colleagues used polyethylene glycol and polyvinyl alcohol organic binders to enhance the adhesive and mechanical properties of the polymer-rich external layer of spray-dried granules (Baklouti *et al.*, 1997). Aduda *et al.*, (1999) also reported that the bulk density and modulus of rupture increased in green and fired kaolinite when the *Corchorus olitorius* organic binder was used in ceramics meant to make charcoal stoves linings. The use of organic binder extracted from the *Corchorus olitorius* has also been effective in improving the thermal conductivity of the kaolinite refractory (Ogacho *et al.*, 2006). Other researchers (Lyckfeldt and Ferreira, 1998) reported that chemically modified starch enhanced mechanical properties and could be applied in the manufacture of filter membranes. More research has been done on the effects of organic binders extracted from *Abelmoschus esculentus* and *Corchorus olitorius* on fracture toughness/strength and the two organic binders were found to improve the toughness of the fired ceramic (Njogu *et al.*, 2008). The thermal shock of kaolin-based refractories was also improved (Njogu *et al.*, 2008; Ogacho *et al.*, 2006b). However, the behavior of organic binders has not been studied in diatomaceous earth based-ceramics intended for water filter membranes.

2.2.1.4 Firing Temperature

The firing temperature of a ceramic water filter is one of the factors affecting its mechanical properties, microstructure, and porosity. Research on CWF has confirmed the importance of firing temperature on mechanical properties, microstructure, and porosity. Andrade *et al* (2019) showed that an increase in firing temperatures results in a mass loss in the membranes. The initial mass loss of around 3.2% that occurred between 50.0 to 420.0 °C was attributed to the evaporation of adsorbed water in the green ceramic and the volatilization of organic matter. The second mass loss of around 2.2 % that occurred between 420.0 °C to 600.0 °C was attributed to the dehydration of kaolinite which resulted in metakaolinite. In the same work, Andrade *et al* (2019), reported that apparent porosity increased as the firing temperature increased from 800.0 °C to 900.0 °C and decreased as shown in Figure 2.4 which also showed that apparent density decreased as the firing temperature increased from 800.0 °C to 900.0 and increased at higher firing temperatures. They attributed the increase in porosity and decrease in porosity to the volatilization of the burn-out (sugarcane bagasse ash). The 30.8% porosity decrease was reported at firing temperatures between 900.0 °C to 1000.0 °C attributed to the liquid phase sintering that filled up some pores caused by the fluxing agent such as feldspar, mica, and other silicates that were present in their raw materials (Andrade *et al.*, 2019).

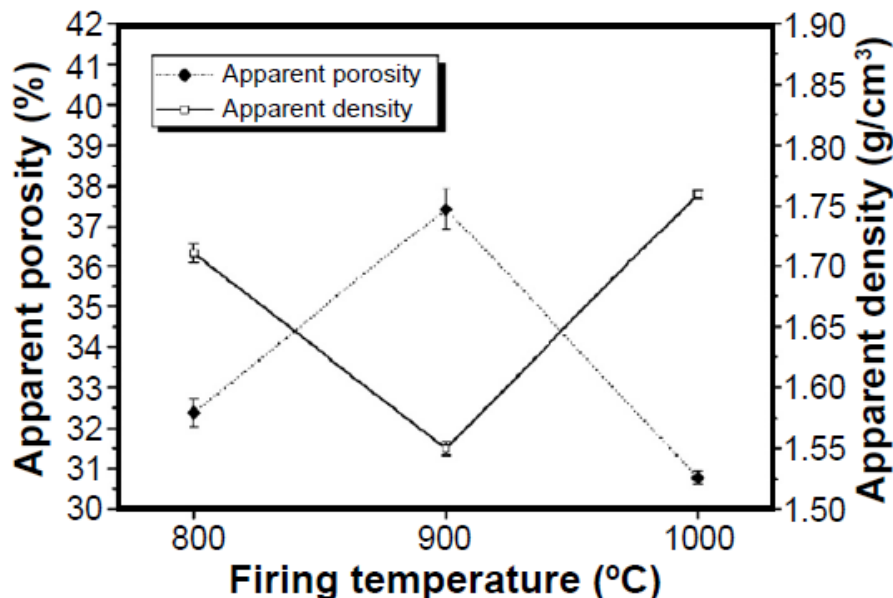


Figure 2.4: Plot of apparent porosity and apparent density against firing temperature of membranes fabricated from kaolinite clay and sugarcane bagasse ash (Andrade *et al.*, 2019)

Akhtar *et al* (2010) reported a density of 1.0gcm^{-3} for green ceramics which increased with increasing firing temperature as shown in Figure 2.5. Initially, the increase is gradual but the change in density becomes rapid beyond $1100.0\text{ }^{\circ}\text{C}$ firing temperature. The porosity of the monoliths, however, followed reverse trends with a gradual decrease in below $1100.0\text{ }^{\circ}\text{C}$ (Akhtar *et al.*, 2010). The monoliths were meant for water or air filtration.

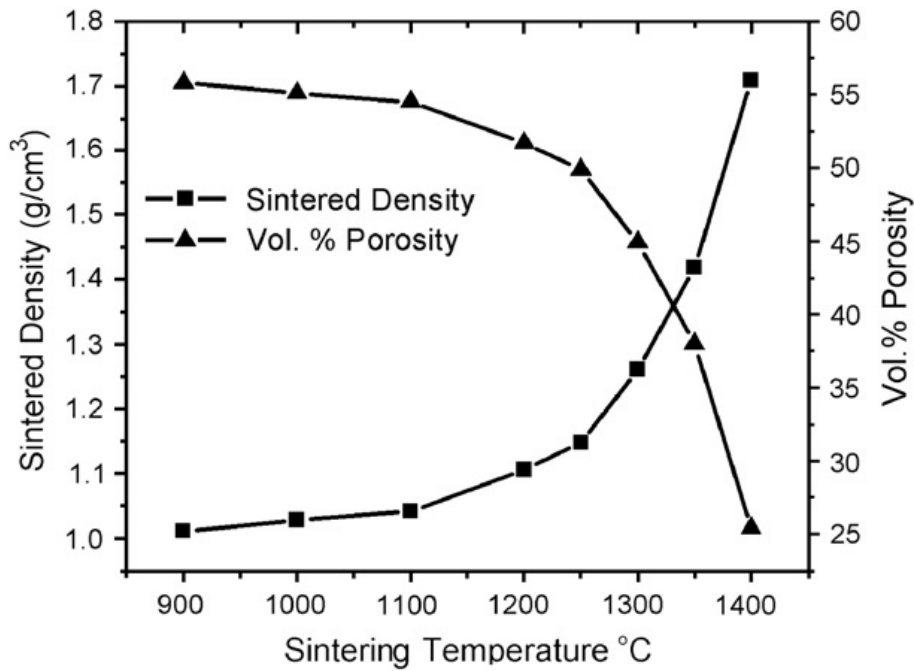


Figure 2.5: The plot of sintered density (g/cm^3) and porosity (vol.%) against sintering temperature ($^{\circ}\text{C}$) of diatomaceous earth monoliths (Akhtar *et al.*, 2010).

In the same work, Akhtar *et al* (2010) reported an increase in compression strength that accompanied the increase in density as the firing temperature increased as shown in Figure 2.6. They, therefore, recommended that the firing temperature of such monoliths (for application in water or air filtration) should not exceed $1000.0\text{ }^{\circ}\text{C}$ (Akhtar *et al.*, 2010). There is, therefore, a need to extend such research to different types of DE including DE-waste.

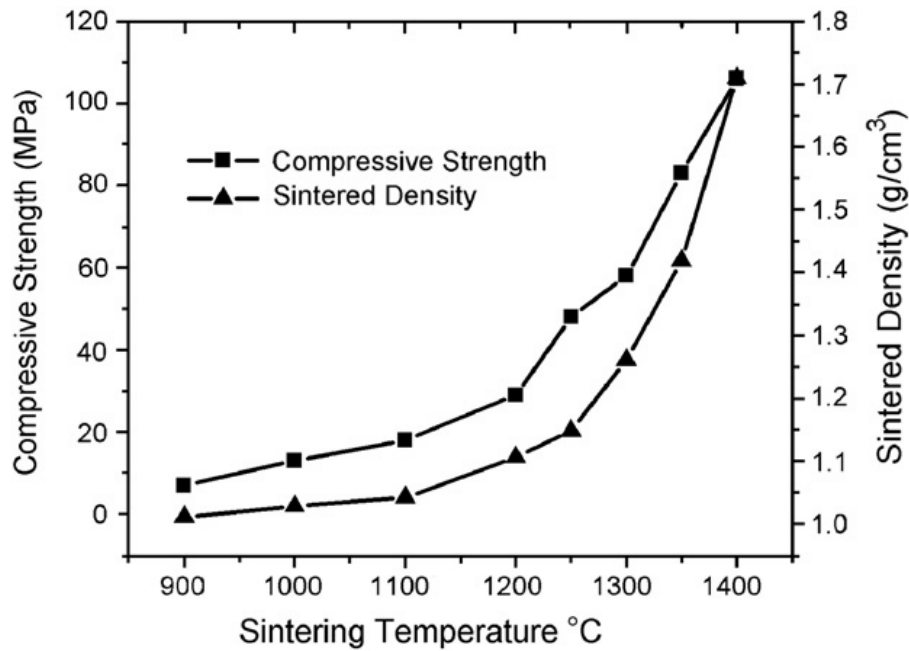


Figure 2.6: The plot of compressive strength and sintered density against the firing temperature of diatomaceous earth monoliths (Akhtar *et al.*, 2010)

2.2.2 Factors Affecting Water Filtration Efficiency

2.2.2.1 Materials' Ratio

The ceramic water filter membranes' raw materials, usually clay powder and burn-out are initially mixed in given ratios to form a homogeneous clay-burnout mixture. However, it shall be shown later in this work ceramic can also be made from other powders apart from clay. The clay powder is usually the main ingredient molded to a given shape forming the filter after firing. The burn-out material such as sawdust, charcoal, and rice husks burn during firing creating pores in the clay matrix of the fired membrane. Consequently, the ratio of these raw materials affects the flow rate and efficiency of the membrane. The more the burnout material the more the porosity, and if the amount of the burnout is not controlled the bacteria in water will pass through the filter during filtration. Akosile *et al* (2020) reported that the membranes fabricated from clay and sawdust ratios of 50:50, 40:60, and 30:70 showed high flow rates and microbial removal efficiency (coliform bacteria and *E. coli*) of more than 75.0% except for 30:70 ratio (Akosile *et al.*, 2020). Kallman *et al* (2010) showed that an increase in the burnout material (sawdust) from 4.0% to 17.0%, resulted in a decrease in bacteria removal (Kallman *et al.*, 2010). Soppe *et al* (2015) reported that an increase in burnout (milled rice husks) in pot filters increased the average flow rates. However, there was an uncorrelated relationship between Log Removal Values (LRV) and the burnout material (Soppe *et al.*,

2015). Yakub *et al.* (2013b) observed an increase in permeability when ceramic pots were fabricated with 35.0% and 50.0% (by volume) sawdust with the average LRV of 6.36 ± 0.54 and 5.67 ± 2.50 respectively (Yakub *et al.*, 2013). The large variance in LRV reported for pots fabricated with 50.0% sawdust, implied that pots were heterogeneous, making the data difficult to compare with the pots fabricated with 35.0% sawdust. Furthermore, there was no trend in the relationship between burnout material and filtration efficiency in the work reported by Rayner *et al.* (2017). Their disk-shaped membranes fabricated from 13.7%, 17.0% and 24.0% sawdust (by weight) of particle size range $250.0 \mu\text{m} - 595.0 \mu\text{m}$ posted an efficiency of average LRV of 2.06 ± 1.33 , 4.00 ± 0.29 , and 2.78 ± 0.16 respectively making the data inconclusive (Rayner *et al.*, 2017). The trend was also not established when the same authors used milled rice husks with pots made of 18%, 19%, and 25% (by weight) milled rice husks recording LRV of 1.93 ± 0.11 , 1.26 ± 0.17 , and 1.26 ± 0.10 respectively (Rayner *et al.*, 2017). The variability reported by Rayner *et al.* (2017), was less than those posted by Yakub *et al.* (2013). Thus the findings show that once the ratio of the raw materials (clay to burnout) can balance the mechanical strength/porosity relationship, the efficiency of the membrane will not be compromised. Other factors that affect the efficiency of the membranes are additives, particle size, membrane thickness, and firing temperature.

2.2.2.2 Particle Size of Raw Materials

The particle size of the raw materials such as clay powder and the burn-out material (sawdust, charcoal, or rice husks) plays an important role in the membrane's porosity and eventually its filtration rate since size exclusion is one of the mechanisms used in water filtration. Earlier research investigating relationships between particle size of clay and bacteria reduction has shown that membranes fabricated from fine-grained powder with uniform particle size distribution reported better efficiency in bacteria reduction than membranes fabricated from clay powder comprising larger, non-uniform particles (Oyanedel-Craver and Smith, 2008).

Venis and Basu (2020) noted that only five out of 21 studies they analyzed, considered particle size of the burn-out material as a contributing factor in the efficiency of water membrane (Venis and Basu, 2020). Thus, research is needed to improve the understanding of burn-out materials' particle size in water filtration. Soppe *et al.* (2015) reported a decrease in log reduction value (LRV) of *E.coli* as the particle size of the burn-out material increased. Membranes fabricated from rice husks with the particle size (medium) of $2.8 \mu\text{m} \pm 0.7$ had an average flow rate of 3.0 L/h. and membranes made from a medium of $0.7 \mu\text{m} \pm 0.2$ had an

average flow rate of 10.1 L/h (Soppe *et al.*, 2015). Servi *et al.* (2013) reported LRV of 3.05 ± 0.80 , 2.04 ± 0.50 , and 2.77 ± 0.8 when they used materials of particles sizes of 388.0 μm , 505.0 μm , and 650.0 μm respectively but the LRV reduced drastically when the average particle size was more than 780 μm (Servi *et al.*, 2013). Thus membranes fabricated from small particles of burn-out material have high efficiency in removing contaminants from water. However, Rayner *et al.* (2017) showed undesirable results from membranes fabricated with 13.7% by mass of sawdust. The sawdust had different ranges of particle sizes 0.250–0.595 μm , 0.595–1.19 μm , and 1.19–2.38 μm yielding LRV of 2.06 ± 1.33 , 4.43 ± 0.402 , and 1.87 ± 0.261 respectively. This result indicated no predictable relationship between particle size and LRV (Rayner *et al.*, 2017). Other researchers have also reported similar undesirable trends in the relationship between burn-out material particle size and LRV of filtered water (Scannell, 2016; Varkey and Dlamini, 2012). Even though the particle size of burn-out material is important in membrane efficiency there are equally other factors that need to be considered and are discussed in the following sections.

2.2.2.3 Membrane Thickness

Servi *et al.* (2013) discussed the effect of ceramic membrane thickness on LRV and observed that as the thickness of the ceramic discs increased from 3.0 mm to 20.0 mm, the LRV increased linearly from 0.0 to 0.6 (Servi *et al.*, 2013). The increase in LRV was attributed to an increased ceramic matrix which provides a large surface area for the contaminant adsorption. However, the thickness has to be controlled as increased thickness reduces the mechanical property of the membrane due to increased pores that act as sources of weakness.

2.2.2.5 Firing Temperature

The firing temperature affects both the porosity, mechanical properties, and flow rate of the membrane. Thus, firing temperature affects the efficiency of the membranes. Soppe *et al.* (2015) studied the impact of firing temperature on LRV and noted a slight decrease in LRV (2.3, 2.1, and 1.9) as the firing temperature increased 800.0 °C, 885.0 °C, and 950.0 °C respectively (Figure 2.7). There was a strong correlation between the firing temperature and membranes' flow rate for the pots fired at 800.0 °C. When the firing temperature increased to 950.0 ° the flow rate decreased from 8.0 L/h to 3.8 L/h.

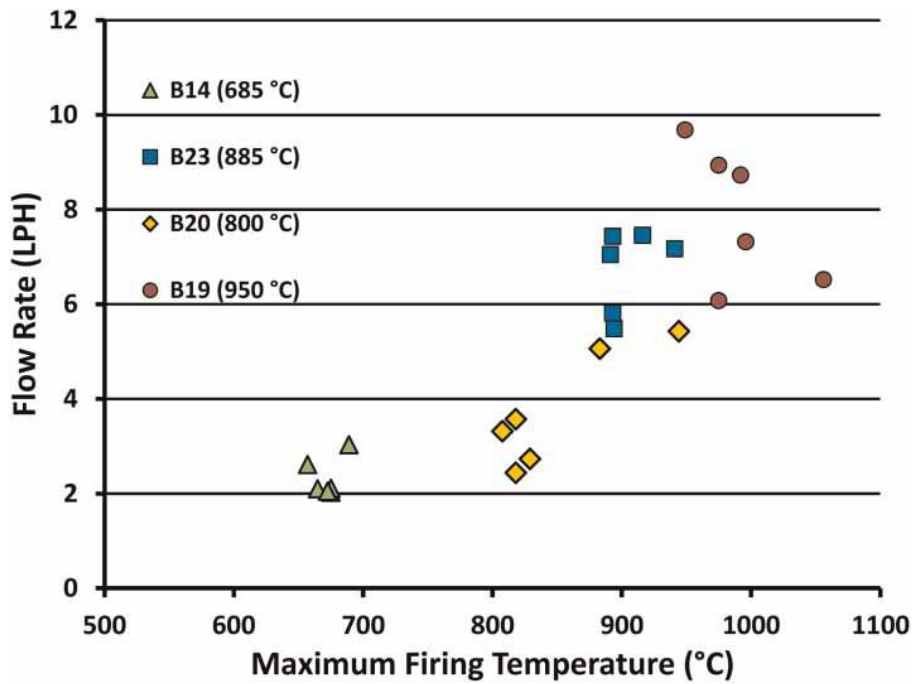


Figure 2.7: The plot of flow rate against firing temperature of porous ceramic pots. B14, B19, B20, and B23 represent the different sample batches. (Soppe et al., 2015)

Increasing firing temperature from 800.0°C to 950.0 °C resulted in very little effect on the bacterial removal efficiency of the membranes such that pots fired at 800, 885 and 950 °C had an average LRVs of 2.3, 2.1 and 1.9, respectively. The small decrease in LRV was attributed to the increase in the pore size (27.8 μm, 28.9 μm, and 30.6 μm) of membranes fired at 800.0 °C, 885.0 °C, and 950.0 °C respectively.

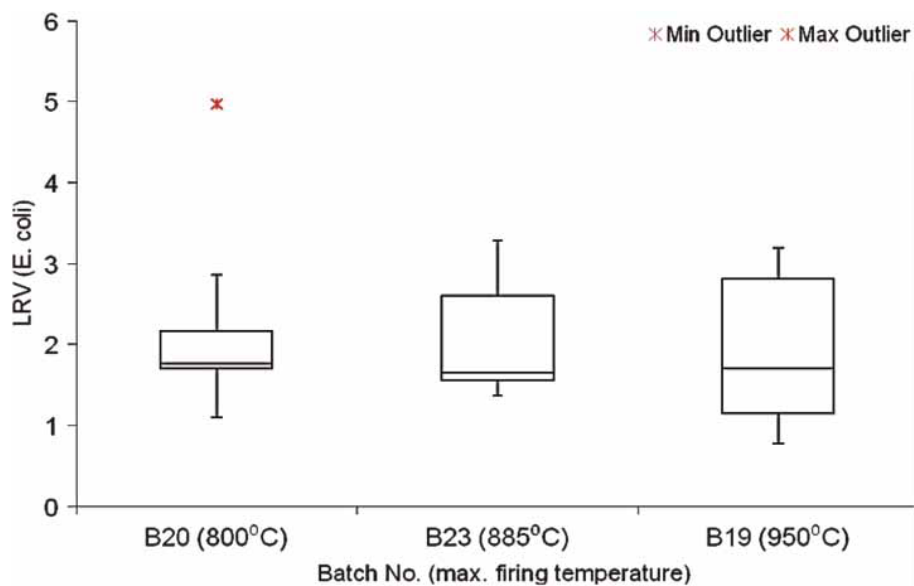


Figure 2.8 The plot of log reduction values (LRV) against firing temperature of filter pots. B19, B20, and B23 represent the different sample batches (Soppe et al., 2015)

Andrade *et al* (2019) reported that permeability and the mean pore size of membranes increased with an increase in firing temperature as shown in Figure 2.9. The fabricated membranes when used as filters reduced the color, turbidity, and pH of the filtered water by 13.0%, 25.0%, and 18.0% respectively. Therefore there is a need to extend the research on the relationship between firing temperature and LRV to concisely elucidate the design parameters that influence the filter performance.

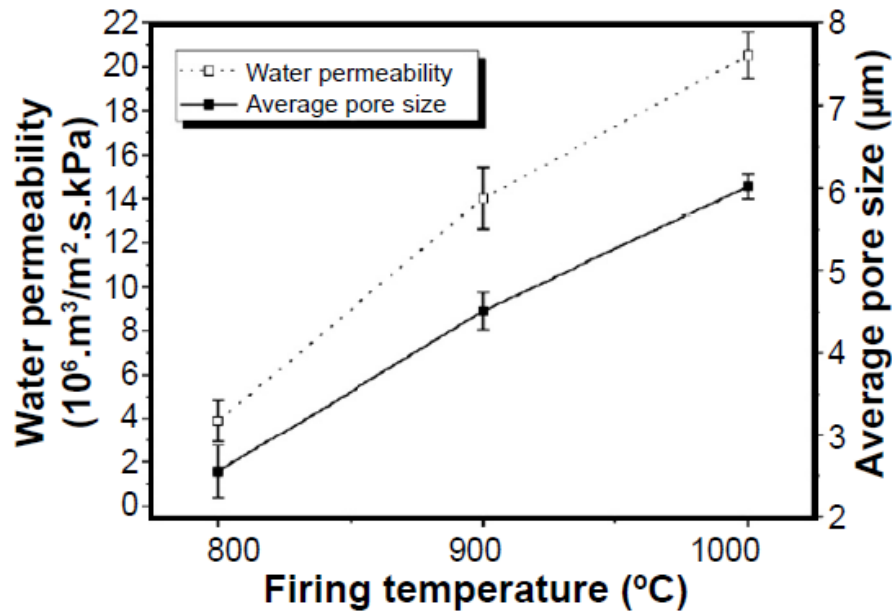


Figure 2.9: Plot of permeability and average pore size against the temperature

2.3 Filtration Models

The efficiency of ceramic membranes in terms of flow rate, permeability, and LRV can be modeled using the existing models (Hatori and Suzuki, 2021; Iritani and Katagiri, 2016; Annan *et al.*, 2014; Schweitzer *et al.*, 2013; Yakub *et al.*, 2012; Van Halem, 2006). Most of these works base their models on the Darcy modified equation

$$J = \frac{N\pi d_m^4 \Delta P}{128\mu L} \quad 2.2$$

where N is the number of tubes per unit of filtration area, ΔP is the change in pressure between the two ends of one of the uniform tubes, μ [Pa.s] stands for the viscosity of the water under filtration, and L [m] represents the tube length (Hatori and Suzuki, 2021; Yakub *et al.*, 2013; Yakub, 2012; van Halem *et al.*, 2009). Yakub (2012) for instance looked at water

flow mechanisms in the frustum-shaped membranes made from varying sawdust content. The flow rate characteristics were considered both at the base and the sides of the membranes (Yakub *et al.*, 2013). However, their work on models did not consider all the statistical parameters in the Darcy equation and its applicability in case the membranes were used to filter water multiple times. In another work, Schweitzer *et al.* (2013) deduced equations that can be used to describe flow rate in both parabolic-shaped and frustum-shaped ceramic membranes. The equations were valid only if the membrane thickness was uniform. They found out that apart from clogging, the number of runs also affected the efficiency of membranes (Yakub *et al.*, 2013a). However, Yakub and colleagues did not fully explain how flow rate, permeability, and or hydraulic pressure are statistically related under multiple runs. Annan *et al.*, 2014, fabricated six different membranes from Ewuya and Iro clays and used them to filter tap water for twelve hours. They repeated the filtration twenty times and noted flow rate and permeability. The flow rate of 1.4 L/h to 3.0 L/h in the first four hours was noted. The flow rate decreased with an increase in time due to clogging and a decrease in hydraulic. The result indicated that flow rate depends on time and the variation of individual membranes. However, there was no clear trend in flow rate when the number of runs was varied up to twenty runs. The average permeability of the six membranes ranged between 0.44×10^{-14} m/s and 2.54×10^{-14} m/s, with an average hydraulic conductivity $k = 1.46 \times 10^{-7}$ m/s (Annan *et al.*, 2014). Halem (2006) also reported a hydraulic conductivity of 1.37×10^{-7} m/s and 1.3×10^{-7} m/s for membranes fabricated in Cambodia and Ghana respectively (Halem, 2006). Oyanedel-Craver and Smith (2008) also got similar values of hydraulic conductivity ranging from 1.15×10^{-7} m/s to 5.01×10^{-7} m/s for membranes fabricated from clay and flour (Oyanedel-Craver and Smith, 2008). Yakub *et al.* (2013) on the other hand reported a permeability range of 0.1×10^{-14} m/s and 5.0×10^{-14} m/s from frustum-shaped ceramic pots (Yakub *et al.*, 2013a). However (Soppe *et al.*, 2015; Schweitzer *et al.*, 2013; Yakub *et al.*, 2013a; Yakub *et al.*, 2012; van Halem *et al.*, 2009) did not explore the causes of fouling in ceramic membranes in detail.

The mathematical theories explaining fouling in ceramic membranes were first put forward by Ruth (1935) who established the mathematical background backing fouling in membranes under constant flow rate and pressure (Ruth, 1935). However, the equations were not fitted with data from real filters. In her later work, she established the equations that fitted the experimental data (Ruth, 1946). Other researchers also reported that fouling takes place either by pore blocking or pore constriction (Iritani and Katagiri, 2016; Iritani and Katagiri, 2016;

Iritani, 2013), cake formation (Salinas-Rodriguez *et al.*, 2015; Chudacek and Fane, 1984; Reihanian *et al.*, 1983), solid adsorption (Fane *et al.*, 1983), and concentration polarization (Kimura and Sourirajan, 1967). Hermans and Bredée, (1935) deduced simple mathematical laws called blocking filtration laws explaining the physical mechanisms of pore blockages in membranes during filtration (Hermans and Bredée, 1935) and Grace (1956) reanalyzed and systematized the performance of nine membranes that were used to filter water contaminated dilute spherical particles. They considered the mechanisms of filtration preceding the cake formation and the possibility of applying the earlier proposed filtration laws. She observed that Standard-Blocking filtration was prevalent in all nine membranes analyzed and noted that the membranes' clogging values were linearly related to the pore radius (Grace, 1956). Later other researchers discussed the four filtration models: cake filtration, complete blocking, intermediate blocking, and standard blocking. Iritani and Katagiri observed that all the filtration laws are generated from a common differential equation and the difference comes about due to the blocking constant (Iritani and Katagiri, 2016). Thus the blocking filtration models are represented with a general equation

$$\frac{d^2t}{dv^2} = k \left(\frac{dt}{dv} \right)^m \quad 2.3$$

and m is the filtration resistance index that can be zero for cake filtration, 1 for intermediate blocking, 1.5 for standard blocking, and 2 for complete blocking (Hatori and Suzuki, 2021; Iritani and Katagiri, 2016; Iritani, 2013; Cheng *et al.*, 2011; Hwang *et al.*, 2007). In deriving the blocking laws it was assumed that the Hagen-Poiseuille flow equation is obeyed in the membrane which is also assumed to be composed of uniform cylindrical pores. Each of the blocking mechanisms, however, is derived from different physical mechanisms (Granger *et al.*, 1985). Hermia (1982) deduced a filtration blocking model that explained the possibility of contaminants accumulating on top of each other on the surface of the filter (Hermia, 1982). Several researchers have used the models either singly or by combining them to explain the reasons behind the decline of flow rate as the filtration time increases (Iritani and Katagiri, 2016; Bolton *et al.*, 2006; Duclos-Orsello *et al.*, 2006; Gironès *et al.*, 2006; Mourouzidis-Mourouzidis and Karabelas, 2006; De Bruijn *et al.*, 2005; Purkait *et al.*, 2005; Boerlage *et al.*, 2002; Ho and Zydney, 2000; Blanpain-Avet *et al.*, 1999; White, 1996; Iritani *et al.*, 1991). Hwang *et al.*, 2007 using membranes of 0.15 μm polymethylmethacrylate particles as contaminants filtering through a 0.2 μm isopore membrane under constant pressure, reported

a blocking index of 0.5 which shifted to zero after a given time of filtration (Hwang *et al.*, 2007). It was also established that the resistance index varied successfully in dead-end microfiltration in protein solutions (Hwang *et al.*, 2007; Bowen *et al.*, 1995) and that the intermediate blocking model precedes the cake filtration model (Hwang *et al.*, 2007; Iritani *et al.*, 2005; Lee, 1997). Iritani and Katagiri (2016) re-examined the blocking mechanism, both in the Newtonian and non-Newtonian fluids under constant pressure and flow rate (Iritani and Katagiri, 2016). However, their work was theoretical and not experimentally verified. Hatori and Suzuki 2021 using Al₂O₃/3Y-ZrO₂ sintered membranes experimentally showed that the decline of flow rate is a result of a combination of models. It was also reported that the standard model was prevalent in the initial stages of filtration and cake filtration was preferred in the late stages of filtration. However, the filtration models have not been used to describe the complicated pore network of diatomaceous earth which has both nano and micropores since the model assumes that the pores are uniform, cylindrical and continuous. A key objective of this current work is to examine the decline mechanisms of flow rate under constant pressure in filtering water contaminated with *E. coli*, Rotavirus, and NaF with a diatomaceous earth membrane.

2.4 Application of Magnetic Field in Water Purification

The application of the magnetic field in water purification has not been fully understood. Many have even produced conflicting views about the subject (Zaidi *et al.*, 2014). Some researchers attribute the purification of water by a magnetic field to molecular nucleation (Kronenberg, 1985). However, molecular nucleation does not explicate how water purification is attained and why the effect of magnetism differs according to the media.

Initial evidence of the application of the magnetic field in water purification was reported in Russia where it was observed that water minerals were deposited on the walls of the boiler and engine machinery causing a reduction in the sizes of the pipes over time (Lychagin, 1974). While investigating this observation it was noticed that the mineral deposited on the walls of the pipes did not stick to them (Karkush *et al.*, 2019; Zaidi, 2016; Szostak and Toy, 1985; Raisen, 1984). It was then later discovered that water was magnetized for a certain time when it interacted with a magnet of proper strength (Lychagin, 1974). The magnetic field was also used for water filtration purposes by altering the physical properties of the water contaminants (Safarzadsseh-Amiri *et al.*, 2011; Ambashta and Sillanpää, 2010; Augusto *et al.*, 2005). However, how the magnetic field caused the aggregation of contaminants in water was

not well understood. The following are some of the views the earlier researchers have put forward in explaining the action of magnetic fields on water contaminants.

2.4.1 Direct Actions on the Dissolved Ions and Water Molecules

Chibowski and Szcześ (2018) reported that water purification can be achieved by a magnetic field acting on the dissolved ions in water causing nucleation (Chibowski and Szcześ, 2018). Nucleation of CaCO_3 in water by the magnetic field strength of 0.3 T applied for 10.0 minutes was reported by Higashitani *et al.*, (1993). Nucleation of CaCO_3 and HCO_3^- was also reported by Madsen, (1995) but in their work, the particle sizes of CaCO_3 reduced as opposed to increasing particle size as reported by Higashitani *et al.*, (1993). Other researchers also observed slower nucleation and sedimentation rates of CaCO_3 precipitated from magnetically treated Na_2CO_3 solutions. The time for magnetic treatment varied from 5.0 min to 70.0 min at 30.0 °C ambient temperature. It was also reported that the magnetic field increased CaCO_3 precipitates. The efficiency to form CaCO_3 precipitates depended on the water flow rates, pH, and time of interaction between the magnetic field and the concentration of CaCO_3 molecules (Fathi *et al.*, 2006a). It is therefore important to explore the nucleation in other water contaminants such as sodium fluoride.

2.1.1 Ion Hydration Changes

It was reported that the magnetic field causes proton spin inversion in diamagnetic salts such as HCO_3^- , initiating a faster transfer of its proton to water resulting in the formation of carbonate ions (Madsen, 1995). Another reason why there was the aggregation of minerals in the pipes was that the magnetic field influenced the hydration of carbonates and modified their equilibration in the polymorph phase (Higashitani *et al.*, 1993). The same phenomenon caused the dehydration of the ionic pair process and the formation of hydrated CaCO_3 precursors for anhydrous CaCO_3 (precipitated calcium carbonate). Thus the magnetic field caused the formation of aragonite precipitates rather than calcite precipitates which is why they do not stick to the walls of the pipes (Chibowski and Szcześ, 2018; Kobe *et al.*, 2003). This mechanism can be explored in the purification of drinking water.

2.4.2 Magnetic Field Effects on Different Salt Solutions

The magnetic field has different effects on different salt solutions (Chibowski and Szcześ, 2018). Strontium sulfate was reported to have precipitated from 0.5 M strontium nitrate

solution and it appeared smaller and more stable when the nitrate solution was magnetized with a 1.0 T magnetic field strength. However, the effect of the same strength of the magnetic field was not observed in sulfate solution of barium, calcium sodium, and silver of the same concentration. Sodium chloride too did not show significant results. The effect of the magnetic field on 0.5 M strontium nitrate lasted for two days but when the solution was heated at 60.0 °C the magnetic memory was lost after 20.0 min (Silva *et al.*, 2015). Thus divalent cations are more susceptible to the magnetic field than monovalent cations, monovalent, and divalent anions (Chibowski and Szcześ, 2018). The effect of magnetic field on different ions of contaminants especially calcium carbonate precipitation was examined by (Chibowski and Szcześ, 2018; Holysz *et al.*, 2007). They reported that the precipitation of CaCO₃ by 0.4 T or 0.5 T magnitude of magnetic field depended on the entropy of hydration of Mg⁺², Fe⁺², and SO₄⁻² of solution (Chibowski and Szcześ, 2018; Holysz *et al.*, 2007). The Fe⁺² showed positive Zeta potential while SO₄⁻² solution showed negative Zeta potential. The effect of a magnetic field of 0.16 T on the Mg⁺² and SO₄⁻² solutions were also reported (Alimi *et al.*, 2009). The solutions were in the presence of the field for 15.0 minutes. A precipitate of MgSO₄ and aragonite was observed when the ionic strength of Mg²⁺ and SO₄⁻² solutions were greater than 0.02M. However, aragonite was precipitated in a 2.0 ppm Fe⁺² solution without the presence of a magnetic field, and when the magnetic field was introduced in the same solution of Fe⁺² the growth of aragonite reduced. Furthermore, separately both the Fe⁺² and magnetic field caused the growth of aragonite (Wang *et al.*, 2012). Thus the concentration of the contaminant which affects the entropy of water plays a key role in the purification of water using magnetic field.

2.4.3 The Cluster Transformation

Water is made up of polar molecules with V-shaped dipoles which make it sensitive to the magnetic field. In the presence of a magnetic field with an appropriate magnitude, the dipole structure can be affected by enhancing the hydrogen bond. Thus, affecting Van der Waal's forces. (Karkush *et al.*, 2019). This happens because magnetization breaks down water molecule structure reducing its linkage angle thereby increasing its acidity and solubility (Wang *et al.*, 2018; Ambashta and Sillanpää, 2010). The change in water molecule structure also results in the water cluster transformation which in turn changes its physical properties (Lee *et al.*, 2003; Iwasaka and Ueno, 1998). Wang *et al* (2012) attributed the growth of aragonite crystals in water to the presence of the magnetic field. They also noted the

temperature and impurity effect of magnetism on the water (Wang *et al.*, 2012). They explained their result using a simple point charge model where the water molecule has a triangular shape with a point charge at each corner of the triangle. Under short ranges interactions, the water molecules interact through Coulombic electrostatic force, and under long-range interactions, the molecules interact through Lennard-Jones potential with the center of the force lying on the oxygen atom (Chibowski and Szcześ, 2018; Wang *et al.*, 2012). Studies further show that the Lorentz force affects the interaction between water molecules and the contaminant ions and destroys the water clusters by encouraging water-water molecule and ion-ion interactions. It also increases the diffusion of the cation in water and decreases anion diffusion (Murad, 2006). A report on the effect of the magnetic field on water contaminated with sodium chloride indicates that the field encouraged Cl^- and Na^+ ion mobility and reinforced the hydrogen bond in water (Chang and Weng, 2008; Chang and Weng, 2006). However, Toledo *et al.* (2008) showed that the Lorentz force weakened the hydrogen bond inter-clusters but strengthened the hydrogen bond intra-clusters of water. Silva *et al.* (2015) attributed the magnetic memory and aggregation of minerals in water to the polarization of bivalent ions by Lorentz force. Silva *et al.* (2015) also agreed with Colic and Morse (1999) that hydration of divalent cations was favored over the hydration of anions (Silva *et al.*, 2015; Colic and Morse, 1999). Silver *et al.* (2015) also observed that a magnetic field increases the viscosity of water (Colic and Morse, 1999). However, Silva *et al.* (2015) observed that the magnetic field neither affected the viscosity of water nor the settling rate of the contaminant particles. Thus the effect of magnetic field on the viscosity of water needs to be explored further.

2.4.4 Capillary Phenomena

The magnetic capillary phenomena (distortion of fluid surfaces) have been reported in liquids, gas, and powdered solids when a 10.0 T magnetic field was applied (Kitazawa *et al.*, 2001). Deformation of water surface by the magnetic field, commonly known as Moses' Effect has also been reported (Kitazawa *et al.*, 2001). Moses' Effect of a 39.0 mm deformation of the water surface was observed when water was placed in a solenoid of 10.0 T. This effect was also noted in cuprum sulfate solution under the influence of 0.56 T and the effect increased when benzene solution was added to it. And NaCl and KCl powder were levitated in the same work (Kitazawa *et al.*, 2001). Thus, capillary phenomena can be used to separate solids from various liquids if their levitation rates are different. In some other work by Nakagawa *et al.*

(1999) airflow was increased by 4.0×10^5 times when 10.0 T was used and the surface tension of water was increased from 71.96 mN/m to 73.31 mN/m in 15.0 min. The surface tension memory was returned 20 minutes after the magnetic field was withdrawn (Nakagawa *et al.*, 1999). Movement on the water surface was reported in circular polyethylene and polypropylene rafts of 5.6 mm diameters with 0.T neodymium magnets (Frenkel *et al.*, 2018). They attributed the movement to the diamagnetic properties of water which were caused by the interplay of contact angle hysteresis and gravity. Bormashenko *et al.* (2008) reported the deformation of the liquid/vapor interface of water. Thus, the magnetic field is best observed in a tube (capillary). Therefore it is necessary to explore the purification of water using magnetic fields to resolve the above issues

Several factors that affect the purification of water using magnetic fields include; the time under which the water molecules are exposed to the magnetic field, the pH of water, and its flow rates (Ambashta and Sillanpää, 2010) and they shall be explored in this work in the purification of water contaminated with *E. coli*, Rotavirus and NaF.

Based on this literature review it is clear that there is a gap between the current technologies in water purification and their applicability in the developing world, particularly cheap and durable (in terms of mechanical strength) but efficient and effective point-of-use water filter technologies. Further, there is limited literature on the efficiency of the magnetic field in the elimination of contaminants from water. It is for these reasons that we are fabricating a composite water filter (diatomaceous earth, activated carbon, and molasses) for filtration of water contaminants and investigating the effectiveness of the magnetic field in water purification. In this work, we shall explore DE, the use of organic binders for strength enhancement, and activated carbon in improving the sensitivity of the microfiltration approach not only to filter microbes but also viruses and fluorides.

CHAPTER THREE: THEORETICAL BACKGROUND

3.1 Factors Affecting Strength of the Ceramic Membranes

Several factors affect the strength of the ceramic membranes which include: types of clay minerals, drying mechanism, particle size, particle size distribution, pore formation, pore-forming agent, ceramic additives such as binders, and firing temperature.

3.1.1 Clay Minerals

Clay is fine-grained earth made up of clay minerals most of whom are crystalline materials that occur naturally and have particle sizes of less than 2.0 μm (Uddin, 2017). Clay minerals are classified based on the number of silica layers they have. Based on this classification we have the two-layer type, three-layer type, regular mixed layer type, and chain-structure types of clay. The two-layer types of clay are made of sheet-like structures consisting of one layer of the aluminum octahedron and another layer of silica tetrahedron. Examples of such clays are halloysites and kaolinites (Annan *et al.*, 2018). The three-layer type of minerals is made of two sheets of tetrahedron silica and one sheet of trioctahedral or dioctahedral silica. Examples of the three-layer type include; cristobalite, beidellite, illite, smectite, sodium montmorillonite, and vermiculite (Bergaya and Lagaly, 2013). Regular mixed layer type comprises ordered sheets with alternate layers of different sheets such as the chloride group. The chain structure type is made of the silica tetrahedron hornblende-like chains joined with the octahedral group of oxygen and hydrolysis having aluminum and magnesium. Examples of chain-structure types of clay minerals include astapungite (palygorskite), spinlite, and wollastonites (Uddin, 2017). Another classification of clay is based on phyllosilicates and here the minerals are classified into three groups: illite, montmorillonite, and kaolinite (Bergaya and Lagaly, 2013). Illite minerals are made of secondary precipitates of either layered alumino-silicate or phyllosilicate, with a 2:1 sandwich of silica tetrahedron – alumina octahedron – silica tetrahedron layers (Uddin, 2017). Montmorillonite is made of a central octahedral alumina sheet sandwiched by two tetrahedral silica sheets. Kaolinites are made of a sheet of tetrahedral silica linked to an aluminum octahedral sheet by oxygen atoms (Annan *et al.*, 2018; Uddin, 2017; Bergaya and Lagaly, 2013). The silica tetrahedron diatomaceous earth combined with organic binders form strong bonds during firing and that is why they are investigated here.

3.1.2 Binders

Additives are any substances that are added to the firing materials. They include binders and nanoparticles which are applied at various levels of fabrication starting with mixing it with the powder to the final stage of the fabricated membranes. The binder is used to agglomerate powders together forming greenware of ceramics. These binders have complex chemical structures and compositions that aid them in their application. There are two types of binders: permanent and temporal binders. Permanent binders are made up of inorganic materials which form permanent bonds with firing materials that do not change even after firing. However, permanent bonds shield off the filtration abilities of clay. The temporal binders are made up of natural or synthetic organic compounds. Examples include cellulose, glues of plants, molasses, and carboxymethyl among others. When they interact with the firing materials they form temporal bonds which strengthen the green ceramic but volatilize during firing. They are relatively cheap as they are either naturally occurring or industrial by-products such as molasses and sulfite. The binding ability of the organic binders is caused by their polymeric behavior and their high molecular weight. They are also composed of active polar groups with extended hydrogen bonding which gives them a strong internal structure that easily breaks down during firing.

3.1.3 Drying Process

Since the ceramic green bodies contain a liquid phase which is usually water or binder in addition to the solid, it is necessary to determine the proportion of the liquid phase. For the sake of simplicity, we are going to treat the liquid in the subsequent sections as water. Moisture content in the greenware is the ratio of the mass of water to the mass of the greenware after it has completely dried. The greenware is considered to be dried when soaked at 110.0 °C for thirty minutes (Oummadi, 2019). The dried material is called the dry basis (DB) expressed in Equation (3.1), where X is the moisture content on a dry basis, $w(t)$ is the sample weight at time t during drying, and w_d is the sample weight dried at 110.0 °C until a constant weight is achieved.

$$X = \frac{w(t) - w_d}{w_d} \quad 3.1$$

There is another way to express the moisture content (X') also called wet basis (WB) as a ratio of the mass of water to the initial total weight of the green sample (w_{init}) as shown in Equation (3.2). This definition is what was adopted in this work.

$$X' = \frac{w(t) - w_d}{w_{init}} \quad 3.2$$

Drying green samples involves the evaporation process which entails the three heat transfers; convection, conduction, and radiation (Scherer, 1990). Sometimes the material is subjected to all these forms or two or one, depending on the conditions. Figure 3.1 shows a schematic representation of water under certain conditions; airflow, relative humidity, heat, and air (Oummadi, 2019). The green ceramic is subjected to similar conditions and if they are not put in an environment to balance these forces they crack.

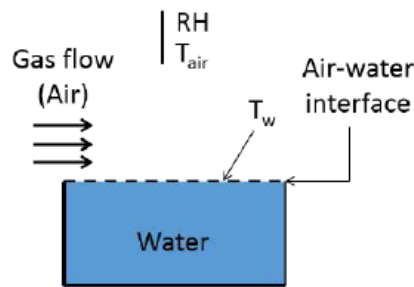


Figure 3.1: A schematic representation of water subjected to different conditions of evaporation. RH , T_{air} , and T_w stand for the relative humidity, ambient temperature, and temperature of water respectively (Oummadi, 2019)

Drying of green ceramic membranes involves different forms of heat transfer from the sample and to the sample as shown in Figure 3.2. To prevent any cracks in the greenware, the material is put under Fourier's conditions shown in Equation (3.3) which must be respected throughout the system. In the Fourier's Equation, heat flux, thermal conductivity, and temperature are symbolized by q , T_{cd} , and T respectively.

$$q = -T_{cd} \nabla T \quad 3.3$$

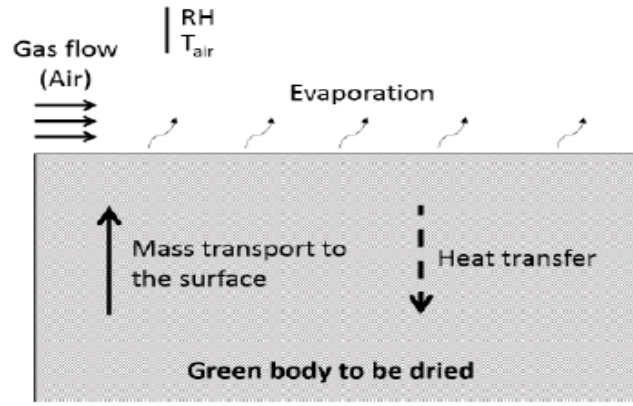


Figure 3.2: A schematic representing evaporation in a porous material. RH , stand for T_{air} for the relative humidity, ambient temperature, and temperature of water respectively (Oummadi, 2019)

The flow of water in the porous material also obeys Darcy's law given in Equation (3.4) where J_L is the flux of the liquid, P_{erm} is the permeability, P is the pressure of the liquid, and η_L is the viscosity of the liquid. The law assumes that the greenware is only composed of solid particles separated by continuous water. Thus Darcy's law involves capillary forces and it assumes that the drying process also depends on the particle size, distribution, and shape which in turn affects the pore size, shape, and distribution (Scherer, 1990). This process is dominant at the initial stages of drying.

$$J_L = -\frac{P_{erm}}{\eta_L} \nabla P \quad 3.4$$

The flow of liquid in the membrane also involves diffusion in the form of water vapor. The diffusion process involves Fick's law stated in Equation (3.5) where J_D is the diffusion flux, D_w is the diffusion coefficient, and C_c is the vapor concentration. It caters to the drying process that takes place when the particles are separated by moisture, and it involves a diffusion process that transports moisture to the surface. The diffusion of air depends on the concentration gradient. The surrounding of the greenware is another factor to consider when drying as heat convective drying affects the process. In convention, it is assumed that there is a thin layer close to the body that experiences the concentration gradient of vapor. The height (H) of the vapor layer is given by Equation (3.6) where C_{slb} is the concentration of the vapor in the solid, C_{clb} vapor concentration at the liquid boundary layer defined by H , C_{air} is the vapor concentration above the boundary layer (Incropera *et al.*, 2007).

$$J_D = -D_w \nabla C_c \quad 3.5$$

$$0.99 = \frac{C_{cslb} - C_{clb}}{C_{cslb} - C_{cair}} = H \quad 3.6$$

The transfer of mass (M_t) is proportional to the vapor concentration across the boundary as shown in Equation (3.7) where k_{M_t} is the coefficient of convection mass transfer. The concentration and vapor pressure are related by the Ideal gas Equation (3.8) where P_s is the saturated pressure of vapor, a_w is the water activity, T_s is the sample temperature after saturation and R is the ideal gas constant.

$$M_t = -k_{M_t} (C_{cair} - C_{cslb}) \quad 3.7$$

$$C_{cair} = RH \frac{P_s(T_{air})}{RT_{air}} \quad 3.8$$

$$C_{cslb} = a_w \frac{P_s(T_s)}{RT_s}$$

Apart from vapor, heat is also transferred into and out of the porous greenware during drying.

3.1.4 Particle Size

The particle size and distribution of clay and burnout material affect the drying process and sintering of the material. Smaller particles tend to form stronger greenware due to their large surface area which allows a high rate of shrinkage. Narrow particle distribution allows a uniform drying process that eliminates microcracks that give rise to cracked ceramics. The pore size and distribution of the forming material affect the pore size, shape, and distribution within the ceramic.

A sintering model, taking into account the effect of particle-size distribution ($f(G)$) and the effect of grain growth was derived by Ting and Lin (1994b). The distribution function is such that the volume fraction is given by Equation (3.9) and when the compact is achieved the total dimensionless volume change is expressed in Equation (3.10)

$$dv = f(G)dG$$

$$\int f(G)dG = 1 \quad 3.9$$

$$\Delta v = K_3 \frac{t^n}{G^{m_o}} f(G)\delta G \quad 3.10$$

where G is the particle or grain size, t^n is the sintering time component and K_{sr} is a constant, and the shrinkage in the powder compact is given by equation (3.11). In Equation (3.11) $F_o(G)$ is the shrinkage rate factor before the grain growth takes place and it depends on the particle size distribution of the powder.

$$S_R = K_{sr}t^n F_o(G) \quad 3.11$$

After the grain growth, the densification rate and the grain growth depend on time and also particle size distribution. Thus, the rate of shrinkage is given by Equation (3.12)

$$R = K_{srd}H(t)F_1(G_o) \quad 3.12$$

Where G_o is the initial particle size and does not depend on time, $F_1(G_o)$ denotes the particle distribution function. $H(t)$ is the grain growth coefficient and K_{srd} is a constant.

Before the occurrence of grain growth, the model predicts that the densification rate increases and then decreases as the particle-size distribution width of the original powder increases. After grain growth occurs, the densification rate decreases as the particle-size distribution width of the starting powder increases (Ting and Lin, 1994b). It is the particles that produce the driving force that controls sintering.

3.1.4.1 Driving Force of Sintering

The process of sintering is mainly based on lowering the excess surface energy of the particles by eliminating pores in between the particles of a loosely bonded green compact to form an agglomerated sintered material (Boch and Niepce, 2010). The green compact is characterized by low mechanical strength and high porosity (Barsoum and Barsoum, 2002). The green compact comprises fine powder that has a high specific surface area associated with the free energy of the system than solid materials of equal masses (Fang, 2010). Thus,

since powders have a high surface area, then the surface energy and free energy of the system in them are equally high. During sintering, the excess energy is responsible for reducing the interparticle pores, facilitating particle-particle interaction, and the formation of strong stable bonds (Kang, 2005).

There are three ways in which the driving force facilitates sintering: First, reduction of total surface area through coarsening of the particles. Coarsening of particles involves increasing the size of particles by applying external thermal energy to the particles without particle-particle interaction (Fang, 2010). That is no bonding. During coarsening, the finer particles assume a guava-like shape and increase in their particle size but there is no bonding that takes place at this stage (Fang, 2010). Thus, coarsening is all about particle growth and it is common in loose powders that have not been consolidated through pressure into a green compact.

Secondly, sintering can be achieved by the replacement of a high-energy solid-vapor interface with a low-energy solid-solid interface by forming grain boundaries (Barsoum and Barsoum, 2002). When powders are pressed, they form green compacts in which each particle is surrounded by vapor (solid-vapor interface) which possesses certain surface energy. If the solid-vapor interface has to be replaced by a solid-solid interface, then the air in between the particle is eliminated and the grain boundary between the particles is formed. The process of forming grain boundaries allows for particle-particle interaction (matter transfer) which results in chemical bonding (Kang, 2005). The solid-solid interface is associated with surface energy which is less than the surface energy associated with the solid-vapor interface. Thus, the formation of the solid-solid interface from a solid-vapor interface results in excess energy difference which serves as a driving force for the sintering process. The first and second processes can take place simultaneously.

Figure 3.3 shows a schematic representation of a green compact body showing the possible processes the particles can undergo during firing. In the front left corner, there is a green compact with loose particles characterized by the solid-vapor (air) interface (Boch and Niepce, 2010). If the green compact is provided with activation energy (thermal energy), then we can have three things happening; coarsening, densification, or both depending on the firing conditions. The conditions include; firing temperatures, rate of heating, nature of the material, and time among others. In Figure 3.3 it has been shown that during sintering particles grow uniformly which is not the case in reality. In practice, some particles grow at

the expense of the other particles. While others may melt, the mass of the material remains constant (Fang, 2010). As mentioned earlier there is no chemical nor mechanical bonding during coarsening. However, coarsening reduces the surface energy of the particles. The second process is densification which involves changing the configuration of particles without changing the size of the particles as shown in Figure 3.3. Densification results in strongly bonded material and if the activation energy is still applied to the system, densification is followed by grain growth (Barsoum and Barsoum, 2002). It can also happen that both coarsening and densification can take place at the same time (Kang, 2005).

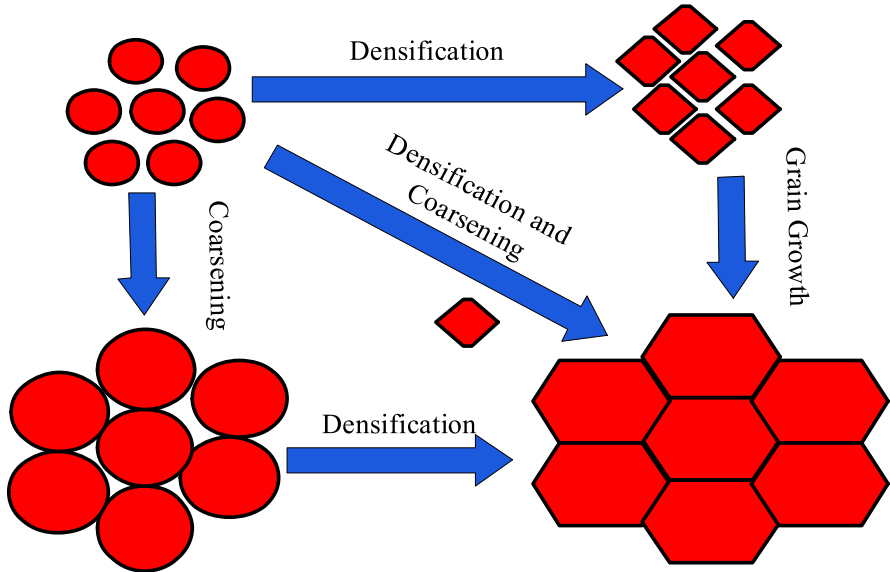


Figure 3.3: A schematic of a compact body showing particle coarsening and grain boundary formation (Kang, 2005)

3.1.4.2 Particle Size and Sintering Processes

There are two main sintering processes; solid-state sintering and liquid phase sintering as shown in Figure 3.4. Solid-state sintering involves particle-particle interaction and often takes place in most materials (Kang, 2005). The liquid phase sintering is common at high firing temperatures and it facilitates the bonding of particles just like an adherence. Some particles in the material melt because they have reached their melting point. As the high temperatures persist more and more particles melt which results in the flow of mass in the form of liquid (Fang, 2010). During this flow, the particles interact resulting in the formation of new structures. The liquid cools at lower temperatures and solidifies to a solid. Thus, both the liquid phase and solid-state sintering enhance particle-particle interaction.

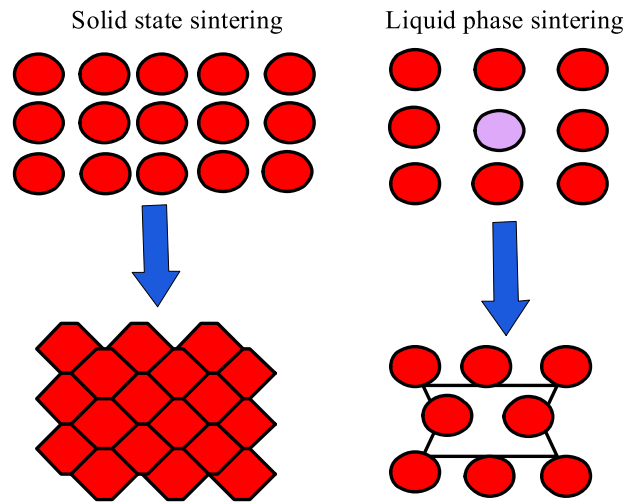


Figure 3.4: A schematic showing the two sintering processes; solid-state sintering and liquid phase sintering (Fang, 2010; Kang, 2005)

3.1.4.3 Effect of Particle Size on Surface Energy

The dihedral angle exists wherever there is a surface energy term and two surfaces in the material being sintered. However, sintering does not take place always except when the sintering condition is met. The condition for sintering demands that the grain boundary energy (γ_{gb}) should be at least less than two times the solid-vapor surface energy (γ_{sv}) as shown in Equations (3.13). That is, at equilibrium the dihedral angle (ϕ) is less than 180.0° as shown in Figure 3.5 (Fang, 2010; Kang, 2005). Applying geometry in Figure 3. 5(a), the relationship between boundary energy, solid-vapor surface energy, and dihedral angle can be expressed in Equation (3.9). Similarly, in the liquid sintering, the equilibrium condition has also to prevail as shown in Figure 3.5 (b), and can be expressed in Equations (3.14).

$$\gamma_{gb} = 2\gamma_{sv} \cos \frac{\phi}{2} \quad (3.13)$$

$$\gamma_{gb} = 2\gamma_{sl} \cos \frac{\phi}{2} \quad 3.14$$

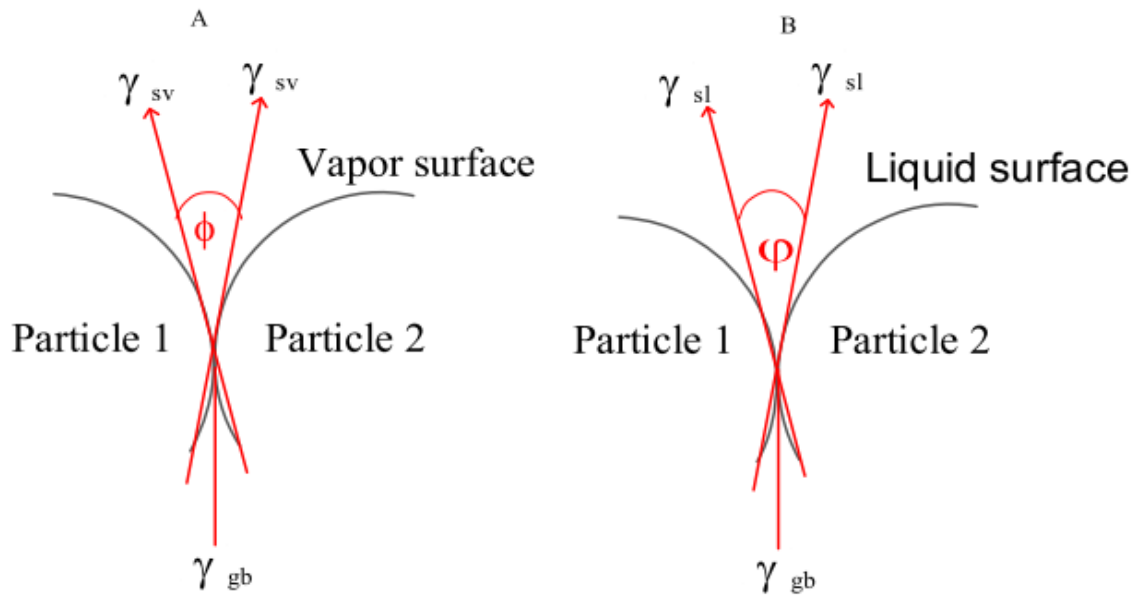


Figure 3.5: The equilibrium condition for surface energy (γ) and dihedral angle in solid-vapor (sv) and solid-liquid (sl) interfaces (Kang, 2005)

3.1.5 Firing Temperature

Firing is an important factor that causes the sintering process. Sintering is a process of consolidating a powder into a compact matter to form an agglomerated monolith by eliminating the interparticle pores with the aid of thermal energy or pressure (Boch and Niepce, 2010; Kang, 2005; Barsoum and Barsoum, 2002). In this work, thermal energy would be used. The cluster of particles in the compact change in shape, structure, and at times size when fired to sintering temperatures (Kang, 2005). Initially, the clay material is milled to powder to increase the surface energy of the particles and for easy mixing with the binder. The mixture is then molded to the intended shape and dried before being fired. When the dried greenware is fired, the particles lose their excess surface energy which is then used to form strong bonds that make up a ceramic material (Boch and Niepce, 2010). The outcomes of sintering are; volume shrinkage, densification, reduced porosity, and improved mechanical strength. In rare cases, we also have grain coarsening if the temperatures are not controlled.

3.1.5.1 Densification and Volume Shrinkage

Densification is the process of reducing the porosity of material during sintering which results in volume shrinkage. This happens because the particles come closer to each other during sintering and result in volumetric shrinkage (Boch and Niepce, 2010). Thus, shrinkage is a result of densification. However, volume shrinkage also takes place in the green compact

during the drying period. Green compacts take different times to dry depending on the method of drying, nature of the material, the volume of the material, particle size, pressing pressure, the shape of the body, and the binder used (Kang, 2005). The drying is characterized by loss of weight and shrinkage which come as a result of evaporation of water or volatilization of the binder.

3.1.5.2 Mechanical Strength

The reason for sintering materials is to improve their mechanical strength. During densification, the pores are reduced in size and their shape also changes (Fang, 2010). As a result of this, the particles interact and bond to form strong materials.

3.1.5.3 Grain Coarsening

Grain coarsening takes place when the sintering conditions are not controlled. It results in the growth of the particles and grains. If sintering has been achieved, the grain growth should take place after particle-particle interaction has been achieved (Kang, 2005). The finished ceramic depends on the materials used in the fabrication and the fabrication technique (Barsoum and Barsoum, 2002). The materials and fabrication techniques used in ceramic processing affect the characteristics of the ceramic in terms of porosity, bulk density, linear shrinkage, and modulus of rupture, among others. When the thermal energy is applied to the greenware, the air in the interparticle spacing is eliminated reducing the contact area even before sintering takes place. Further reduction in the contact area takes place if thermal energy is applied to the already sintered material reducing the solid-solid interfaces causing the crystals to grow (Boch and Niepce, 2010). Both crystal and grain growth are not encouraged in cases where one needs a porous ceramic but if the ceramic is needed for its mechanical properties then crystal and grain growth are encouraged.

3.1.5.4 Stages of Sintering

The process of sintering is divided into three stages; namely the initial stage, intermediate stage, and final stage (Kang, 2005). The stages are differentiated based on the geometry of the pores and their sizes, volume, and shape. Sintering is a time and temperature-dependent phenomenon which results in the densification of a material (Boch and Niepce, 2010). Sintering kinetics follow different mechanisms of mass transport in different stages of sintering. The following are the discussions on the stages of sintering;

b) Initial stage

In this stage, the conglomeration of particles takes place, the contact area increases (neck growth) from zero to 20.0%, and the maximum increase in density is up to 65.0% of the theoretical density (Fang, 2010). Figure 3.6 (a) shows the initial stage of the sintering process where the particles are just touching each other. There is no deformation of particles in terms of shape and size. The particles are in their original position. Figure 3.6 (b) marks the end of the initial stage of sintering. The particles have undergone physical and geometrical changes. The initial stage of sintering has been completed and the necking process has started. By the end of the initial stage, the contact area of the particles would have increased by 20.0% from the initial contact (Boch and Niepce, 2010).

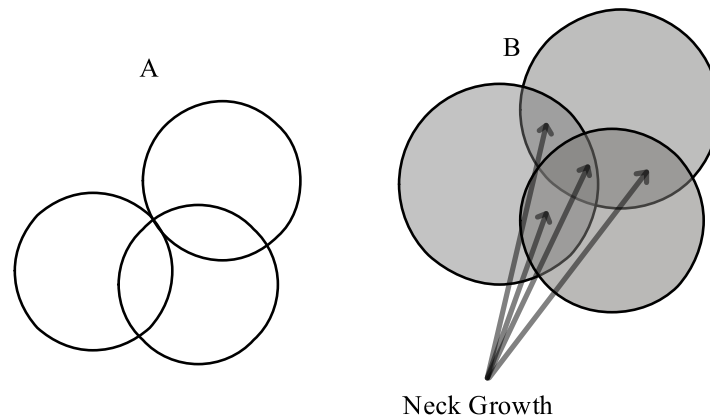


Figure 3.6: shows the initial stage of the sintering process. In (a) the particles are just touching each other and in (b) the necking process has been initiated and the contact area of the particles has increased up to 20%

There are three atomic mechanisms of mass transport during the initial stage of sintering. The solid-state sintering dominates the initial stage of sintering which involves three types of mass transport. Namely, vacancy diffusion, evaporation-condensation, and creep (viscous flow) (Boch and Niepce, 2010). The driving force in the evaporation-condensation mechanism is the vapor concentration gradient between the concave/convex-shaped surfaces of particles and the flat surfaces (Fang, 2010). Thus, the change of curvature initiates the driving force. The driving force only initiates the neck process by enhancing the bond area and its strength (Kang, 2005). Figure 3.7 shows the neck area at the initial stage of sintering. There is no change in the particle dimension, no shrinkage, and densification. At the initial stage, the radius r of the particles does not change but the radius of curvature at the neck area keeps on changing with the radius of the contact area. Each particle extends its neck by a length of x

causing a change in pressure and later the neck grows. The rate of neck growth and change have a positive correlation.

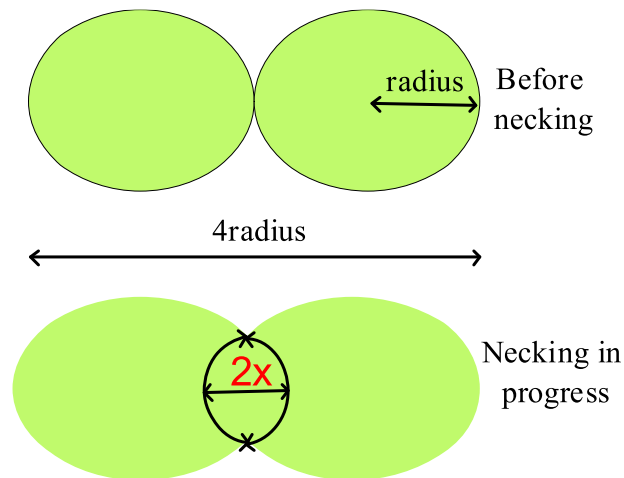


Figure 3.7: Shows the neck area at the initial stage of sintering as the particles maintain the particle distance; the two particles have an equal radius before the necking process and each particle has a neck arch of x

Solid-state sintering is the most prevalent in the intermediate stage of sintering. By the end of the initial stage of sintering, the particles have developed neck growth. Thus there is no further neck growth in the intermediate stage of sintering (Boch and Niepce, 2010). There are concave and convex surfaces within the same particle. The neck-area region has a concave-shaped curvature while the region away from the neck has convex-shaped curvature. The difference in surfaces creates vacancy concentration with the concave surface having a high concentration of vacancies. Thus, the vacancies move away from the neck area (concave surface) to a low concentration area (convex surface) (Fang, 2010). The movement of these vacancies follows different paths shown in Figure 3.8, namely, volume (lattice) diffusion, surface diffusion, and grain boundary diffusion. When the vacancies move, they leave behind voids which are replaced by the surrounding atoms. Thus, materials move to fill in voids left behind (Kang, 2005). This results in the formation of the grain boundary. The vacancies can move through the lattice itself. That is, through the solid (bulk) itself or the surface as shown in Figure 3.8. The vacancies create point defects caused by the negative concave curvature and move to cause equilibrium in the system. In the presence of external energy such as thermal energy, the vacancies will distribute themselves along with the system in the regions of low concentration (Barsoum and Barsoum, 2002). This distribution can follow different paths indicated in Figure 3.8. The overall effect of this movement is dimensional change and grain growth. That is, the distance between the two particles reduces as shown in Figure 3.8.

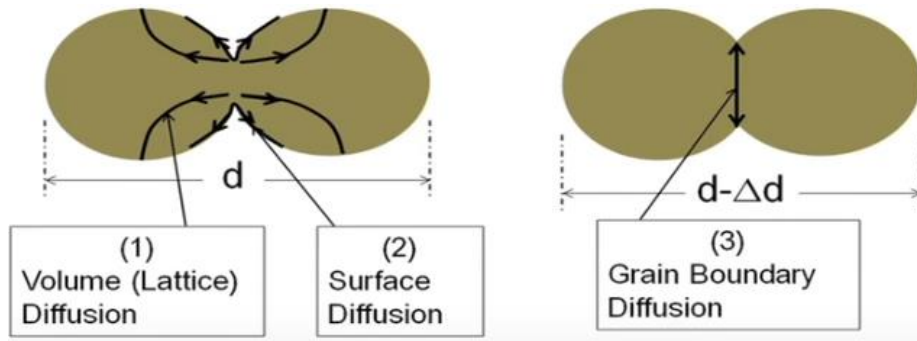


Figure 3.8: The paths followed by the vacancy movement from the neck region to other parts of the particle (Fang, 2010)

One of the physical results of sintering is shrinkage. Since the distance between the particles is changing the overall effect in the material being sintered will be the linear reduction in the dimension of the material. If the linear change in dimension can be denoted as ΔL , then, the plot of ΔL against time at two different temperatures is shown in Figure 3.9. Initially, the effect of temperature on shrinkage is fast and then slows down with time to a constant shrinkage rate (Barsoum and Barsoum, 2002).

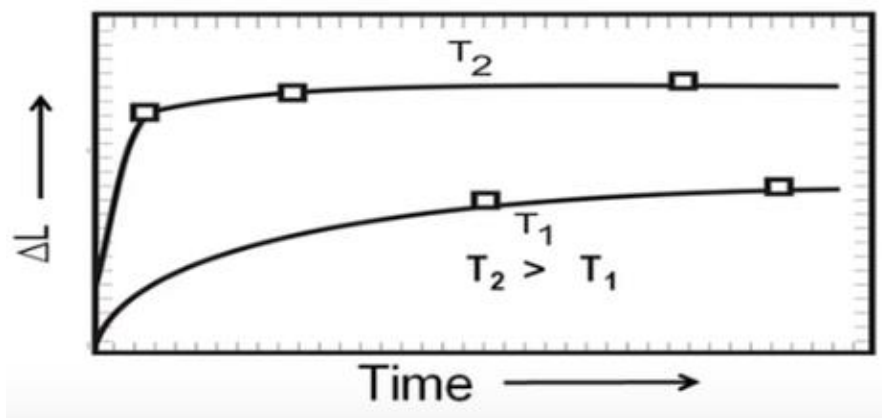


Figure 3.9: A schematic showing the rate of shrinkage of a material undergoing an intermediate stage of sintering at two different firing temperatures T_1 and T_2 (Kang, 2005)

Among the three diffusion routes, the activation energy for the lattice diffusion is the highest followed by the grain boundary and surface diffusion in descending order (Fang, 2010). Thus, the lattice diffusion is dominant at high sintering temperatures while surface diffusion is dominant at low sintering temperatures. The effect of surface and grain boundary diffusion is highly felt most in small particles. Lattice diffusion dominates in large particles for a longer time at high temperatures. These processes take place in all stages of sintering. There is also the viscous flow mechanism of sintering that enhances shrinkage. At the melting point of

some elements in the material, some particles get softened and others melt into viscous fluid whose transport depends on viscous flow forces (Boch and Niepce, 2010). As some particles melt and move, they get replaced by the surrounding particles causing shrinkage in the material. The result of the viscous flow mechanism is thus linear shrinkage of the material which can be expressed in Figure 3.10 and Equation (3.15). At the beginning of sintering, the pore is enclosed by the square of vertices 1, 2, 3, and 4 which serve as solid vapor boundaries. As the sintering continues, the vertices shrink into a pore, and the grain boundaries are introduced (Barsoum and Barsoum, 2002).

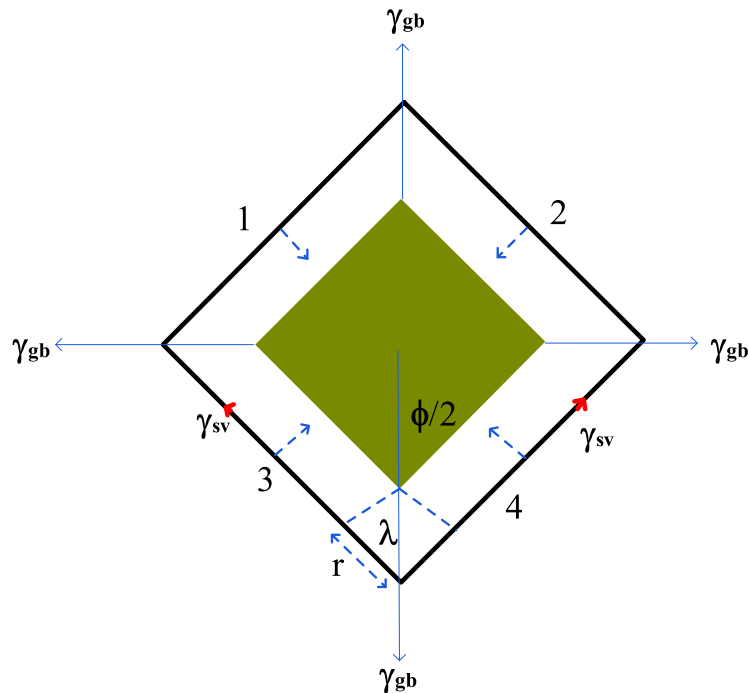


Figure 3.10: The pore with vertices 1, 2, 3, and 4 manifesting the viscous flow mechanism of linear shrinkage (Kang, 2005); γ stands for the surface energy, gb for grain boundary, and sv for solid-vapor with ϕ and λ as the dihedral angles

$$\frac{\Delta L}{L} = \frac{3\gamma_{sv}}{4\eta_L} t \quad 3.15$$

where η_L represents the viscosity of the viscous fluid that melted during the sintering process, L is the original length, ΔL is changing in length and t is the time taken to fire the material.

Another effect of sintering is the filling of pores in the material by the flowing fluid. However, the filling of pores and shrinkage stop when the pores become thermodynamically stable, such that the further sintering process does not remove or fill any pore. This happens when the conditions of sintering in Equation (3.16) are obeyed. The equation proves that the

energy gained by creating a grain boundary is twice the energy used in reducing the pore at the solid vapor boundaries (Fang, 2010).

$$\frac{E_g}{E_l} = \frac{2\Gamma\gamma_{sv}}{Z\gamma_{gb}} \quad 3.16$$

where E_g is energy gained E_l is energy lost, Γ is the eliminated solid vapor surface, and Z is the additional grain boundary created. Additionally, for the pores to be eliminated the number of grains around the pore must be less than a certain critical number n_c and $n_c = \frac{360}{(180-\phi)}$.

Large particles cause particle coarsening, which prohibits sintering.

c) Intermediate Stage

The intermediate stage which doubles up as the longest stage of sintering improves densification up to 90.0% and is characterized by continuous pores and solids (Kang, 2005). Figure 3.11 shows the schematic diagram of the intermediate stage sintering. In this stage, the particles have changed in shape and geometry. The spherical particles have now turned into polyhedral-shaped particles joined together with continuous pores (Barsoum and Barsoum, 2002). The polyhedral shape has allowed an increase in contact area with other particles.

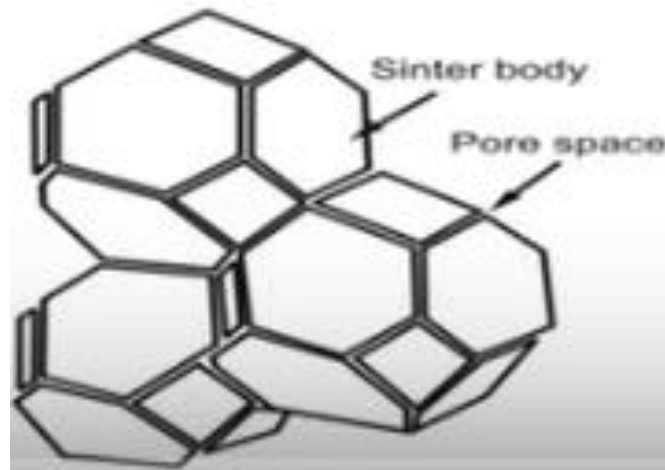


Figure 3.11: The intermediate stage of the sintering process that comprises polyhedral continuous solid phase and linear pores (Kang, 2005)

The polyhedral-shaped particles are now grains that have different planer phases. The solid phase is also continuous and has a much larger volume (90.0%) than the volume of pores (10.0%) (Boch and Niepce, 2010). The pores are more cylindrical and linear and the mathematical derivations are similar to those carried out in the early stage.

d) Final Stage

In this stage, the continuous pores get separated to form numerous isolated pores of lenticular or spherical shape as shown in Figure 3.12 depending on where they are situated in the material (Fang, 2010). Pores near the grain boundaries assume the lenticular shape while pores away from the grain boundaries tend to take up a spherical shape (Kang, 2005). The pore volume decreases significantly because 90.0% of densification has already taken place. Most of the pores here are not continuous and are located at the corners of the polyhedral or on special occasions the pores may be found on the grains themselves as shown in Figure 3.12 (Barsoum and Barsoum, 2002). However, the solid phase remains continuous and grain boundaries are thinner as most of the pores near the grain boundaries have been eliminated (Boch and Niepce, 2010). Thus the volume of the pores reduces significantly.

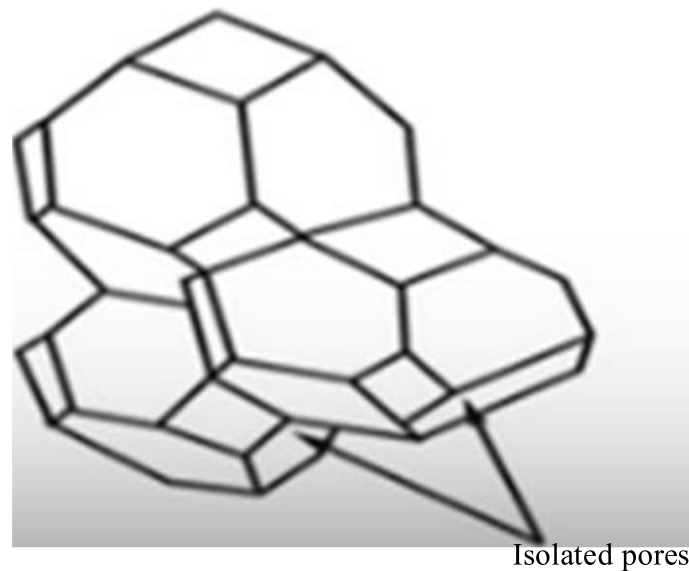


Figure 3.12: The isolated pores in the final stage of sintering located on the polyhedral grain (Kang, 2005)

3.1.5.5 Principles of the mechanical properties of ceramics

Inglis' Theory and Griffith's Theory explain the mechanical properties of Ceramics.

a) Inglis Theory

Inglis' theory was the first principle on solid fracture. It is expressed in Equation (3.17) and it demands that the rupture of the inter-atomic bonds generate new surfaces and enhance surface energy (Barsoum and Barsoum, 2002).

$$\sigma_{th} = \left(\frac{\sigma_y \gamma}{a_o} \right)^{1/2} \quad 3.17$$

where σ_{th} is the theoretical cohesive strength, a_o is the inter-atomic spacing, σ_y represents Young's modulus and γ stands for the surface energy. The theoretical value is always higher than the experimental values due to the defects in the material. It is the stress concentration at the crack tip that is of concern. This stress concentration is expressed by the Inglis Theory expressed in Figure 3.13 which shows an elliptical crack with a sharp tip in a material. If the length of the crack is L_c , L_t is the crack tip, σ_s is the stress on the material and if $L_c \gg L_t$ then the maximum stress (σ_{smax}) the material can hold before collapsing

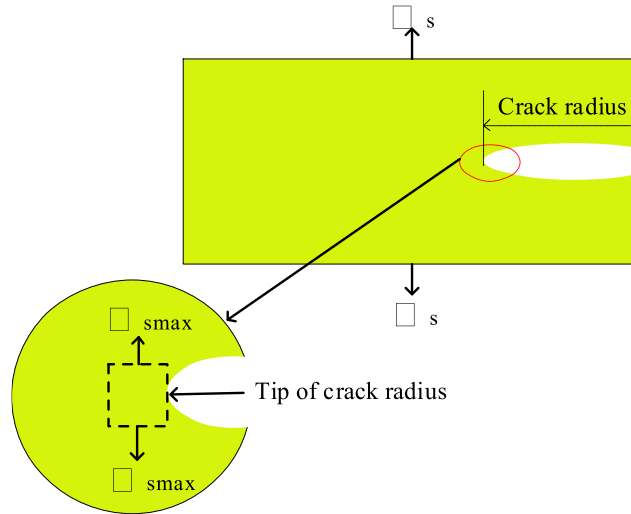


Figure 3.13 Schematic showing the stress concentration at the crack tip as explained in Inglis theory and σ is the load the ceramic can hold without breaking

The stress experienced at the tip of the breaking crack in terms of external stress is expressed in Equation (3.18). Stress intensification at the crack tip enhances the propagation of the crack and if the crack is propagated the result will be a fracture. Many dislocations in a material may result in cracks too.

$$\sigma_{smax} = \left(1 + 2\sqrt{\frac{L_c}{L_t}} \right) \sigma_s \approx 2\sqrt{\frac{c}{\rho}} \sigma_s \quad 3.18$$

Where L_c is the crack radius, L_t is the crack tip, σ_s is the stress caused by the crack, and σ_{smax} is the maximum stress. If σ_{smax} is far much greater than σ_s then there will be no fracture. Thus,

for the fracture to take place σ_{smax} must be equal to σ_{th} such that the critical stress σ_c is given by Equation (3.19).

$$2\sigma_s \sqrt{\frac{L_c}{L_t}} = \left(\frac{E\gamma}{a_o}\right)^{1/2} \Rightarrow \sigma_c = \left(\frac{E\gamma L_t}{4a_o L_c}\right)^{1/2} \quad 3.19$$

For Inglis' theorem, L_t is equal to a_o . Thus, the stress required for fracture σ_{Inglis} is given by Equation (3.20).

$$\sigma_{Inglis} = \left(\frac{\sigma_y \gamma}{4L_c}\right)^{1/2} \quad 3.20$$

b) Griffith's Theory

Griffith's theory seems to be the most accepted in explaining brittle fracture. It puts into consideration the changes in energy during fracture. Particularly the changes in surface energy and strain energy. The elastic energy U_{elas} stored in the material is given in Equation (3.21).

$$U_{elas} = \frac{1}{2} \varepsilon \sigma_s = \frac{\sigma_s^2}{2\sigma_y} \quad 3.21$$

$$U = U_o + VU_{elas} = U_o + \frac{V\sigma_s^2}{2\sigma_y}$$

Where U_{els} is the total elastic energy, σ_s is the stress initiated by the crack, U_o represents the energy in a material without applying external force and V stands for the volume of the material under investigation.

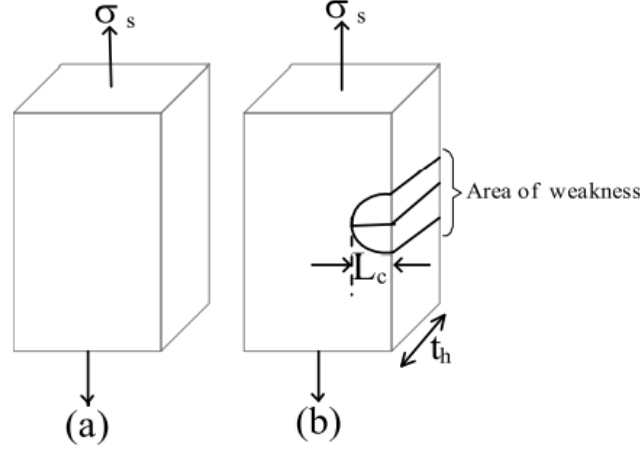


Figure 3.14: Shows the sample with thickness t_h under the strain of σ_s . In (a) the sample has no crack and sample (b) has a crack of length L_c

At equilibrium the differential of elastic energy is zero, the applied stress is equivalent to fracture stress and the crack length is equivalent to the critical crack length (Kang, 2005). After the crack length reaches the critical point, the system does not need any external energy to propagate the crack (Fang, 2010). The crack shall propagate instantaneously and the system shall continue losing energy.

The critical crack length is $c_{crit} = \frac{4\gamma\sigma_y}{\pi\sigma_f^2}$, the fracture stress is $\sigma_f = 2\sqrt{\frac{\gamma\sigma_y}{\pi c_{crit}}}$ and the crack takes place only when the applied stress is greater than or equal to fracture stress. The other condition for the fracture to take place is that the crack length must be at the critical point or greater than the critical point. When the two conditions are combined, they lead to Griffith's theory expressed in Equation (3.22). The first term refers to the stress intensity factor (K_I) and the second term is called fracture toughness or critical stress intensity factor (K_{Ic}).

$$\sigma_f \sqrt{\pi c_{crit}} \geq 2\sqrt{\gamma\sigma_y} \quad 3.22$$

A more generalized representation of the stress intensity factor puts into consideration the location and orientation of the crack and the loading pattern shown in Equation (3.23). The orientation, location, and loading pattern are represented by the constant ζ .

$$K_I = \zeta\sigma_y \sqrt{\pi L_c} \quad 3.23$$

For materials with appreciable plastic deformation, critical stress intensity factor K_{Ic} the total toughness W_c unlike in ceramic material where we have fracture toughness. There are different modes of cracks. The crack can take an opening mode, sliding mode, or a tearing mode

In ceramics, the tensile strength is also called flexural strength because the material is homogeneous (Fang, 2010). When a ceramic material is bent only the extreme grains experience the largest stress so, if those grains are free from defects, the flexural strength will be controlled by the strength of those intact 'grains'. However, if the same material was subjected to only tensile forces then all the grains in the material are at the same stress and failure will initiate when the weakest grain reaches its limiting tensile stress (Kang, 2005). Therefore, it is common for flexural strengths to be higher than tensile strengths for the same material. Conversely, a homogeneous material with defects only on its surfaces (e.g., due to scratches) might have a higher tensile strength than flexural strength (Barsoum and Barsoum, 2002).

If we do not take into account defects of any kind, it is clear that the material will fail under a bending force shown in Figure 3.15 which is smaller than the corresponding tensile force. The two forces will induce the same failure stress, whose value depends on the strength of the material. For a cylindrical sample, the resulting stress under an axial force is given by Equation (3.24).

$$\sigma = \frac{8LD}{\pi D_s^3} \quad 3.24$$

Where L is the fracture load N/m^2 and D is the distance between supporting rolls and D_s is the sample diameter.

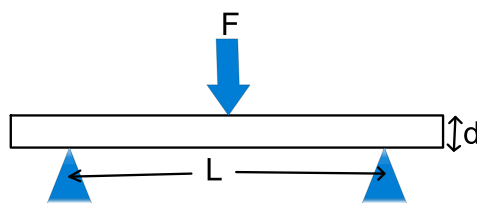


Figure 3.15: A Schematic diagram of a bend (three-point test) where L is the distance between two supporting loads, d is the diameter of the sample and F is the fracture load

3.2 Relationship Between Porosity and Mechanical Strength

Several approaches have been proposed to explain the relationship between porosity and mechanical strength. The first deals with the mechanical strain analysis on materials assuming stress concentration and pore shape. The second one considers the effect of cross-section geometry as pertinent in the porosity-strength relationship. The last approach focuses on the effect of micromechanics such as the effect of pore and stress concentrations.

3.2.1 Minimum Contact Area Model (MCA)

This theory indicates that transverse rupture also called modulus of rupture or bend strength or flexural strength of a material, in this case, ceramic membrane, depends on the minimum solid (contact) area. Thus, Young's modulus decreases exponentially with an increase in porosity as derived by (Andersson, 1996). The equation first assumes a large porous isotropic ceramic and has stress remotely applied to it. Secondly, the shape of the pores and packing geometry is independent of the fluctuations in porosity. Below is the summary of the derivation.

Consider an axial pore with a diameter of $2c$ units and $2a$ units shown in Figure 3.16. The pore is contained in a large isotropic material whose axis of rotation is Z and is tilted to z' with an angle ϕ confined within the huge isotropic material. When the stress σ_p is applied to the pore as shown in Figure 3.16, the surface of the pore undergoes deformation in a differential ellipsoid volume of Equation (3.25).

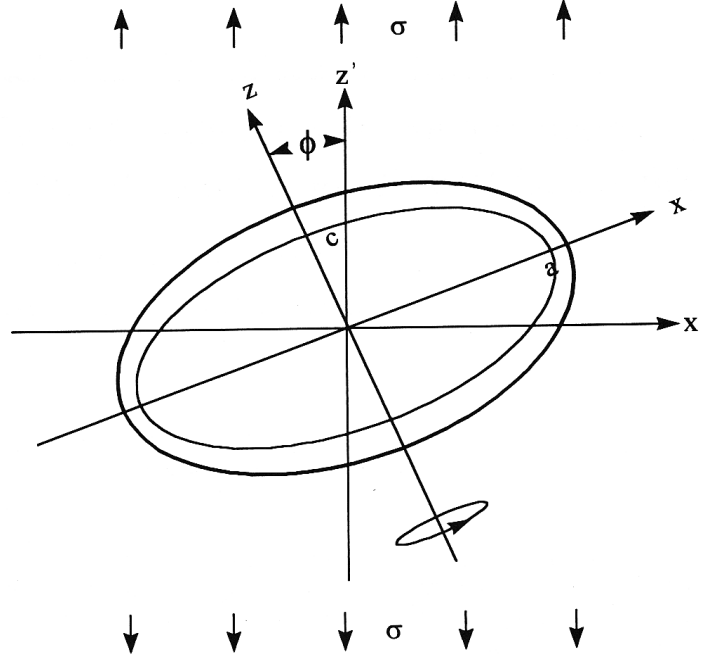


Figure 3.16: A pore contained in a large isotropic material whose axis of rotation is Z and is tilted to z' with an angle ϕ (Andersson, 1996)

$$dU_{\sigma} = \sigma dV(a, c, \sigma_p, \phi) = 2\sigma \left[\begin{array}{l} dw(x, y, a, \sigma_p, \phi) dx dy \\ + du(y, z, a, c, \sigma_p, \phi) dx dz \end{array} \right] \quad 3.25$$

where u and w are the displacements of the pore surface in the x - and z - directions, respectively, and their differentials are given in Equations (3.26) and (3.27) respectively.

$$du(y, z, a, c, \sigma, \phi) = \frac{2(1-\nu^2)}{\sigma_{Eo}\sigma_E(k_a)} a \left(1 - \frac{y^2}{a^2} - \frac{z^2}{k_a^2 a^2} \right)^{1/2} \sin^2 \phi d\sigma \quad 3.26$$

$$dw(x, y, a, \sigma, \phi) = \frac{4(1-\nu^2)}{\pi\sigma_{Eo}} a \left(1 - \frac{x^2}{a^2} - \frac{y^2}{a^2} \right)^{1/2} \cos^2 \phi d\sigma \quad 3.27$$

Where σ_{Eo} is the initial elastic modulus $E_E(k_a)$ is the complete elliptic integrals, k_a is the aspect ratio (c/a), and ν is Poisson's ratio. Notice that the pore is elliptical and its volume is given by equation (3.28).

$$V = \frac{4\pi ka^3}{3} \quad 3.28$$

If Equations (3.26), (3.27), and (3.28) are substituted in Equation (3.25) and the resultant integrated the result will be as shown in Equation (3.29).

$$U_\sigma = \frac{(1-2^2)}{\sigma_{Eo}k_a} \sigma^2 \left(\frac{2 \cos^2 \phi}{\pi} + \frac{k \sin^2 \phi}{\sigma_E(k)} \right) V_p \sigma \quad 3.29$$

From equation (3.29) any orientation of pores can be considered but two cases are of importance: aligned and randomly oriented pores. Equation (3.30) and Equation (3.31) give the expressions for aligned and random distribution functions $I(\phi, \sigma)$ respectively.

$$\bar{U}_\sigma = \frac{\int_0^{2\pi} \int_0^{\pi/2} I(\phi, \theta) U_\sigma(\phi) \sin \phi d\phi d\theta}{\int_0^{2\pi} \int_0^{\pi/2} I(\phi, \theta) \sin \phi d\phi d\theta} \quad 3.30$$

$$\bar{U}_\sigma(\text{random}) = \frac{2(1-\nu^2)}{3\pi k \sigma_{Eo}} \left(1 + \frac{\pi k}{\sigma_E(k)} \right) \sigma^2 V_p \quad 3.31$$

When the remotely applied energy remains constant and the pore volume increases, then there will be a net increase in the body's strain energy. The reverse is true for fixed grip conditions. Thus, U_1 , strain energy of a large volume (V) of a ceramic and has a pore subjected to a remotely applied fixed strain, σ_E , is

$$U_1 = \frac{\sigma_{E1} \varepsilon^2 V}{2} = \frac{\sigma_{Eo} \varepsilon_P^2 V}{2} - \frac{\sigma_{Eo} \varepsilon_P^2 V_p}{2} - \frac{g(\nu, k, \phi) V_p}{2} \quad 3.32$$

Where σ_1 is the apparent elastic modulus of the body containing the single pore, ε_P is porosity, and V_p is the volume of pores

$$g(\nu, k, \phi) = \frac{2(1-\nu^2)}{k} \left(\frac{2}{\pi} \cos^2 \phi + \frac{k}{\sigma_E(k)} \sin^2 \phi \right) \quad 3.33$$

Solving for U_I results in

$$U_1 = U_o \left[1 - (1 + g(v, k, \phi)) \frac{V_p}{V} \right] \quad 3.34$$

If n aligned pores are introduced independently, the effective elastic modulus, σ_E , after introducing the n^{th} pore into the body with a net effective modulus of σ_{En} , can be written as

$$\sigma_{En} = \sigma_{En-1} \left[1 - (1 + g(v, k, \phi)) \frac{V_p}{V} \right] = E_{n-2} \left[1 - (1 + g(v, k, \phi)) \frac{V_p}{V} \right]^2 = \sigma_{Eo} \left[1 - (1 + g(v, k, \phi)) \frac{V_p}{V} \right]^n \quad 3.35$$

substituting $\frac{f_p}{n}$ for $\frac{V_p}{V}$ where the former is the fraction of pores denoted as f_p divided by the number of pore n and later is the volume fraction of pore volume V_p divided by the entire volume of the material.

$$\sigma_{En} = \sigma_{Eo} \left[1 - (1 + g(v, k, \phi)) \frac{f_p}{n} \right] \quad 3.36$$

Comparing series expansions of the Equations (3.36) and (3.33) we get,

$$\begin{aligned} \sigma_{En}(\text{aligned}) &= \sigma_{Eo} \exp \left[-(1 + g(v, k, \phi)) f_p \right] \\ &= \sigma_{Eo} \exp \left\{ - \left[1 + \frac{2(1-v^2)}{k} \left(\frac{2}{\pi} \cos^2 \phi + \frac{k}{E(k)} \sin^2 \phi \right) \right] f_p \right\} \end{aligned} \quad 3.37$$

And the energy under random orientation is

$$\sigma_{En}(\text{random}) = \sigma_{Eo} \exp \left\{ - \left[1 + \frac{4(1+v^2)}{3\pi} \left(\frac{\sigma_E(k) + \pi k}{k\sigma_E(k)} \right) \right] f_p \right\} \quad 3.38$$

Equations (3.37) and (3.38) are similar to Equation (3.39)

$$\sigma = \sigma_o \exp(-b\varepsilon_p) \quad 3.39$$

where σ is the Young's Modulus of the fired material, σ_o is the Young's Modulus of a material that has attained full densification, b parameter is dependent on pore orientation and structure.

The b parameter moreover depends on the fabrication methods which determine solid-phase and pore-phase behavior, which eventually affect the quantity of closed and open pores. P represents volume fraction porosity.

There are several shortcomings in Equation (3.39): it does not include pore interactions and intersections that characterize high porosities. It is thus limited to a low porosity of less than 40.0% (Andersson, 1996). Further, the equation fails at the boundary of $\sigma = 0$ at $P = 1$ (Boccaccini and Fan, 1997).

3.2.2 Stress Concentration Effects (SCE) Model

Due to the limitations in the MCA model the second approach called the stress concentration effects (SCE) model tries to address the aforementioned limitations. The model indicates that Young’s modulus depends on the pore shape and stress concentration. The model predicts that the fracture strength-porosity of a ceramic material obeys a binomial function derived by (Phani and Niyogi, 1987). In its derivation, a porous ceramic material shown in Figure 3.17 is considered. The body has a uniform cross-sectional area A with length l , and it is under the stress of a load W applied in direction x and has a porosity P . The infinitely small change in elongation ($\Delta\delta$) of volume $A dx$ is shown in Equation (3.40).

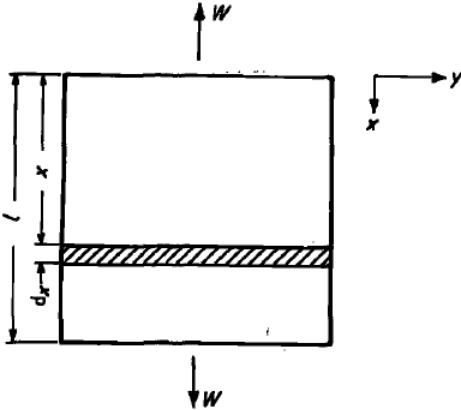


Figure 3.17: A porous ceramic material under tension with applied force W

$$\Delta\delta = \frac{\left(\frac{W}{A_x}\right)}{\sigma_{Eo}} dx \tag{3.40}$$

Where A_x is the solid area of cross-section present in dx . The total elongation is thus a sum of all the innately small elongations given by Equation (3.41)

$$\delta = \sum \Delta\delta = \int_0^l \frac{W}{\sigma_{Eo} A_x} dx \quad 3.41$$

Just like in the MCA model derivations, let the σ_E be the apparent elastic modulus σ of the body and Equation (3.41) becomes Equation (3.42),

$$\sigma = \frac{\left(\frac{W}{A}\right)}{\left(\frac{\delta}{l}\right)} \quad 3.42$$

Substituting Equations (3.41) and (3.42) we get Equation (3.39).

$$\frac{1}{\sigma} = \frac{1}{\sigma_o l} \int_0^l \frac{A}{A_x} dx \quad 3.43$$

However, if ε_{px} is equal to the mean porosity in the volume $A dx$ then $\frac{A_x}{A} = 1 - \varepsilon_{px}$ Equation (3.40) becomes

$$\frac{1}{\sigma} = \frac{1}{\sigma_o l} \int_0^l \frac{dx}{1 - \varepsilon_{px}} \quad 3.44$$

The integral can only be evaluated if porosity is expressed as a function of x , something that is impossible and can only be possible in ideal situations. For real systems Equation, (3.44) can be expressed as in Equation (3.45)

$$\sigma = \sigma_o f(1 - \varepsilon_p) \quad 3.45$$

The function $f(1 - \varepsilon_p)$ represents average porosity ε_p and must satisfy the boundary conditions of $\sigma = \sigma_o$ for $\varepsilon_p = 0$ and $\sigma = 0$ for $\varepsilon_p = 1$. The only binomial function that satisfies these conditions is of the form shown in Equation (3.46). The ceramic materials constants are denoted as η , $a = 1/\varepsilon_{pc}$. ε_{pc} represents critical porosity in which there are zero Young's moduli.

$$\sigma = \sigma_o (1 - a\varepsilon_p)^\eta \quad 3.46$$

This model addresses the challenges of boundary conditions through the exponent η in which pore orientation, structure, and shape are addressed with respect to the stress axis and Poisson's ratio.

$$\eta = 1.21 \left(\frac{z}{x} \right)^{1/3} \sqrt{1 + \left[\left(\frac{z}{x} \right)^{-2} - 1 \right]} \cos^2 \phi \quad 3.47$$

Where ϕ is the angle between the direction of the applied stress and the axis of rotational for the spheroids in which the pores are oriented and $\alpha = z/x$ is the aspect ratio, α is the average pore shape also known as the axial ratio of spheroids. The SCE assumes that the pores are microstructurally spheroidal. As a result, it considers ceramic materials as made up of only two-phase composites comprising spheroids and a continuous matrix phase. Spheroids also possess a regular mathematically particular geometry that consists of an equal surface-to-volume ratio in the grains and pores. Spheroids' shapes depend on the aspect ratio such that for

$\alpha \rightarrow 1$	prolate spheroids change to needle-shaped spheroids
$\alpha \rightarrow 0$	Spheroids become oblate spheres
$\alpha = 0$	Oblate spheroids change to disc-shaped spheres

Three factors are of importance in the SCE model: orientation of the pores, shape, and distribution (Roberts and Garboczi, 2000; Phani and Niyogi, 1987).

The orientation, on the other hand, is determined by the cosine factor in Equation (3.43). For the random orientation in isotropic ceramic material the orientation factor $\cos^2\phi$, will be equal to 0.33. Therefore, with adequate details on the structure of porosity including the analysis of quantitative microstructures, η can be computed and used to envisage the fracture strength of porous ceramic materials (Boccaccini and Fan, 1997).

The advantage of the SCE model expressed in Equation (3.47) is that it is valid in different ranges of possible porosity-strength relationships such as the boundary conditions. However, this model SCE assumes that the microstructure of porosity is independent of the Poisson's ratio. That is, Poisson's ratio is not affected by porosity. This assumption may be misleading because the Poisson's ratio is calculated from the Young's and Shear modulus which are both dependent on the porosity (Kováčik, 2006).

There has been a debate as to which of the MCA and SCE models predicts most accurately the mechanical property-porosity relationship in ceramic materials. The two models and other models are shown in Table 3.1.

Table 3.1: The models to predict the relationship between mechanical strength and porosity

Model	Details	Conditions	Material	References
$\sigma = \sigma_o e^{-b\varepsilon_p}$ (MCA)	Depends on porosity and the minimum area of contact	$\varepsilon_p < 0.5$	Isotropic	(Nyongesa and Aduda, 2004; Andersson, 1996; Rice, 1989)
$\sigma = \sigma_o (1 - 1.9\varepsilon_p + 0.9^2)$	Depends on closed pore concentration	$\varepsilon_p \leq 0.5$	Isotropic	(Boccaccini and Fan, 1997; Mackenzie, 1950)
$\sigma = K_c \sigma_o \left(\frac{\rho}{\rho_s} \right)^n$	Depends on relative density, pore type, and open porosity	$\varepsilon_p < 0.4$ $K_c \cong 1$ $1 < n < 2$	Isotropic	(Ashby and Medalist, 1983)
$\sigma = \sigma_o (1 - a\varepsilon_p)^n$ (SCE)	Depending on the porosity and porosity geometry of closed pores	$\varepsilon_p < 0.4$	Anisotropic	(Boccaccini and Fan, 1997)
$\sigma = \sigma_o \frac{(1 - \varepsilon_p)^2 R}{\varepsilon_p + (1 - \varepsilon_p) R}$ $R = \frac{d_\beta}{d_\alpha}$	Depends on porosity, pore size ratio R , pore geometry, and topology of the entire porosity	$R < 1$	Anisotropic	(Kingery <i>et al.</i> , 1976)

3.2.3 Porosity-Density Relationship

In ceramics, porosity refers to the void in a body and it is a ratio of the volume of voids to the entire volume of the body. Thus, porosity ranges between 0 and 1 and it can also be expressed as a percentage ranging from 0% and 100%. Some materials such as porcelains can be sintered to zero porosity. Such materials are usually sintered up to temperatures where all the pores get filled up. Naturally, increasing temperatures of sintering bring most elements closer to their melting point (Fang, 2010). The melted matter flows and fills up existing pores. Thus, it is paramount in research that porosity is investigated across varying temperatures. There exists a relationship between the bulk density of a material ρ and the pore volume porosity as shown in Equation (3.48).

$$\varepsilon_p = 1 - \left(\frac{\rho}{\rho_t} \right) \quad 3.48$$

Where ρ_t is the material's density and volume and density are given by equations (3.49) and (3.50) respectively

$$\rho = \frac{m}{V_b} \quad (3.49)$$

$$\varepsilon_p = \frac{V_o}{V_b} \quad (3.50)$$

where m is the mass of the sample, V_b is the bulk volume and V_o are the volume of open pores

3.3 Filtration Theory

Porous water filter membranes have two mechanisms of filtration, namely: media layer surface removal and depth filtration. The media layer surface removal is the dominant mechanism where water contaminants are retained on the membrane surface. The sizes of the retained contaminants are bigger than the pore size of the membrane. Depth filtration is a secondary mechanism where contaminants smaller than the pore size of the membranes are retained in the dead ends of the pores and some are trapped by the randomly oriented filter matrix (Venis and Basu, 2020).

3.3.1 Type of Clay

The composition of the elements present in the clay powder determines the tendency of contaminants to attach themselves to the surface of the membrane. The most common clay minerals are chlorite, illite, kaolinite, montmorillonite, and smectite. Illite, kaolinite, and montmorillonite are generally used in water filtration because of their layered structure, specific surface, high chemical, and mechanical stability (Lin and Juang, 2002; Krishna *et al.*, 2000; Bailey *et al.*, 1999). Clay adsorbs contaminants from the environment by exchanging either their anions or cations because it contains exchangeable cations (Na^+ , K^+ , Ca^{2+} , Mg^{2+} , H^+ , and NH^+) and anions (Cl^- , SO_4^{2-} , NO_3^- , and PO_4^{3-}) (Zhang *et al.*, 2010; Velde, 1995; Haan and Bolt, 1963). The ions and anions can exchange with their counterparts in water without affecting the structure of clay (Srinivasan, 2011). The adsorption of contaminants in clay is also aided by the existence of Lewis and Bronsted acidity (Reddy *et al.*, 2009; Brown and Rhodes, 1997; Billingham *et al.*, 1996). When clay surface comes in contact with water polluted with metal ions, the water molecule dissociates releasing H^+ on the surface. The Bronsted acidity can also occur in tetrahedral structures when there is a net charge resulting from the exchange of Si^{+4} with Al^{+3} releasing H_3O^+ cations (Reddy *et al.*, 2009). The edges and faces of clay structures are made of Si-O-Al bonds. These bonds rupture during ceramic water filters (CWF) processing leaving Al^{3+} at the edge making the edges capable of

adsorbing contaminants in water through ion-dipole interactions, ion exchange, coordination, hydrophobic bonding, van der Waals interactions, and H-bonding (Brown and Rhodes, 1997). The type and strength of the interaction are determined by the type and structures in the clay. There are several active sites in the clay minerals which include Bronsted acid sites, Lewis acid sites, oxidizing sites, reducing sites, and surface hydroxyl groups. The bronsted site is created by interactions of the tetrahedral aluminum or silicon bonds with interlayer water molecules and it donates a proton. The Lewis acid site receives an electron from the dehydroxylation process. The octahedral structures in most clay minerals give rise to the oxidizing sites because of the presence of the cations in these sites caused by the adsorbed oxygen. Similarly, the presence of cations in clay minerals gives rise to reducing sites. At the same time, at the edges of octahedral cations there exists a hydroxyl group that gives another active site for the clays. It is these active sites that are responsible for the adsorption of contaminants from water during filtration.

There are numerous ways of blocking the entry of contaminants into the water membranes. Equally, several mechanisms promote contaminants adhering to the walls of ceramic pores and getting trapped within dead ends of ceramic pores. These filtration mechanisms include adsorption, coagulation sedimentation, and size exclusion.

3.3.2 Adsorption

Adsorption of contaminants on the membrane refers to the contaminant's tendency to adhere to the surface of the membrane due to attractive forces between the membrane and the contaminant (Ruiping *et al.*, 2009). The force creates a region of low potential energy and high molecular density of the liquid near the membrane surface. There are different types of adsorption; bio-sorption, chemisorption, and physical adsorption. Bio-sorption involves microbes and viruses getting adsorbed on the membrane (Annan *et al.*, 2018). Adsorption is called chemical adsorption if it involves chemical interaction between the adsorbate (contaminant) and the adsorbent (membrane surface). Chemisorption involves electron transfers between the contaminant and the membrane surface which give rise to chemical bonds between the contaminant and the membrane. Physical adsorption involves weak forces such as frictional forces, adhesive-cohesive interactions, and Van der Waal forces that enable the contaminant to physically attach itself to the membrane (Yao *et al.*, 1971). Usually, the adsorption of the contaminants on the membrane is affected by the type of water to be filtered, the nature of the membrane, and the contaminant. The nature of the membrane and its

surface area play important roles in water filtration as they determine the type of contaminant to be adsorbed and their (contaminants) quantity. The type of the water including its pH and temperature among others also plays a crucial role in contaminant adsorption. The concentration of the contaminant, its nature, and the presence of other contaminants also affect the adsorption process (Bellona *et al.*, 2004). The amount of contaminant (mg/g) absorbed in a given time t can be determined by Equation (3.51). In water, the adsorption results in the accumulation of solid contaminants on the surface of the membrane. The contaminant remaining in the water reaches a dynamic equilibrium with the contaminant adsorbed on the membrane. The amount of contaminants that can be adsorbed on the membrane is a function of its concentration in water and the temperature (Annan *et al.*, 2018). Thus the amount of contaminants adsorbed on the membrane depends on the adsorption isotherms. The isotherms model in Equation (3.51) shows the number of contaminants adsorbed at constant temperature (Meenakshi *et al.*, 2008).

$$Q_t = \frac{(C_{co} - C_{cf})V}{m} \quad 3.51$$

where C_{co} (mg/L) is the initial concentration of the contaminant and C_{cf} (mg/L) is the final concentration of the contaminant in the water of volume (V) after a time (t) and m (g) is the mass of the membrane. Other models that explain adsorption in water include the Langmuir model which is valid for the mono-layer system. In this work, we shall focus on monolayer models.

3.3.3 Size Exclusion

Membranes with pores smaller than the contaminant size use the size exclusion mechanism to purify water, where the contaminants are physically prevented from going through the small pores. Microbes such as *E. coli* (3 μm) are usually excluded from water using CWF due to their bigger size than pores of between 0.3 μm and 2.5 μm (Annan *et al.*, 2018)

3.3.3.1 Filtration Models

Four filtration models can be used to describe the water filtration process by porous filters. This classification is based on the pore diameter d_m of the membrane and the contaminant's size d_p of the water contaminant. These models are: 1) cake-filtration, 2) standard blocking, 3) complete blocking, and 4) intermediate blocking (Hatori and Suzuki, 2021).

3.3.3.2 Cake Filtration Model

This model represents filtration in porous ceramic filters where the pore diameter (d_m) is smaller than the size of the water contaminant (d_p) ($d_m < d_p$) (see Figure 3.18(a)).

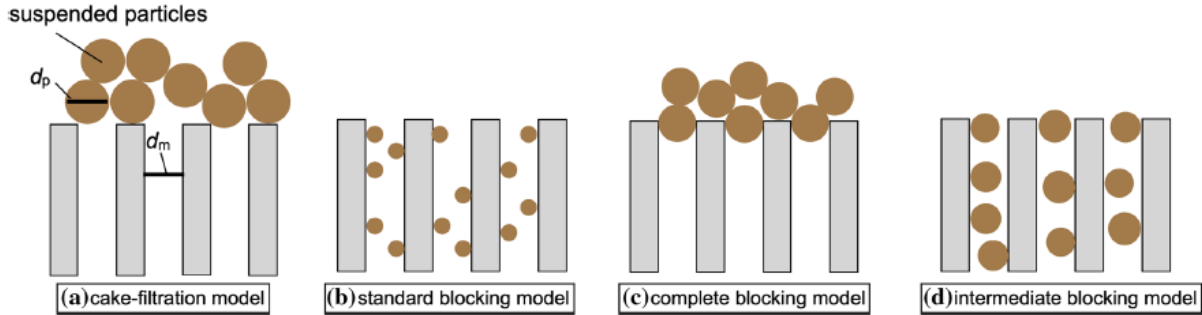


Figure 3.18: Herman-Brede'e models; d_m : pore size of membrane filter, and d_p : the particle size of suspended material (Hatori and Suzuki, 2021; Iritani and Katagiri, 2016)

Thus the contaminants are deposited on the membranes forming a 'cake layer,' which hinders the filtration process. The concentration of the retained contaminants gradually increases forming a cake layer that serves as a filter medium with a relatively lower initial pressure drop than in the main membrane. In this model mechanisms like gravity, diffusion and inertia are used to eliminate the contaminants from water. To handle the models mathematically it is assumed that the membranes are made up of circular tubes. It is further assumed that the tubes are made up of uniform inner diameter and length. To calculate flow rate J per unit of filtration area, we assume that the membrane is made of several identical tubes bundled together and they obey Hagen Poiseuille's Equation (3.52).

$$J = \frac{N\pi d_m^4 \Delta P}{128\mu L} \quad 3.52$$

where N represents the number of tubes per unit of filtration area, ΔP [Pa] is the change in pressure between the two ends of one of the uniform tubes, μ [Pa.s] stands for the viscosity of the water under filtration, and L [m] represents the tube length. Thus under constant pressure, the rate of filtration is shown in Equation (3.53).

$$J = \frac{N\pi d_m^4 \Delta P}{128\mu(L_f + L_c)} \quad 3.53$$

where L_f [m] is the membrane length, and L_c [m] is the tube length corresponding to the cake layer resistance which is expressed in Equation (3.54).

$$L_c = -\alpha_c \cdot C_c \cdot V_A \quad 3.54$$

where α_c [m³/kg] is the resistance of the cake filtration, C_c [kg/ m³] is the concentration of the

contaminant, and V_A is the filtrate volume per unit area. Then the filtration rate is given by Equation

$$J = J_o \frac{1}{1 + K_c V_A} \quad 3.55$$

where J_o is the initial flow rate per unit of filtration area, K_c is the occlusion coefficient in the cake-filtration model.

3.3.3.3 The Standard Blocking Model

In the Standard Blocking Model pore diameter of the membrane is greater than the contaminants' particle size ($d_m > d_p$) as shown in Figure 3.18(b). The contaminants are deposited on the inner parts of the pore walls during filtration causing pore shrinkage. The resistance in the Standard Blocking Model can be obtained in Equation (3.56) while the flow rate is given by Equation (3.57) respectively

$$\frac{d_p (N \pi d_m^2 L / 4)}{dt} = -\alpha_s \cdot J \cdot C_c \quad 3.56$$

$$J = \left(1 - \frac{K_s V_A}{2} \right)^2 \quad 3.57$$

and α_s [1/kg] is the occlusion coefficient of standard model filtration and K_s is the blocking coefficient in the Standard Blocking Model.

3.3.3.4 The Complete Blocking Model

Figure 3.18(b) shows the schematic representation of the complete blocking model. In this model both the pore diameter and contaminants particle size are equal ($d_m = d_p$). Thus the membranes' pores become sealed during filtration decreasing their porosity. Equation (3.58) describes how the model removes the contaminants in water in a given time and Equation (3.59) shows the flow rate in this model

$$\frac{dN}{dt} = -\alpha_b \cdot J \cdot C_c \quad 3.58$$

$$J = J_o (1 - K_b V_A) \quad 3.59$$

where K_b [1/m] is the coefficient of blocking in the Complete Blocking model.

3.3.3.5 The Intermediate Blocking Model

This model incorporates phenomena that are between the standard blocking model and the Complete Blocking Model. In the intermediate blocking model, the pore diameter is either equal to or greater than the contaminants' particle size ($d_m \geq d_p$). Equation (3.60) describes contaminant removal in the Intermediate Blocking Model and Equation (5.61) shows the rate of flow of water in the same model.

$$\frac{dN}{dt} = -\alpha_i \cdot J \cdot C_c \cdot N \quad 3.60$$

$$J = J_o \exp(-K_i V_A) \quad 3.61$$

where $K_i[1/m]$ is the coefficient of Intermediate Blocking Model models.

3.4 Analytical Techniques

The analytical techniques here refer to the procedures used to acquire the data analyzed in this work. They include crystallography techniques such as x-ray fluorescence and diffraction; and the scanning electron microscope.

3.4.1 X-ray Fluorescence

Figure 3.19 shows electrons bound to the atom by a positive charge of the nucleus and they are arranged in different shells ($K, L, M \dots$) depending on the atomic mass Z of the atom (Halliday *et al.*, 2001). The electrons closer to the nucleus, for instance, electrons on K -shell, are more strongly bound to the atom than the electrons away from the nucleus like electrons in the M shell (Puri and Babbar, 2010). There are also sub-shells ($\alpha, \beta, \gamma \dots$) in the shells which are occupied by electrons based on Pauli's exclusion principle, and are responsible for the different transitions that produce the x-ray fluorescence characteristic spectrum (Ghoshal, 2007). Figure 3.19 shows a Kossel diagram illustrating K_α and L_α transitions in a silicon atom.

When an x-ray beam hits the sample as shown in Figure 3.19, the atom absorbs energy E_k and emits an electron from the inner shell (K shell) leaving a hole. This makes the atom unstable and to stabilize it an electron from higher shells, for instance, L (with energy E_L) or M (with energy E_M) moves in to replace the displaced electron (Ghoshal, 2007). In doing so, the atom emits x-rays of lower energy which can be detected as peaks in a spectrum and there are different peaks for each atom and each transition hence the term characteristic spectrum.

Equations (3.62) and (3.63) show how the energy of K_α and K_β transitions are obtained (Puri and Babbar, 2010).

$$E_{K_\alpha} = E_K - E_L = h\nu(K_\alpha) \quad 3.62$$

$$E_{K_\beta} = E_K - E_M = h\nu(K_\beta) \quad 3.63$$

where E is energy, h is Planck's constant, ν is frequency, K , L , M are shells, α and β are sub-shells.

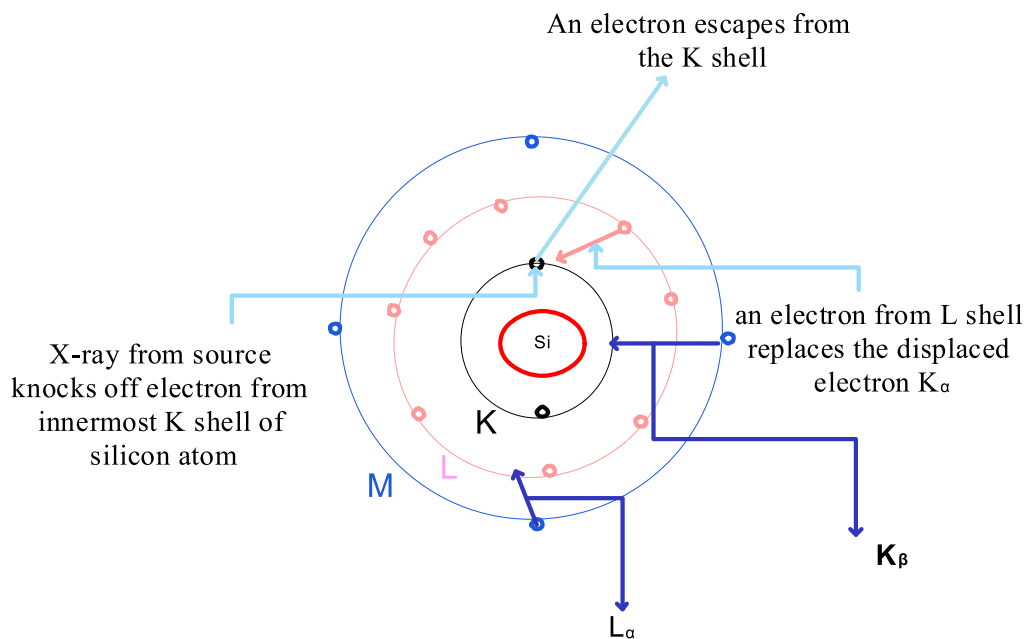


Figure 3.19: A Kossel diagram showing the K_α x-ray transition of the silicon atom. Other shells (M and L) are also shown (Halliday et al., 2001)

3.4.2 X-ray diffraction

X-ray diffraction is an elastic scattering of an x-ray beam caused by an x-ray beam of comparable wavelength with the interplanar distance which gives direct information on the lattice structure and atomic information of the sample (Puri and Babbar, 2010). Consider two beams of x-ray light P and Q incident as shown in Figure 3.20. The distance BD is equal to the interplanar distance, d . From Figure 3.20 it is clear that ray Q travels an extra distance of AB as compared to ray P . Similarly, the reflected ray Q' travels an extra distance of BC as compared to the reflected ray of P . From Figure 3.20 it is clear too that AB is equal to BC implying that ray Q travels an extra distance of the sum of AB and BC as compared to ray P , and for a constructive interference being shown in Figure 3.20, the path difference is equal to the integral of the wavelength, λ (Ghoshal, 2007).

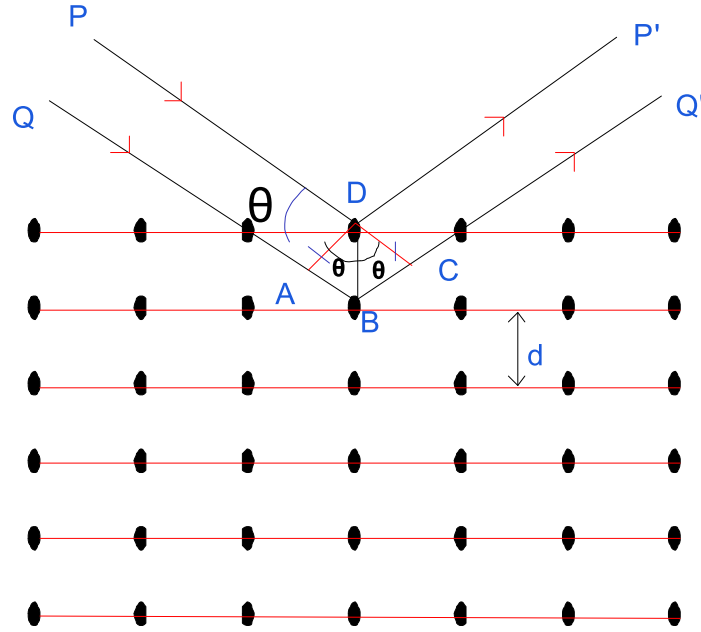


Figure 3.20: Bragg's reflection under constructive interference. Ray P and Q strike two successive planes at a glazing angle θ (Ghoshal, 2007)

If n is the integral difference, then using the trigonometric function, we are justified to write Equation (3.64) which is Bragg's law.

$$2d \sin \theta = n\lambda \quad 3.64$$

And if $n = 1$ in Equation (3.64) then we get the first-order diffraction. In the characteristic spectrum, this first-order diffraction is given in Equation (3.65). The first-order diffraction gives the most intense peaks followed by the second-order, and so on (Ghoshal, 2007).

$$\sin \theta = \frac{\lambda}{2d} \quad 3.65$$

The characteristic spectra obtained from the x-ray diffraction give the Miller indices shown in Equation (3.66) which can be used to calculate the crystal's atomic fractional coordinates, lattice parameters, and space group if the x-ray wavelength is known.

$$d_{(hkl)} = \frac{a}{(h^2 + k^2 + l^2)^{1/2}} \quad 3.66$$

Where d is the interplanar distance, a is the interatomic distance, h , k , and l are Miller indices. Thus, d is maximum when the interplanar distance is equal to the interatomic distance and the Miller indices are minimal (first-order) (Halliday *et al.*, 2001).

3.4.3 Crystallinity

The test material is assumed to be amorphous if the XRD pattern forms broad peaks and crystalline if it is characterized by sharp peaks (Lee and Santmartí, 2018). However, most of the time the amorphous and crystalline characteristics can be expressed in the same peak. In such cases, the ratios of amorphous and crystalline properties are calculated using Equation (3.67)

$$\%C = \frac{I_c - I_a}{I_c} \quad 3.67$$

Where $\%C$ is the percentage of crystallinity, I_a is the intensity height of the minimum intensity of the major peaks that correspond to the amorphous content of the sample, and I_c is the height of the highest peak that corresponds to the amount of crystalline material (Lee and Santmartí, 2018).

3.4.4 Scanning Electron Microscope (SEM)

The scanning electron microscope uses kinetic energy to introduce interaction between secondary electrons in the sample. The electrons are generated from the tungsten filament represented as an electron gun shown in Figure 3.21. The emitted electrons are produced by applying high thermal energy to the target (tungsten) and are accelerated to the anode by a high potential difference. The high-energy electrons generate two types of beams of electrons when it interacts with the sample; primary scattered electrons with high energy and secondary electrons which have comparatively low energy. The primary electrons are crucial in studying the morphology and topography of the samples. The secondary electrons (backscattered electrons) give details on the contrast and elemental composition of the samples. The primary and secondary electrons together produce signals that give information about the surface topography, morphology, and composition of the specimen. To get the said information the detectors and scintillators aid in breaking down the signal into electric current using photomultipliers which then send the signal to the cathode ray tube. This produces noncolored images. The number of secondary electrons that reach the detector on the nature of the sample such that raised surfaces appear brighter than depressed surfaces.

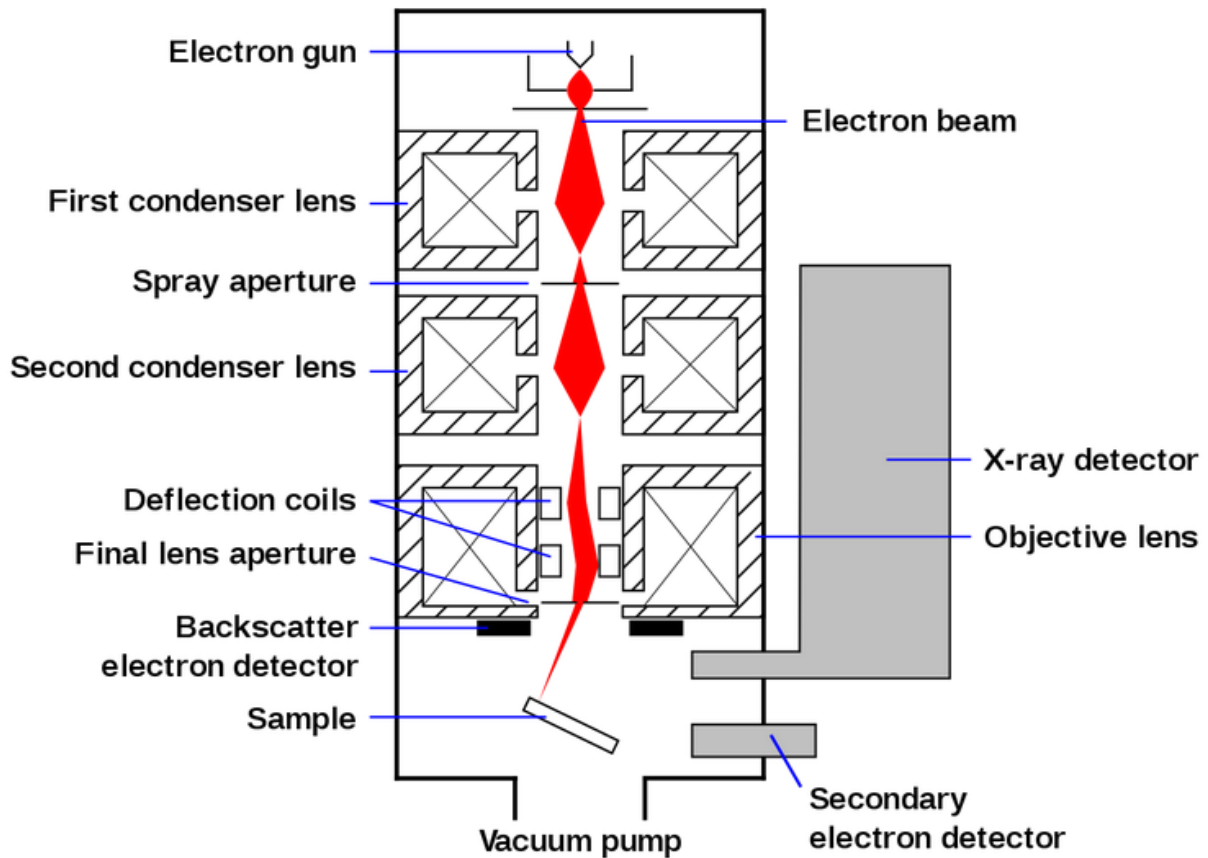


Figure 3.21: The schematic representation of the scanning Electronic Microscope

3.5 Concept of Magnetic Field Application

3.5.1 Magnetization and Magnetic Field Susceptibility

Particles (molecules) of contaminants and molecules of water can either be classified as positively charged or negatively charged and their magnetization can be measured by Equation (3.68).

$$M = \chi_v \cdot H \tag{3.68}$$

where M is the magnetization of a molecule after exposure to H , H is the magnetic field, and χ_v is the magnetic susceptibility of magnetized electrons.

Water is a polar molecule where the center of gravity of the slightly positive hydrogen nuclei coincides with the center of gravity of the slightly negative oxygen nuclei. Molecular contaminants can be classified as either polar or nonpolar. Figure 3.22 shows the arrangement of polar and nonpolar molecules in the presence and absence of the magnetic field (Zaidi *et al.*, 2014). When the magnetic field is absent, both polar and nonpolar molecules are

positioned randomly. Thus, the negative and positive charges in polar molecules cannot attach even though there are collisions among the molecules and nonpolar molecules remain in random motion. However, in the presence of the magnetic field, the polar molecules get more easily aligned than the nonpolar molecules due to the slight charge the polar molecules possess. Thus both polar and nonpolar molecules get aligned in the direction of the applied magnetic field (Vick, 1991) as shown in Figure 3.22. The alignment of molecules causes the contaminants to coagulate and aggregate. Furthermore, the number of dipoles in alignment increases with an increase in the intensity of the magnetic field. The magnetization of the contaminants' particles that result in coagulation and aggregation proves that magnets can be used to remove contaminants from water.

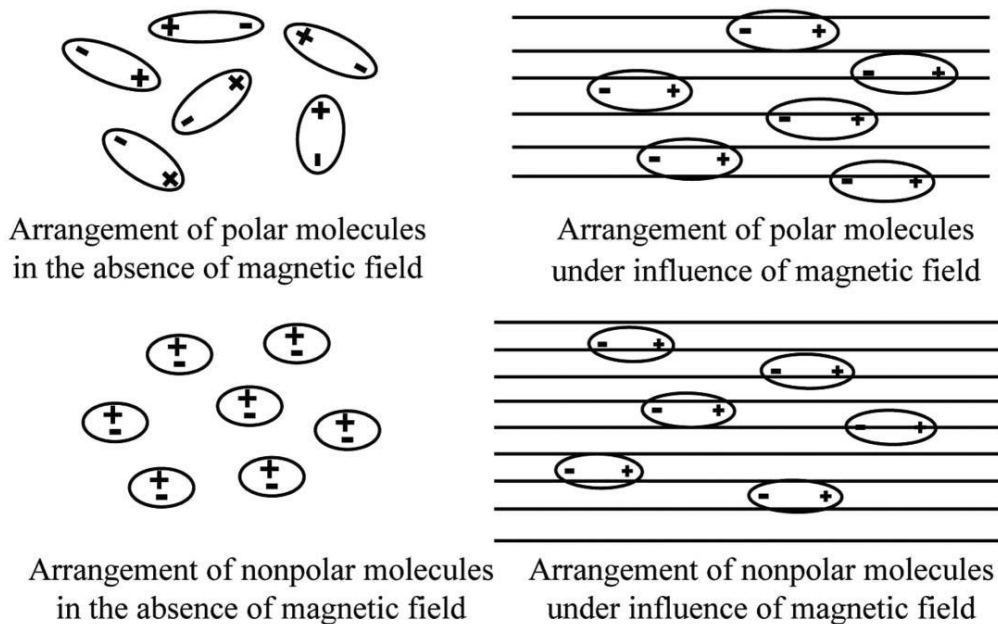


Figure 3.22: The arrangement of polar and nonpolar molecules in the presence and absence of the magnetic field (Zaidi *et al.*, 2014)

3.5.2 Magnetic Gradient

The effectiveness of water purification using a magnetic field depends on the magnetic strength and gradient (Chibowski and Szcześ, 2018; Oshitani *et al.*, 1999). The magnetization M and the magnetic field H in the material of volume V give rise to the energy E shown in Equation (3.69) and can be simplified to Equation (3.70). To get Equation (3.69) we assume that the magnetic strength M is uniformly distributed in the material and is parallel to the material load, where χ_o is the initial magnetic susceptibility of the material when there is no applied magnetic field. The differential, dH/dx , is the magnetic gradient and it refers to the rate of change of the magnetic field strength in the x-direction

$$E = -VM.H = -V(\chi_v.H).H \quad 3.69$$

$$F = -(dE / dx) = (\chi_v - \chi_o)VH(dH / dx) \quad 3.70$$

When all the molecules are aligned the magnetic field in the material becomes uniform and there will be no magnetic gradient and force (Kronenberg, 1985). Thus the contaminants will not be separated from the water as the contaminants' molecules will not experience force. The volume of water to be purified also plays an important role as a small volume of water gets aligned faster than bigger volumes (Oshitani *et al.*, 1999). To get the highest magnetic force that would separate contaminant particles from water, therefore the highest magnetic gradient is needed and alternating magnetic strength offers a higher (magnetic gradient) than a static magnetic field (Franzreb and Holl, 2000; Iwasaka and Ueno, 1997).

The magnetic gradient can be used in magnetic filtration to remove suspended contaminants and starch from water (Dauer and Dunlop, 1991). Magnetic filtration can be achieved by circulating water with charged particles of contaminants through magnetized coils. The permanent magnet that is responsible for magnetizing is located outside the water pipes and the poles are alternated to create an alternating magnetic field of high gradient due to the combination of the coil magnet and the permanent magnet (Hirschbein *et al.*, 1982). When water flows through the coil, the contaminant's charged particles are attracted to the coil and separated from the water. The amount of contaminants attracted to the coil depends on the magnetic gradient which in turn depends on coil characteristics and the strength of the permanent magnet (Johan, 2003).

3.5.3 Lorentz Force

Lorentz force acts on the contaminants' particles moving through the magnetic field. The particle charge, orthogonal vector component, and its velocity linearly affect the Lorentz force (Baker and Judd, 1996) as shown in Figure 3.23. When the charged particles of the contaminant flow normal to the direction of the field in the same plane, a Lorentz force is generated as indicated in Equation (3.71) which is also normal to the direction of the charged particles and the field (Spiegel, 1998; Bruk *et al.*, 1987). If the z -plane is the direction of Lorentz force, then the charges on the surfaces of the contaminant's particles will be displaced causing the contaminant's molecules to be unstable. When the unstable molecules collide with each other, aggregation of the molecules occurs (Spiegel, 1998; Vick, 1991). The

Lorentz force has also been used in crystallization to form water nuclei, enhancing dissolution in water, and stabilizing double-layer distortion of coordinated water (Zaidi *et al.*, 2014).

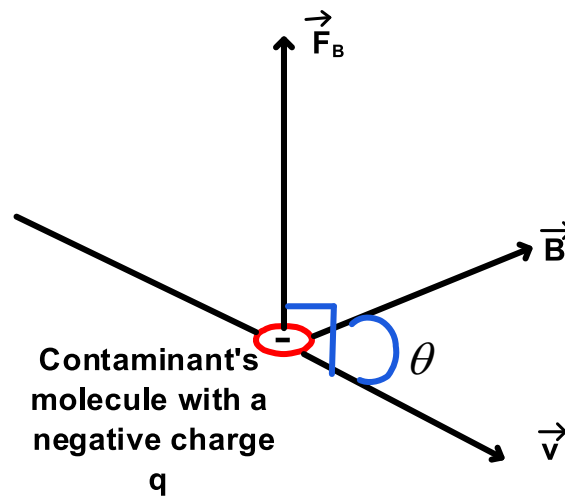


Figure 3.23: A contaminant molecule with a negative charge q in water with a velocity v under the influence of force \vec{F}_B caused by a magnetic field \vec{B} (Puri and Babbar, 2010)

$$F_B = q\vec{v} \times \vec{B} \quad 3.71$$

where F_B is the Lorentz force acting on the contaminants, q is the charge on the contaminant particle, v is the velocity linearly orthogonal to the magnetic field B , and the resultant Lorentz's

3.5.4 Magnetic memory

When the magnetic field interacts with water it affects its kinetic energy and the momentum of the dipolar molecules resulting in particle aggregation and stable molecules larger than the initial water molecules (Lychagin, 1974). The stability and large size of the aggregated molecules make it difficult for them to resume their initial state resulting in magnetic memory (Johan, 2003). However, the changes in the water structure are not permanent and the duration under magnetic memory can be retained differ depending on the contaminant. For particle contaminants, higher magnetic memory has been shown to increase particle aggregation but for microorganisms, magnetic memory depends on their magnetic susceptibility (Lychagin, 1974). When the magnetic susceptibility of a certain material exceeds a certain level the organism may die or show growth reduction (Lebkowska *et al.*, 2011; Lychagin, 1974).

CHAPTER FOUR: MATERIALS AND METHODS

4.1 Sourcing of Materials

All the materials used in this work were sourced locally from Kenya. And the chemicals used were of analytical standards. The distilled water was prepared in our laboratories.

4.1.1 Diatomaceous Earth and Charcoal

The pure diatomaceous earth, DE-A, and DE-B, under the brand name of Kensil 90 and Kensil SSF, and diatomaceous earth waste (DE-waste) were sourced from African Diatomite Industries Limited (ADIL) situated at Kariandusi near Gilgil, Nakuru County, Kenya. The difference between DE-A and DE-B is in the age of the fossil from which they were extracted. DE-A was extracted from a fossil estimated to be one million years old, and the fossil from which DE-B was extracted is estimated to be three million years old. Wet Potter's Clay was sourced from Kitabisi, Bungoma County, Kenya. The wet clay was sun-dried for seven days. Both the Potter's clay and diatomaceous earth were ground as specified in Table 4.1 using a ball mill (Fritch model, Germany) to increase the surface area of the particles. The charcoal used was made from kitchen wastes such as potato and banana peels which were burnt under limited oxygen for five hours to produce charcoal. The hot charcoal was then cooled for twenty-four hours at room temperature of 24.0 °C. The freshly made charcoal was later ground for 25.0 minutes using the aforementioned ball mill whose settings are indicated in Table 4.1.

Table 4.1: The setting for the Ball mill used in grinding charcoal diatomaceous earth

Sample	No. of balls used	Time (Minutes)	Revolution	Reverse
Charcoal	25	25.0	200	1
Diatomaceous Earth	25	25.0	200	1
DE-waste	25	25.0	200	1
Clay	25	45.0	200	2

4.1.1 The Organic Binders and Molasses

The black strap (*C* Molasses) was sourced from the Nzoia Sugar Company Ltd and was used as received. Fresh green plants, some of which are used as vegetables: *Abelmoschus esculentus* (*Okra*), *Aloe vera*, *Basella alba* (*Nderema*), and *Corchorus olitorius* (*Mrenda*)

whose local names are given in the parentheses, from which the organic binders were obtained were sourced from Muthurwa Open Market, Nairobi, Kenya. The leaves were picked from the stalk and washed three times using distilled water. The washed vegetables were left on kitchen sieves for twelve hours to drain the excess water accumulated from washing. After the excess water was removed, the masses of the green vegetables were taken using an electronic weighing machine. Two kilograms of each vegetable were separately boiled for fifteen minutes by adding an equal amount (2.0 L) of distilled water to it. The boiled leaves were left to cool for twelve hours and then sieved using kitchen sieves. Subsequently 30.0 ml of each filtrate, here referred to as a binder, was taken for viscosity measurement to determine the resistance to the flow of the binders. The process was repeated for each binder, and the respective binder filtrates were stored in a fridge at approximately 6.0 °C to prevent degradation of the binders, awaiting use in the fabrication of the water filter test samples/membranes and modulus of rupture (MOR) test samples.

4.2 Material Characterization

The powder was characterized in terms of particle size, and elemental analysis using XRD and XRF. The binder was characterized in terms of organic matter, and viscosity.

4.2.1 Particle Size

The particle sizes of the pure diatomaceous earth, diatomaceous earth waste, charcoal, and clay powders were analyzed by a Particle Sizer (Malvern Panalytical Master sizer 3000) through air dispersion. The background measurement was done for 15.0 seconds and the sample measurement was also done for 15.0 seconds. Before taking the measurement the obscuration lower limit was set at 0.5 seconds, the upper limit was set at 15.0 seconds and the obscuration filtering was enabled for 30.0 seconds. The data processing mode was set at fine powder mode and the result range was not limited. Each sample was measured three times and the average result was noted.

4.2.2 X-Ray Fluorescence Analysis

The elemental characterization of the diatomaceous earth samples was done using an energy dispersive X-ray fluorescence (EDXRF) spectrometer (ED XRF CG Spectrometer Rigaku). The EDXRF device parameters were set as displayed in Table 4.2. The secondary targets were Al, Cu, Mo, and RX9. All the secondary targets were used because the elements

suspected to be present in the samples had varied atomic mass with some elements like sodium having low atomic mass and others having high atomic mass. There were three types of samples, clay, DE-A, DE-B, and DE-waste.

Table 4.2: The Specifications of the Energy Dispersive X-Ray Fluorescence Spectrometer for carrying out elemental analysis

Detector	High-performance Silicon Drift Detector (SDD)
Tube type	Air-cooled
Atmosphere	Vacuum
Tube Voltage	20 kV
Tube current	70 μ A
Secondary	5

Two grams of each powder were put in the sample caps. The diameter of the caps and the sample height was noted. The process of taking the XRF pattern of the organic binders and molasses was similar to the one of DE powder except that the measurements were taken in air and at ambient temperature.

4.2.3 X-ray Diffraction of Diatomaceous Earth Powder

The crystal structure of the milled DE-A, DE-B, and DE-waste powder was analyzed by an Empyrean, PANalytical–X-ray diffractometer equipped with a robotic arm sample exchange, using Cu target $K\alpha = 0.15406$ nm radiation, operating at 40 mA and 45 kV. The mean grain size G_s was calculated using Debye-Scherrer’s Equation (Patterson, 1939) is shown in Equation (4.1).

$$G_s = \frac{c_s \lambda}{b \cos \phi_H} \quad 4.1$$

where c_s is the Scherrer’s constant, λ is the wavelength of XRD excitation, b is the FWHM and ϕ is the angle at which the XRD spectra show the highest peak. The extent of crystallinity in the XRD pattern was determined by Equation (4.2).

$$\% Conc = \frac{I_c - I_a}{I_c} \quad 4.2$$

where $\% Conc$ is the percentage of crystallinity, I_a is the intensity height of the minimum intensity of the major peaks that correspond to the amorphous content of the sample and I_c is

the height of the highest peak that corresponds to the amount of crystalline material (Lee and Santmartí, 2018).

4.3 Estimation of Organic and Inorganic Matter

To determine the organic matter in the binders and molasses, the individual organic matter was measured, namely: reducing sugars, proteins, and fats.

4.3.1 Reducing Sugars

First, the presence of glucose in the samples was tested using Benedict's solution, then 25.0 ml of each sample was put in different test tubes. The blank sample constituted ionized water only. Thereafter 5.0 ml of Benedict reagent was added to each sample. Each mixture was then heated in a water bath until the samples' color changed to brick-red with a precipitate. The same procedure was repeated with samples with known concentrations ranging from 0.0% to 100.0% glucose concentration. Initially, the Spectrophotometer (Spectronic 200) was calibrated and then the absorbance of the samples with known concentrations of glucose was measured. A standard curve of absorbance against glucose concentration was then drawn. The absorbance of the samples in the cuvette was also measured one by one. Using the standard curve of the known samples the absorbance of the binders was marched with their respective concentration.

4.3.2 Fats

To estimate the number of fats in the sample the saponification value was used. The saponification value of the standard samples with the known concentration ranging from 0.0% to 100.0% by mass was found by the titration method. First, 1.0 ml of each standard sample was mixed with 5.0 ml of 99.9% ethanol and stirred till the sample had fully dissolved. The content was transferred to the conical flask. Then 25.0 ml of 0.5M ethanolic KOH was added to the samples. Meanwhile, the blank sample was prepared by mixing 10.0 ml of ethanol and 25.0 ml of 0.5M ethanolic KOH in a conical flask. All samples were covered and heated in a water bath for 30.0 minutes after which the flasks were opened and allowed to cool at room temperature. A similar procedure was followed for the binders. The absorbance of each sample was noted as discussed in Section 4.3.1. The standard curve of absorbance against the concentration of the known samples was plotted. The concentration of the binders was obtained by tracing their absorbance on the standard curve.

4.3.3 Proteins (Kjeldahl Technique)

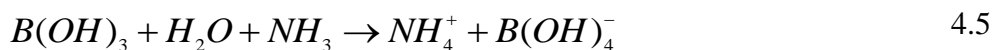
To carry out the protein test, three pieces of Kjeltabs were added to 50.0 ml of each binder. The tabs have potassium sulfate that serves as a catalyst and copper sulfate that helps in increasing the boiling temperature. Later 15.0 ml of 99.9% sulphuric acid was added to the binder-Kjeltabs mixture. The samples were left for 1.0 hours to digest to break down protein into ammonia and other components shown in Equation (4.3). Meanwhile, the heating block was heated to 420.0 °C and the samples were heated at this temperature for 75.0 minutes. After heating the samples turned into green color and on cooling for twenty minutes the sample turned blue.



The samples were later diluted with 75.0 ml of deionized water and distilled. In carrying out distillation 25.0 ml of 1.0% boric acid together with bromocresol green indicator was added into a flask, the flask was tightly closed and placed in the fume chamber, and the safety door closed. After which, the steam generator was turned on to convert 60.0 ml of 35.0% NaOH into steam which was later pumped in the flask holding the sample to liberate ammonia. The distillation was carried out for 5.0 minutes, which generated ammonia as shown in Equation (4.4).



To capture ammonia as shown in Equation (4.5) 10.0% boric acid solution was added to the sample



Upon completion of distillation, the flasks holding the samples were placed on the magnet stirrer, and 10.0% of hydrochloric acid was slowly added to the sample. The diluted acid initiated back-titration as shown in Equation (4.6). The titration was considered complete when the sample turned slightly pink.



The volume of hydrochloric acid was then noted and a 6.25 feed factor was used to calculate the amount of protein present in the sample as shown in Equation (4.7).

$$Amount_{protein} = \frac{V_{HCl+sample} - V_{HCL} \times 14.01}{M_{sample}} \quad 4.7$$

4.3.4 Viscosity

Viscosity is the measure of the binder's resistance to flow. Viscosity affects the workability and hence mechanical strength of the greenware. To get the viscosities of molasses and the different extracted binders, 30.0 ml of each binder was put in identical measuring cylinders and 5.0g of identical spherical marbles were slowly dropped in the equal volume of binder in the identical measuring cylinders. The time taken by marbles to reach terminal velocities in the cylinders was noted in Table 4.3. The density of the binders and the time taken by the marbles to attain terminal velocity were also noted.

Table 4.3: The parameters used in determining the viscosity of the binders extracted from the green leaves

Name of the liquid	Volume (ml)	Time (s)	Flux (ml/s)	Mass (g)	Density (Kg/m ³)
Distilled water	30.0	0.20	150.0	30.15	1.005
<i>Abelmoschus esculentus</i>	30.0	50.10	590.0	33.08	1.103
<i>Aloe vera</i>	30.0	0.28	107.400	35.00	1.167
<i>Basella alba</i>	30.0	0.35	85.710	37.26	1.242
<i>Corchorus olitorius</i>	30.0	35.40	0.850	34.95	1.165
<i>Molasses</i>	30.0	40.00	0.750	38.22	1.274

4.4 Fabrication of Green Ceramics Membranes

The milled DE-A, DE-B, and DE-waste were separately mixed with the milled charcoal in the ratios 65:35, 70:30, 75:25, 80:20, 85:15, 90:10, 95:5, and 100:0 by mass. The mixture of charcoal and DE powder was then mixed with a specific organic binder (that had been prepared from the plants/vegetables and stored as described earlier in Section 4.1.2. The DE powder and binder were mixed in the ratio of 2:1 by mass and kneaded. The samples were covered with polythene bags and left to age for 24.0 hours. Thereafter 5.0g of the plasticized

respective doughs were placed in a mold and then uniaxially pressed at 2.0 MPa in a hydraulic press to form discs of 2.5 cm diameter by 0.5 cm thickness for DE-A, 1.5 cm by 0.8 cm for DE-B, and 1.5 cm by 0.3 cm for DE-waste respectively. The variation in the thickness of discs was caused by variation in the densities: 2.3 g/cm³, 1.6 g/cm³, 1.4 g/cm³, and 1.9 g/cm³ for clay, DE-A, DE-B, and DE-Waste respectively. For purposes of studying the effect of binder concentration on bulk density, porosity, and mechanical strength, the binders were diluted as-boiled concentration (hereby referred to as the 100.0% concentration) to different concentrations up to 0.0% which was ionized water. The dilution of binders was done by adding ionized water to form 0.0%, 11.1%, 22.2%, 33.3%, 44.4%, 56.0%, 67.0%, 78.0%, 89.0% and 100.0. Samples meant to investigate the modulus of rupture (MOR) were prepared by extrusion as described above to form cylindrical rolls of 15.0 cm in length by 2.5 cm in diameter for the three-point test.

4.4.1 Greenware Drying and Sintering

The freshly made discs and rolls were dried in ambient conditions (at room temperature) for 48.0 hours and furnace-dried for 30.0 minutes at 110.0 °C in the furnace (LH 15/14 1706997 Nabortherm furnaces). The samples were then fired to various maximum temperatures of 700.0 °C to 1150.0 °C at a 3.2 K/min heating rate as this was the minimal heating rate that produced membranes without visible cracks. The discs and rolls were soaked at the firing temperature for 2.0 hours. Thereafter, they were left to cool to room temperature for 48.0 hours. Five of each samples made from various binders and at different binder concentrations were soaked in 5.0 ml molasses for 24.0 hours. Later, the molasses-soaked membranes were heat-treated in an anaerobic environment at 600.0 °C at a heating rate of 3.2 K/min to get activated carbon impregnated in them. The membranes were then cooled for 24.0 hours to room temperature.

4.4.2 Measuring the Physical Properties and Mechanical Properties

The physical properties: bulky density and shrinkage of the green and fired membranes were determined from the dimensions of the discs and rolls. The porosity of the membranes was also determined.

4.4.2.1 Bulk Density

The dimension of the green and dried discs and rolls were measured using Vernier calipers and a micrometer screw gauge. The mass, diameter, and thickness (length for the cylindrical rolls) of the green and fired membranes were noted and the volume of the fired membrane (V_f) was calculated. Using the volume and mass of the green and fired membranes, the bulky densities (ρ) were calculated.

4.4.2.2 Porosity (ϵ_p)

The dimensions and mass (M_1) of the samples were noted then the samples were immersed in boiling water for 15.0 minutes one by one. After fifteen minutes the samples were removed from boiling water and their masses (M_2) were noted immediately. The difference between the two masses ($M_2 - M_1$) was noted as the mass of water that occupied the porous part of the membrane. The volume (V_{op}) of water that occupied the porous part of the ceramic was calculated as the ratio of the mass of water to the density of water as shown in Equation (4.8). The density of water was taken as 1000.0 Kg m^{-3} . The apparent porosity of the fabricated membrane was determined as the quantity of water absorbed by a given sample using Archimedes' principle (Christopher and Fischer, 1992) given in Equation (4.9).

$$V_{op} = \frac{M_2 - M_1}{\rho} \quad 4.8$$

4.4.2.3 Volume Fraction Porosity

$$\epsilon = \frac{V_{op}}{V_{sample}} \quad 4.9$$

Where V_{op} is the volume of the open pores accessible to water and V_{sample} is the sample bulk volume.

4.4.2.4 Shrinkage

The dimensions obtained in Section 4.4.2.1 were used to calculate the percentage of linear drying shrinkage (%LDS) of the dried discs using Equation (4.10).

$$\%LSD = \left[\frac{L_g - L_d}{L_g} \right] \times 100\% \quad 4.10$$

where L_d and L_g are the lengths of the freshly fabricated (not dried) and the completely dried green ceramic respectively. Similar measurements were also done on the sintered samples and the linear firing shrinkage was determined using equation (4.11),

$$\%LFS = \left[\frac{L_f - L_g}{L_f} \right] \times 100\% \quad 4.11$$

Where L_f is the length of the fired membrane.

4.4.2.5 Mechanical Strength

The three-point test was employed in the measurement of the modulus of rupture (MOR) of the membranes as per the Japanese Industrial Standard (Aduda *et al.*, 1999) using the Universal Testing Instrument (Model EN 77065 7108CCN) 60000 N. The distance between the two supports was 8.4 cm and the loading had a speed of 4.2mm min⁻¹. After the fracture, the MOR was calculated using Equation (4.12).

$$\sigma = \frac{8LD}{\pi D_s^3} \quad 4.12$$

where L is the fracture load N/m² and D is the distance between supporting rolls (meters) and D_s is the sample diameter (meters).

4.5 Microstructural Analysis

The microstructural analysis of the membranes comprised of XRD, XRF, and SEM analysis.

4.5.1 XRF and XRD

The XRF and XRD of membranes were fired at the various temperatures ranging from 700.0 °C to 1150.0 °C, and carbon-activated membranes were taken. First, the dimensions of the samples were noted and the settings used in measuring XRF and XRD powders were also applied here.

The elemental analysis of diatomaceous earth and binder was done by ED-XDRF machine of NEX CG - Energy Dispersive X-ray Fluorescence Spectrometer available in the Department of Physics University of Nairobi model X shown in Figure 4.3. The elemental analysis was done to find out the elements present in the raw materials and their proportions in each sample.



Figure 4.1: The Energy Dispersive X-Ray Fluorescence Spectrometer used in elemental analysis of diatomaceous earth and the binder

The spectrometer was set to operate at -275 °C without a filter, background, overlap, back time, and limit of detection. The tube current and voltage were 75 mA and 40 kV respectively and the peak time was 60 seconds. The detector was fixed and flowrate type with 0.1° collimator masked at 40 mm.

The crystal structure of the milled Pure DE-A, Pure DE-B, and DE-waste powder were analyzed by an Empyrean, PANalytical–X-ray diffractometer equipped with a robotic arm sample exchange, using Cu target $K\alpha = 0.15406$ nm radiation, operating at 40 mA settings and 45 kV. The extent of crystallinity in the XRD pattern was determined by Equation 4.2.

4.5.2 Microstructure and Morphology Determination

The microstructures and morphological details of the fired membranes were studied using a high-resolution electron microscope (Carl Zeiss Gemini SEM500) integrated with Energy Dispersive Spectroscopy, Wavelength Energy Dispersive Spectroscopy, and elemental analysis techniques. The tube current was optimized at 70 μ A and a voltage of 20 kV. Before microscopy, the clay and diatomaceous-based membranes were edged and coated with gold to

make them conductive. Edging the samples removes any impurity on the sample that might have come due to handling and exposes fresh surfaces that will give a precise measurement. Furthermore, clay and diatomaceous-based ceramics are insulators, and coating makes them conductive aiding in charging when the samples come in contact with the electron beam. The coating was done for 60.0 seconds using a Denton Vacuum sputter coater at 100 milliTorr and 30 mA as shown in Figure 4.1. The carbon-activated samples were not coated as they were able to charge without any coating.



Figure 4.2: The setup of the Denton Vacuum sputter coater at 100 milliTorr used for coating the samples.

4.6 Filtration

4.6.1 Flow Rate

To measure flow rate, 1.0 L of water was poured into the cartridge hosting the water membrane and the mass of the filtrate from the membrane was noted as a function of time. The interval of time was 5 minutes up to 30 minutes. The volume of water obtained every five minutes was then calculated as a ratio of the mass to the density of water taken as 1000 kg/m^3 . To get the flow rate, the gradient of the graph of the volume of filtrate against the time of discharge was calculated.

4.6.2 The Permeability of the Membrane

The permeability (P_{erm}) of the membrane was calculated using Darcy's law shown in Equation (4.13) where f_r represents the flow rate of the membrane, L_f is the length of the membrane, A is the cross-sectional area of the membrane g is the acceleration due to gravity,

μ , ρ , and h are viscosity, density, and height of water respectively. The viscosity of ionized water was found as 1000.2 (Pa.s) at a room temperature of 24.0 °C.

$$P_{erm} = \frac{f_r \mu L_f}{A \rho g h} \quad 4.13$$

4.6.3 Biological Analysis

The individual contaminants: *E. coli*, sodium fluoride, and Rotavirus were prepared at different concentrations as discussed in the following sections. The different solutions were filtered by the newly fabricated membranes.

4.6.3.1 *E. Coli* Filtration Test

Before the *E. coli* test, the membranes and the containers were sterilized by autoclaving at 121.0 °C for fifteen minutes. The MacConkey Broth Purple w/ BCP solution was prepared by dissolving 40.0 g into 1.0 L of distilled water and then boiled to dissolve into a purple solution. The solution was distributed in inverted Durham tubes according to the Most Probable Number procedure of testing micro-organisms in water (Chevallier *et al.*, 1982; Evans *et al.*, 1981). The samples were classified as either double or single strength as shown in Figure 4.2. For purposes of minimizing contamination, the Durham tubes and their contents were also autoclaved at 121.0 °C for fifteen minutes.



Figure 4.3: The pure double and single strength MacConkey Broth Purple w/ BCP solution filtered by the fabricated membranes

At the same time, the *E. coli* was inoculated from the stock to the plate and incubated at 37.0 °C for 18.0 to 24.0 hours under Cystine-Lactose-Electrolyte-Deficient Agar (CLED agar). Later the plate was visually examined for the growth of characteristic colonies as shown in Figure 4.3. Several colonies were then taken from the culture emulsified in sterile distilled water to obtain a suspension of 10^8 concentrations of the colony-forming unit, CFU/ml.



Figure 4.4: Characteristic colonies of Escherichia coli incubated under Cystine-Lactose-Electrolyte-Deficient Agar for at least twenty-four hours

The suspension was then passed through the newly fabricated membranes assembled in the cartridges as shown in Figure 4.4. The filtrate was collected in a sterile tube 5.0 ml of each filtrate was added to the MacConkey broth purple solution and left for 24.0 hours to allow the growth of *E. coli* as shown in Figure 4.5.

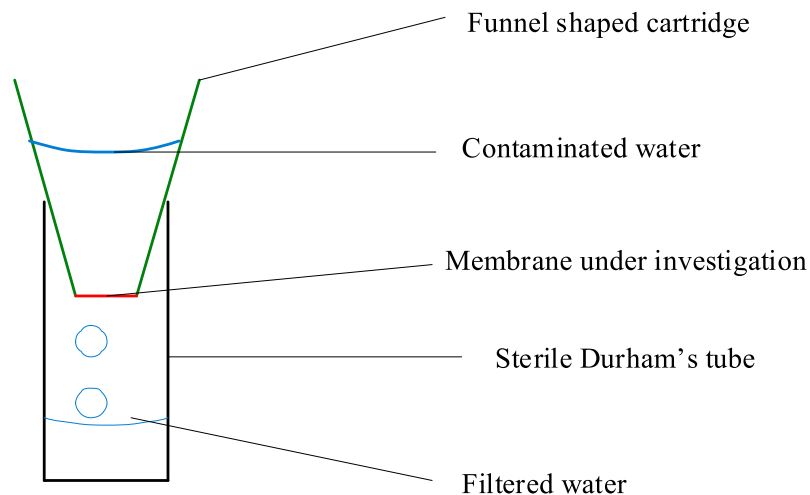


Figure 4.5: The schematic representation of the setup used to filter the contaminated water

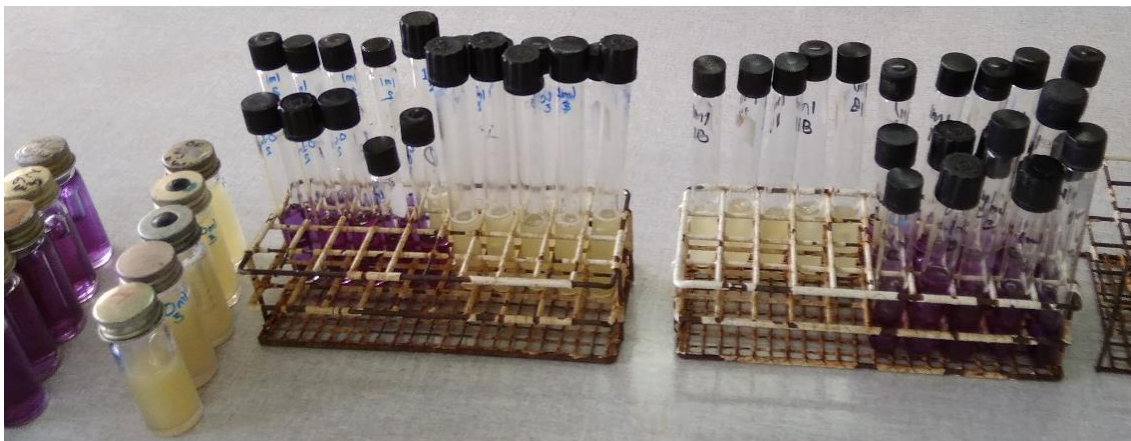


Figure 4.6: Image of MacConkey broth laced with filtered water from fabricated membranes and cultured for 24 hours to test the presence of *Escherichia coli*. The yellow color shows a positive result and the purple shows a negative result.

Later the 10^8 was diluted from 10^8 to 10^1 CFU/ml to determine the effect of concentration on the efficiency of removal of *E. coli* from water by the fabricated membranes. The amount of *E. coli* in the filtrate was determined by the Enzyme-linked immunosorbent assay ELISA. This was done in triplicate and then averaged to avoid errors.

4.6.3.2 ELISA Test

To prepare the diluent, 0.5 g of peptone was mixed with 4.25 g of NaCl uniformly and then dissolved in 500.0 ml of ionized water. The mixture was stirred and autoclaved at $121.0\text{ }^\circ\text{C}$ for 15.0 minutes obtained and cooled. Three drops of the prepared diluent were put in a sterile test tube and mixed with 25.0 ml of filtered water. One drop of the content was added to the ELISA stripe as shown in Figure 4.6 and left for fifteen minutes to allow the antigen to react

with the sample. After five minutes the positive samples showed two lines at the control and test points while the negative test only showed one line at the control.

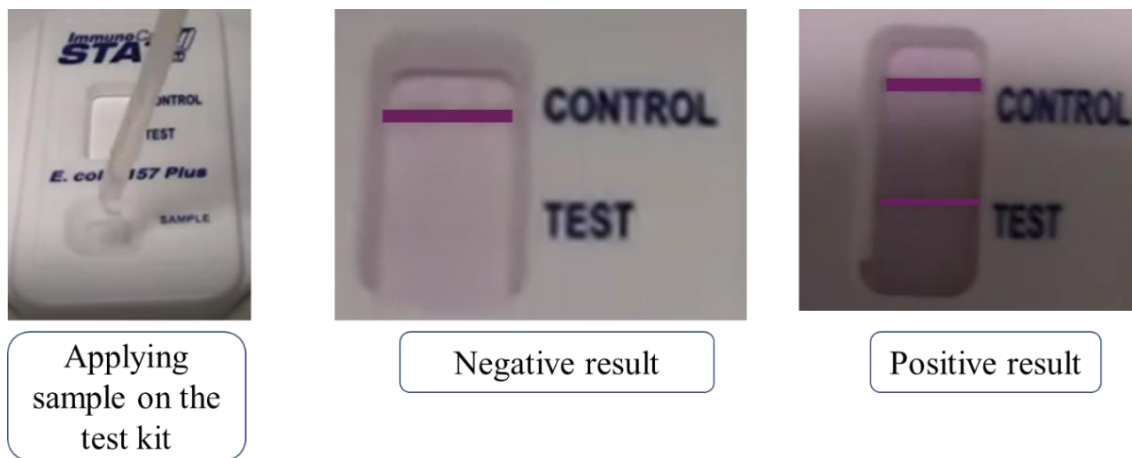


Figure 4.7: showing how the samples suspected to have *E.coli* were treated and the negative and positive result presentation

The absorbance of the positive samples was taken and compared with the absorbance of the known samples using a standard curve as described in Section 4.3.

4.6.3.3 Rotavirus Filtration Test

The membranes that passed the *E. coli* tests were taken for the Rotavirus filtration tests. Later, attenuated Rotavirus of 10^6 viral particles/ml was mixed in ionized water to form different Rotavirus concentrations of 10^1 viral particle/ml to 10^5 viral particle/ml. The solutions were then filtered by the sterilized membranes assembled in the cartridges. The filtrates were collected in sterile 50.0 ml bottles. Two drops of the filtered water were mixed with the buffer, shook, and left for five minutes. Two drops of the sample were placed in the sample well while the remaining were stored at $-20.0\text{ }^\circ\text{C}$ and were defrosted to room temperature when needed. The content was left for 15.0 minutes at the sample well of the ELISA test. The positive result showed two lines at the control and the reaction site while the negative result only showed one single line at the control site as shown in Figure 4.7. Later the absorbance of the samples was also determined using the standard curve plotted from the known samples.

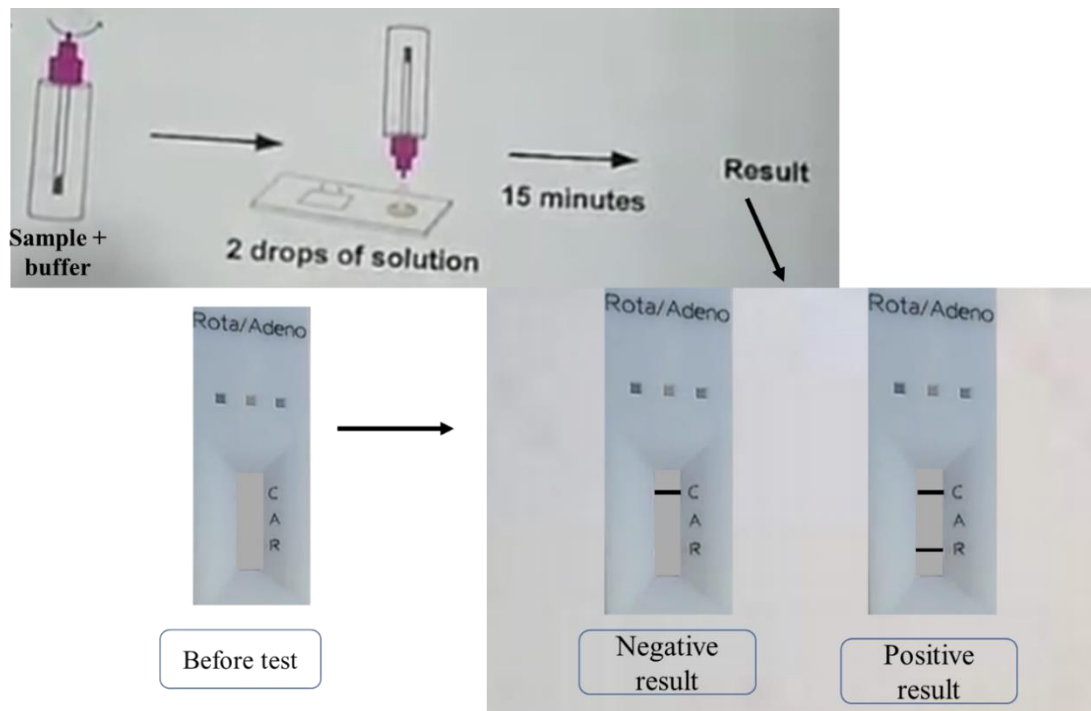


Figure 4.8: The Procedure for carrying out the ELISA Test for Rotavirus samples and the presentation of the results

4.6.3.4 Sodium Fluoride Removal Test

To determine the defluoridation abilities of the membranes, 50.0 g of sodium fluoride (Sigma-Aldrich, St. Louis) of analytical standards were dissolved in 1.0 liters of water to form a highly concentrated 500.0 mg/l NaF solution whose pH was noted. For purposes of determining the efficiency contaminant removal efficiency of the membranes, the contaminated solutions were diluted separately to different concentrations of sodium fluoride, ranging from 50.0 mg/l to 5.0 mg/l. Each suspension was then passed through the membranes assembled in the cartridges and the filtrates were collected in sterile 50.0 ml bottles. The pH of samples with known concentrations was used to determine the concentration of the unknown samples using a standard curve.

4.6.3.5 Varying the Pressure of Water

The disc-shaped membranes were fitted in the cartridge connected to a syringe fitted with a pressure pump and gauge as shown in Figure 4.8. The pressure of water varied from 5.0 kPa to 50.0 kPa. Beyond 50.0 kPa the water bounced back hindering the filtration process and some membranes broke. The water contaminated with different contaminants was investigated one by one.

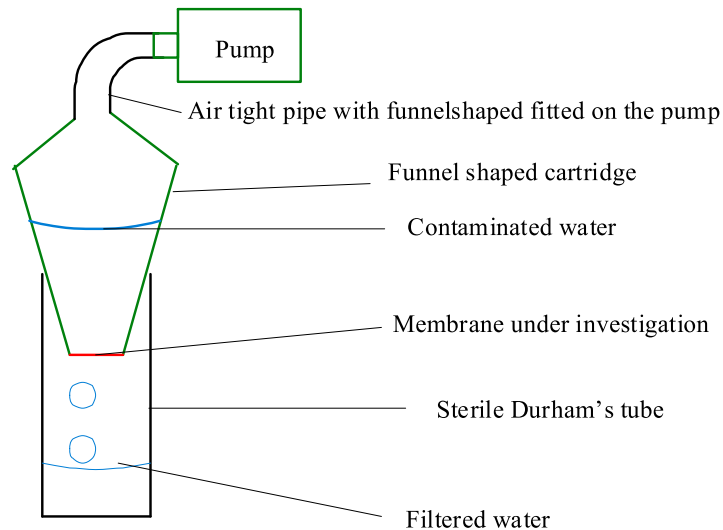


Figure 4.9: The filtration set up in which the disc-shaped membranes were fitted in the cartridge connected to a syringe fitted with a pressure pump

4.6.4 Aspect Ratio α

Sets of four micrographs taken from membranes of porosity of 0.12, 0.18, 0.22, and 0.28 taken from Pure DE-A, Pure DE-A, and DE-waste. The aspect ratio was calculated by dividing the minor axis by the major axis just as it was described by (Mukhopadhyay and Phani, 1998; Phani and Niyogi, 1987). The axis was chosen arbitrarily and later interchanged. The ratios were classified as described by (Roberts and Garboczi, 2000; Andersson, 1996; Phani and Niyogi, 1987) such that the result of unity predicted prolate spheroids or needle-shaped spheroids, and as α approached zero spheroids were equated to oblate spheres. Five micrographs from one membrane with known porosity were used to calculate the aspect ratio. An average of the number of occurrences of different aspect ratios was noted.

4.7 Magnetic Field Test

4.7.1 *Escherichia Coli* Removal Test

The *E. coli* solution of 10^6 CFU/ml was prepared as described in Section 4.6.1 and diluted to form ten liters of 10^1 CFU *E. coli* solution. At an ambient temperature of 24.0 °C, the 10^1 CFU/ml solution was made to circulate in a 1.5 cm (diameter) pipe under a static magnetic field of 0.8 T provided by ten one Tesla Neodymium cylindrical permanent magnets of 1.5 cm (diameter) by 4 cm thickness). The magnets were clipped on a plastic pipe, 10.0 cm apart as shown in Figure 4.9.



Figure 4.10: The setup used to filter contaminated water across the 0.8 T magnetic field

The water circulation time ranged from 0.5 hours to 9.0 hours. The concentration of *E. coli* was noted after every half an hour and its concentration in water was determined using ELISA. Before the contamination of the ionized water, the effect of the static magnetic field on the pH of the ionized water was studied by circulating the water in the presence and absence of the magnetic field for 9.0 hours and the pH was noted after every 30.0 minutes. Then a constant volume of 10.0 liters of different solutions of the contaminated water was made to circulate (one at a time) through the pipe at varying velocities of 0.1 ml/s to 2.0 ml/s. Later the ambient temperature under which the experiments were carried out varied from 16.0 °C to 40.0 °C in steps of 2.0 °C and the concentration of the contaminants were noted using ELISA.

4.5.1 Rotavirus Removal Test

Attenuated Rotavirus of 10^6 viral particles/ml was mixed in ionized water to form different Rotavirus concentrations of 10^1 viral particle/ml to 10^5 viral particle/ml. Ten liters of 10^5 viral particles/ml were made to circulate at 2.0 ml/s for nine hours in the absence and presence of a 0.8 T static magnetic field. After every 30.0 minutes, the water that had passed through the magnetic was tested for Rotavirus using the rapid test, and the amount of Rotavirus was determined by the standard curve described in Section 4.6.3. The pH of the solution was also noted after every half hour. Finally, a 10^1 viral particle/ml solution was circulated for nine hours at different ambient temperatures ranging from 16.0 °C to 40.0 °C in steps of 2.0 °C,

and the concentration of the virus was noted at the various ambient temperatures. At the ambient temperature of 24.0 °C, the speed of the solution was also varied from 0.0 ml/s to 2.0 ml/s in steps of 0.2 ml/s and the concentration of the virus was noted at the various velocities. To calculate the speed of water a colored stone of 0.01 g was added to the water and the time it took for it to cover one meter in a colorless pipe was noted.

4.5.2 Sodium Fluoride Removal Test

In 10.0 liters of water, 5.0 g of sodium fluoride powder was added and stirred to form a 0.5 g/l fluoridated solution. This solution was then circulated for nine hours in the absence and presence of 0.8 T static magnetic fields at an ambient temperature of 24.0 °C. The pH of the water was then noted after every 30.0 minutes. Later the velocity of water was varied as described earlier and the pH of the fluoridated solution was noted. The ambient temperature under which the defluoridation experiment was carried out also varied from 16.0 °C to 40.0 °C in steps 2.0 °C and the pH of the solution was obtained.

CHAPTER FIVE: RESULTS AND DISCUSSIONS

5.1 Characterization of Raw Materials

The raw materials comprised; DE powder, potter's clay, plant-derived organic binders, and molasses. The DE was characterized in terms of particle size and elemental composition. The binders and molasses were characterized in terms of elemental composition, organic composition, and viscosity.

5.1.1 Particle Size Distribution

Figure 5.1 shows the result of the diatomaceous earth (DE) samples categorized respectively as (a) DE-A, (b) DE-B, (c) DE-waste, and (d) charcoal particle distribution functions. All the distributions were asymmetric with the volume density distribution of particles skewed to the left. Table 5.1 gives the descriptive statistics of the particle sizes of the samples. The mean particle sizes were 15.3 μm , 12.1 μm , 133.6 μm , and 134.0 μm for DE-A, DE-B, DE-waste, and charcoal respectively. DE-A and DE-B had particle sizes less than 110.0 μm . The mean size of the particles of DE-A, DE-B, DE-waste, and charcoal comprised 75.3%, 98.1%, 91.2%, and 88.8% of their particles respectively. The skewed distribution and the cumulative frequency distribution functions showed that the powders used for sintering were within the accepted limit of nano-and microscale (<500 μm) (Rahimian *et al.*, 2009) encouraging the flow of surface energy during firing. The smaller the size of the particle, the higher the concave curvature and the faster the necking sintering process between the particles (Rahimian *et al.*, 2009; Chaim *et al.*, 2008; Kang, 2005).

Table 5.1: The descriptive statistics of particle size for DE-A, DE-B, DE-waste and charcoal powder

DescriptiveStatistical	Particle size (μm)			
	DE-A	DE-B	DE-waste	Charcoal
Sample				
Mean	15.31	12.09	133.62	134.01
Standard deviation	0.02	0.03	0.52	0.48
Minimum particle size (μm)	0.11	0.12	0.34	1.04
Maximum particle size (μm)	101.64	62.82	1040.78	1041.33

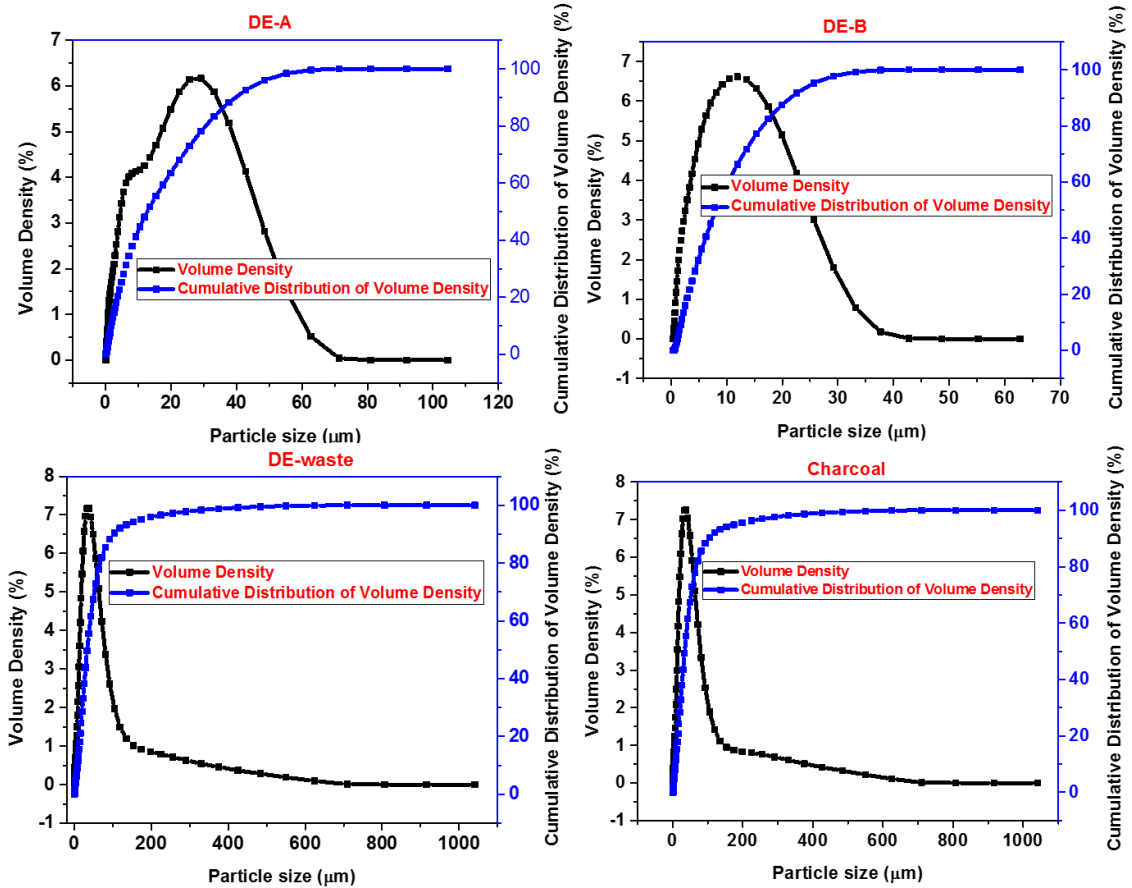


Figure 5.1: The volume density and cumulative distribution frequency of volume density of particle sizes of DE-A, DE-B, DE-waste, and charcoal powder as measured by Malvern Panalytical Master Sizer 3000

5.1.2 X-Ray Fluorescence and Diffraction Composition of DE Raw Materials

Figure 5.2 shows the histogram of the elemental composition of DE-A, DE-B, DE-waste, and Potter's clay.

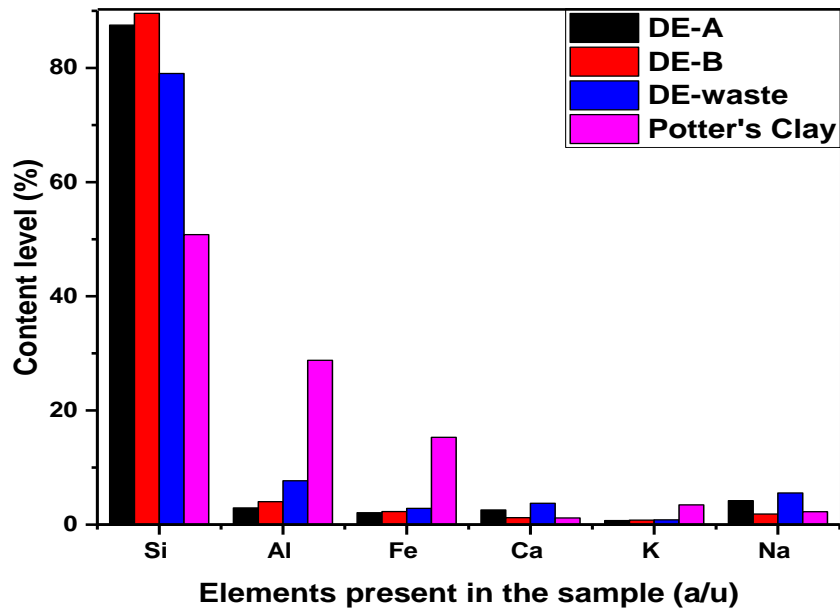


Figure 5.2: The histogram of the elemental composition of the diatomaceous earth powder (DE-A, DE-B, and DE-waste) and Potters' Clay obtained from x-ray fluorescence spectroscopy

The silica content of DE-A was 87.5%, and 89.6% for DE-B. Thus, the two samples were classified as high silica content materials as they contain silica content greater than 85.0% and are often used in the filtering industry (Akhtar *et al.*, 2010). Silica is made of tetrahedron bonds that form strong bonds with metallic ions during firing resulting in strong ceramics. It is this high content of silica that was responsible for the whitish color manifested in the powder. Aluminum oxide was around 2.9% in DE-A and 4.0% in DE-B and the difference was attributed to the clay minerals present in the DE (Bailey *et al.*, 2018). The other oxides present in both DE-A and DE-B were CaO, Na₂O, K₂O, and MgO responsible for fluxing during firing.

DE-waste had a lower content of silica (79.0 %) than pure DE. This is because the mining process targets extracting silica in the pure samples thus the reduced content of silica in the waste. On the other hand, metallic oxides were higher in DE-waste than in the pure DE powder because metallic oxides especially iron oxides are ejected as wastes in the mining process. The presence of silica and calcium oxides in DE-waste was responsible for the whitish color of the DE-waste powder (Benjakul *et al.*, 2004).

The Potter's clay was characterized by the reddish color caused by the iron oxides (Davey *et al.*, 1975). The Potter's clay had the lowest content of SiO₂ (50.8%) among the four powders used in this work but the highest aluminum (28.8%) and iron (15.3%) contents. The high content of aluminum oxide explains why clay samples formed a stickier (waxy) greenware

compared to those from the diatomaceous earth (DE). Aluminum aids in plasticizing the greenware because of its plate-like structures (aluminum octahedral sheet). The DE powder was able to agglomerate in the presence of water and the organic binder because of the silicate tetrahedral sheet. Both the silicate and aluminum octahedral sheets were held together with an O-H-O bond that bonded with the (OH) bond present in the binder and water (Andrade *et al.*, 2011). The capillary forces and opposite charges between water or binder molecules and the clay molecules caused the attraction of the clay particles to the water (binder) molecules resulting in the agglomeration of the powder. The aluminum and iron oxide in Potter's clay powder were attributed to volcanic weathered rocks that give rise to clay (Velde and Druc, 1999). Samples from DE had a high content of sodium oxide attributed to the calcination process where sodium carbonate was added in the DE extraction process (Izuagie *et al.*, 2016a). The other metallic oxides were in traces and within acceptable limits for the fabrication of membranes.

The elemental analysis of the pure DE samples as obtained in this study was nearly similar to those obtained by (Izuagie *et al.*, 2016a; Akhtar *et al.*, 2010; Akhtar *et al.*, 2009). There were also traces of non-metals such as phosphorus and sulfur associated with wollastonite (Saadaldin and Rizkalla, 2014), a compound that can coexist with DE. The DE-waste had a similar elemental constituent as the pure DE samples obtained in the literature (Izuagie *et al.*, 2016a; Akhtar *et al.*, 2009; Barré *et al.*, 2008).

5.1.3 X-Ray Diffraction Analysis

The X-ray diffraction characteristic spectra of the DE-A, DE-B, and DE-waste powder are displayed in Figure 5.3, from which it is noted that all the samples were polycrystalline solids with a regular arrangement of atoms and molecules that were exhibited as peaks in the spectra (Sakizci *et al.*, 2009; Jia *et al.*, 2007). The XRD spectra of DE-A, DE-B, and DE-waste matched that of cristobalite, quartz, and wollastonite. It was found that DE-A had the highest level of cristobalite, quartz, and wollastonite followed by DE-waste and pure DE-B respectively.

The crystallinity percentage was calculated using Equation (4.2) adopted from (Lee and Santmartí, 2018). The crystallinity varied among the samples. The order of crystallinity in descending order was DE-A (97.2%), DE-waste (94.1%), DE-B, and (92.8 %). DE-B powder had lower crystallinity because of its high content of aluminum and calcium associated with

the active volcanic ash (Wada and Harward, 1974). The interplanar spacing distance given in Table 5.2 was calculated using Bragg's Equation discussed in Section 3.4.2 and shown in Equation (5.1)

$$G_s = \frac{c_s \lambda}{b \cos \phi_H} \quad 5.1$$

where c_s is the Scherrer's constant, λ is the wavelength of XRD excitation, b is the FWHM and ϕ_H is the angle at which the XRD spectra show the highest peak.

The grain size of DE-A was found as 38.2 nm, DE-B at 39.9 nm, and DE-waste at 42.8 nm, in line with results found in the literature (Akhtar *et al.*, 2010; Akhtar *et al.*, 2009), and which are acceptable grain sizes for diatomaceous earth powder (Kruis Einar *et al.*, 1993).

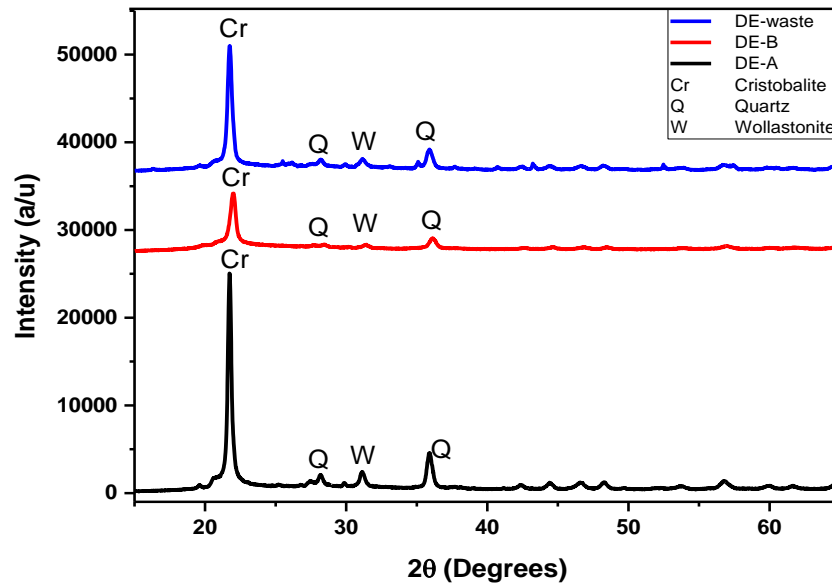


Figure 5.3: X-ray characteristic spectra of pure diatomaceous earth samples and diatomaceous earth waste

Table 5.2: The 2θ values at which peaks occurred for pure diatomaceous earth samples and diatomaceous waste with the interplanar distance and the crystals associated with them. (Cr - Cristobalite, Q – Quartz, and W - wollastonite)

Pure DE-A	2 θ ($^{\circ}$)	21.8	25.3	28.3	31.2	36.1	42.4	44.5	46.7	48.5	53.7	56.9	59.9
Pure DE-B		21.9	-	-	31.3	36.2	-	-	-	-	-	-	-
DE-waste		22.0	25.4	28.4	31.0	36.0	42.6	44.6	46.7	48.4	54.1	57.0	
Interplanar distance d (\AA)		4.1	3.5	3.2	2.9	2.5	2.1	2.0	2.0	1.9	1.7	1.6	1.5
Types of Crystal		Cr	Q	W	W	Q	Cr	Cr	Cr	Cr	Cr	Cr	Cr

5.1.4 Characteristics of the Binders and Molasses

Figure 5.4 shows the percentage of (a) elemental content, (b) and organic matter present in the organic binders extracted from *Abelmoschus esculentus*, *Aloe vera*, *Basella alba*, and *Corchorus olitorius*.

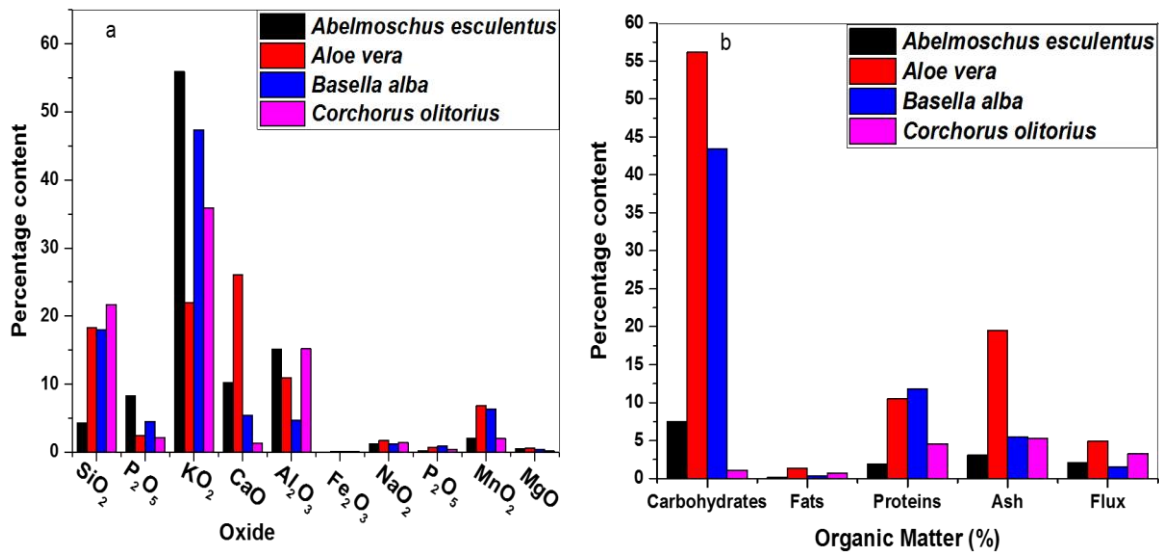


Figure 5.4: The percentage of elemental content (a) and organic matter (b) present in the binders extracted from *Abelmoschus esculentus*, *Aloe vera*, *Basella alba*, and *Corchorus olitorius*

All the binders were characterized by comparatively high content (20.0% – 55.9%) of potassium ions, which is necessary for plant growth (Barré *et al.*, 2008) as it regulates the opening and closing of stomata in plants and that is why it was highest (55.9%) in *Basella alba* which has broad leaves. The opening and closing of stomata regulate the intake of CO₂ in plants. Calcium is also crucial in plant nutrition, growth, and cell wall deposition (White

and Broadley, 2003). Sodium ions are wastes in plants (Mäser *et al.*, 2002) and that is why their content was quite low in fresh leaves used in this work. The metallic ions necessary for plant growth such as Ca^{+2} and K^{+} were highest in *Basella alba*. All the binders showed the presence of silica with *Abelmoschus esculentus* having the highest content. Silica in plants guards them against external stress by strengthening their cell walls. It also guards the plants against fungal infection by regulating water and mineral uptakes (Ma and Yamaji, 2006). *Basella alba* had the highest organic matter (carbohydrates, proteins, and total flux). Other binders (*Abelmoschus esculentus*, and *Corchorus olitorius*) also had a high content of carbohydrates and proteins composed mainly of polysaccharides. The polymeric behavior of these binders was attributed to these polysaccharides which upon heating formed longer chains (Ochoa-Villarreal *et al.*, 2012). The *Aloe vera* binder had the least organic matter. The polymeric behavior of the *Aloe vera* binder was also lost upon boiling. *Aloe vera* is made up of monosaccharides and proteins, which upon heating there were aggregation and denaturation of proteins. Further heat causes fluidity in plant lipids, denaturing enzymes, and degrading proteins (Lima *et al.*, 2013). Thus, it is recommended that the *Aloe vera* binder be extracted without boiling.

Table 5.3 shows the elemental and organic content of the molasses used in this work. Molasses had a similar composition of oxides and organic matter as the binders because the molasses was extracted from *Saccharum officinarum* (sugar cane) which is a plant just like the binders. However, the elemental content in molasses was higher because sugar cane is a large grass bigger than the shrubs from which the binders were extracted. At the same time, the content of carbohydrates in molasses was highest at 75.8% because of its high content of sucrose.

Table 5.3: The percentage of the elemental and organic content of molasses

Oxides in Molasses	Percentage by Mass	Content
SiO ₂	1.4	
Al ₂ O ₃	1.6	
Fe ₂ O ₃	0.1	
CaO	1.2	
MgO	3.1	
SO ₃	0.8	
K ₂ O	11.4	
Na ₂ O	0.2	
P ₂ O ₅	0.4	
MNO	0.1	
Flux	1.8	
Carbohydrates	75.8	
Fats	0.1	
Ash	1.7	
TOTAL	99.7	

The viscosity values of the binders and molasses used in this study are shown in Figure 5.5. The result shows that the viscosity of *Abelmoschus esculentus* was the highest followed by *Corchorus olitorius*. This means that *Abelmoschus esculentus* had more molecular mass and polymer chains than the *Corchorus olitorius*, *Basella alba*, and *Aloe vera* in that order. As pointed out earlier, *Aloe vera* lost its viscosity upon boiling the leaves in water due to its high hydrolysis ability as explained earlier (Ahlawat and Khatkar, 2011). The viscosity of molasses was high, closer to the viscosity of *Abelmoschus esculentus*. The viscosity of molasses was high because of its high carbohydrate content. The carbohydrates are made up of long chains - C-OH bonds which comprise individual monosaccharide units held together by glycosidic.

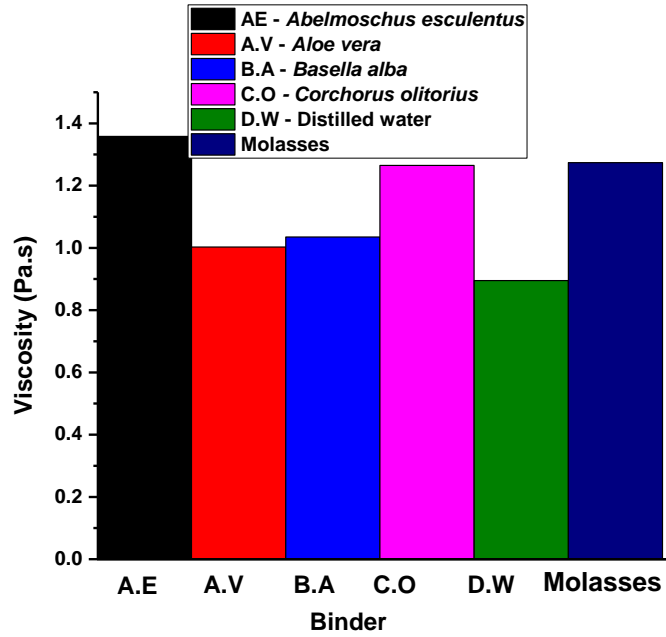


Figure 5.5: Viscosity of the molasses and the extracted binders measured at room temperature of 22 °C. The symbols A.E, C.O, B.A, A.V, and D.W stand for *Abelmoschus esculentus*, *Aloe vera*, *Basella alba*, *Corchorus olitorius*, and distilled water respectively. (Distilled water was used as the reference since the plants were all boiled in distilled water)

5.2 Physical Properties of the DE Greenware and Fired Membranes

5.2.1 Linear Drying Shrinkage

The results of the linear drying shrinkage (LDS) are shown in Figure 5.6. The LDS of green samples was found to increase with an increase in the binder concentrations. The shrinkage was caused by the loss of moisture from the samples which can be explained in two ways; bound and unbound moisture. The bound moisture corresponds to water molecules bound to the potter's clay particles because of the cohesive force between the binder molecules and the powder particles (Baklouti *et al.*, 1997). The unbound moisture freely moves out of the sample causing shrinkage (Oummadi, 2019). At the initial stage of drying, the green ceramic is comprised of DE or clay particles separated by continuous water or binder in liquid form. At this stage, the dominant mechanism of drying the material is liquid flow through the pores. The liquid flows aided by the pressure gradient described by Darcy's Equation shown in Equation (5.2).

$$J_L = -\frac{P_{erm}}{\eta_L} \nabla P$$

5.2

where J_L is the flux of the liquid, P_{erm} is the permeability, P is the pressure of the liquid, and η_L is the viscosity of the liquid. Diluting the binder with water introduced a repulsion force between the binder and water molecules. The repulsion force in turn reduced the adhesive force between the binder and the clay/DE molecules resulting in a decrease in the rate of shrinkage.

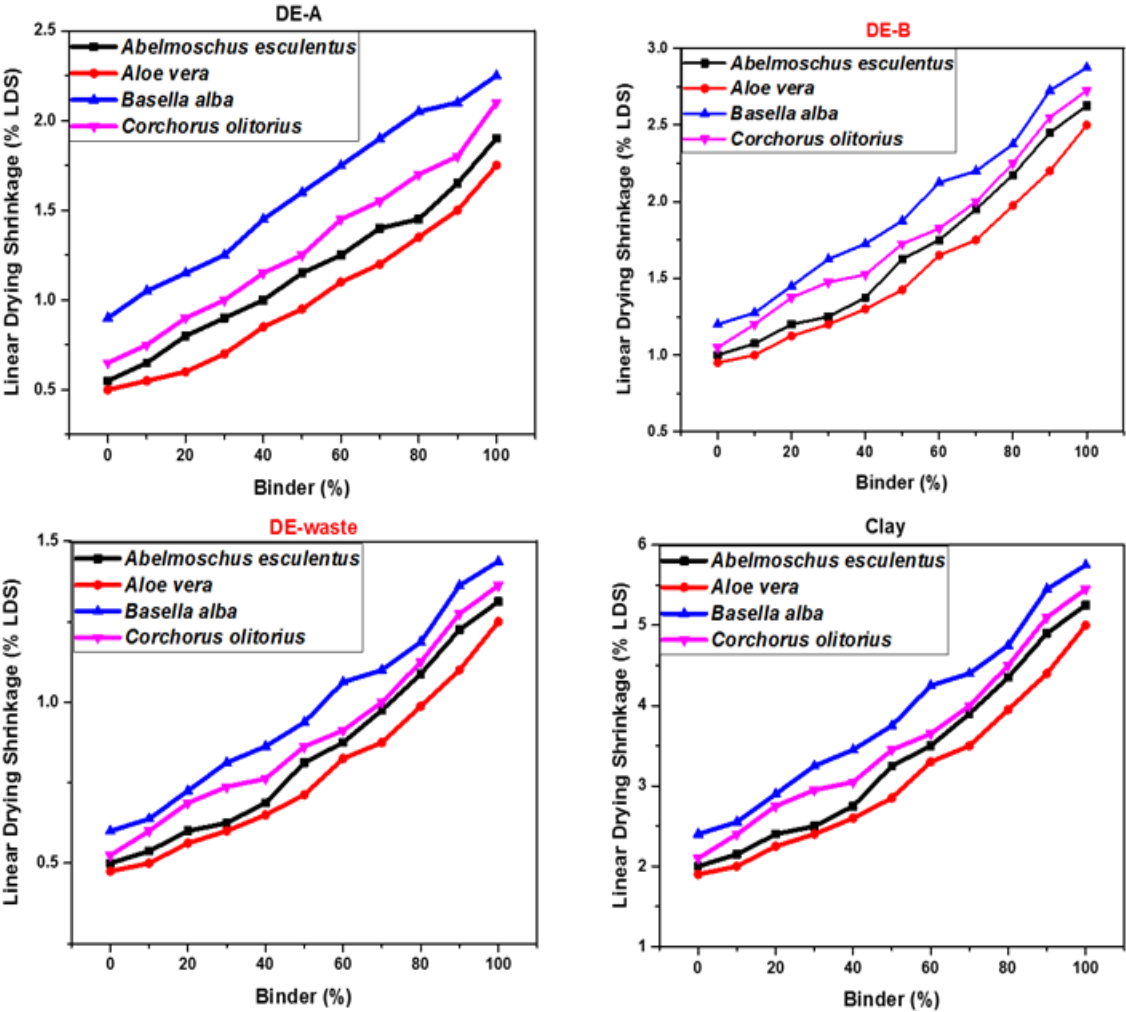


Figure 5.6: Variation of linear drying shrinkage with binder content in dried pure diatomaceous earth, the diatomaceous earth waste, and Potter’s clay discs

As drying advances, the DE/clay particles separate from each other, and the liquid that flows out of the material is replaced by air through diffusion. Moisture is then transported as vapor through the pores to the green ceramic surface. On the surface, the moisture is removed using convection mechanisms discussed in Section 3.13. This diffusion can then be related to the concentration gradient according to Fick’s law. The diffusion process involves Fick’s law stated in Equation (5.3) where J_D is the diffusion flux, D_w is the diffusion coefficient, and $Conc$ is the vapor concentration.

$$J_D = -D_w \nabla Conc$$

5.3

Thus, shrinkage was caused by loss of moisture attributed to the capillary pressure created by a capillary gradient between solid-liquid and solid-vapor interfaces (Scherer, 1990). Samples fabricated from Potter's clay shrunk most as clay absorbed more water due to its plate-like structures and lost most of the water due to osmotic pressure during drying. Averagely the clay samples shrunk by 5.0% which agrees with the results available in the literature (Ketelaars *et al.*, 1994; Scherer, 1990). DE-B had the highest rate of shrinkage among the DE samples followed by DE-A and DE-waste-based samples had the least shrinkage. The order of shrinkage in DE samples was; $LDS_{DE-B} > LDS_{DE-A} > LDS_{DE-Waste}$. The order of shrinkage was attributed to the difference in the particle size distributions of these materials. DE-B had the finest particles that give rise to the greatest surface area, thus, most intra-particle forces.

The different scenarios of the interaction between binders and particles are shown in Figure 5.7. In Figure 5.7(a), the particles are far apart, so even when the agglomeration takes place the bonds formed from such interaction would be weak. In Figure 5.7(b) the particles are close and the binder can wet the particles resulting in stronger agglomeration and shrinkage than in Figure 5.7(a). In the last scenario in Figure 5.7(c) the binder is highly viscous and could not wet the particle. Air trapped in the interparticle would lead to weak agglomeration and shrinkage. The above scenarios explain why samples fabricated with *Basella alba* have a high rate of shrinkage as they had high levels of polysaccharides coupled with moderate viscosity of 1.0 Pa.s. However, *Aloe vera* had a high content of monosaccharides which denatured upon boiling thus losing its binding ability, as already noted in section 5.1.4. Thus the rate of shrinkage depended on the type of powder, particle size, and nature of the binder.

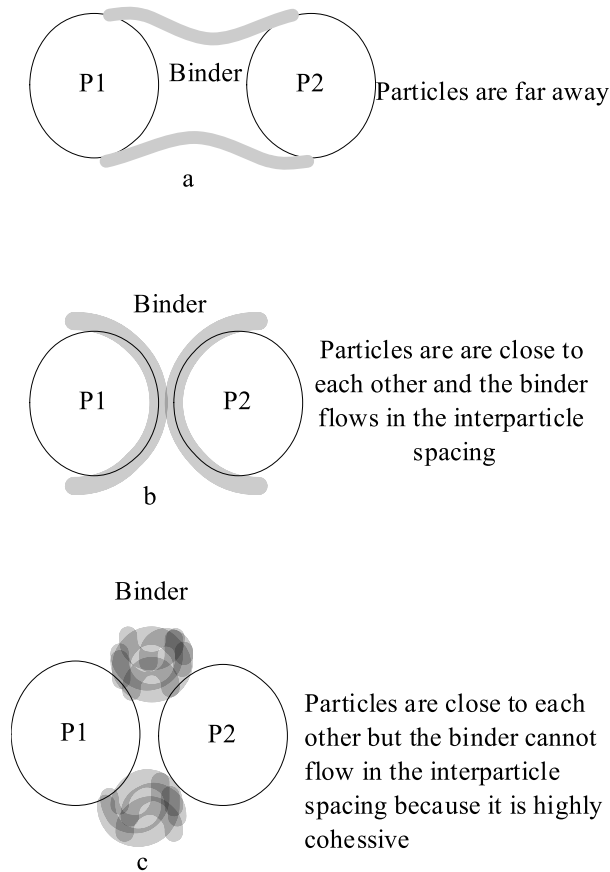


Figure 5.7: The different scenarios of the interaction of the organic binder and the particles

5.2.2 Linear Firing Shrinkage (LFS)

Figure 5.8 shows how LFS varied with firing temperature in membranes fabricated with *Basella alba* binder. Clay membranes shrunk least due to large particle sizes in the powder used in fabricating the membranes, unlike the DE particles which were smaller than the potter's clay. Thus the high rate of shrinkage in DE-based membranes. Smaller particles have a high surface area and surface energy which caused particle-particle interaction resulting in higher shrinkage. When the surface energy was activated with thermal energy during firing, the solid-vapor interface was converted to a solid-solid interface reducing the pore size of the material (Boch and Niepce, 2010). The reduced pore size caused the shrinkage in the material (Fang, 2010). Thus the higher rate of shrinkage meant a reduction in the size and volume of the samples. Higher firing temperature increased the kinetic energy of the particles inducing particle diffusion and high amplitude of vibration which caused them to realign into a periodic arrangement forming crystals. Samples fabricated from *Basella alba* had the highest rate of shrinkage because of the high content of proteins (Figure 5.4, Section 5.1.4) in the binder

which causes increased binding ability. Other binders showed similar results but with a lower rate of shrinkage. The descending order of rate shrinkage was *Basella alba*, *Corchorus olitoris*, *Abelmoschus esculentus*, and *Aloe vera* as shown in Table 5.4.

Table 5.4: Firing temperature and the linear firing shrinkage of DE-waste membranes fabricated with 50% binders obtained from Basella alba, Corchorus olitoris, Abelmoschus esculentus, and Aloe vera

Firing Temperature (°C)	Linear firing Shrinkage (%)			
	<i>Abelmoschus esculentus</i>	<i>Aloe vera</i>	<i>Basella alba</i>	<i>Corchorus olitoris</i>
700.0	5.1	4.8	6.0	5.4
720.0	5.4	5.0	6.1	5.8
740.0	5.7	5.2	6.2	6.0
760.0	5.9	5.5	6.4	6.2
780.0	6.1	5.8	6.6	6.4
800.0	6.4	6.0	6.8	6.7
820.0	6.6	6.3	7.1	6.8
840.0	6.8	6.6	7.6	7.0
860.0	7.1	6.8	8.0	7.5
880.0	7.5	7.2	8.1	7.9
900.0	7.9	7.5	8.4	8.2
920.0	8.0	7.9	8.8	8.6
940.0	8.5	8.1	8.9	8.8
960.0	8.8	8.4	9.2	9.0
980.0	9.0	8.5	9.5	9.3
1000.0	9.1	8.8	9.8	9.5
1020.0	9.4	9.0	10.0	9.7
1040.0	9.8	9.4	10.1	9.9
1060.0	9.9	9.6	10.4	10.0
1080.0	10.1	9.7	10.8	10.5
1100.0	10.3	9.9	10.8	10.6
1120.0	10.4	10.0	10.8	10.6
1160.0	10.5	10.0	10.8	10.6

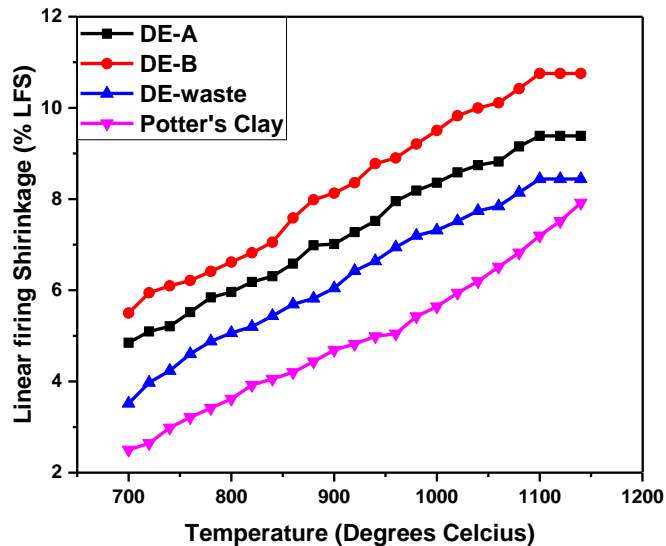


Figure 5.8: Linear firing shrinkage of DE, DE-Waste, and Potter's clay membranes fabricated with *Basella alba* binder against firing temperature

5.2.3 Bulk Density

Figure 5.9 shows the plot of bulk density of the greenware discs DE, DE-waste, and Potter's clay against the binder concentration used during the fabrication of membranes. The pattern mimics that of shrinkage. Thus the explanation given in Section 5.2.2 is also invoked here. There was an increase in bulk density with an increase in the binder concentration attributed to shrinkage of the material during drying as discussed in Section 5.2.1. The bulk density of the discs improved by 7.3% in DE-A, 8.5% in DE-B, 4.2% in DE-waste, and 6.0% in Potter's clay. The difference was attributed to the different particle sizes, elemental compositions of the powder, and the presence of diatom-based nano-pores.

The particle size affects the compressibility of the powder. Uniform particles compress more than non-uniform particles. This is why DE samples reported high density attributed to their small and uniform-sized particles reported in Section 5.1.1. On the other hand, irregular particles may fold onto themselves creating pores that may not be removed during pressing and drying causing low bulk density. It was noted that green samples fabricated with *Basella alba* showed higher bulk density than other binders due to its moderate viscosity, and organic and inorganic composition just as discussed in Section 5.2.1.

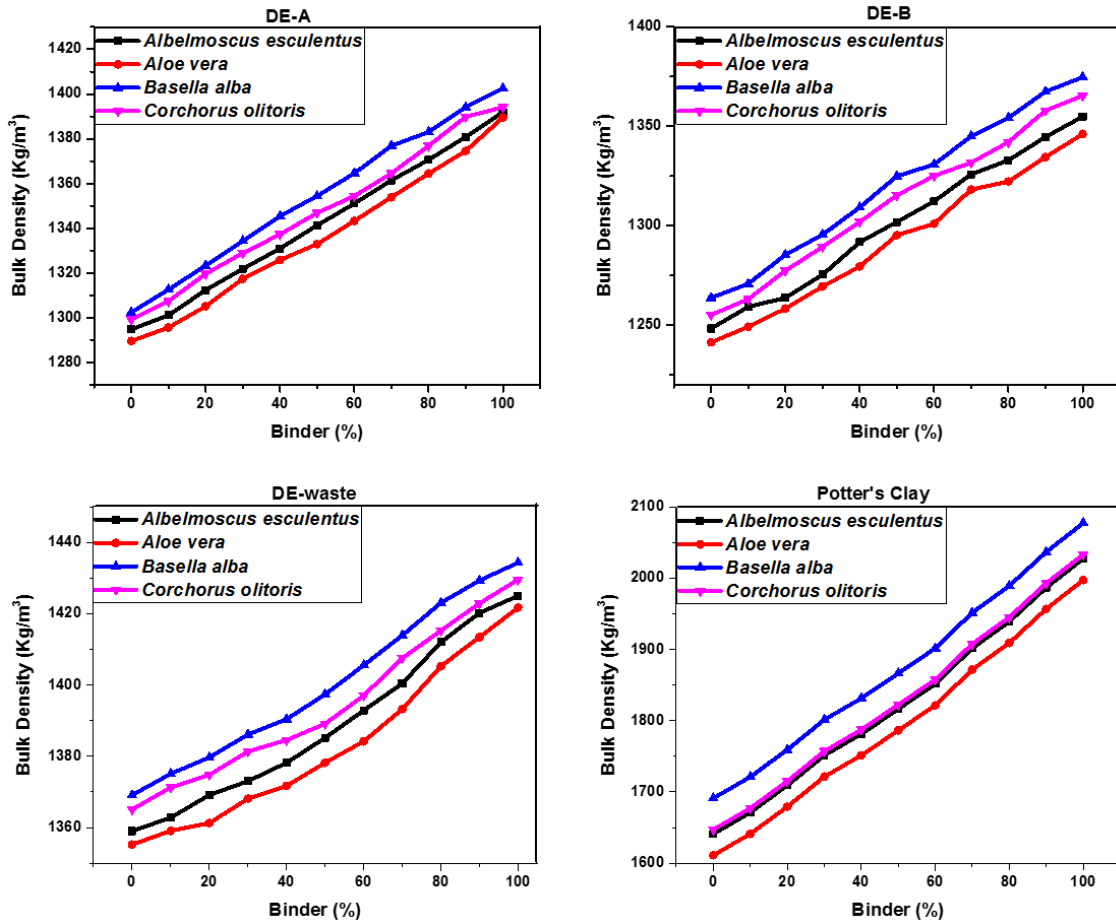


Figure 5.9: The plot of bulk density against the binder concentration used in the fabrication of diatomaceous earth and Potter's clay green membranes

When the dried green samples were fired at different firing temperatures the bulk density increased as shown in Figure 5.10. The increase in bulk density was caused by the increased particle-particle interaction as discussed in section 5.2.2.

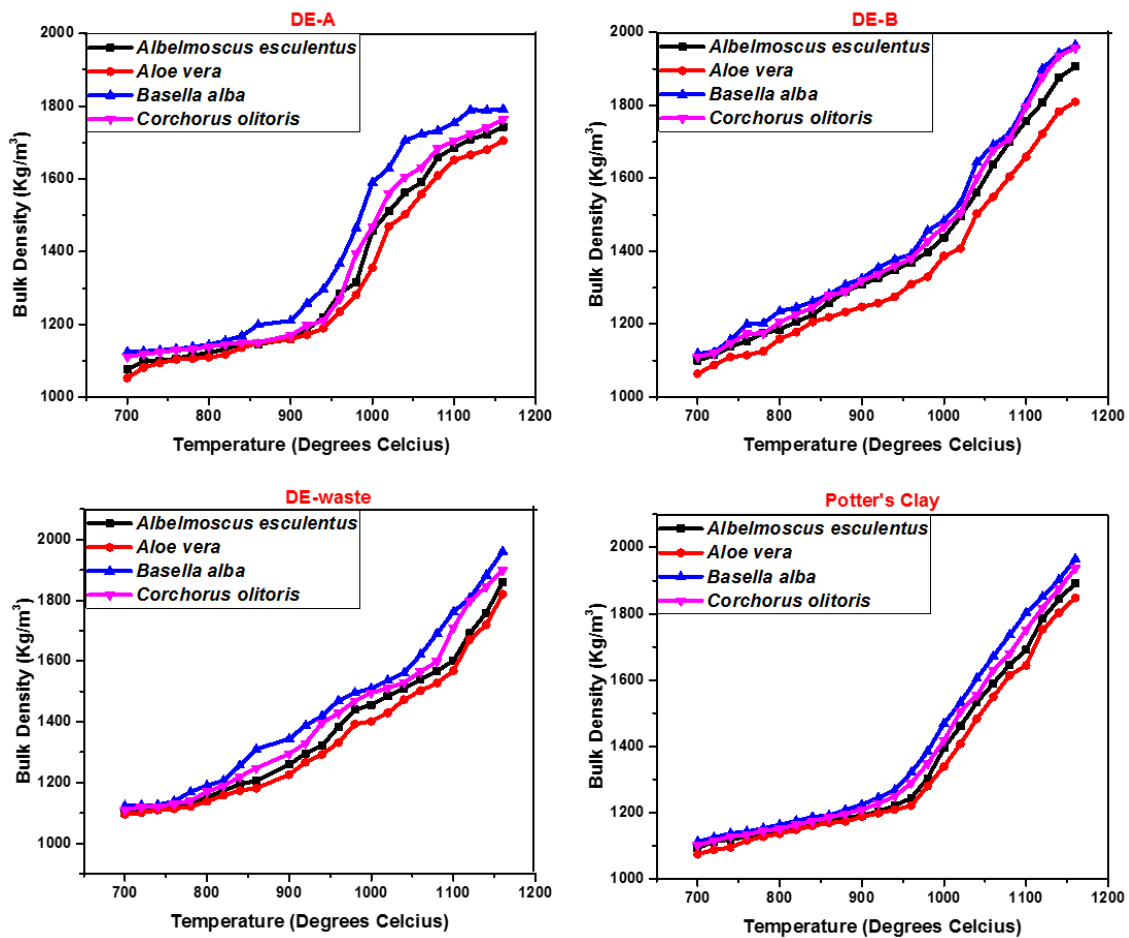


Figure 5.10: The plot of bulk density (Kg/m^3) against firing temperature of diatomaceous earth (DE-A, DE-B, and DE-waste), and Potter's clay fired at varying temperatures

5.3 Mechanical Properties

5.3.1 Modulus of Rupture (MOR) Green Samples

The plot of the MOR of the green DE and Potter's clay against the binder concentration used in the fabrication of the samples is shown in Figure 5.11. The MOR was distinctive in the different materials with the samples with the highest content of silica (DE-B) having the highest MOR. This is because silicon has many active sites such as Bronsted acid, Lewis acid, oxidizing sites, reducing sites, and surface hydroxyl groups which allow more binding sites (Venis and Basu, 2020). Even though aluminum also has active sites, silicon has more. Furthermore, Potter's clay has a high content of aluminum characterized by shrink-swell behavior which introduced cracks. Large swelling occurs when water is absorbed and when the water dries up these clays contract (shrink). The presence of these clay minerals is what allows soils to have the capacity to shrink and swell. The clay minerals include montmorillonite and illite. The amount of these minerals in a powder determines the severity

of the shrink-swell capacity and that is why shrink and swell on the greenware contributed to lower MOR.

The MOR increased with increased binder concentration because of the increased amount of ions in the binder which get bound to the clay/DE particles due to attractive forces. The presence of polysaccharides also enhanced the binding ability of silica and aluminum. Samples made from *Basella Alba* and *Corchorus olitorius* had higher MOR, which was attributed to the high levels of polysaccharides (shown in Figure 5.5, Section 5.1.4) that get attached to the active site of the DE and clay particles thereby increasing the MOR.

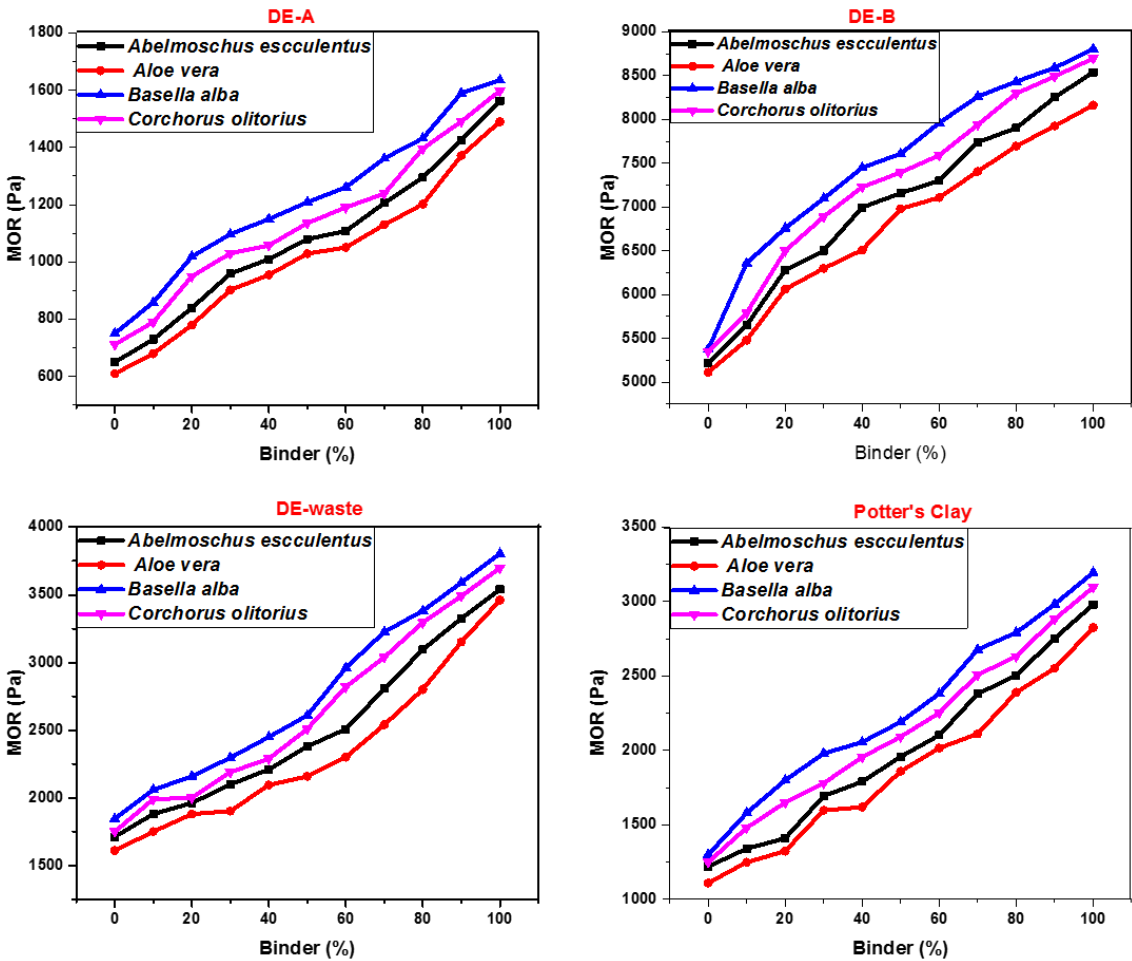


Figure 5.11: A plot of the MOR of the green DE, DE-Waste, and Potter's clay samples against the binder concentration used in the fabrication

5.3.2 Modulus of Rupture (MOR) fired Samples

Firing the green samples increased the mechanical strength (MOR) as shown in Figure 5.12. DE-B showed the highest MOR at all temperatures attributed to the small particle sizes (Figure 5.1.), high content of silica (see Table 5.1), and strong greenware Clay (See Fig. 5.10).

Silica has a layered structure, specific surface, high chemical, and mechanical stability at the fired temperatures investigated (Oyanedel-Craver and Smith, 2008; Lin and Juang, 2002; Krishna *et al.*, 2000; Bailey *et al.*, 1999). Comparatively, membranes formed from DE-A had the least bulk density and the least MOR despite DE-A having a high content of silica. This is because of the diatom-based pores on the particles of DE-A which were not affected by interparticle densification and could only fill up during vitrification, a stage which was not achieved by the firing temperatures (700.0 °C – 1150.0 °C) investigated in this study. The Potter's clay was made up of 28.8% aluminum which vitrifies at lower temperatures (around 660.6 °C) thereby filling up most of the pores and causing its membranes to have the least porosity. Both silicon and aluminum were able to form new bonds during firing by exchanging either their anions or cations because they both possess exchangeable cations such as Na⁺, K⁺, Ca²⁺, Mg²⁺, and H⁺ and anions SO₄²⁻ and PO₄³⁻ (Zhang *et al.*, 2010; Velde, 1995; Haan and Bolt, 1963). The exchange of anions and cations takes place without interfering with the structure of the material. However, the bonds of the structures break during firing leaving net charges in the form Si⁴⁺ with Al³⁺ which readily form stable bonds resulting in new bonds which cause densification and increased MOR (Reddy *et al.*, 2009). Furthermore firing at higher temperatures than 660.6 °C weakens the Si-O-Al bonds and at times breaks these bonds leaving Al³⁺ at the edge. The edge of the particles then becomes an adsorption surface and can encourage coordination, H-bonding, hydrophobic bonding, ion-dipole interactions, ion exchange, and van der Waals interactions that cause densification (Brown and Rhodes, 1997). Indeed the sites in the clay and DE minerals encourage densification through ion exchange and the formation of new bonds. Membranes fabricated from *Basella alba* produced the highest MOR because they had formed the strongest greenware.

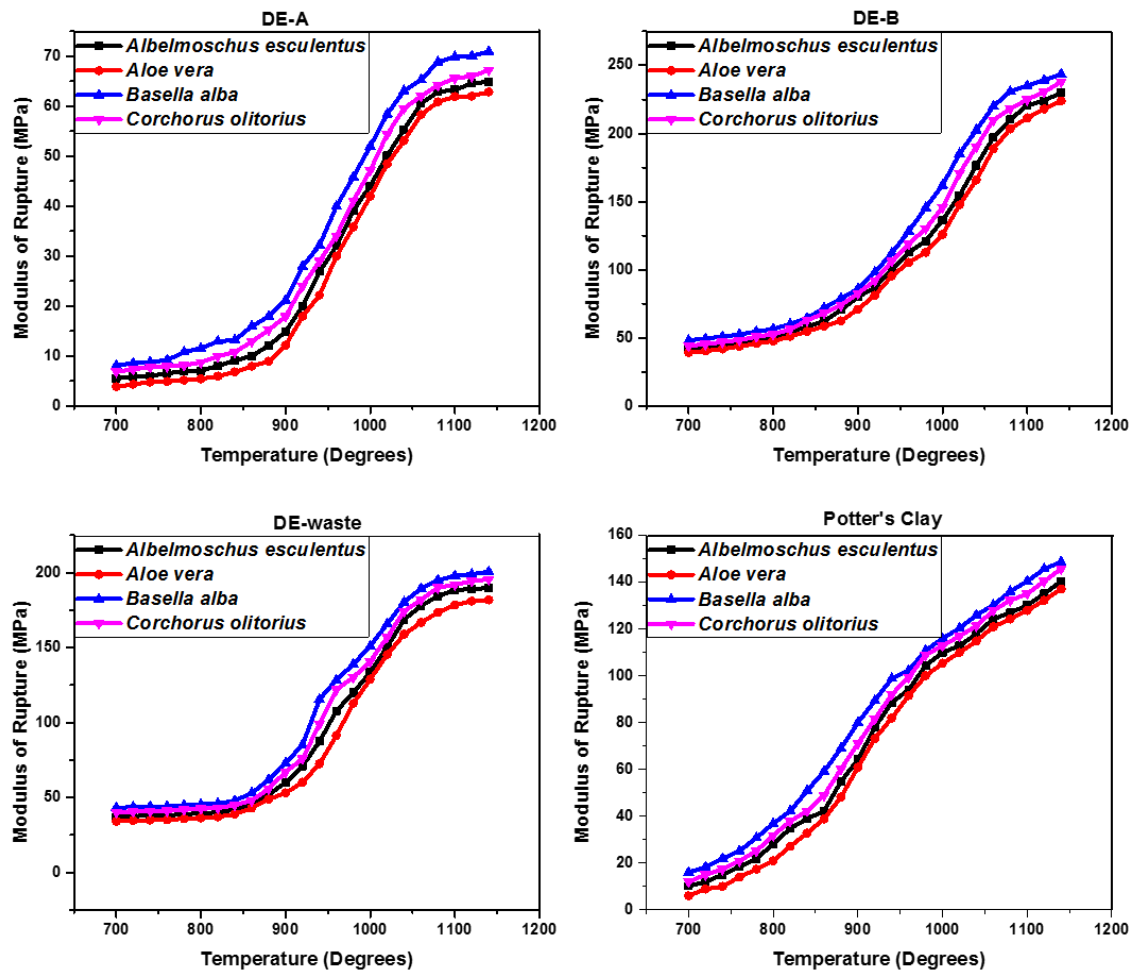


Figure 5.12: The relationship of MOR against firing temperature (700.0 °C to 1150.0 °C) of the membranes of diatomaceous earth (DE-A, DE-waste, Pure DE-B) and Potter's clay formed with different organic binders

Figure 5.13 shows the relationship between porosity and firing temperature of DE, DE-Waste, and Potter's clay membranes fabricated using different binders and fired at varying temperatures (700.0 °C to 1150.0 °C). Porosity decreased with an increase in firing temperature. The driving force of sintering that results in increased densification and hence reduced porosity and consequently increased mechanical property was supplied by thermal energy (Boch and Niepce, 2010). When the dried greenware was fired, the particles lost their excess surface energy which was used to form strong bonds that improved the bulk density and MOR of the material. The higher the firing temperature the higher the surface energy was released and more bonds formed increasing the MOR, and bulk density. However, firing the material at higher temperatures densifies the material and reduces the porosity as shown in Figure 5.14. Sintering mainly lowered the excess particle energy by reducing the interparticle pores and forming an agglomerated sintered material (Boch and Niepce, 2010). Sintering replaced the solid-vapor interface with either a solid-liquid interface or a solid-solid interface

which took place at different firing temperatures depending on the nature of the material. Thus from Figure 5.14 the optimal temperature of firing DE-B membranes is around 900.0°C.

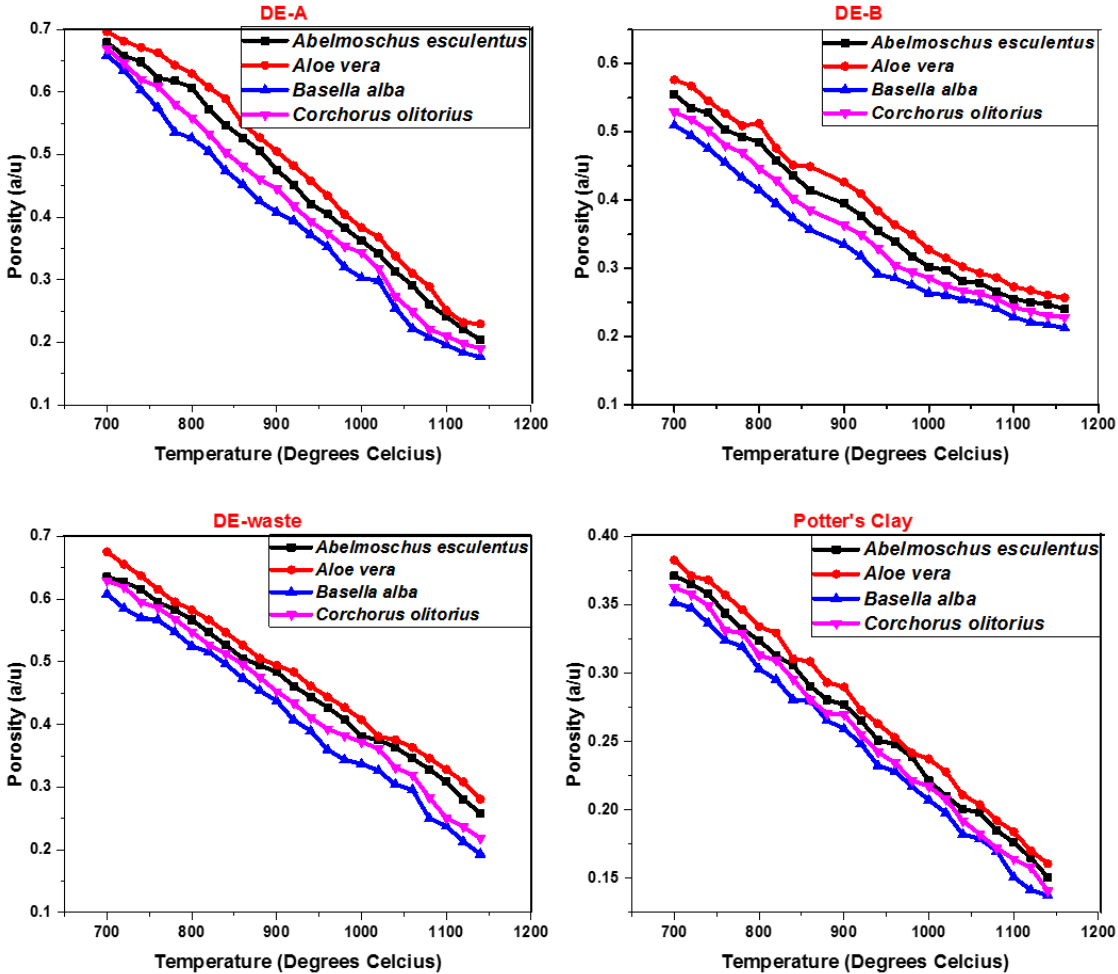


Figure 5.13: Volume fraction porosity against sintering temperature of diatomaceous based pellets (DE-waste, DE-A, and DE-B) bound by different organic binders (*Basella alba*, *Aloe vera*, *Corchorus olitorius*, and *Abelmoschus esculentus*)

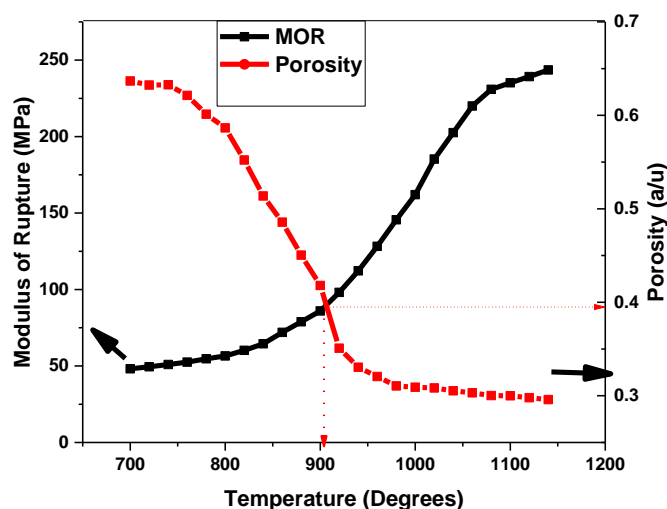


Figure 5.14: The plot of MOR and porosity against firing temperature of DE-B membrane fabricated with *Basella alba*

Figures 5.15 (a), (b), and (c) shows the XRD spectra for DE-A, DE-B, and DE-waste membranes fabricated with *Basella alba* binder and fired at 750.0 °C, 800.0 °C, 900.0 °C, 950.0 °C, 1000.0 °C, and 1150.0 °C. The spectra show an increase in intensity from 750.0 °C to 800.0 °C attributed to particle-particle interaction. Thermal energy initiates mass flow eliminating the particle-air boundary and replacing it with the particle-particle boundary. However, from 900.0 °C to 950.0 °C, the intensity reduced due to the formation of α -cristobalite (Farid, 2014). Using Equation. (4.1) and Equation (4.2) the grain size and the crystallinity were calculated and plotted against temperature as shown in Figure 5.15 (d). An increase in firing temperature increased crystallinity and grain size of silica up to 900.0 °C when silica transforms to α -cristobalite. From 1000.0 °C to 1150.0 °C the intensity of XRD spectra increases again as the formation of β -cristobalite sets in (Şan and Özgür, 2009). At the same time, crystallinity and grain size also increased with increased firing temperature. This study was focused on producing porous ceramic membranes and firing the samples beyond 1000.0 °C reduced the porosity of the membrane considerably and consequently, temperatures beyond 1150.0 °C were not investigated. Thus, the optimal firing temperature for membranes fabricated from this material was in the range of 900.0 °C to 950.0 °C. The grain size increased with an increase in the firing temperature because temperature increases thermal energy which in turn increases nucleation and bonding. The most crystalline membrane was the DE-B membrane followed by DE-waste then DE-A.

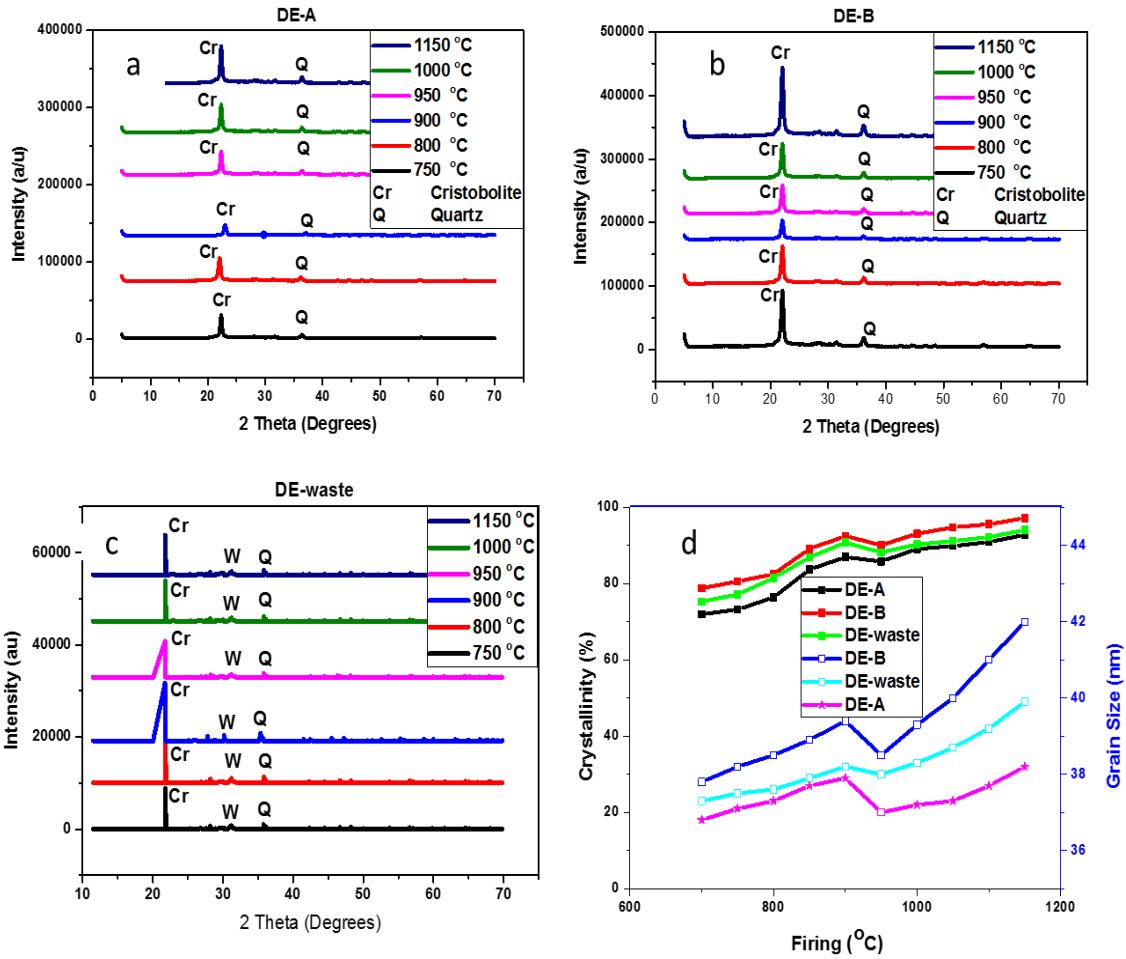


Figure 5.15: The XRD pattern of DE-A (a), DE-B (b), and DE-waste (d) membranes for samples fabricated with *Basella alba* and fired at 750.0 °C, 800.0 °C, 900.0 °C, 950.0 °C, 1000.0 °C, and 1150.0 °C and (d) shows the plot crystallinity and grain size against firing temperature

Figure 5.16 shows the micrographs of DE-waste membranes fired at 750.0 °C, 800.0 °C, 850.0 °C, 900.0 °C, 1000.0 °C, and 1100.0 °C. There was no or little necking observed in the particles of the samples fired at 750.0 °C and the particles were predominant because the thermal energy supplied was barely enough to initiate the initial stage of sintering. That the necking between the particles was weak (the solid-vapor interphase) is confirmed by the low MOR reported earlier in this section. The membranes were also highly porous with some pores having large pore sizes up to 99.8 μm . The vitrification of some particles and the formation of larger necks between the particles were observed when the firing temperature was increased to 800.0 °C. The pores in the membranes fired at 800.0 °C to 850.0 °C were smaller than the ones observed in the membranes fired at 750.0 °C. The cracks were still observed in these membranes indicating that 800.0 °C and 850.0 °C firing temperatures did not generate enough thermal energy to facilitate bond formation within the particles.

However, the necking process and vitrification process were noted in the membranes fired at 800.0 °C and 850.0 °C as shown in Figure 5.16. Some pores were filled by the flowing liquid and the remaining ones were reduced in size. At 900.0 °C, some particles had started bonding increasing solid-solid interaction and the solid-vapor phase decreased while the solid-solid phase was initiated. The strong bonds between the particles explain the improved MOR, bulk density, and reduced porosity caused by the solid-solid phase. Beyond 1000.0 °C firing temperature, most of the pores had reduced significantly and grain boundaries formed. Crystals were visible both at 1000.0 °C and 1100.0 °C firing temperatures. The few pores were in nanometers with some pores being as small as 12.8 nm. Thus the optimal firing temperature for the DE-waste was in the range of 900.0 - 950.0 °C as the membranes produced at this temperature are both porous and mechanically strong to withstand household handling.

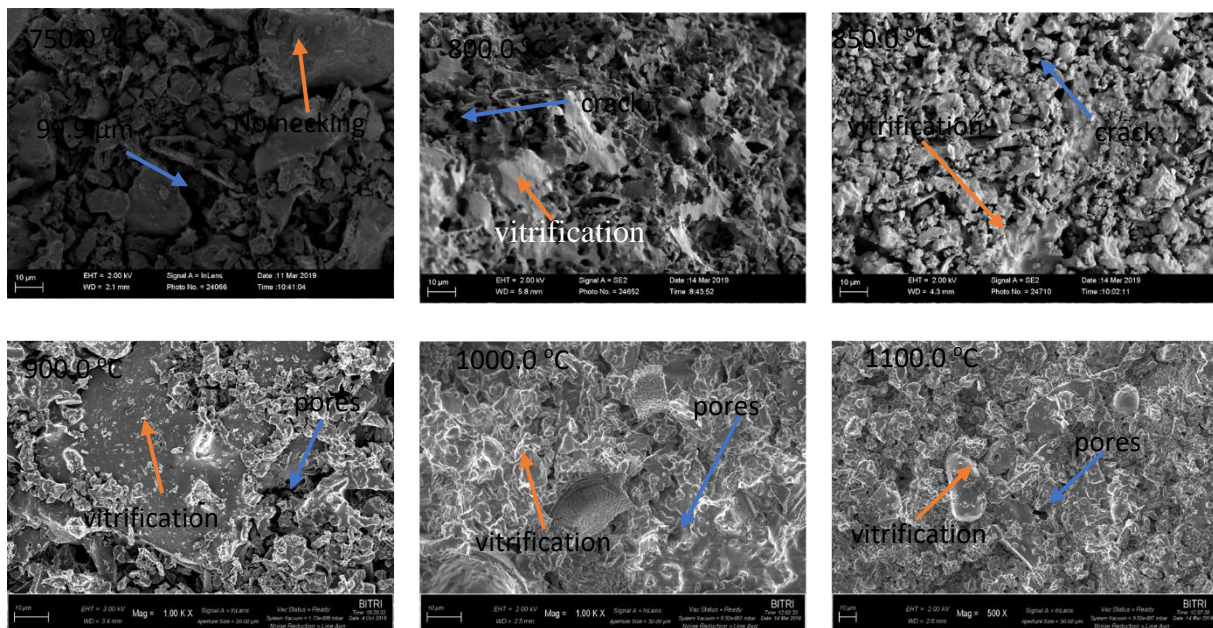


Figure 5.16: The micrographs of DE-waste membranes fired at 750.0 °C, 800.0 °C, 850.0 °C, 900.0 °C, 1000.0 °C, and 1100.0 °C

5.4 Effect of Charcoal on the Membranes Strength

Figure 5.17 shows the plot of MOR and porosity against the percentage mass of the amount of charcoal used to fabricate DE-waste and Potter's clay membranes. The porosity increased with an increase in the percentage mass of charcoal, but on the contrary, the MOR was found to reduce with an increase in the percentage mass of charcoal. Charcoal is a burn-out material that increased the number of pores in the membranes after firing. During firing, especially above 700.0 °C, the charcoal burned to ashes leaving only pores in the fired membranes

(Mitchell and Gluskoter, 1976). The more the mass of charcoal the more the pores formed and the bigger the size of charcoal particle the bigger pores of the membranes.

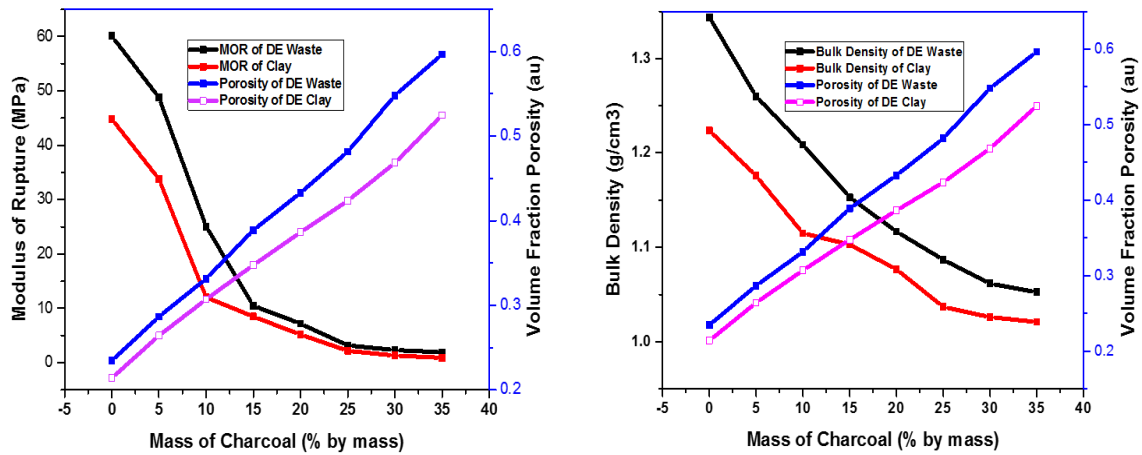


Figure 5.17: Relationship of porosity against the content of charcoal in DE earth membranes with different organic binders and fired at a constant temperature of 900.0°C under air

5.5 Effect of the Organic Binders

Figure 5.18 shows the plot of porosity against the percentage concentration of the binder for membranes fired at 900.0 °C. There was a steady decrease in porosity up to the optimal content of the binder at 50.0%. Below 50.0% concentration, the presence of fluxing material (Na₂O, K₂O, Mg, and CaO) in the binder accelerated the particle-particle causing densification that resulted in decreased porosity, and increased linear firing shrinkage, and MOR, as shown in Figures 5.18, 5.19, and 5.20 respectively. Further increase in the binder content resulted in an increase in porosity due to burning out of the excess binder, which then left pores that contributed to a decrease in LFS. Thus, 50.0% of dilution was recommended for the fabrication of membranes.

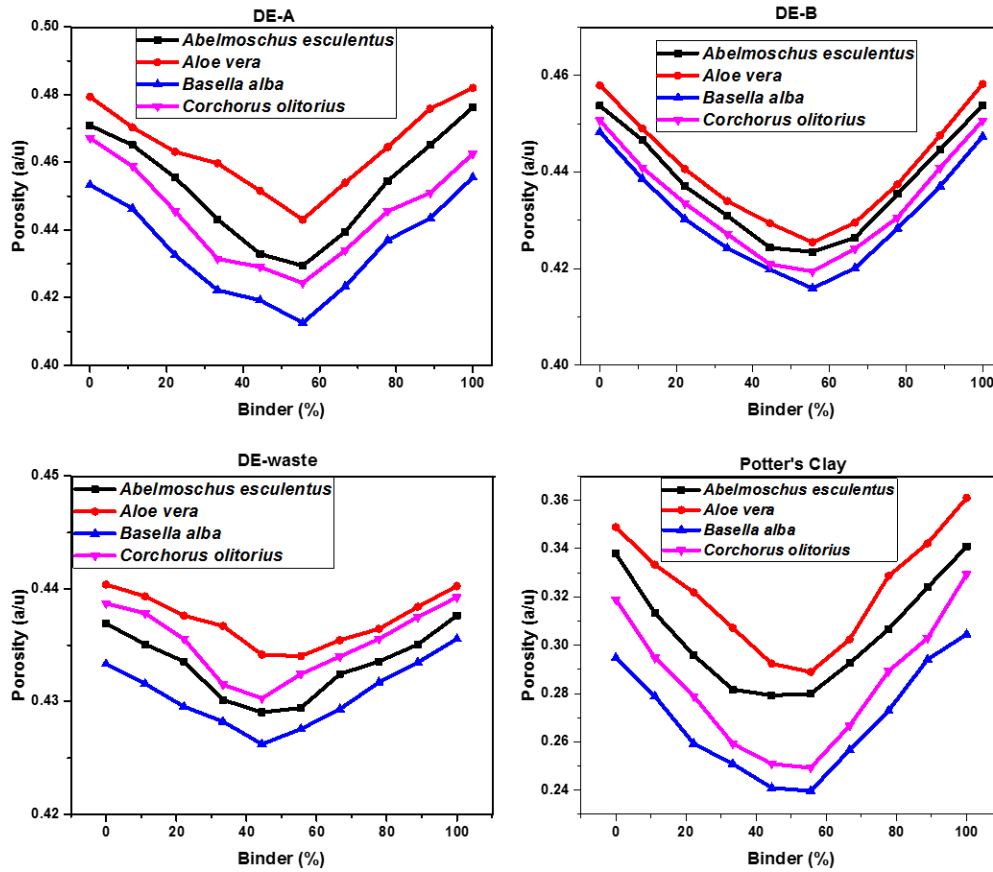


Figure 5.18: Average porosity of diatomaceous earth sand Potter's clay samples against the binder percentage concentration at a constant temperature of 900.0 °C for DE-A, DE-B, DE-waste, and clay membranes

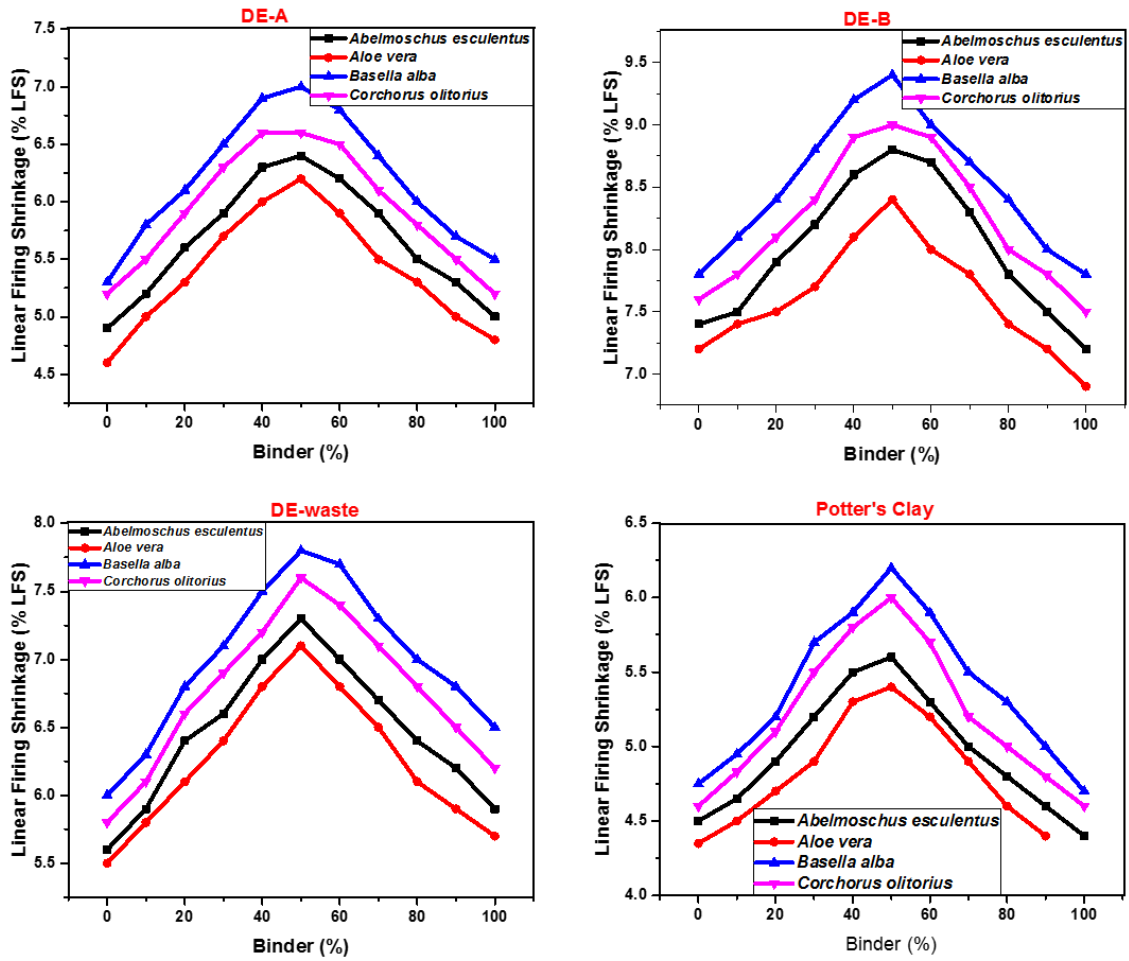


Figure 5.19: The variation of linear firing shrinkage (LFS) with the binder in pure diatomaceous earth samples and the waste membranes fired at 900.0 °C

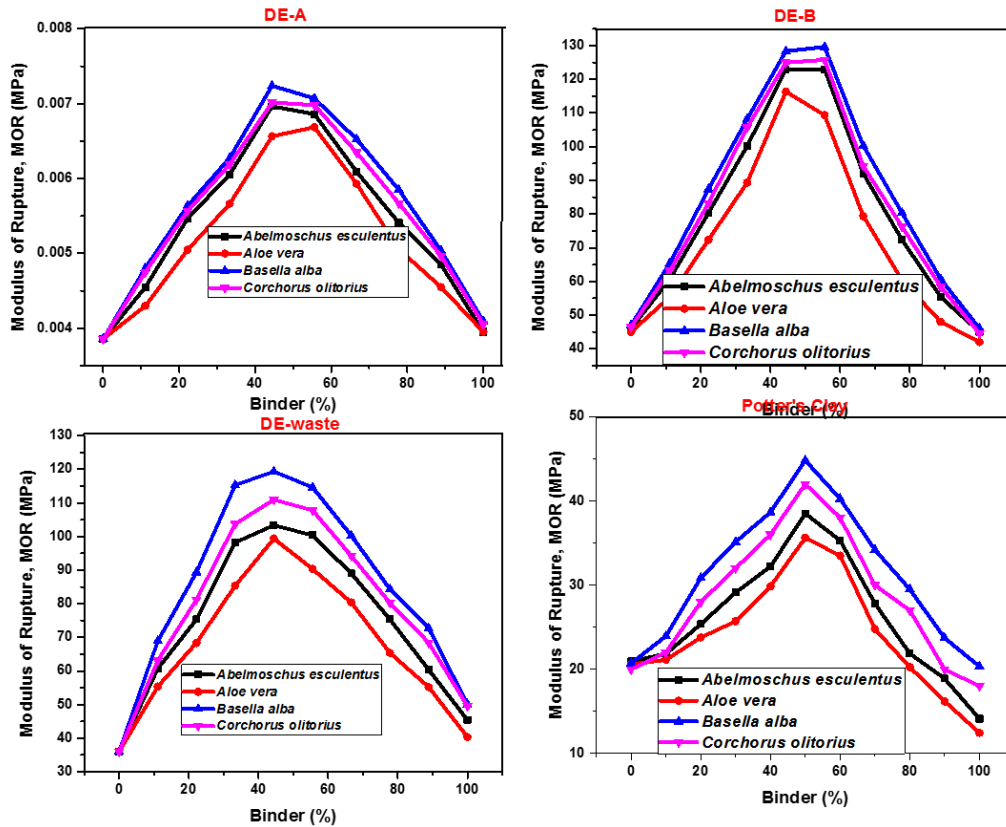


Figure 5.20: Average modulus of rupture against binder concentration (*Abelmoschus esculentus*, *Aloe vera*, *Basella alba*, and *Corchorus olitorius*) of DE and Potter's membranes fired at 900.0 °C

Figure 5.21 shows the percentage increase in strength in DE samples used in fabricating the samples with 0.0% of the binder (plain water used) as the reference value. All binders improved the MOR of the membranes ranging from 33% to 160.0% increase. *Basella alba* was found to form membranes with the highest MOR with a percentage increase of 175.1%, 61.8% 158.0%, and 45.1% in DE-A, DE-B, DE-waste, and Potter's clay respectively. To improve the performance of the *Aloe vera*-based binder this work proposes that the extraction of the binder from the leaves be done without boiling to eliminate the hydrolysis process that destroyed the polymer chains (Ahlawat and Khatkar, 2011).

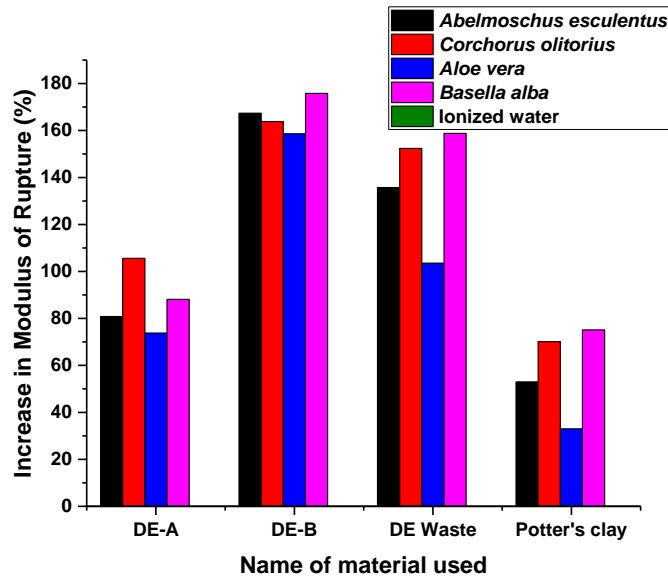


Figure 5.21: The percentage increase in strength (MOR) in DE-A, DE-B, DE-waste and Potter's clay membranes fabricated with *Abemoschus esculentus*, *Aloe vera*, *Basella alba*, and *Corchorus olitorius*

5.6 Porosity-Mechanical Property Relationship

In this section, the relationship between bulk density, porosity, and MOR is discussed. The relevant models that explain these relationships are also discussed. The effects of pore diameter and aspect ratio on porosity are also presented.

5.6.1 Porosity-Bulk Density Relationship

The relationship between porosity and bulk density of DE-A membranes is shown in Figure 5.21; it is an inverse linear relationship. The root means square (R^2) values were found to be higher than 0.9 indicating that the fit was good as shown in Table 5.5. Membranes made from DE-A had a density of 1230.3 kg/m^3 to 1257.9 kg/m^3 . These values are lower than the ones reported in the green membranes in Section 5.2.2. This is because the green ceramics contains, moisture, binder, and powder fluxes which were eliminated from samples during drying and firing living pores filled with air. The membranes made from the *Aloe vera* binder had the lowest density because of their high porosity.

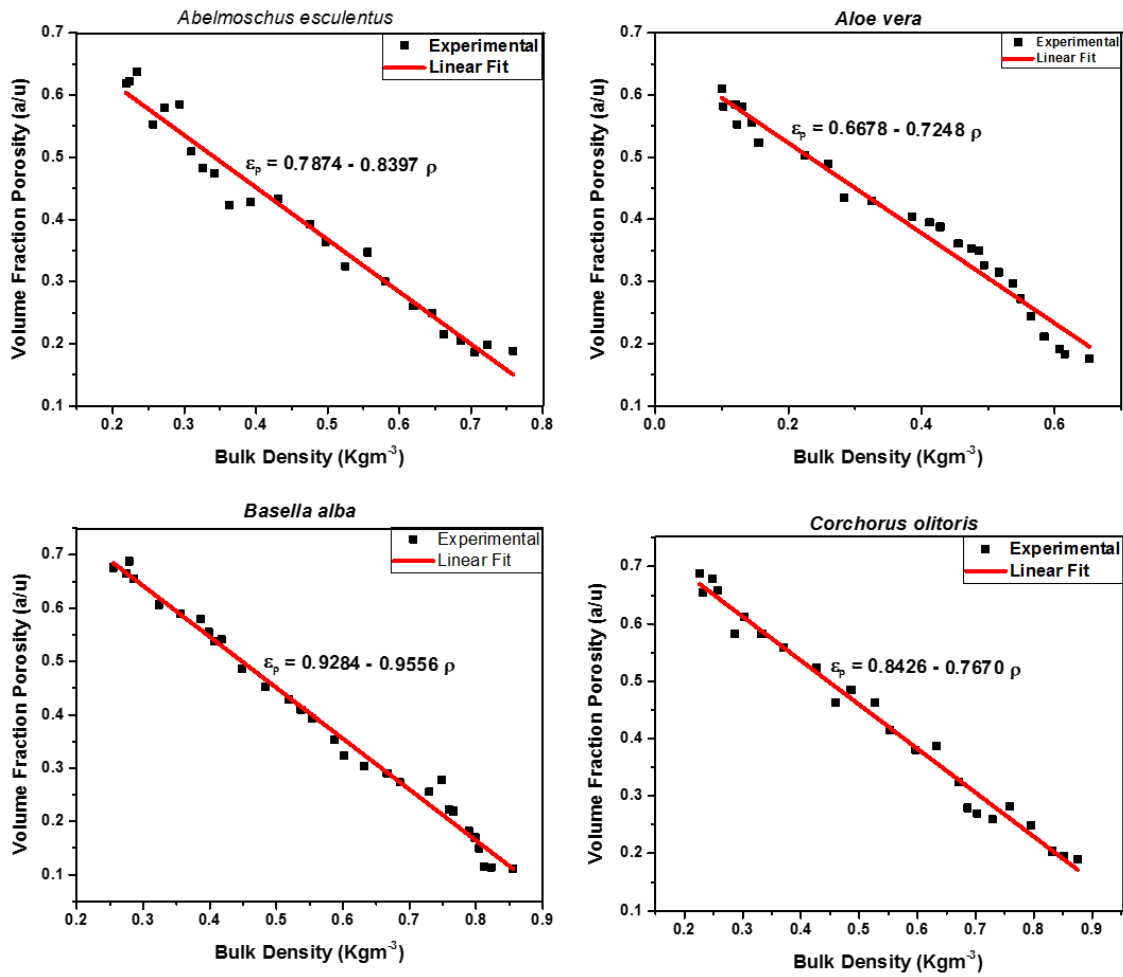


Figure 5.22: The linear fit and scatter plot of the relationship between bulk density and volume fraction porosity of diatomaceous earth A membranes fabricated with different binders

Table 5.5: The components of linear fits extracted from diatomaceous earth A models

Binder	Intercept ρ_0	Gradient m	ρ_0^{-1} (kg/m ³)	m^{-1} (kg/m ³)	R-Squared	Pearson's r
<i>Abelmoschus sculentus</i>	0.7873	-0.8397	1270.1	1190.9	0.9708	-0.9853
<i>Aloe vera</i>	0.6678	-0.7248	1497.5	1379.8	0.9726	-0.9862
<i>Basella alba</i>	0.9284	-0.9556	1077.1	1046.5	0.9887	-0.9943
<i>Corchorus olitorius</i>	0.8426	-0.7670	1186.8	1303.8	0.9850	-0.9925

Membranes fabricated from DE-B showed comparable results to DE-A as shown in Figure 5.23. However, the results of DE-B showed lower values of density than DE-A as shown in Table 5.6. These results confirm that DE-A is denser than Pure DE-B just as it was found experimentally. The plot also confirms that membranes incorporating *Aloe vera* and *Abelmoschus esculentus* had the least bulky density of 802.1 kg/m³ and 967.0 kg/m³.

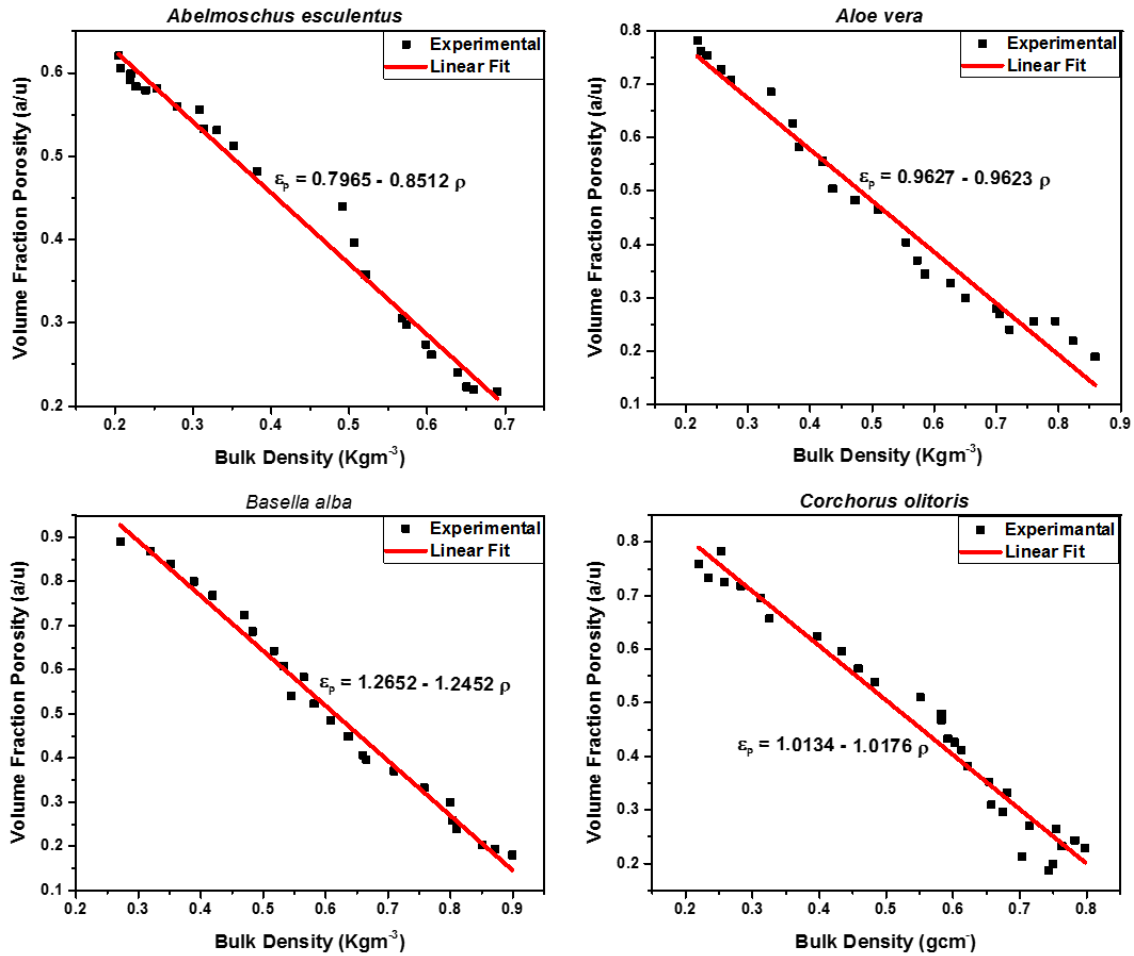


Figure 5.23: The linear fit and scatter plot of the relationship between bulk density and volume fraction porosity of diatomaceous earth B membranes fabricated with different binders

Table 5.6: The y-intercept, gradient, and their inverse values as predicted by a linear fit of diatomaceous earth B membranes. The R-Squared and Pearson's are also shown

Binder	Intercept ρ_o	Gradient m	ρ_o^{-1} (Kg/m ³)	m^{-1} Kg/m ³	R-Squared	Pearson's r
<i>Abelmoschus esculentus</i>	0.7965	-0.8512	1255.5	1174.9	0.9831	-0.9915
<i>Aloe vera</i>	0.9628	-0.9623	1038.6	1039.1	0.9708	-0.9853
<i>Basella alba</i>	1.2652	-1.2452	790.4	803.1	0.9873	-0.9936
<i>Corchorus olitorius</i>	1.01341	-1.0175	986.7	967.0	0.9850	-0.9925

The DE-waste had the highest solid density of 1979.2 kg/m³ among the three DE samples handled in this work because it had the least levels of silica and diatom-like structures.

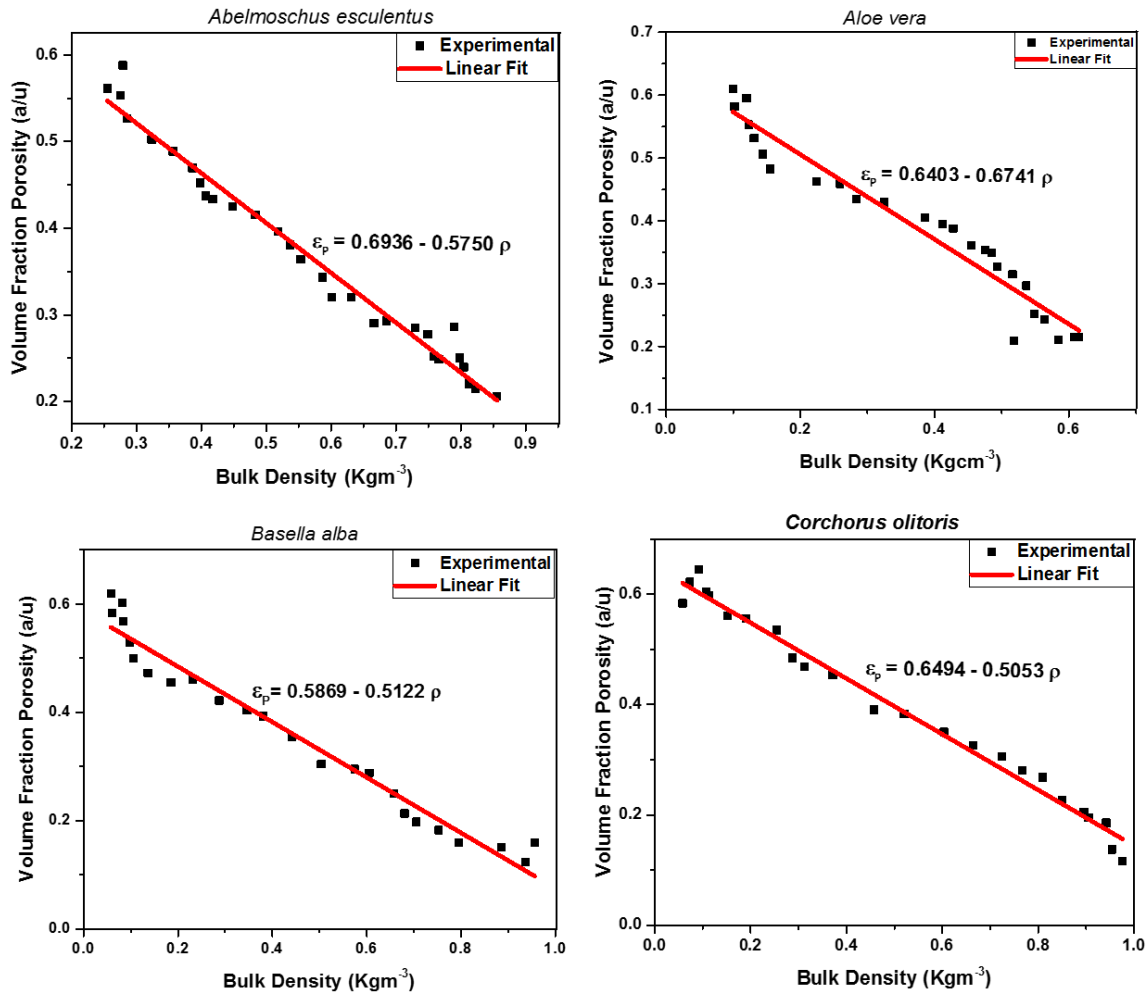


Figure 5.24: The linear fit and scatter plot of the relationship between bulk density and volume fraction porosity diatomaceous earth waste membranes fabricated with different binders

Table 5.7: The y-intercept, gradient, and their inverse values as predicted by a linear fit of diatomaceous earth waste membranes. The R-Squared and Pearson's are also shown

Binder	Intercept ρ_o	Gradient m	ρ_o^{-1} (kg/m ³)	m^{-1} (kg/m ³)	R-Squared	Pearson's r
<i>Abelmoschus esculentus</i>	0.6937	-0.5750	1441.6	1904.3	0.9755	-0.9877
<i>Aloe vera</i>	0.6403	-0.6741	1640.3	1483.5	0.9383	-0.9686
<i>Basella alba</i>	0.5869	-0.5122	1703.8	1952.2	0.9649	-0.9823
<i>Corchorus olitorius</i>	0.6494	-0.5053	1539.8	1979.2	0.9848	-0.9925

5.6.2 Effect of Pore Diameter on Bulk Density

Figure 5.24 shows the plot of bulk density against the pore size of membranes DE-waste sintered at 900.0 °C. The bulk density and pore size were inversely related. This relationship confirmed that the bigger the pore size the more porous the membrane. The fittings of R^2

greater than 0.9 showed a highly correlated relationship. However, the correlation was negative as shown by Pearson's correlation r of greater than -0.9794.

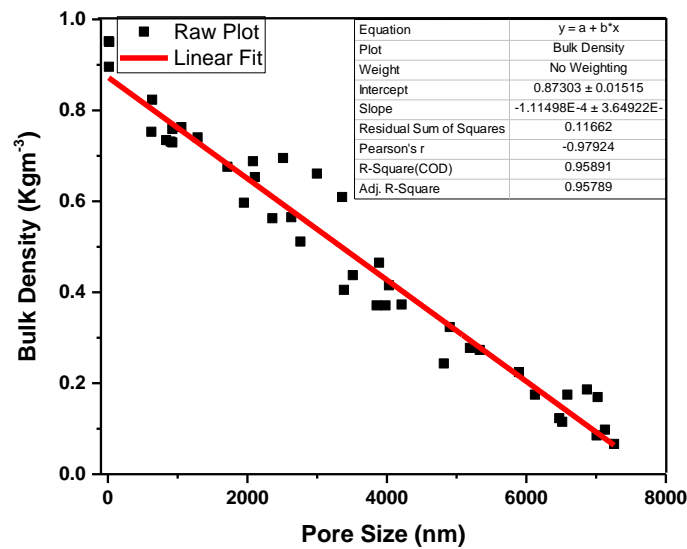


Figure 5.25: The relationship between bulk density and pore size of diatomaceous earth waste fabricated with *Basella alba* binder

5.6.3 Aspect Ratio

Figure 5.25 shows a bar chart of the number of occurrences against the aspect ratio of membranes of porosities 0.12, 0.18, 0.22, and 0.28 for DE-A, DE-B, and DE-waste. It was observed that fired diatomaceous earth had all forms of pore shapes as discussed in the literature (Pappas, 2005; Du Buf *et al.*, 1999). However, these shapes vary in number. That is, some shapes occurred more frequently than others. There was no difference in aspect ratio when the axes were interchanged implying that the orientation of the pores did not affect the porosity. The sphere-like and oblate-like pores were caused by the cylindrical diatoms that characterized the micrographs of the proceeding sections. Furthermore, most of the pores in this work were at the nano-level evidenced by the 4.2 nm pores on the basket-like diatom. An increase in porosity reduced the occurrence of oblates and spherical pores. At the same time, an increase in porosity increased the occurrence of the aspect ratio of 0.1 – 0.3 and 0.6 – 0.8 just as predicted by (Kingery *et al.*, 1976).

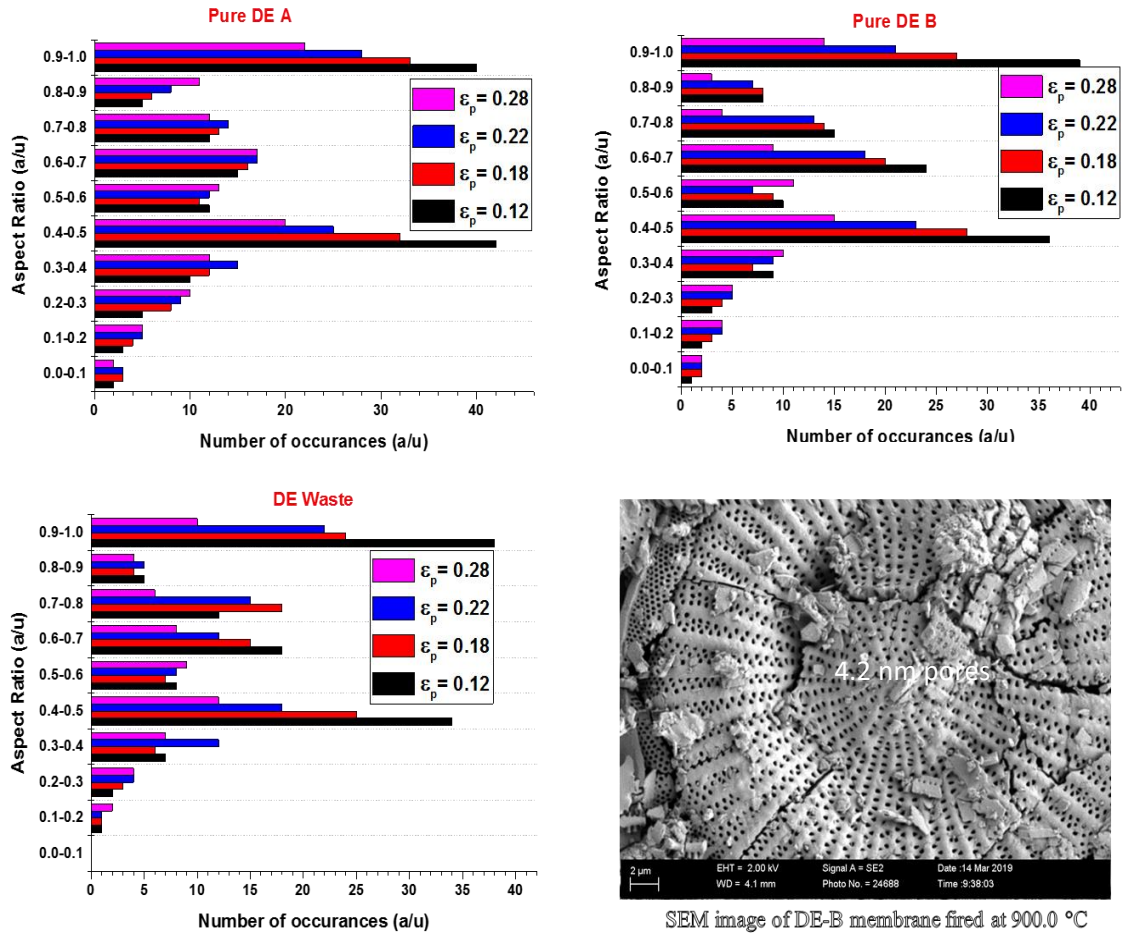


Figure 5.26: The bar chart of the number of occurrences against the aspect ratio of membranes of porosities ϵ_p 0.12, 0.18, 0.22, 0.28 and the SEM image of DE-B membrane fired at 900.0 °C

5.6.4 Comparison of the Experimental Data with the Minimum Contact Area and Stress Concentration Effects Models

Figure 5.27 shows the minimum contact area (MCA) model and stress concentration effect (SCE) model Equation (5.4) and Equation (5.5) respectively

$$\sigma = \sigma_o \exp(-b\epsilon_p) \quad 5.4$$

$$\sigma = \sigma_o (1 - a\epsilon_p)^\eta \quad 5.5$$

In Equation (5.4) σ is the MOR of the membrane after applying the load, σ_o is the MOR of the membrane without the load, b is a constant determined by the fabrication methods and ϵ_p is the porosity of the material. In Equation (5.5) η and α are constants. η represents the pore structure, orientation, and shape; α represents the critical porosity at zero Young's moduli.

Equations (5.4) and (5.5) were fitted on the experimental data of relative MOR against the volume fraction porosity of Pure DE-A. The relative values were obtained using Equation (5.6)

$$\sigma_r = \frac{\sigma - \sigma_o}{\sigma} \quad 5.6$$

It was observed that the MCA model fitted the experimental data in all binders better than the SCE model as shown in Figure 5.26.

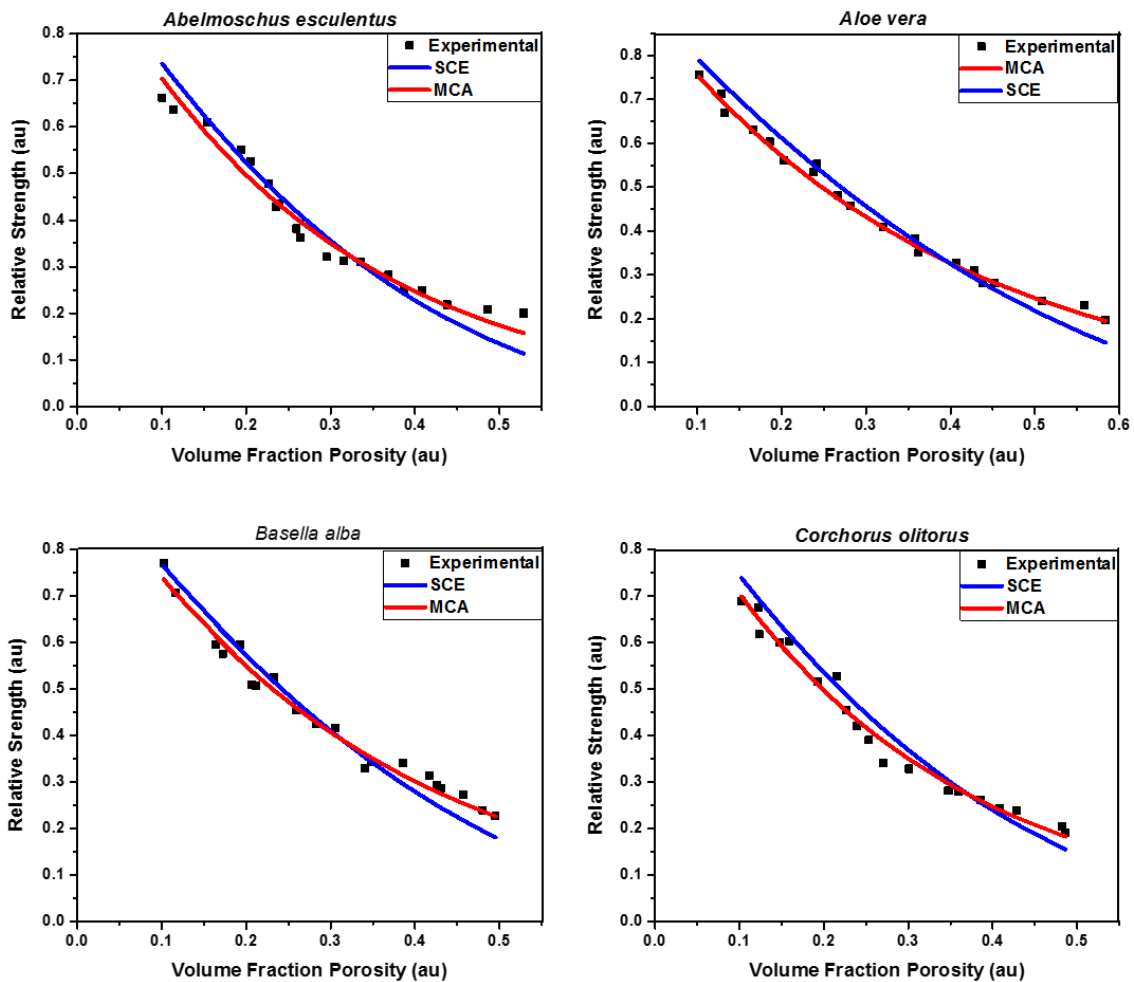


Figure 5.27: The scatter plot relative strength of Pure DE A membranes sintered at not 900.0 °C against volume fraction porosity fitted with MCA and SCE models

Table 5.8 shows the values of the constants b and η used in the fitting MCA and SCE models respectively. The statistical values of R^2 and Pearson's correlation r obtained after fitting the models were also shown in Table 5.8. The values of b ranged between 2.8 and 3.5 for the four binders used in fabricating Pure DE-A. These values were similar to those found in the literature (Nyongesa and Aduda, 2004). The constant b was associated with fabrication

techniques and it varied according to pore structures (She *et al.*, 2002). Thus, the values obtained from modeling DE-A were lower or equal to the average value of 3.5

The values of η varied from 2.2 to 2.9 and were less than those found by (Nyongesa and Aduda, 2004) who found the value of η as 3.5. The difference can be attributed to the nature of the material. The membranes in this work were fabricated from silicious DE but (Nyongesa and Aduda, 2004) investigated kaolinite samples. However, the values found here were comparable to those reported in the literature ($\eta = 2.5$) (Boccaccini and Boccaccini, 1997; Boccaccini, 1994; Coble and Kingery, 1956).

The values of R^2 and Pearson's correlation r confirmed that the MCA model gave the best fit as it was characterized by high values of R^2 and r . The Pearson's correlation was negative further affirming the inverse relationship between strength and porosity. The values of r and R^2 for MCA were all greater than $|0.9|$, indicating that the fits were good and highly correlated.

Table 5.8: Summary of the materials used together with calculated values of empirical parameters based on Equations 5.4 and 5.4 respectively

Binder Used	Minimum Contact Area (MCA) Model for Pure DE-A membranes			Stress Concentration Effect (SCE) Model for Pure DE-A membranes		
	b	R^2	r	η	R^2	R
<i>Abelmoschus escculentus</i>	3.5	0.9565	-0.9458	2.9	0.9331	-0.9251
<i>Aloe vera</i>	2.8	0.9971	-0.9925	2.2	0.9965	-0.9658
<i>Basella alba</i>	3.0	0.9925	-0.9914	2.5	0.9037	-0.9014
<i>Corchorus olitorius</i>	3.5	0.9363	-0.9169	2.8	0.9258	-0.9148

Figure 5.28 shows the scatter plot of relative strength against volume fraction porosity that was fitted with MCA and SCE models for membranes fabricated with DE-B. The results were similar to those obtained from DE-A. The MCA model again fitted the experimental data better than the SCE model. Membranes bound by *Basella alba* were also characterized by high values of b ($b = 3.7$) which was attributed to increased densification. The values of η were also similar to those found in DE-A. The R^2 and r were again greater than $|0.9|$ indicating good fitting and strong negative correlations between relative strength and volume fraction porosity

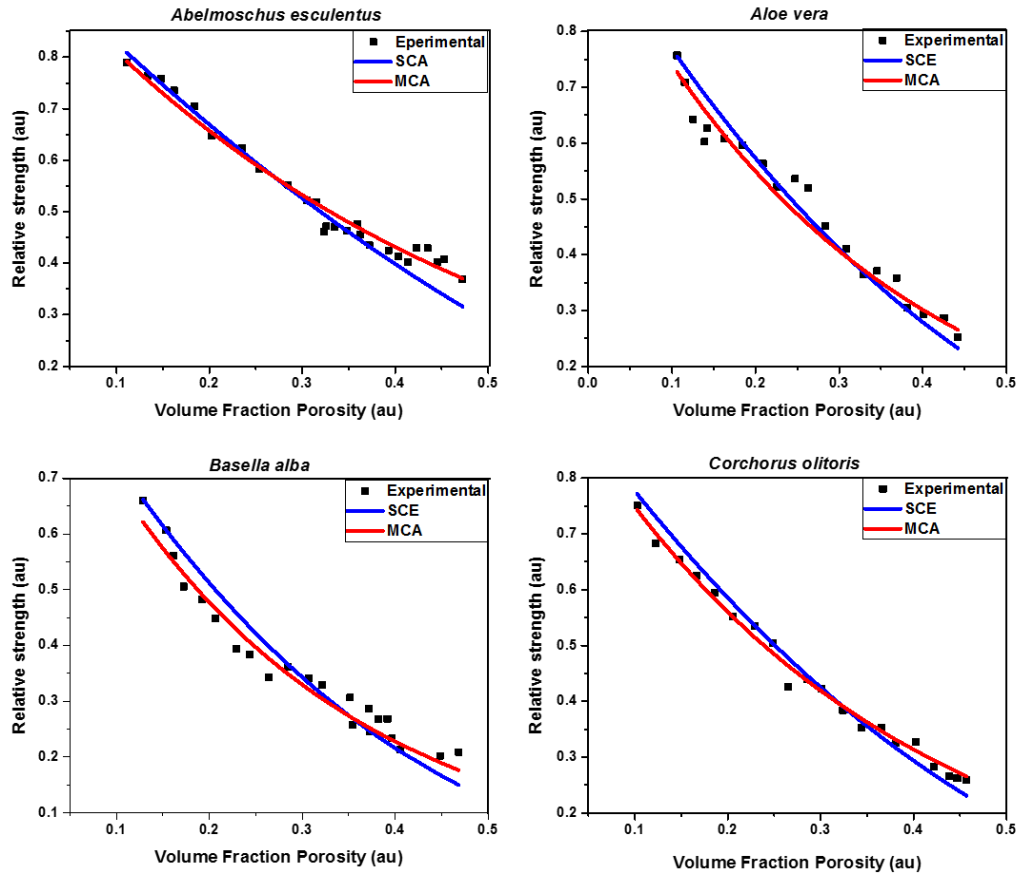


Figure 5.28: The experimental data of relative strength against volume fraction porosity of DE-B membranes fitted with MCA and SCE models

Table 5.9: The constants b and η obtained from MCA and SCE fit respectively. The R^2 values and Pearson's correlations are also shown

Binder Used	Minimum Contact Area (MCA) Model for DE-B membranes			Stress Concentration Effect (SCE) Model for DE-B membranes		
	b	R^2	r	η	R^2	R
<i>Abelsonchus esculentus</i>	2.1	0.9956	-0.9859	1.8	0.9689	-0.9587
<i>Aloe vera</i>	3.0	0.9991	-0.9958	2.5	0.9758	-0.9655
<i>Basella alba</i>	3.7	0.9994	-0.9517	3.0	0.9485	-0.9361
<i>Corchorus olitorius</i>	2.9	0.9865	-0.9758	2.4	0.9268	-0.9258

Figure 5.29 shows the MCA and SCE fits on the experimental data of DE Waste sintered at 900.0 °C. The volume fraction porosity of DE-Waste was lower than that obtained in DE-A and DE-B (less than 0.4). This was attributed to diatom-like pores which were mostly cylindrical. The MCA model still fitted the data better than SCE just as in the pure diatomaceous earth, and the membranes fabricated with *Basella alba* binder had the highest values of b and η .

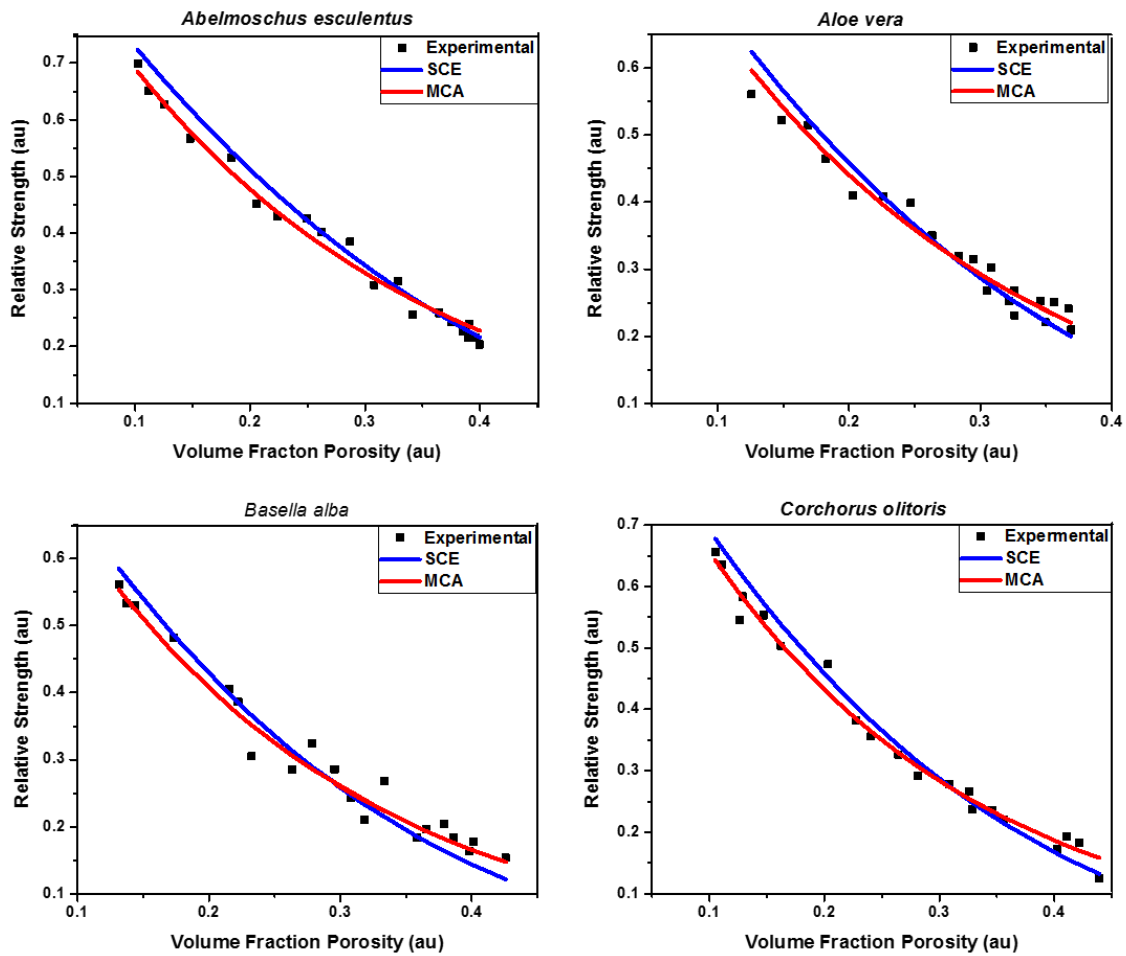


Figure 5.29: The plots of relative strength against volume fraction fitted with MCA and SCE models. The membranes were sintered at 900.0 °C.

Table 5.9 shows the constants of MCA and SCE fits on experimental data of DE Waste sintered at 900.0 °C. Among the three diatomaceous membranes, DE-B membranes had the best fits followed by DE-waste and then DE-A. This order mimicked the strength of the membranes.

Table 5.10: The constants of MCA and SCE fit on experimental data of DE Waste sintered at 900 °C

Binder Used	Minimum Contact Area (MCA) Model for DE Waste membranes			Stress Concentration Effect (SCE) Model for DE Waste membranes		
	b	R^2	r	η	R^2	r
<i>Abelmoschus esculentus</i>	3.7	0.9878	0.9789	3.0	0.9014	0.8851
<i>Aloe vera</i>	4.1	0.9925	0.9856	3.5	0.9548	0.9368
<i>Basella alba</i>	4.5	0.9978	0.9902	3.8	0.9965	0.9856
<i>Corchorus olitoris</i>	3.5	0.9965	0.9858	4.2	0.9954	0.9658

5.7 Purification Efficiency

5.7.1 Flow Rate

The graphs in Figure 5.30 show the plots of the volume of water filtered against the time taken to filter uncontaminated ionized water with membranes fired at 800.0 °C, 900.0 °C, 1000.0 °C, 1100.0 °C, and 1150.0 °C. The graph shows that volume of water filtered increases with an increase in the filtration time. The gradient of these plots gives rise to the flow rate. The plots show that the flow rate decreased with an increase in firing temperature; confirming that increasing firing temperature reduced porosity.

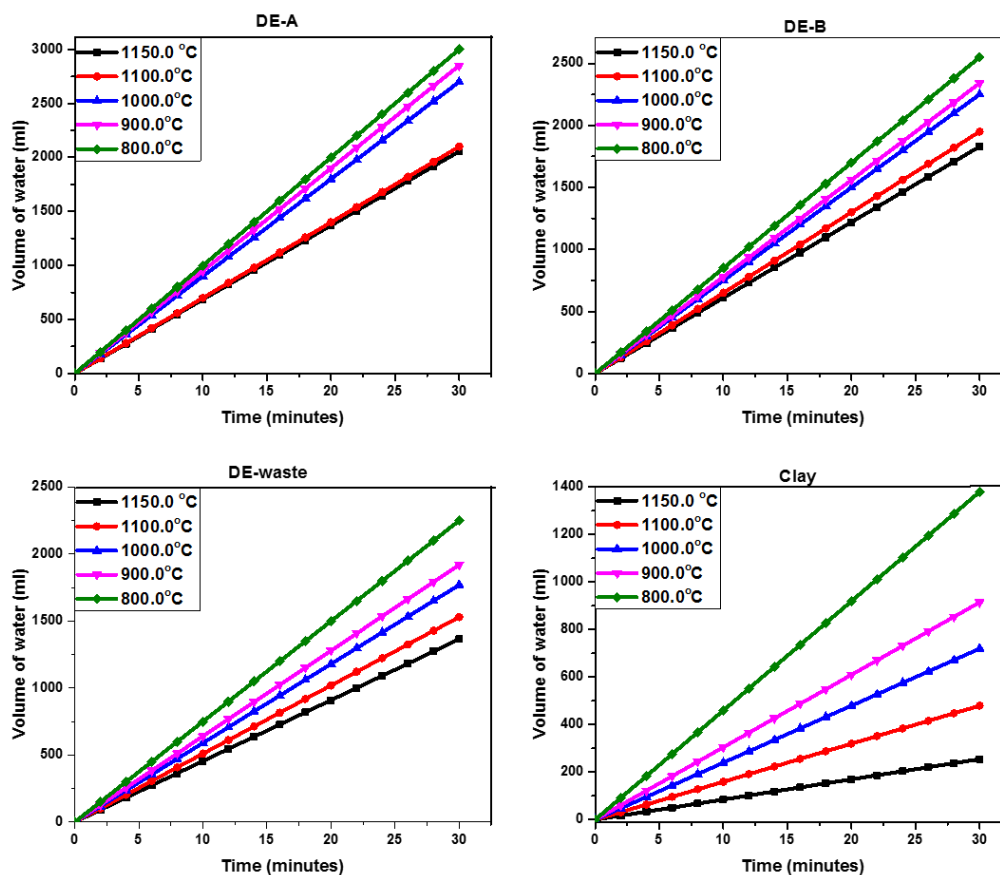


Figure 5.30: The plot of the volume of water filtered against the time taken to filter water for membranes fabricated with *Basella alba* and fired at 800.0 °C, 900.0 °C, 1000.0 °C, 1100.0 °C, and 1150.0 °C

When the permeability was compared with porosity for the membranes fabricated with *Basella alba* and fired at 900.0 °C - Figure 5.31, the results show that membranes that reported high porosity equally showed high permeability. This is because both permeability and porosity are affected by the same parameters such as pore size and pore connectivity.

Figure 5.30 (b), however, shows that carbon activating the membranes reduced the porosity of the membrane to 0.26, 0.24, 0.2, and 0.19 for DE-A, DE-B, DE-waste, and clay respectively; permeability was also reduced to 129.2 mD, 127.4 mD, 124.3 mD, and 120.0 mD for DE-A, DE-B, DE-waste, and clay respectively. The increased porosity and permeability at the same time indicated that the pores were continuous.

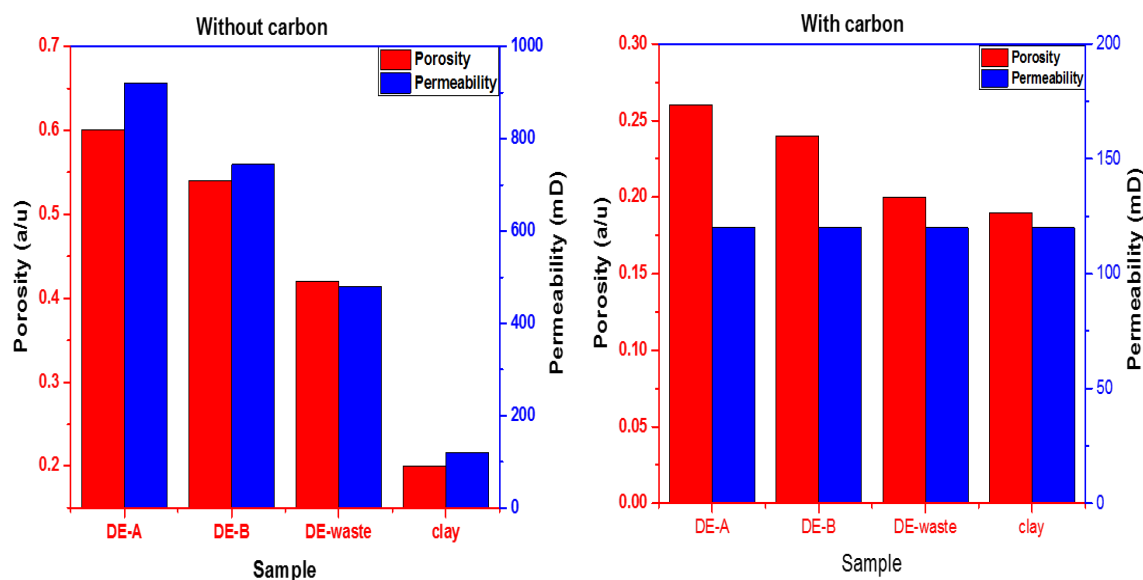


Figure 5.31: The column chart showing the porosity of membranes from DE-A, DE-B, DE-waste, and clay fabricated with *Basella alba* and fired at 900.0 °C. In (a) the membranes are without carbon and in (b) the membranes are carbon activated

The flow rates and volume of water contaminated with 10^3 CFU/ml *E.coli* and filtered with DE-A, DE-B, DE-waste, and Potter's clay membrane fired at 900.0 °C were plotted against time as shown in Figure 5.32. It was observed that flow rates are highest at the beginning of filtration because the pressure of water was highest. As the water continues to discharge a lower pressure was attained at its base resulting in a lower flow rate. Similar observations were reported by (Nigay *et al.*, 2019). It was further noted that the DE-based membrane exhibited relatively higher flow rates than those of the Potter's clay filters, a difference attributed to the higher porosity possessed by the DE membranes as reported in Section 5.6.1. This porosity was caused by the high number of pores in DE membranes attributed to the presence of diatomaceous structures visible in these membranes (See Figures 5.33 (a) and (c)). Among the diatomaceous membranes, DE-waste recorded the lowest flow rates as a result of its limited diatom-like structure. Figure 5.33 (c) confirms the absence of diatomaceous structures in membranes of DE-waste membranes.

Figure 5.32 also shows that the flow rate, i.e., the volume of water discharged from the membranes per unit time, is initially quite high, especially for the diatomaceous membranes, in the first two hours but then reduces to a nearly a constant value as the time of filtration progresses. Even if DE-waste membranes did not discharge as much as pure DE-based membranes they are 55.5% better than conventional ceramic filters made from Potter's clay. From this result, the DE-waste membranes recorded higher flow rates, i.e., had a higher filtration rate than Potter's clay. It is established that the DE-waste has not been applied in water filtration yet if used these membranes would be preferred to clay-based membranes among the household users. Thus DE-waste should be considered in water filtration.

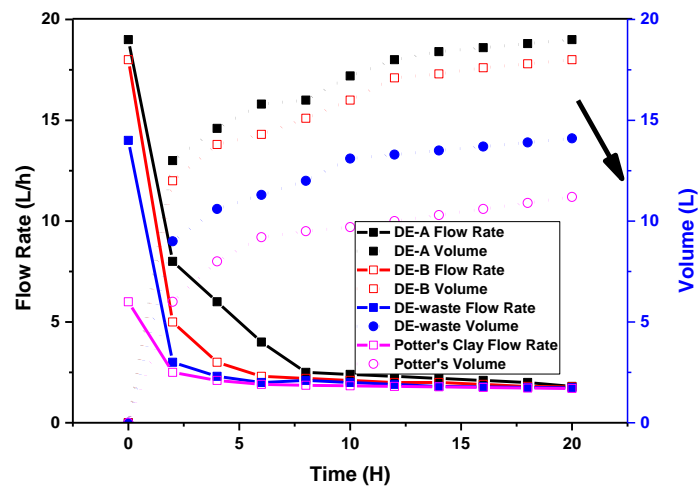


Figure 5.32: The plot of flow rates and volume of water against time. The water was contaminated with 10^3 CFU/ml *E.coli* and filtered with DE-A, DE-B, DE-waste, and Potter's clay membrane fabricated by *Basella alba* and fired at 900.0°C

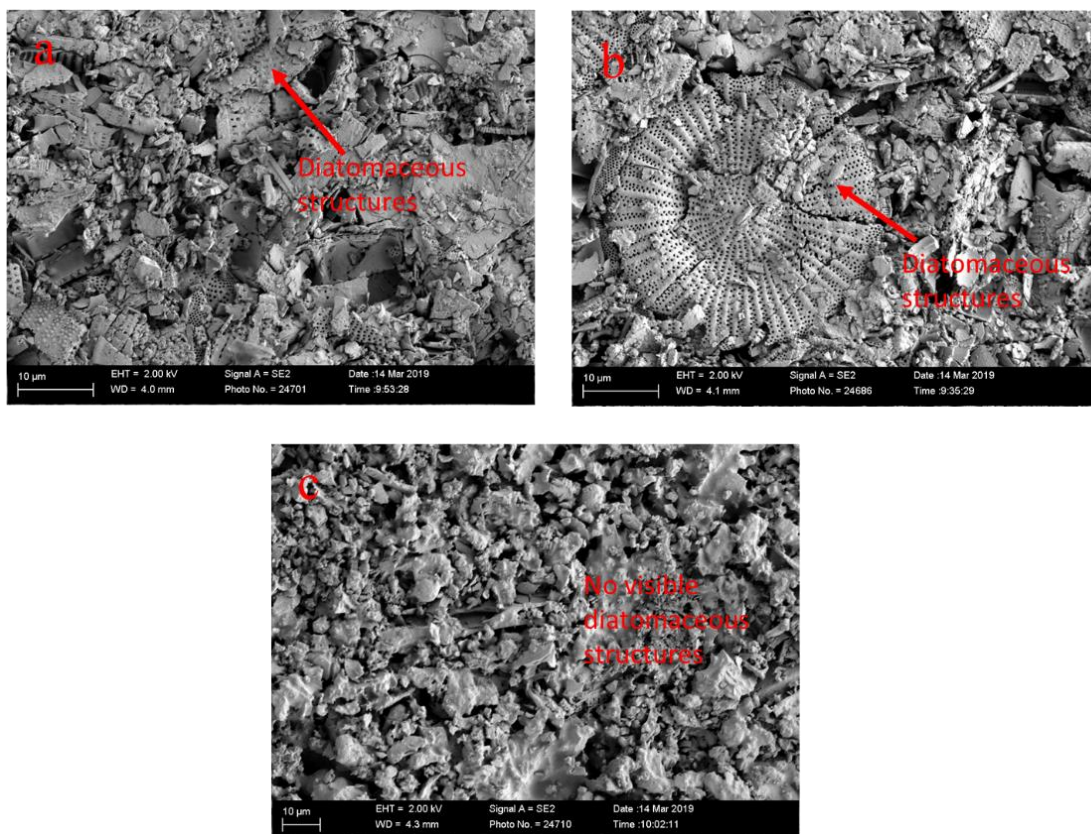


Figure 5.33: Micrograph of DE-A (a), DE-B (b), and DE-waste (c) membranes fired at 850.0 °C. The DE-A and DE-B membranes are characterized by diatomaceous structures but DE-waste lacks such structures

5.7.2 Filtration Efficiency

Figure 5.34 shows the bar chart of the filtration efficiency of the membranes fabricated with DE-A, DE-B, DE-waste, and clay in filtering water contaminated with *E.coli*, NaF, and Rotavirus. It was found that all DE membranes fabricated were able to decontaminate water due to the electrostatic forces that exist between the filter and the contaminant. All membranes were able to remove more than 99.9% of *E.coli* whose cylindrical size is of the order 1.0 μm - 2.0 μm. Therefore *E.coli* could not pass through the nanopores of the membranes. It was also observed that membranes fabricated from plain ionized water (no binder added) were only able to adsorb 56.8% to 58.3% of NaF and Rotavirus respectively. However, when organic binders were used, the deflouridation efficiency in DE-A membranes improved to 85.6%; and 89.2% in DE-B. The removal of Rotavirus on the other hand improved to 95.5%, and; 98.3% in DE-A and DE-B membranes respectively. The enhanced efficiency was attributed to reduced porosity causing most of the contaminants to either remain on the surface of the filter, particularly in the cases of *E.coli* that were bigger than the pores of the filters. Samples fabricated with DE-B showed higher efficiency than that of DE-

A because they were characterized by lower porosity. Membranes made from *Basella alba* and DE-B were able to defluoridate and remove Rotavirus from water at the efficiency of 89.4% and 98.3% respectively.

The decontamination of water was attributed to the adsorption of contaminants which was possible due to the cristobalite and diatom structures of the membranes. The cristobalite octahedra structure has a capacity for cation exchange which enhances contaminant adsorption (Farid, 2014). The same structure enhances contaminant adsorption through intra-particle diffusion. Apart from the lattice structures, the membranes also had diatomaceous structures with large surface area, adsorption capacities, and ion exchange abilities which aid in decontaminating the water (Izuagie *et al.*, 2016a). The firing of the membrane ruptures the Si-O-Al bond leaving Al^{3+} to attract contaminants to its site. It was also noted that the fabricated membranes exhibited the lowest purification efficiency of water contaminated with NaF. This is because for defluoridation to take place the OH group had to be exchanged to the ceramic membranes result in the decrease of water pH (Bhatnagar *et al.*, 2011). The chemical reaction slows down the adsorption capabilities.

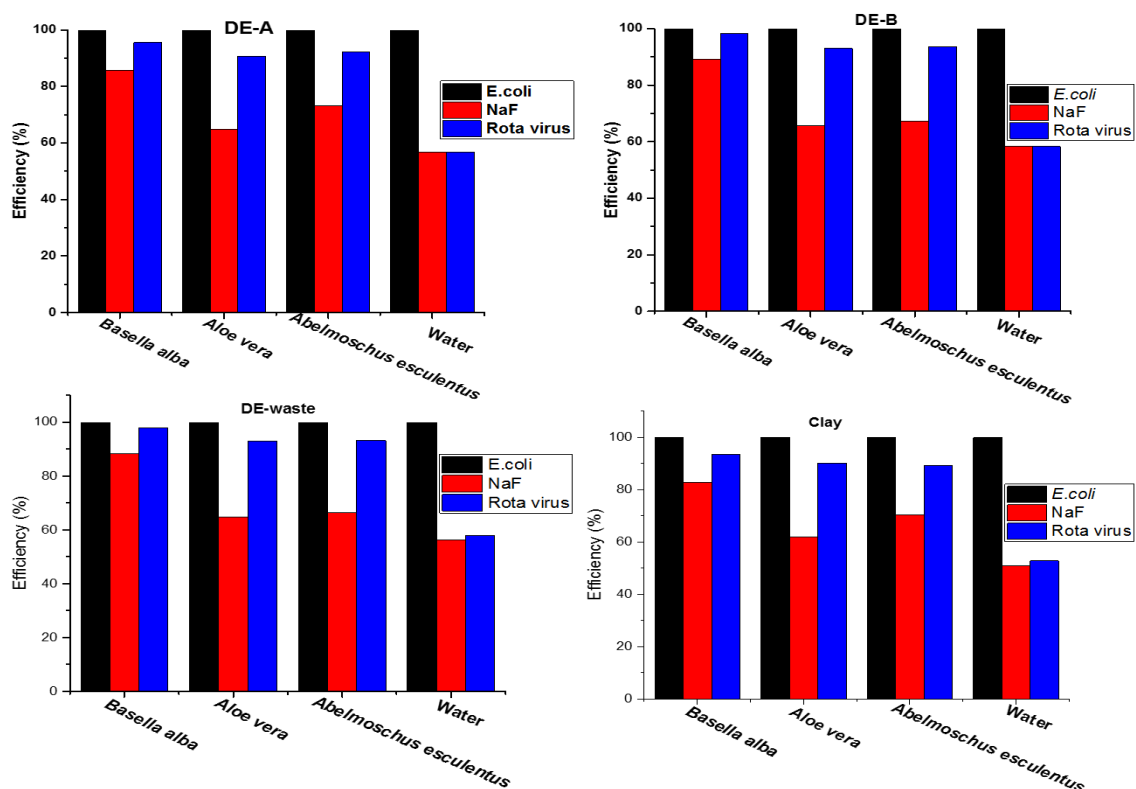


Figure 5.34: The bar chart of the percentage filtration efficiency of the 0.48 porosity membrane fabricated with DE-A DE-B, DE-waste, and clay combined with different binders:

Abelmoschus esculentus, *Aloe vera*, and *Basella alba* in filtering water contaminated with *E.coli*, NaF, and Rotavirus

5.7.3 Models

The flux of water contaminated with the three contaminants; *E. coli* (10^3 CFU/ml), Rotavirus (10^3 viral particle/ml), and NaF (1.0 g/ml) and filtered with DE-A membrane fired at 900.0 °C were modeled with the complete blocking (Equation (5.7)), standard blocking (Equation (5.8)), intermediate blocking (Equation (5.9)), and cake filtration (Equation (5.10)) as shown in Figure 5.35.

$$J = J_o (1 - K_b V_A) \quad 5.7$$

$$J = \left(1 - \frac{K_s V_A}{2}\right)^2 \quad 5.8$$

$$J = J_o \exp(-K_i V_A) \quad 5.9$$

$$J = J_o \frac{1}{1 + K_c V_A} \quad 5.10$$

where J_o is the initial flow rate per unit of filtration area, V_A is the filtrate volume per unit area, K_b is the coefficient of blocking in the complete blocking model models, K_s is the blocking coefficient in the standard blocking model, K_i is the coefficient of intermediate blocking model models, and K_c is the occlusion coefficient in the cake-filtration model.

All the plots showed linear fit as predicted in the literature (Iritani and Katagiri, 2016). The contaminants reach the membrane surface due to gravitational pressure and convection current. As shown in Table 5.11, for water contaminated with the three contaminants, the plots did not show good fits as the values R^2 of all four models were less than 0.9. This can be attributed to having different sizes of contaminants. On the other hand, the models showed better fits for water contaminated with single contaminants as shown in Figures 5.36, 5.37, and 5.38, and Table 5.11. Water contaminated with *E. coli* showed the best fit with values of R^2 around 0.95 because *E. coli* is larger than the pore size consistent with the assumptions in the theory. This was followed by water contaminated with Rotavirus which showed R^2 values of approximately 0.94. Rotavirus is smaller than the pore size of the membrane reported in

this work. As a result, it gets deposited on the pore walls reducing the pore size, cross-sectional area, and adsorption surfaces where the contaminants could be deposited. The fitting of the models to the results for water contaminated with NaF was noted to be not as good as in the cases of water contaminated with either *E. coli* or Rotavirus. This could be attributed to the fact that some dissolved fluoride could not be adsorbed on the membrane surfaces. These findings are consistent with the comparatively lower filtering efficiency for water contaminated with NaF as reported in Section 5.7.2. The complete blocking and intermediate blocking models give better predictions for water contaminated with *E. coli*, and with all the contaminants as shown in Table 5.10. This can also be attributed to the size of *E. coli* which is bigger than most of the membrane pores. Initially, the flow rate is high but as filtration progresses the flow rate decreases due to blocking. Meanwhile, standard blocking plots were best fitted by data from water contaminated with NaF and Rotavirus. This is because these contaminants are smaller than the pores and are adsorbed on pore walls reducing the pore diameter gradually as the filtration progresses. The resistance to the flow rate was found to vary with the type of contaminant as shown in Table 5.10. Samples with different contaminants reported poor correlation and fit due to their different sizes. Water contaminated with *E. coli* also showed high resistivity in all models while fluoridated water showed the lowest resistivity.

Generally, none of the fittings showed fits of $R^2 = 0.99$ because the pores did not have uniform diameters, some pores were non-continuous and antiparallel as postulated in the models (Hatori and Suzuki, 2021; Iritani and Katagiri, 2016). The membrane resistance could also have caused the low correlation reported in this work.

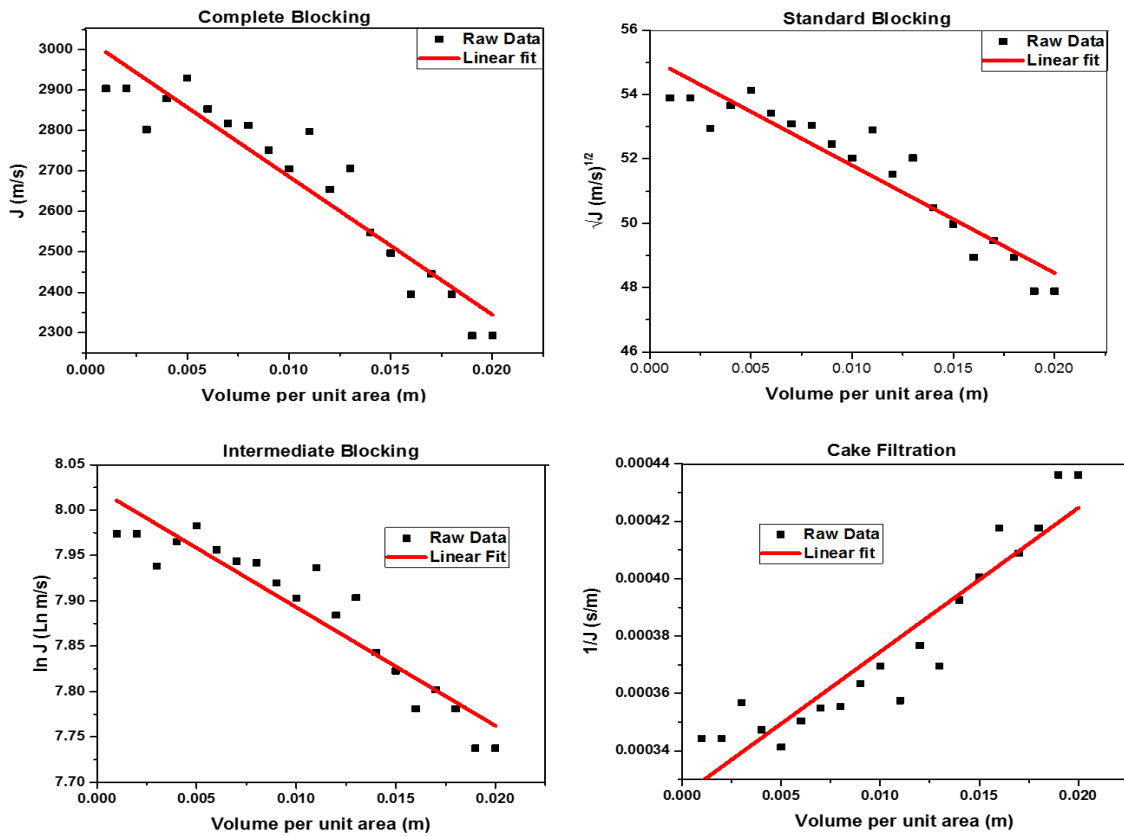


Figure 5.35: The models of complete blocking, standard blocking, intermediate blocking, and cake filtration are represented graphically using data derived from filtering water contaminated with *E.coli*, 10^3 CFU/ml, 10^3 viral particles, and 1.0 g/ml

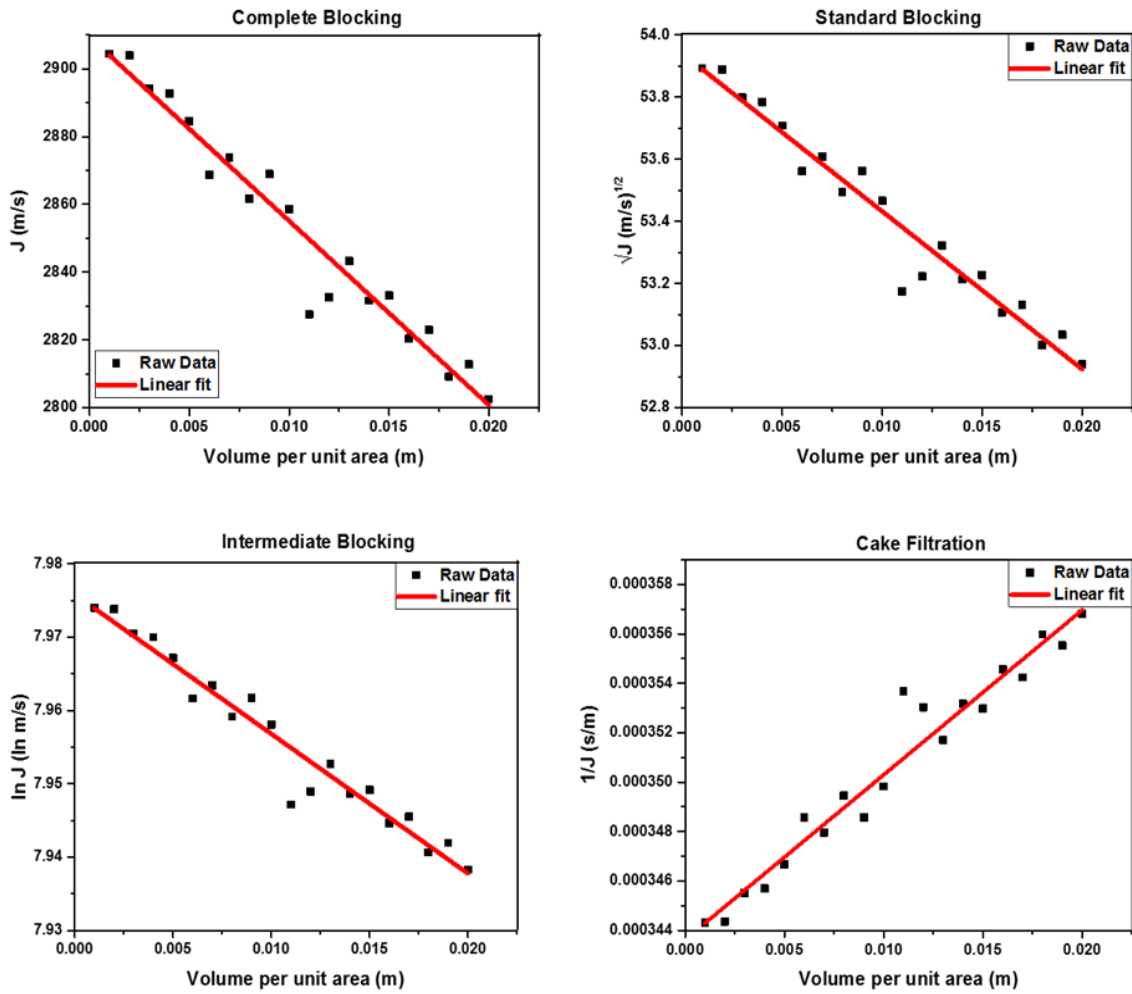


Figure 5.36: The models of complete blocking, standard blocking, intermediate blocking, and cake filtration are represented graphically using data derived from filtering water contaminated with *E. coli*, 10^3 CFU/ml

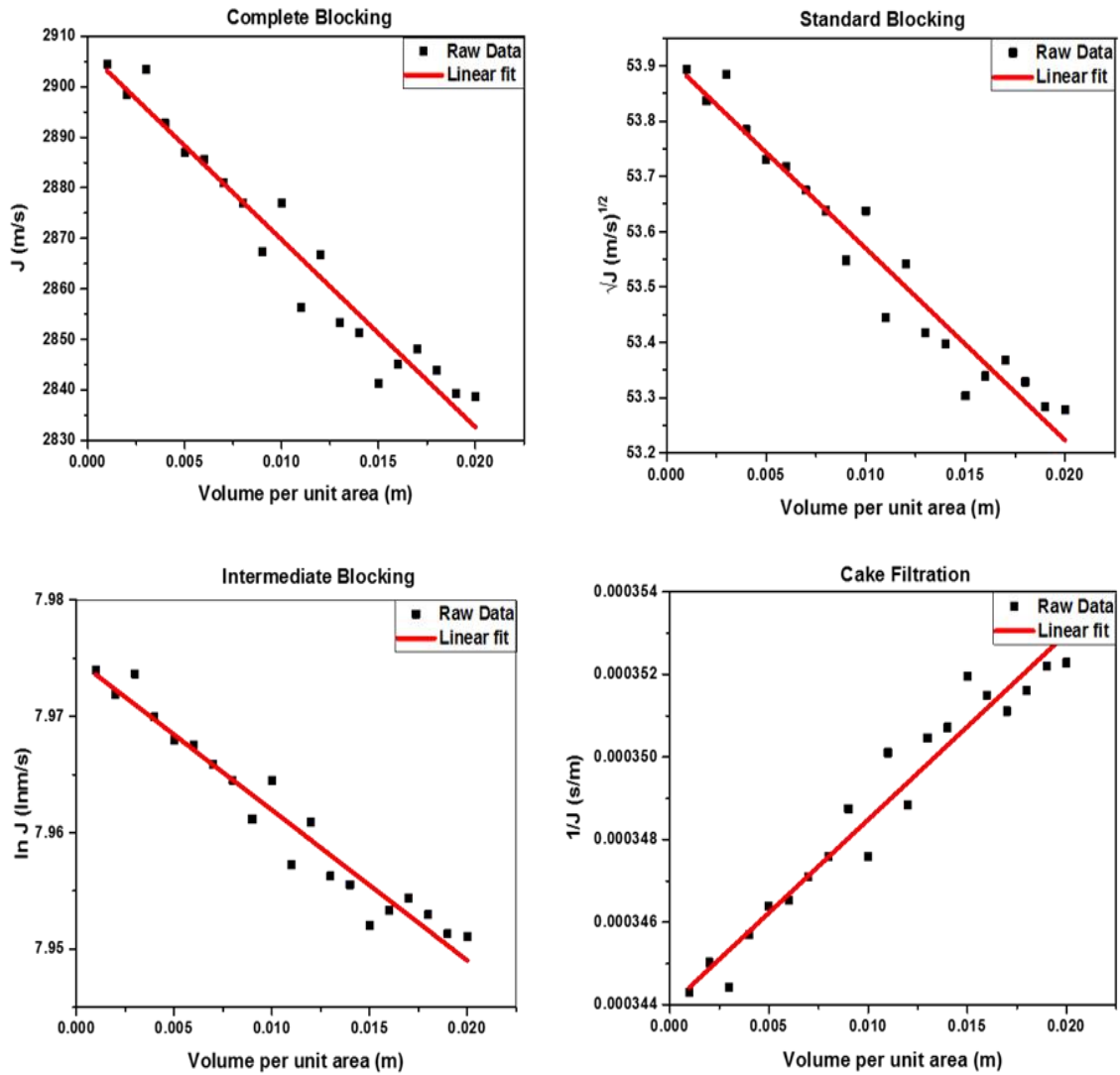


Figure 5.37: The models of complete blocking, standard blocking, intermediate blocking, and cake filtration are represented graphically using data derived from filtering water contaminated with Rotavirus, 10^3 viral particles/ml

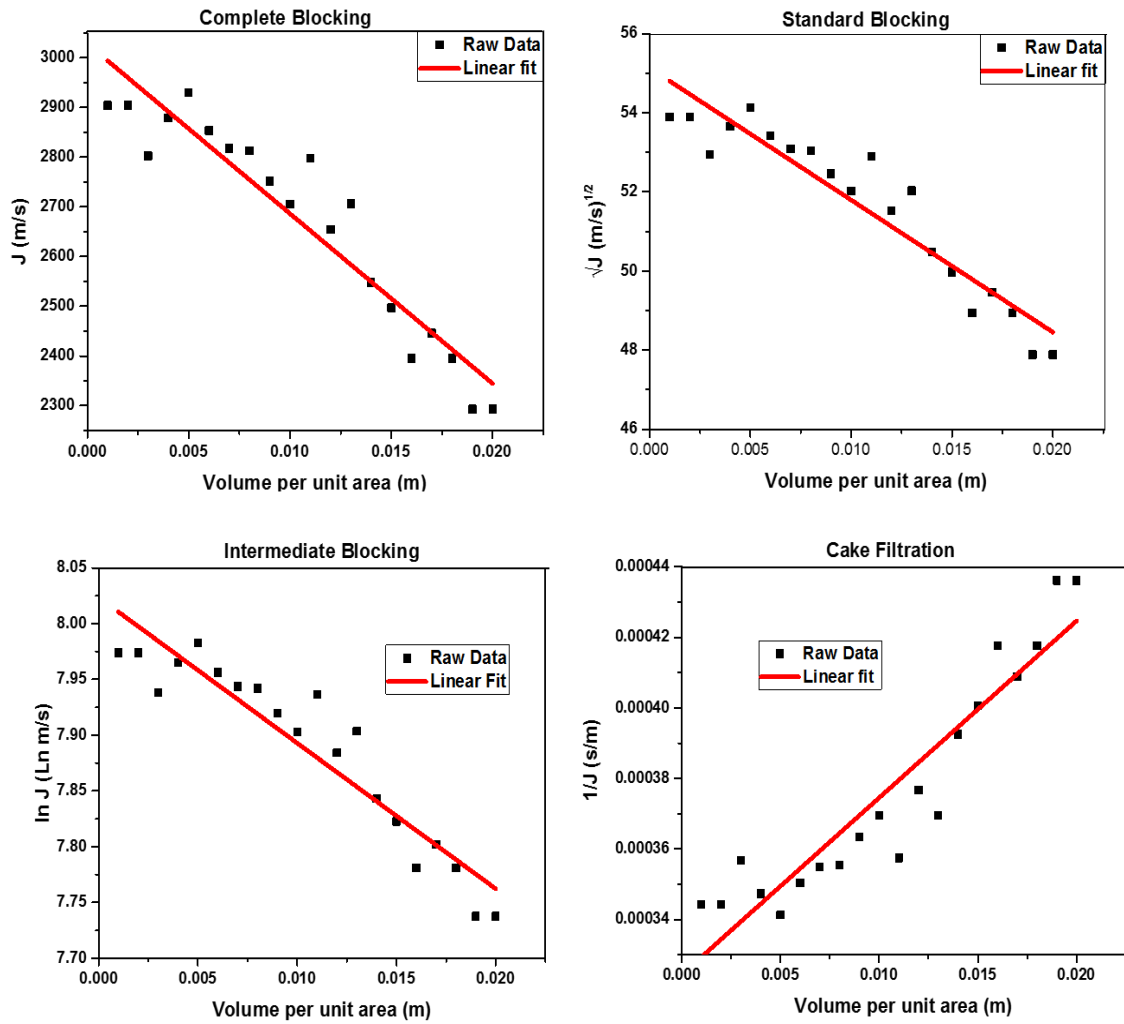


Figure 5.38: The models of complete blocking, standard blocking, intermediate blocking, and cake filtration are represented graphically using data derived from filtering water contaminated with 5 mg/ml, Sodium fluoride solution

Table 5.11: The fitting parameters of Complete Blocking, Cake Filtration, Intermediate Filtration, and Standard Filtration Models developed from water contaminated with *E. coli*, Rotavirus, and sodium fluoride

Models	Intercept	Gradient	R Squared	Pearson correlation	Blocking Resistance
All Contaminants					
Complete blocking	3028.3	-34189.3 s ⁻¹	0.8923	-0.9446	34189.3 s ⁻¹
Cake Filtration	3.2 x 10 ⁻⁴	5.0e ⁻³	0.8737	0.9347	5.0e ⁻³ s
Intermediate Filtration	8.0	-13.1	0.8837	-0.9401	13.1 ms ⁻¹
Standard filtration	55.1	-334.0	0.8881	-0.9424	90.0 s ^{-1/2}
<i>E. coli</i>					
Complete blocking	2909.4	-5432.9 s ⁻¹	0.95220	-0.9758	5432.9 s ⁻¹
Cake Filtration	6.7 x 10 ⁻⁴	3.4e ⁻⁴	0.9515	0.9755	3.4e ⁻⁴ s
Intermediate Filtration	8.0	-1.9	0.9519	-0.9756	1.9 ms ⁻¹
Standard filtration	53.9	-50.8	0.9517	-0.9756	13.8 s ^{-1/2}

Rotavirus					
Complete blocking	2906.9	-3711.4	0.9491	-0.9742	3711.4 s ⁻
Cake Filtration	4.0 x 10 ⁻⁴	4.5e ⁻⁴	0.9492	0.9745	4.5e ⁻⁴ s
Intermediate Filtration	8.0	-1.3	0.9494	-0.9737	1.3 ln ms ⁻
Standard filtration	53.9	-34.6	0.9497	-0.9748	9.4 s ^{-1/2}
Sodium Fluoride					
Complete Blocking	11667.9	-28779.1	0.9276	-0.9632	28779.1 s ⁻
Cake Filtration	8.6 x 10 ⁻⁴	2.2e ⁻⁴	0.9238	0.9611	2.2e ⁻⁴ s
Intermediate Filtration	9.4	-2.5	0.9258	-0.9622	2.5 ln ms ⁻
Standard filtration	108.0	-135.1	0.9288	-0.9627	0s ^{-1/2}

5.7.4 Blockage after Number of Runs

When the membranes were used to filter water repeatedly the flow rate reduced as the number of runs increased as shown in Figure 5.39. This was caused by reduced porosity as some pores were blocked by the contaminants while at times the pore sizes were reduced due to contaminants getting adsorbed on the walls of the pores. Membranes fabricated from DE-A with *Basella alba* as the binder exhibited the highest flow rate in filtering all the contaminants separately and even when the contaminants were combined because of their high porosity. At the same time, DE-A membranes took the longest time to get clogged. It was also observed that the flow rate reduced faster as the number of runs increased while filtering all the contaminants combined than when filtering each contaminant separately. Moreover, the flow rate reduced most in membranes that filtered *E. coli* when each contaminant was filtered separately. This was attributed to the large size of this contaminant which makes it hard to pass through the nanopores of the membrane which were confirmed by the models discussed earlier in this Section.

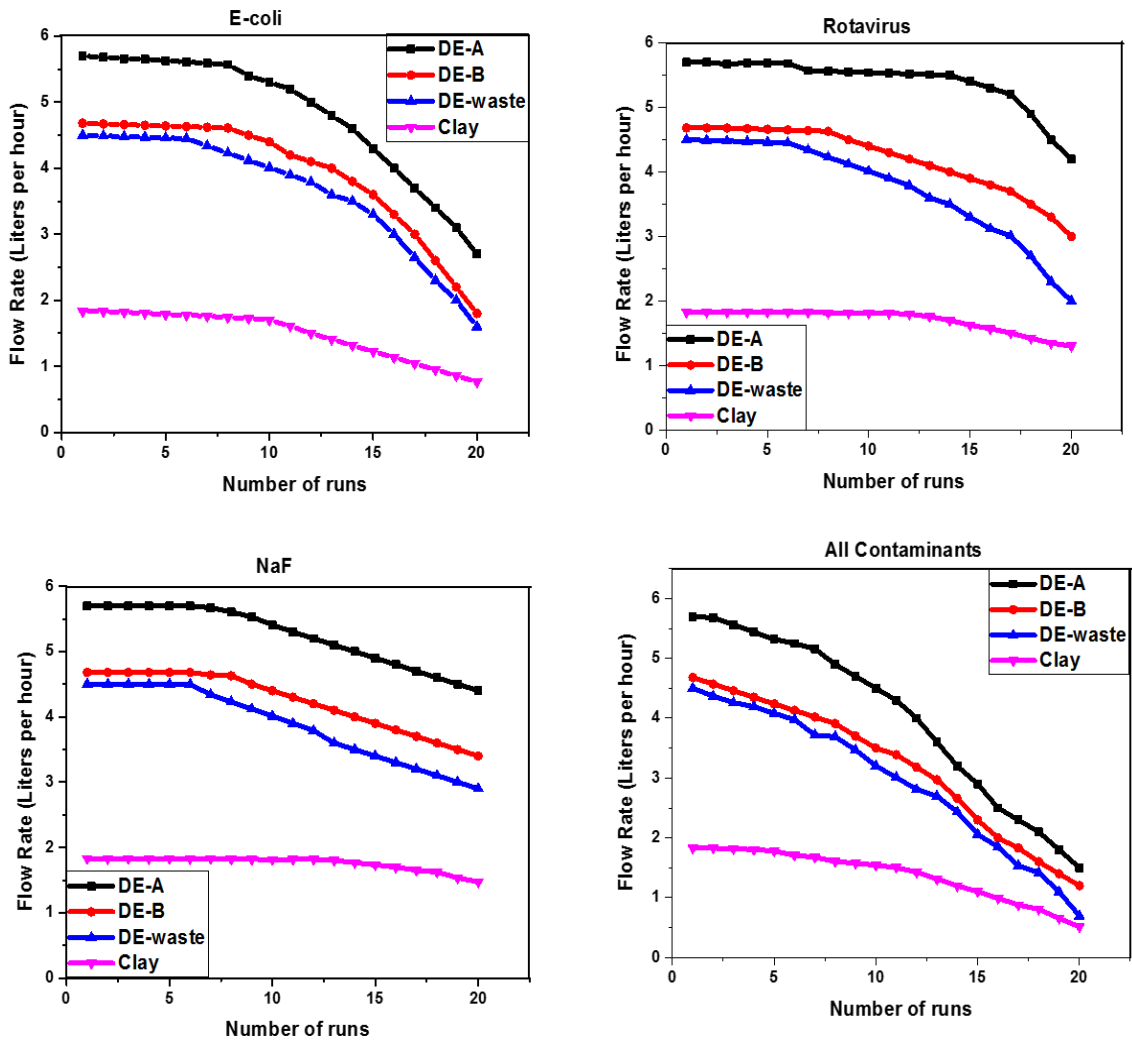


Figure 5.39: Plot of flow rate against the number of runs of DE-A, DE-B, DE-waste, and clay membranes fabricate with *Basella alba* and fired at 900.0 °C

When the flow rate of water contaminated with the three contaminants was fitted with a parabolic fit it was predicted that by the twentieth run, the flow rate was around one liter per hour indicating that the membranes need to be regenerated regularly to maintain their efficiency.

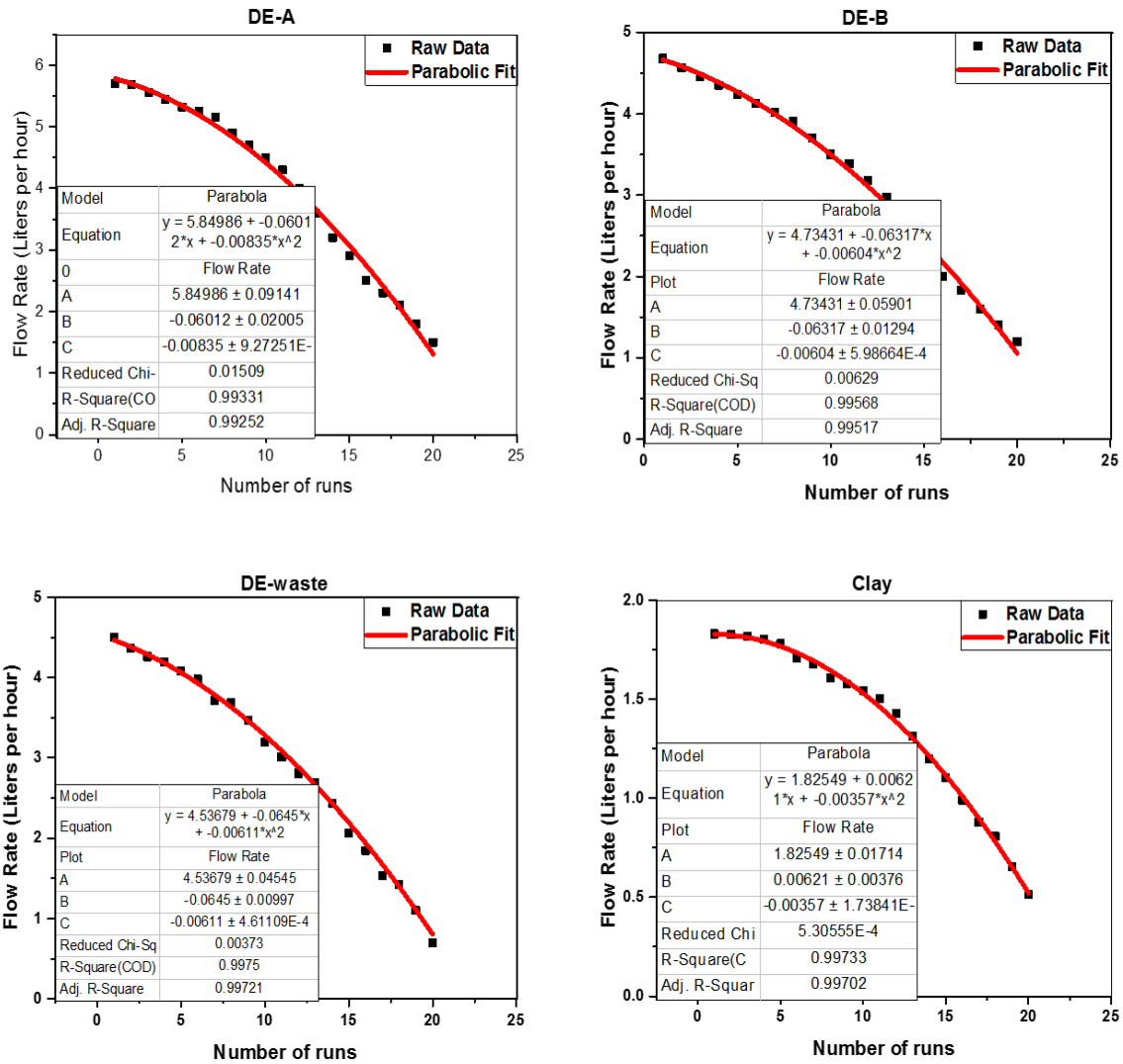


Figure 5.40: The plot of flow rate against the number of runs for DE-A membranes fabricated with *Basella alba* and fired at 900.0 °C

5.8 Purification Using Magnetic Fields

5.8.1 pH of Water

Figure 5.41 shows the pH of different water solutions circulated in the presence and absence of the 0.8 T static magnetic field at an ambient temperature of 24.0 °C. The pH of the ionized water decreased with an increase in the circulation time because the static magnetic field made the water acidic by enhancing its OH bond (Chang and Weng, 2006; Hosoda *et al.*, 2004). The pH was found to reduce most in fluoridated water because NaF forms Na⁺ and F⁻ ions in water aligned themselves in the presence of the external magnetic field causing the decreased pH. *E. coli* on the other hand produced acidic wastes (Shiga toxin) that reduced the pH of its solution (Frank *et al.*, 2011; Tarr *et al.*, 2005; Paton and Paton, 1998). However, *E.*

coli reused some of the acidic wastes in proton form for transportation of minerals, which explains why the observed slope of pH is lower than the one observed in NaF. The pH of the water solution containing Rotavirus coincided with the one of ionized water as shown in Figure 5.39 because the multiplication of RNA viral particles involves the mechanism of transporting protein which leads to the build-up of viral proteins in viroplasm (Silvestri *et al.*, 2004) and does not affect the pH of its surrounding. On the whole, a static magnetic field was found to alter the pH of the water just as was reported in the literature (Fathi *et al.*, 2006).

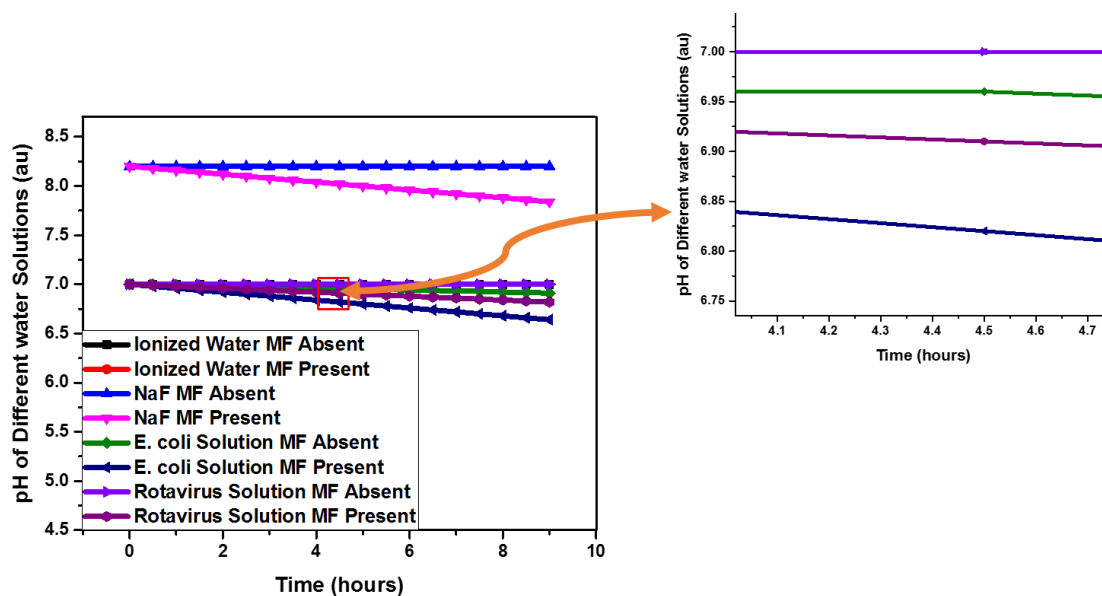


Figure 5.41: The pH value of different water solutions circulated in the presence and absence of a 0.8 T static magnetic field at an ambient temperature of 24.0 °C

5.8.2 Effect of Time

The replication curves of *E. coli* and Rotavirus at the ambient temperature of 24.0 °C are shown in Figure 5.42. The replication of *E. coli* was found to increase with an increase in circulation time because the cells of the bacteria subdivide continuously to form new cells (Trueba and Koppes, 1998). The presence of a static magnetic field slowed down the replication of the bacteria because the production of the oxygen free radicals in water by magnetic fields made the water slightly acidic by enhancing the hydrogen bond and killing the pathogens (Pang and Deng, 2008). In the presence of a magnetic field, the molecules aligned themselves to the applied magnetic field (Kurzeja *et al.*, 2013), which in turn affected the embedded ion channel altering their activation kinetics (Kurzeja *et al.*, 2013; Rosen, 1993). Furthermore, the magnetic field affected the behavior of the long-lived ionic quantum states causing an imbalance in ion-protein stability which resulted in the death of pathogens (Ji *et*

al., 2009b). The replication of Rotavirus also increased with time due to similar reasons and the presence of the static magnetic field also slowed down its multiplication. It is this same acidity that influenced the pH of the fluoridated water observed earlier in Figure 5.40. The decrease in the concentration of the contaminants can also be attributed to the magnetic memory and their magnetic susceptibility. When the magnetic susceptibility of a certain material exceeds a certain level the organism may die or show growth reduction due to particle aggregation and change in pH of water that causes (Lebkowska *et al.*, 2011; Lychagin, 1974).

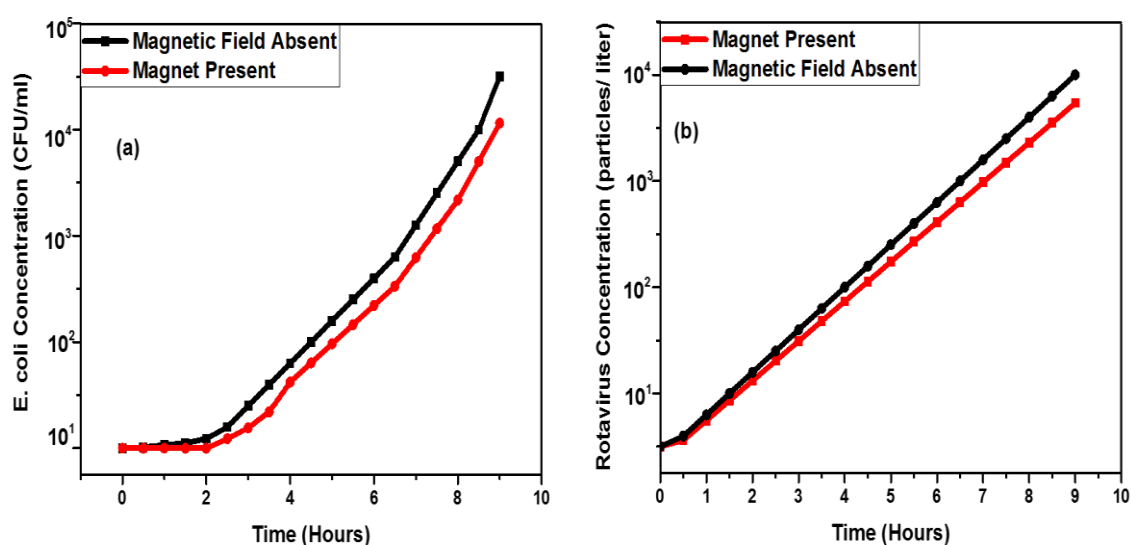


Figure 5.42 The replication curves of (a) *Escherichia coli*, (b) and *Rotavirus Pathogens* in the presence and absence of the static magnetic field at an ambient temperature of 24.0 °C

5.8.3 Effect of Temperature

Figure 5.43 shows the concentration of *E. coli* (Figure 5.41(a)), *Rotavirus* (Figure 5.41(b)), and sodium fluoride (Figure 5.41(c)) in the water under the magnetic field of 0.8 T. The water was flowing at a flow rate of 2.0 ml/s and was at different temperatures. An increase in temperature increased the enzyme activities which in turn increased the protein activities essential for the *E. coli* growth increased; which explains why the replication of the bacteria increased continuously from 16.0 °C to 37.0 °C as shown in Figure 5.41(a). However, from 37.0 °C to 40.0 °C the protein phases became saturated and there was no increase in the number of bacteria when the temperature of the water was increased because the activities of the bacteria are enzyme sensitive. As shown in Figure 5.41(b), the growth of *Rotavirus* was found to decrease with an increase in temperature just as was reported in the literature (Atchison *et al.*, 2010). An increase in the ambient temperature caused the outer envelope of

the virus to melt to a liquid phase thereby slowing down the multiplication of the virus. This liquid phase allowed other elements of water to mix with it causing the death of the virus. On the other hand, an increase in temperature increased the pH of fluoridated water as shown in Figure 5.41(c) because more and more NaF was dissolved in water and increased its pH.

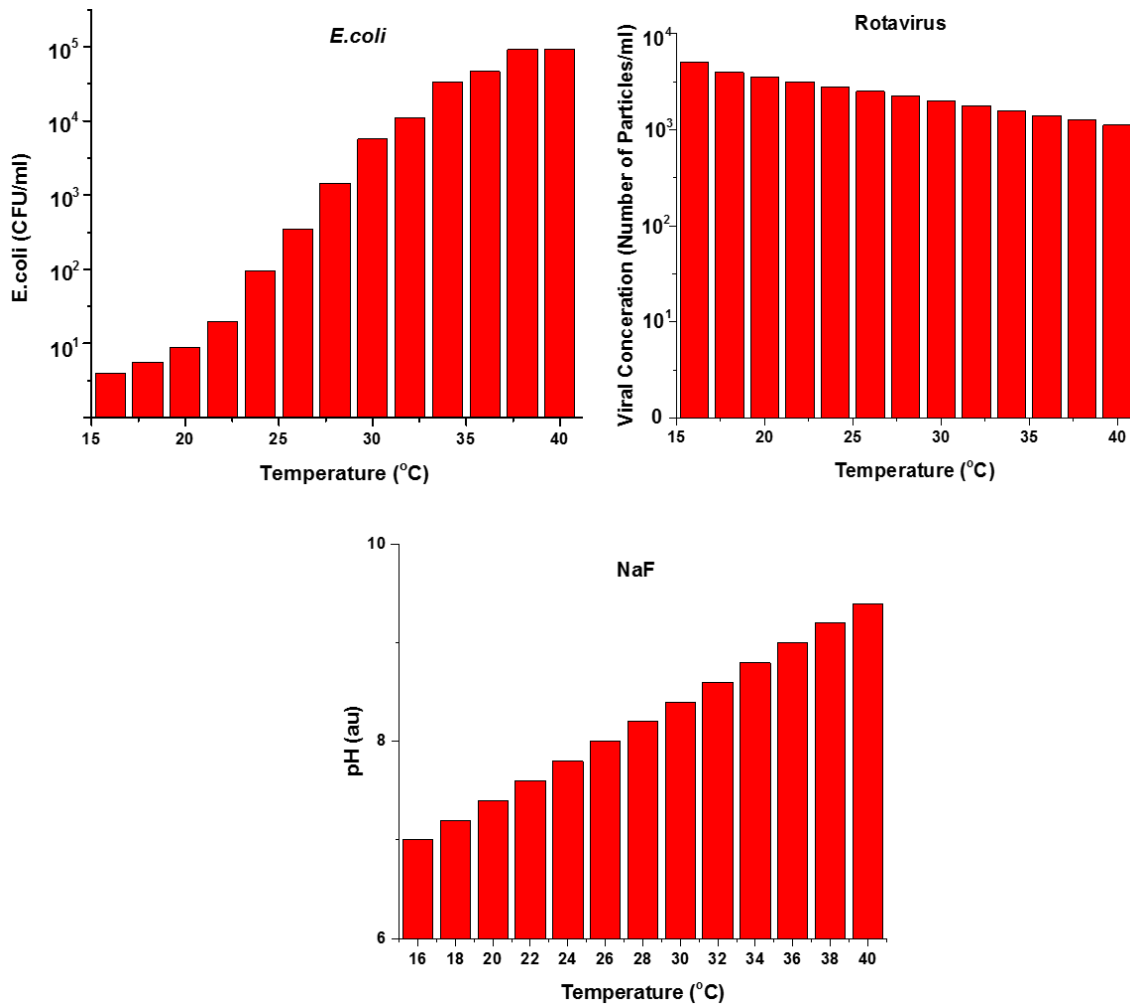


Figure 5.43 The variation of (a) *E. coli* concentration, (b) Rotavirus concentration, and (c) pH of NaF solutions under a 0.8 T magnetic field with the flow rate of 2.0 ml/s and varying temperature

5.8.4 Effect of the Flow Rate of Water

Table 5.11 shows the velocity of water contaminated with *E. coli*, Rotavirus, and NaF and the efficiency of purification obtained after a 0.8T magnetic field was used to purify the water. It was found that the flow rate of water had very little effect on the replication of *E. coli* and Rotavirus because diamagnetism changes observed in this work are initiated by atomic orbital states of the material and the applied static magnetic field. Hence the flow rate of water does not affect the replication of the living organisms (Ghoshal, 2007; Kittel, 2005).

Table 5.12: The velocity of contaminated water and the effective percentage efficiency obtained when a 0.8 T magnetic field was used to purify the water

Flow rate (ml/s)	The efficiency of purification of contaminants (%)		
	<i>E. coli</i>	Rotavirus	NaF
0.2	14.11	9.27	6.34
0.4	14.1	9.27	6.33
0.6	14.1	9.26	6.32
0.8	14.09	9.26	6.32
1.0	14.09	9.25	6.31
1.2	14.08	9.25	6.3
1.4	14.07	9.24	6.3
1.6	14.07	9.24	6.3
1.8	14.06	9.24	6.29
2.0	14.05	9.23	6.29

5.8.5 Magnetic Field Purification Efficiency

Figure 5.41 shows the plot of the efficiency of purification of water in a static magnetic field against the time used to purify the water at an ambient temperature of 37.0 °C. In the first five hours, the purification efficiency of *E. coli* and Rotavirus increases rapidly because the organisms had not adjusted to living with the effects of the magnetic field. These effects include reduced pH in water, instability in the ion-protein ratio in the embedded ions of the organism, and the change in the kinetics of the organisms' stability. Further, exposure to the magnetic fields allowed the pathogens to adjust to these changes resulting in a reduced purification rate. Similarly, the defluoridation curve was steep during the five hours because most of the NaF molecules were not aligned to the applied static field. But as the fluoridated water continued circulating the molecules got fully aligned to the applied field causing increased acidity of water. Using the optimal temperature, (37.0 °C for *E. coli*, 16.0°C for Rotavirus, and 40.0 °C for NaF), and a time of 9.0 hours the magnetic field was able to reduce NaF by 14.1%, *E. coli* by 9.8%, and 7.1% Rotavirus. The concentrations of the contaminants after nine hours of purification were 8.6 mg/l, 4.1E⁵ CFU/ml, and 4.0E³ viral particles per liter of NaF, *E. coli*, and Rotavirus respectively. The above concentrations are way above the recommended levels for safe drinking water. *E. coli* and Rotavirus should be non-detectable in any 100.0 ml of drinking water as recommended by the World Health Organization and sodium fluoride should range from 0.5 mg/L to 1.0 mg/L. Thus, purification of water from the three contaminants to recommendable levels using a static magnetic field from permanent magnets was not achieved.

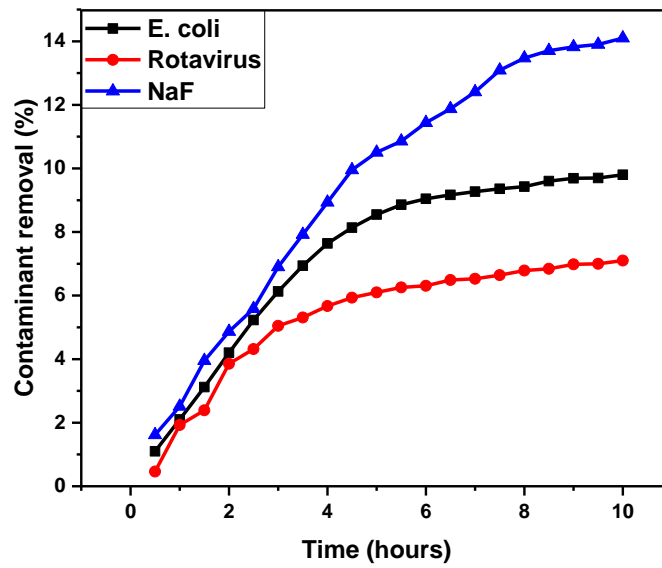


Figure 5.44. The plot of the contaminants' purification efficiency against time used to purify the water in a static magnetic field at an ambient temperature of 24.0 °C.

CHAPTER SIX: CONCLUSION

In this work, the investigation of the point-of-use water purification efficacy of fabricated diatomaceous earth-based filter membranes, and a static magnetic field has been done. The study established the following:

1. Diatomaceous earth (DE) samples mined at Kariandusi have diatom origins with dominant cylindrical-shaped and basket-shaped diatoms. The DE-waste is partially made up of diatoms of similar composition as the pure DE. Both the waste and pure DE are composed of more than 80.0% silica and more than 5.0% alumina making the waste an equal candidate in the fabrication of filtration membranes just like the pure DE materials. It was further established that both the raw DE-fired DE materials were crystalline and the crystallinity of DE increased with the increased firing temperature. The organic binders were mainly composed of metallic ions necessary for fluxing the organic matter that enhanced the binding ability of the green ceramics. The presence of carbohydrates and proteins in *Abelmoschus esculentus*, *Basella alba*, and *Corchorus esculentus* made them viscous but *Aloe vera* lost its viscosity upon boiling.
2. The green ceramics were found to shrink upon drying with Potter's clay posting the highest linear drying shrinkage of 5.0%. The bulk density of the green ceramics also improved by 7.3% in DE-A, 8.5% in DE-B, 4.2% in DE-waste, and 6.0% in Potter's clay. Linear firing shrinkage equally followed the same trend with the DE-B membrane fabricated from *Basella alba*.
3. The addition of binders improved the modulus of ruptures of the dried green ceramics and fired membranes with DE-B posting the highest values of MOR. Membranes made from *Basella alba* had the highest MOR with a percentage increase of 175.1%, 61.8% 158.0%, and 45.1% in DE-A, DE-B, DE-waste, and Potter's clay respectively
4. The morphological characteristics of the membranes were much affected by the firing temperature. High firing temperatures above 1000.0 °C affected the pore morphology resulting in reduced porosity with DE-based membranes showing sphere-like and oblate-like pores nanopores.
5. Consequently, the filtrate flow rate was found to vary with firing temperature and the material used to fabricate the membranes. DE-based membranes reported high flow rates than clay-based membranes. All membranes were able to remove more than 99.9% of *E. coli*. However, the membranes fabricated from plain ionized water were only able to

adsorb 56.8% to 58.3% of NaF and Rotavirus respectively. Fabricating membranes with 50.0% binder concentration improved the defluoridation and virus removal efficiency to 85.6%; 95.5%, and 89.2%; 98.3% for DE-A and DE-B membranes respectively. Membranes made from *Basella alba* and DE-B were able to defluoridate and remove Rotavirus from water at the efficiency of 89.4% and 98.3% respectively.

6. The DE-based powder had a higher content of silica than Potter's clay and produced highly porous and mechanically stronger membranes than the latter. The filtrate flow rate of DE-based membranes produced at the optimal temperature of 900.0 ranged between 4.0 to 6.0 liters per hour. Water filtration using DE-based membranes fitted complete blocking and standard models of filtration than cake and intermediate models of filtration
7. This work has shown that molasses can be used to fabricate activated carbon of 450.0 Kg/m³ bulk density. The presence of this activated carbon in DE-waste improved the bulk density (hence reducing the porosity) and MOR of the DE-waste fabricated membrane, which also exhibited improved decontamination efficiency of *E. coli*, Rotavirus, and NaF. Application of pressure of 50.00 kPa reduced the efficiency of the membranes in the adsorption of Rotavirus and NaF.
8. The use of a static magnetic field in water purification reduced NaF in water by 14.1% and slowed the growth of pathogens by 9.8% and 7.1% in the case of *E. coli* and Rotavirus respectively. However, this technique does not defluoridate, and purify water of *E. coli* and Rotavirus to recommended levels.

RECOMMENDATIONS FOR FURTHER WORK

This study has successfully shown that a static magnetic field should not be used independently in water purification but should be used in conjunction with other methods to purify water to recommendable levels. More research should also be done in this area to improve the efficiency of water purification using magnetic fields. Furthermore, an analysis should be carried out on the regeneration of DE-based membranes.

Acknowledgment

This work would not have been complete without the financial support of the International Science Program (ISP) and Gandhi Smarak Nidhi Foundation for providing the funds necessary for research. I also acknowledge East African Diatom Industries for providing the diatomaceous earth samples. All electron microscopy under this work was performed using the Thermo Scientific Apreo instrument housed at Rowan University. The instrument was funded by the U.S. National Science Foundation (contract #: CBET1625816). The SEM usage time was paid for by Rowan University under the REDI-SPARC initiative, and for this I am grateful. My sincere thanks go to the University of York for the three-month fellowship organized by the International Relations under the Three-Minute Thesis Program that improved our structural and morphological analysis. I sincerely acknowledge the staff and students of the University of Nairobi, Physics Department for the enabling conducive environment for this research. Finally, I am grateful to my supervisors Prof. Francis Nyongesa, Prof. Bernard Aduda, and Dr. Zephania Birech for the supervision, and mentorship.

I thank my mum Maayi Victorina Nekesa and Dad, Papa Maurice Simiyu who taught me the importance of education. When the pressure of work and study was too much their voices from the grave kept on reminding me to persevere and finish. My gratitude goes to my brother Zakayo for organizing the samples for me from the village. My sisters Phaustine, Florence, Emily, Evelyne, Prexides, and Janet, thank you for sending the foodstuffs from the village. I was able to spend a sleepless night because my stomach was full. For my Religious Superior, Sr. Louise Onyeanusi, HHCJ you were more than a mother, thank you for being patient with me even when it seemed like I will never complete the studies. My little sisters Mary Magdaline Mutuku, HHCJ, and Scholastica Kavita, HHCJ thank you for doing the extra duties I had in the convent. Your help allowed me to get extra time to do the research. Thanking my friends Godwin, Jacinta, Lilian, Sheila Bisach, Sheila Otieno, Brian, Gloria, Victor, and Obila for their moral and financial support. Finally, I thank the Almighty God for the good health of mind and body He granted me during the research.

REFERENCES

- Abdeljawad, D. (2019). Literature Review on the Effects of Water Fluoridation on the Human Health.
- Adham, S. S., Trussell, R. S., Gagliardo, P. F., and Trussell, R. R. (1998). Rejection of MS-2 virus by RO membranes. *Am. Water Works Assoc. J.* **90**, 130.
- Aduda, B. O., Nyongesa, F. W., and Obado, G. (1999a). Improving the green and fired fracture strength of a kaolinite ceramic using some vegetable syrup. *J. Mater. Sci. Lett.* **18**, 1653–1655.
- Aduda, B. O., Nyongesa, F. W., and Obado, G. (1999b). Improving the green and fired fracture strength of a kaolinite ceramic using some vegetable syrup. *J. Mater. Sci. Lett.* **18**, 1653–1655.
- Ahlawat, K. S. and Khatkar, B. S. (2011). Processing, food applications and safety of aloe vera products: a review. *J. Food Sci. Technol.* **48**, 525–533.
- Ahmed, J. A., Moturi, E., Spiegel, P., Schilperoord, M., Burton, W., Kassim, N. H., Mohamed, A., Ochieng, M., Nderitu, L., Navarro-Colorado, C., and others (2013). Hepatitis E outbreak, Dadaab refugee camp, Kenya, 2012. *Emerg. Infect. Dis.* **19**, 1010.
- Ahmed, S. (2017). A Low-Cost Drinking Water Treatment System For Slum Dwellers of Dhaka City, Bangladesh and Comparative Study with Commercially Manufactured Water Filters. PhD Thesis, Idaho State University.
- Akhtar, F., Rehman, Y., and Bergström, L. (2010). A study of the sintering of diatomaceous earth to produce porous ceramic monoliths with bimodal porosity and high strength. *Powder Technol.* **201**, 253–257.
- Akhtar, F., Vasiliev, P. O., and Bergström, L. (2009). Hierarchically porous ceramics from diatomite powders by pulsed current processing. *J. Am. Ceram. Soc.* **92**, 338–343.
- Akosile, S. I., Ajibade, F. O., Lasisi, K. H., Ajibade, T. F., Adewumi, J. R., Babatola, J. O., and Oguntuase, A. M. (2020). Performance evaluation of locally produced ceramic filters for household water treatment in Nigeria. *Sci. Afr.* **7**, e00218.
- Alaazi, D. A. and Aganah, G. A. (2020). Understanding the slum–health conundrum in sub-Saharan Africa: a proposal for a rights-based approach to health promotion in slums. *Glob. Health Promot.* **27**, 65–72.
- Al-Bastaki, N. (2004). Removal of methyl orange dye and Na₂SO₄ salt from synthetic waste water using reverse osmosis. *Chem. Eng. Process. Process Intensif.* **43**, 1561–1567.
- Alimi, F., Tlili, M., Maurin, G., and Gabrielli, C. (2009). Influence of magnetic field on calcium carbonate precipitation in the presence of foreign ions. *Электронная Обработка Материалов*.
- Ambashta, R. D. and Sillanpää, M. (2010). Water purification using magnetic assistance: a review. *J. Hazard. Mater.* **180**, 38–49.

- Amini, M., Mueller, K., Abbaspour, K. C., Rosenberg, T., Afyuni, M., Møller, K. N., Sarr, M., and Johnson, C. A. (2008). Statistical modeling of global geogenic fluoride contamination in groundwaters. *Environ. Sci. Technol.* **42**, 3662–3668.
- Andersson, C. A. (1996). Derivation of the Exponential Relation for the Effect of Ellipsoidal Porosity on Elastic Modulus. *J. Am. Ceram. Soc.* **79**, 2181–2184.
- Andrade, F. A., Al-Qureshi, H. A., and Hotza, D. (2011). Measuring the plasticity of clays: A review. *Appl. Clay Sci.* **51**, 1–7.
- Andrade, R. M., Jaques, N. G., Sousa, J., Dutra, R. P. S., Macedo, D. A., and Campos, L. F. A. (2019). Preparation of low-cost ceramic membranes for microfiltration using sugarcane bagasse ash as a pore-forming agent. *Cerâmica* **65**, 620–625.
- Annan, E., Agyei-Tuffour, B., Bensah, Y. D., Konadu, D. S., Yaya, A., Onwona-Agyeman, B., and Nyankson, E. (2018). Application of clay ceramics and nanotechnology in water treatment: A review. *Cogent Eng.* **5**.
- Annan, E., Mustapha, K., Odusanya, O. S., Malatesta, K., and Soboyejo, W. O. (2014). Statistics of flow and the scaling of ceramic water filters. *J. Environ. Eng.* **140**, 04014039.
- Arno, J. L. and Vermeulen, R. M. (2002). Fluorine abatement using steam injection in oxidation treatment of semiconductor manufacturing effluent gases. Google Patents.
- Ashby, M. F. and Medalist, R. F. M. (1983). The mechanical properties of cellular solids. *Metall. Trans. A* **14**, 1755–1769.
- Atchison, C. J., Tam, C. C., Hajat, S., Pelt, W. van, Cowden, J. M., and Lopman, B. A. (2010). Temperature-dependent transmission of rotavirus in Great Britain and The Netherlands. *Proc. R. Soc. B Biol. Sci.* **277**, 933–942.
- Attinti, R., Wei, J., Kniel, K., Sims, J. T., and Jin, Y. (2010). Virus'(MS2, ϕ X174, and Aichi) attachment on sand measured by atomic force microscopy and their transport through sand columns. *Environ. Sci. Technol.* **44**, 2426–2432.
- Augusto, P. A., Castelo-Grande, T., and Augusto, P. (2005). Magnetic classification in health sciences and in chemical engineering. *Chem. Eng. J.* **111**, 85–90.
- Bailey, H. L., Kaufman, D. S., Sloane, H. J., Hubbard, A. L., Henderson, A. C. G., Leng, M. J., Meyer, H., and Welker, J. M. (2018). Holocene atmospheric circulation in the central North Pacific: A new terrestrial diatom and $\delta^{18}\text{O}$ dataset from the Aleutian Islands. *Quat. Sci. Rev.* **194**, 27–38.
- Bailey, S. E., Olin, T. J., Bricka, R. M., and Adrian, D. D. (1999). A review of potentially low-cost sorbents for heavy metals. *Water Res.* **33**, 2469–2479.
- Baker, J. S. and Judd, S. J. (1996a). Magnetic amelioration of scale formation. *Water Res.* **30**, 247–260.
- Baker, J. S. and Judd, S. J. (1996b). Magnetic amelioration of scale formation. *Water Res.* **30**, 247–260.

- Baklouti, S., Chartier, T., and Baumard, J. F. (1997). Mechanical properties of dry-pressed ceramic green products: the effect of the binder. *J. Am. Ceram. Soc.* **80**, 1992–1996.
- Banks, D., Reimann, C., Røyset, O., Skarphagen, H., and Sæther, O. M. (1995). Natural concentrations of major and trace elements in some Norwegian bedrock groundwaters. *Appl. Geochem.* **10**, 1–16.
- Barré, P., Montagnier, C., Chenu, C., Abbadie, L., and Velde, B. (2008). Clay minerals as a soil potassium reservoir: observation and quantification through X-ray diffraction. *Plant Soil* **302**, 213–220.
- Barsoum, M. and Barsoum, M. W. (2002). “Fundamentals of ceramics.” CRC press.
- Bautista-Toledo, I., Rivera-Utrilla, J., Ferro-Garcia, M. A., and Moreno-Castilla, C. (1994). Influence of the oxygen surface complexes of activated carbons on the adsorption of chromium ions from aqueous solutions: effect of sodium chloride and humic acid. *Carbon* **32**, 93–100.
- Baylink, D. J., Duane, P. B., Farley, S. M., and Farley, J. R. (1983). Monofluorophosphate physiology: the effects of fluoride on bone. *Caries Res.* **17**, 56–76.
- Bello, O. S., Adegoke, K. A., and Oyewole, R. O. (2014). Insights into the Adsorption of Heavy Metals from Wastewater using Diatomaceous Earth. *Sep. Sci. Technol.* **49**, 1787–1806.
- Bellona, C., Drewes, J. E., Xu, P., and Amy, G. (2004). Factors affecting the rejection of organic solutes during NF/RO treatment—a literature review. *Water Res.* **38**, 2795–2809.
- Benjakul, S., Visessanguan, W., and Kwalumtharn, Y. (2004). The effect of whitening agents on the gel-forming ability and whiteness of surimi. *Int. J. Food Sci. Technol.* **39**, 773–781.
- Bergaya, F. and Lagaly, G. (2013). General introduction: clays, clay minerals, and clay science. In “Developments in Clay Science,” Vol. 5, pp1–19. Elsevier.
- Bhardwaj, V. and Mirliss, M. J. (2005). Diatomaceous Earth filtration for drinking water. *Water Encycl.* **1**, 174–177.
- Bhatnagar, A., Kumar, E., and Sillanpää, M. (2011). Fluoride removal from water by adsorption—A review. *Chem. Eng. J.* **171**, 811–840.
- Bielefeldt, A. R., Kowalski, K., and Summers, R. S. (2009). Bacterial treatment effectiveness of point-of-use ceramic water filters. *Water Res.* **43**, 3559–3565.
- Billingham, J., Breen, C., and Yarwood, J. (1996). In situ determination of Brønsted/Lewis acidity on cation-exchanged clay mineral surfaces by ATR-IR. *Clay Miner.* **31**, 513–522.
- Bird, B. H., Githinji, J. W., Macharia, J. M., Kasiiti, J. L., Muriithi, R. M., Gacheru, S. G., Musaa, J. O., Towner, J. S., Reeder, S. A., Oliver, J. B., and others (2008). Multiple virus lineages sharing recent common ancestry were associated with a large Rift Valley fever outbreak among livestock in Kenya during 2006–2007. *J. Virol.* **82**, 11152–11166.
- Blanchard, R. L., Hahne, R. M., Kahn, B., McCurdy, D., Mellor, R. A., Moore, W. S., Sedlet, J., and Whittaker, E. (1985). Radiological sampling and analytical methods for National Primary Drinking Water Regulations. *Health Phys.* **48**, 587–600.

- Blandin, G., Verliefde, A. R., Comas, J., Rodriguez-Roda, I., and Le-Clech, P. (2016). Efficiently combining water reuse and desalination through forward osmosis—reverse osmosis (FO-RO) hybrids: a critical review. *Membranes* **6**, 37.
- Blanpain-Avet, P., Fillaudeau, L., and Lalande, M. (1999). Investigation of mechanisms governing membrane fouling and protein rejection in the sterile microfiltration of beer with an organic membrane. *Food Bioprod. Process.* **77**, 75–89.
- Boccaccini, A. R. (1994). Comment on “dependence of ceramic fracture properties on porosity.” *J. Mater. Sci. Lett.* **13**, 1035–1037.
- Boccaccini, A. R. and Fan, Z. (1997). A new approach for the Young’s modulus-porosity correlation of ceramic materials. *Ceram. Int.* **23**, 239–245.
- Boccaccini, D. N. and Boccaccini, A. R. (1997). Effect of pore shape on the ultrasonic velocity–porosity correlation in sintered materials. 3.
- Boccardo, V. N. (1993). Paint removing compositions and methods for the manufacture and use thereof.
- Boch, P. and Niepce, J.-C. (2010). “Ceramic Materials: Processes, Properties, and Applications.” John Wiley & Sons.
- Boerlage, S. F., Kennedy, M. D., Dickson, M. R., El-Hodali, D. E., and Schippers, J. C. (2002). The modified fouling index using ultrafiltration membranes (MFI-UF): characterisation, filtration mechanisms and proposed reference membrane. *J. Membr. Sci.* **197**, 1–21.
- Bolton, G., Lacasse, D., and Kuriyel, R. (2006). Combined models of membrane fouling: Development and application to microfiltration and ultrafiltration of biological fluids. *J. Membr. Sci.* **277**, 75–84.
- Bormashenko, E., Pogreb, R., Bormashenko, Y., Musin, A., and Stein, T. (2008). New investigations on ferrofluidics: ferrofluidic marbles and magnetic-field-driven drops on superhydrophobic surfaces. *Langmuir* **24**, 12119–12122.
- Botello-Zubiate, M. E., Alvarez, A., Martínez-Villafañe, A., Almeraya-Calderon, F., and Matutes-Aquino, J. A. (2004). Influence of magnetic water treatment on the calcium carbonate phase formation and the electrochemical corrosion behavior of carbon steel. *J. Alloys Compd.* **369**, 256–259.
- Bowen, W. R., Calvo, J. I., and Hernandez, A. (1995). Steps of membrane blocking in flux decline during protein microfiltration. *J. Membr. Sci.* **101**, 153–165.
- Brahman, K. D., Kazi, T. G., Afridi, H. I., Naseem, S., Arain, S. S., and Ullah, N. (2013). Evaluation of high levels of fluoride, arsenic species and other physicochemical parameters in underground water of two sub districts of Tharparkar, Pakistan: a multivariate study. *Water Res.* **47**, 1005–1020.
- Brown, D. R. and Rhodes, C. N. (1997). Brønsted and Lewis acid catalysis with ion-exchanged clays. *Catal. Lett.* **45**, 35–40.

- Brown, J., Sobsey, M. D., and Loomis, D. (2008). Local drinking water filters reduce diarrheal disease in Cambodia: a randomized, controlled trial of the ceramic water purifier. *Am. J. Trop. Med. Hyg.* **79**, 394–400.
- Bruk, O. B., Klassen, V. I., and Krylov, O. T. (1987). Mechanism of magnetic treatment of disperse systems. *Sov. Surf. Eng. Appl. Electrochem. Elektronmaya Obrab. Materiolo* **6**, 45–50.
- Bundi, M., Shah, M. M., Odoyo, E., Kathiiko, C., Wandera, E., Miring’u, G., Guyo, S., Langat, D., Morita, K., and Ichinose, Y. (2019). Characterization of *Vibrio cholerae* O1 isolates responsible for cholera outbreaks in Kenya between 1975 and 2017. *Microbiol. Immunol.* **63**, 350–358.
- Cai, R., Yang, H., He, J., and Zhu, W. (2009). The effects of magnetic fields on water molecular hydrogen bonds. *J. Mol. Struct.* **938**, 15–19.
- Campos, J. C., Borges, R. M. H., Oliveira Filho, A. M., Nobrega, R., and Sant’Anna, G. L. (2002). Oilfield wastewater treatment by combined microfiltration and biological processes. *Water Res.* **36**, 95–104.
- Cannon, M. J., Hyde, T. B., and Schmid, D. S. (2011). Review of cytomegalovirus shedding in bodily fluids and relevance to congenital cytomegalovirus infection. *Rev. Med. Virol.* **21**, 240–255.
- Chaim, R., Levin, M., Shlayer, A., and Estournes, C. (2008). Sintering and densification of nanocrystalline ceramic oxide powders: a review. *Adv. Appl. Ceram.* **107**, 159–169.
- Chang, K.-T. and Weng, C.-I. (2008). An investigation into the structure of aqueous NaCl electrolyte solutions under magnetic fields. *Comput. Mater. Sci.* **43**, 1048–1055.
- Chang, K.-T. and Weng, C.-I. (2006). The effect of an external magnetic field on the structure of liquid water using molecular dynamics simulation. *J. Appl. Phys.* **100**, 043917.
- Chappell, J. S., Ring, T. A., and Birchall, J. D. (1986). Particle size distribution effects on sintering rates. *J. Appl. Phys.* **60**, 383–391.
- Cheng, Y.-L., Lee, D.-J., and Lai, J.-Y. (2011). Filtration blocking laws: Revisited. *J. Taiwan Inst. Chem. Eng.* **42**, 506–508.
- Chibowski, E. and Szcześ, A. (2018). Magnetic water treatment—A review of the latest approaches. *Chemosphere* **203**, 54–67.
- Choubisa, S. L. and Choubisa, D. (2016). Status of industrial fluoride pollution and its diverse adverse health effects in man and domestic animals in India. *Environ. Sci. Pollut. Res.* **23**, 7244–7254.
- Christopher, B. R. and Fischer, G. R. (1992). Geotextile filtration principles, practices and problems. *Geotext. Geomembr.* **11**, 337–353.
- Chudacek, M. W. and Fane, A. G. (1984). The dynamics of polarisation in unstirred and stirred ultrafiltration. *J. Membr. Sci.* **21**, 145–160.

- Cittanova, M.-L., Lelongt, B., Verpont, M.-C., Geniteau-Legendre, M., Wahbe, F., Prie, D., Coriat, P., and Ronco, P. M. (1996). Fluoride ion toxicity in human kidney collecting duct cells. *Anesthesiol. J. Am. Soc. Anesthesiol.* **84**, 428–435.
- Clark, K. N. and Elmore, A. C. (2011). Bacteria removal effectiveness of ceramic pot filters not applied with colloidal silver. *Water Sci. Technol. Water Supply* **11**, 765–772.
- Clasen, T. F., Brown, J., Collin, S., Suntura, O., and Cairncross, S. (2004). Reducing diarrhea through the use of household-based ceramic water filters: a randomized, controlled trial in rural Bolivia. *Am. J. Trop. Med. Hyg.* **70**, 651–657.
- CLASEN, T., PARRA, G. G., BOISSON, S., and COLLIN, S. (2005). Household-based ceramic water filters for the prevention of diarrhea: a randomized, controlled trial of a pilot program in Colombia. *Am. J. Trop. Med. Hyg.* **73**, 790–795.
- Coble, R. L. (1973). Effects of particle-size distribution in initial-stage sintering. *J. Am. Ceram. Soc.* **56**, 461–466.
- Coble, R. L. and Kingery, W. D. (1956). Effect of porosity on physical properties of sintered alumina. *J. Am. Ceram. Soc.* **39**, 377–385.
- Colic, M. and Morse, D. (1999). The elusive mechanism of the magnetic ‘memory’ of water. *Colloids Surf. Physicochem. Eng. Asp.* **154**, 167–174.
- Considine, R., Denoyel, R., Pendleton, P., Schumann, R., and Wong, S.-H. (2001). The influence of surface chemistry on activated carbon adsorption of 2-methylisoborneol from aqueous solution. *Colloids Surf. Physicochem. Eng. Asp.* **179**, 271–280.
- Cutler, D. and Miller, G. (2005). The role of public health improvements in health advances: the twentieth-century United States. *Demography* **42**, 1–22.
- Dauer, R. R. and Dunlop, E. H. (1991). High gradient magnetic separation of yeast. *Biotechnol. Bioeng.* **37**, 1021–1028.
- Davey, B. G., Russell, J. D., and Wilson, M. J. (1975). Iron oxide and clay minerals and their relation to colours of red and yellow podzolic soils near Sydney, Australia. *Geoderma* **14**, 125–138.
- De Bruijn, J. P. F., Salazar, F. N., and Bórquez, R. (2005). Membrane blocking in ultrafiltration: a new approach to fouling. *Food Bioprod. Process.* **83**, 211–219.
- De Haan, F. A. M. and Bolt, G. H. (1963). Determination of anion adsorption by clays. *Soil Sci. Soc. Am. J.* **27**, 636–640.
- Dolatyar, M. and Gray, T. S. (2000). The politics of water scarcity in the Middle East. *Environ. Polit.* **9**, 65–88.
- Du Buf, H., Bayer, M., Droop, S., Head, R., Juggins, S., Fischer, S., Bunke, H., Wilkinson, M., Roerdink, J., and Pech-Pacheco, J. (1999). Diatom identification: a double challenge called ADIAC. In “Proceedings 10th International Conference on Image Analysis and Processing,” pp734–739. IEEE.

- Duclos-Orsello, C., Li, W., and Ho, C.-C. (2006). A three mechanism model to describe fouling of microfiltration membranes. *J. Membr. Sci.* **280**, 856–866.
- Edelson, L. H. and Glaeser, A. M. (1988). Role of particle substructure in the sintering of monosized titania. *J. Am. Ceram. Soc.* **71**, 225–235.
- Evans, T. iM, LeChevallier, M. W., Waarvick, C. E., and Seidler, R. J. (1981). Coliform species recovered from untreated surface water and drinking water by the membrane filter, standard, and modified most-probable-number techniques. *Appl Env. Microbiol* **41**, 657–663.
- F. Kruis Einar, Karl, A. K., Sotiris, E. P., and Brian, S. (1993). A Simple Model for the Evolution of the Characteristics of Aggregate Particles Undergoing Coagulation and Sintering: *Aerosol Science and Technology: Vol 19, No 4. Taylor Francis* **19**, 514–526.
- Fan, C.-S. and Li, K.-C. (2013). Production of insulating glass ceramics from thin film transistor-liquid crystal display (TFT-LCD) waste glass and calcium fluoride sludge. *J. Clean. Prod.* **57**, 335–341.
- Fane, A. G., Fell, C. J. D., and Suki, A. (1983). The effect of pH and ionic environment on the ultrafiltration of protein solutions with retentive membranes. *J. Membr. Sci.* **16**, 195–210.
- Fang, Z. (2010). “Sintering of advanced materials: fundamental and processes.” Cambridge, UK: Woodhead Publishing Limited.
- Farid, S. B. (2014). Effect of additives on sintering of α -cristobalite. *J. Mater. Sci.* **49**, 4133–4138.
- Farrah, S. R., Preston, D. R., Toranzos, G. A., Girard, M., Erdos, G. A., and Vasuhdivan, V. (1991). Use of modified diatomaceous earth for removal and recovery of viruses in water. *Appl Env. Microbiol* **57**, 2502–2506.
- Fathi, A., Mohamed, T., Claude, G., Maurin, G., and Mohamed, B. A. (2006a). Effect of a magnetic water treatment on homogeneous and heterogeneous precipitation of calcium carbonate. *Water Res.* **40**, 1941–1950.
- Fathi, A., Mohamed, T., Claude, G., Maurin, G., and Mohamed, B. A. (2006b). Effect of a magnetic water treatment on homogeneous and heterogeneous precipitation of calcium carbonate. *Water Res.* **40**, 1941–1950.
- Fayer, R. (2004). Cryptosporidium: a water-borne zoonotic parasite. *Vet. Parasitol.* **126**, 37–56.
- Fewtrell, L. and Bartram, J. (2001). “Water quality: guidelines, standards, and health: assessment of risk and risk management for water-related infectious disease.” World Health Organization, Geneva.
- Fewtrell, L., Kaufmann, R. B., Kay, D., Enanoria, W., Haller, L., and Colford, J. M. (2005). Water, sanitation, and hygiene interventions to reduce diarrhoea in less developed countries: a systematic review and meta-analysis. *Lancet Infect. Dis.* **5**, 42–52.
- Fojt, L., Strašák, L., Vetterl, V., and Šmarda, J. (2004). Comparison of the low-frequency magnetic field effects on bacteria *Escherichia coli*, *Leclercia adecarboxylata* and *Staphylococcus aureus*. *Bioelectrochemistry* **63**, 337–341.

- Frank, C., Werber, D., Cramer, J. P., Askar, M., Faber, M., Heiden, M. an der, Bernard, H., Fruth, A., Prager, R., and Spode, A. (2011). Epidemic profile of Shiga-toxin-producing *Escherichia coli* O104: H4 outbreak in Germany. *N. Engl. J. Med.* **365**, 1771–1780.
- Franzreb, M. and Holl, W. H. (2000). Phosphate removal by high-gradient magnetic filtration using permanent magnets. *IEEE Trans. Appl. Supercond.* **10**, 923–926.
- Frenkel, M., Danchuk, V., Multanen, V., and Bormashenko, E. (2018). Magnetic field inspired contact angle hysteresis drives floating polyolefin rafts. *Colloid Interface Sci. Commun.* **22**, 38–41.
- Fulton, G. P. (2000a). Diatomaceous earth filtration for safe drinking water. American Society of Civil Engineers Reston, VA.
- Fulton, G. P. (2000b). Diatomaceous earth filtration for safe drinking water. American Society of Civil Engineers.
- Gabrielli, C., Jaouhari, R., Maurin, G., and Keddam, M. (2001). Magnetic water treatment for scale prevention. *Water Res.* **35**, 3249–3259.
- Gehr, R., Zhai, Z. A., Finch, J. A., and Rao, S. R. (1995). Reduction of soluble mineral concentrations in CaSO₄ saturated water using a magnetic field. *Water Res.* **29**, 933–940.
- George, I., Crop, P., and Servais, P. (2001). Use of β -D-galactosidase and β -D-glucuronidase activities for quantitative detection of total and fecal coliforms in wastewater. *Can. J. Microbiol.* **47**, 670–675.
- Gergely, S., Bekassy-Molnar, E., and Vatai, G. (2003). The use of multiobjective optimization to improve wine filtration. *J. Food Eng.* **58**, 311–316.
- Getachew, T., Hussen, A., and Rao, V. M. (2015). Defluoridation of water by activated carbon prepared from banana (*Musa paradisiaca*) peel and coffee (*Coffea arabica*) husk. *Int. J. Environ. Sci. Technol.* **12**, 1857–1866.
- Ghoshal, S. N. (2007). “Atomic Physics (Modern Physics).” S. Chand Limited.
- Giesche, H. (1994). Synthesis of monodispersed silica powders I. Particle properties and reaction kinetics. *J. Eur. Ceram. Soc.* **14**, 189–204.
- Giesche, H. and Matijević, E. (1994). Preparation, characterization, and sinterability of well-defined silica/yttria powders. *J. Mater. Res.* **9**, 436–450.
- Gironès, M., Lammertink, R. G., and Wessling, M. (2006). Protein aggregate deposition and fouling reduction strategies with high-flux silicon nitride microsieves. *J. Membr. Sci.* **273**, 68–76.
- Gitari, W. M., Izuagie, A. A., and Gumbo, J. R. (2020). Synthesis, characterization and batch assessment of groundwater fluoride removal capacity of trimetal Mg/Ce/Mn oxide-modified diatomaceous earth. *Arab. J. Chem.* **13**, 1–16.
- Grace, H. P. (1956). Structure and performance of filter media. II. Performance of filter media in liquid service. *AIChE J.* **2**, 316–336.

- Granger, J., Dodds, J., and Leclerc, D. (1985). Filtration of low concentrations of latex particles on membrane filters. *Filtr. Sep.* **22**, 58–60.
- Greenlee, L. F., Lawler, D. F., Freeman, B. D., Marrot, B., and Moulin, P. (2009). Reverse osmosis desalination: water sources, technology, and today's challenges. *Water Res.* **43**, 2317–2348.
- Gutierrez, L., Li, X., Wang, J., Nangmenyi, G., Economy, J., Kuhlenschmidt, T. B., Kuhlenschmidt, M. S., and Nguyen, T. H. (2009). Adsorption of rotavirus and bacteriophage MS2 using glass fiber coated with hematite nanoparticles. *Water Res.* **43**, 5198–5208.
- Halem, D. van, Laan, H. van der, Heijman, S. G. J., Dijk, J. C. van, and Amy, G. L. (2009). Assessing the sustainability of the silver-impregnated ceramic pot filter for low-cost household drinking water treatment. *Phys. Chem. Earth Parts ABC* **34**, 36–42.
- Halliday, D., Resnick, R., and Krane, K. S. (2001). "Physics, Volume 2," 5th edition ed. John Wiley & Sons, New York.
- Harrison, P. T. (2005). Fluoride in water: a UK perspective. *J. Fluor. Chem.* **126**, 1448–1456.
- Hatori, R. and Suzuki, Y. (2021). Effect of sintering temperature on water-purification performance of Al₂O₃/3Y-ZrO₂ membrane filters. *J. Mater. Sci.* **56**, 9668–9677.
- Haydar, S., Ferro-Garcia, M. A., Rivera-Utrilla, J., and Joly, J. P. (2003). Adsorption of p-nitrophenol on an activated carbon with different oxidations. *Carbon* **41**, 387–395.
- Hermans, P. H. and Bredée, H. L. (1935). Zur kenntnis der filtrationsgesetze. *Recl. Trav. Chim. Pays-Bas* **54**, 680–700.
- Hermia, J. (1982). Constant pressure blocking filtration laws: application to power-law non-Newtonian fluids.
- Herzog, R. E., Shi, Q., Patil, J. N., and Katz, J. L. (1989). Magnetic water treatment: the effect of iron on calcium carbonate nucleation and growth. *Langmuir* **5**, 861–867.
- Higashitani, K., Kage, A., Katamura, S., Imai, K., and Hatade, S. (1993). Effects of a magnetic field on the formation of CaCO₃ particles. *J. Colloid Interface Sci.* **156**, 90–95.
- Hirschbein, B. L., Brown, D. W., and Whitesides, G. M. (1982). Magnetic separations in chemistry and biochemistry. *Chemtech* **12**, 172–179.
- Ho, C.-C. and Zydney, A. L. (2000). A combined pore blockage and cake filtration model for protein fouling during microfiltration. *J. Colloid Interface Sci.* **232**, 389–399.
- Holysz, L., Szczes, A., and Chibowski, E. (2007). Effects of a static magnetic field on water and electrolyte solutions. *J. Colloid Interface Sci.* **316**, 996–1002.
- Hosoda, H., Mori, H., Sogoshi, N., Nagasawa, A., and Nakabayashi, S. (2004). Refractive indices of water and aqueous electrolyte solutions under high magnetic fields. *J. Phys. Chem. A* **108**, 1461–1464.

- Huang, X., Marsh, K. L., McVerry, B. T., Hoek, E. M., and Kaner, R. B. (2016). Low-fouling antibacterial reverse osmosis membranes via surface grafting of graphene oxide. *ACS Appl. Mater. Interfaces* **8**, 14334–14338.
- Hunter, P. R. (2009). Household water treatment in developing countries: comparing different intervention types using meta-regression. *Environ. Sci. Technol.* **43**, 8991–8997.
- Hwang, K.-J., Liao, C.-Y., and Tung, K.-L. (2007). Analysis of particle fouling during microfiltration by use of blocking models. *J. Membr. Sci.* **287**, 287–293.
- Igbinigun, E., Fennell, Y., Malaisamy, R., Jones, K. L., and Morris, V. (2016). Graphene oxide functionalized polyethersulfone membrane to reduce organic fouling. *J. Membr. Sci.* **514**, 518–526.
- Incropera, F. P., Lavine, A. S., Bergman, T. L., and DeWitt, D. P. (2007). “Fundamentals of heat and mass transfer.” Wiley.
- Iritani, E. (2013). A review on modeling of pore-blocking behaviors of membranes during pressurized membrane filtration. *Dry. Technol.* **31**, 146–162.
- Iritani, E. and Katagiri, N. (2016). Developments of blocking filtration model in membrane filtration. *KONA Powder Part. J.* **33**, 179–202.
- Iritani, E., Mukai, Y., Furuta, M., Kawakami, T., and Katagiri, N. (2005). Blocking resistance of membrane during cake filtration of dilute suspensions. *AIChE J.* **51**, 2609–2614.
- Iritani, E., Sumi, H., and Murase, T. (1991). Analysis of filtration rate in clarification filtration of power-law non-Newtonian fluids–solids mixtures under constant pressure by stochastic model. *J. Chem. Eng. Jpn.* **24**, 581–586.
- Iwasaka, M. and Ueno, S. (1998). Structure of water molecules under 14 T magnetic field. *J. Appl. Phys.* **83**, 6459–6461.
- Iwasaka, M. and Ueno, S. (1997). Effects of gradient magnetic fields on diffusion process of glycine in water. *IEEE Trans. Magn.* **33**, 4254–4256.
- Izuagie, A. A., Gitari, W. M., and Gumbo, J. R. (2016a). Defluoridation of groundwater using diatomaceous earth: optimization of adsorption conditions, kinetics and leached metals risk assessment. *Desalination Water Treat.* **57**, 16745–16757.
- Izuagie, A. A., Gitari, W. M., and Gumbo, J. R. (2016b). Synthesis and performance evaluation of Al/Fe oxide coated diatomaceous earth in groundwater defluoridation: towards fluorosis mitigation. *J. Environ. Sci. Health Part A* **51**, 810–824.
- Jha, S. K., Mishra, V. K., Sharma, D. K., and Damodaran, T. (2011). Fluoride in the environment and its metabolism in humans. In “Reviews of Environmental Contamination and Toxicology Volume 211,” pp121–142. Springer.
- Ji, W., Huang, H., Deng, A., and Pan, C. (2009a). Effects of static magnetic fields on *Escherichia coli*. *Micron* **40**, 894–898.

- Ji, W., Huang, H., Deng, A., and Pan, C. (2009b). Effects of static magnetic fields on *Escherichia coli*. *Micron* **40**, 894–898.
- Jia, Y. F. and Thomas, K. M. (2000). Adsorption of cadmium ions on oxygen surface sites in activated carbon. *Langmuir* **16**, 1114–1122.
- Jia, Y., Han, W., Xiong, G., and Yang, W. (2007). Diatomite as high performance and environmental friendly catalysts for phenol hydroxylation with H₂O₂. *Sci. Technol. Adv. Mater.* **8**, 106–109.
- Johan, S. (2003). Effect of magnetic field on the sedimentation of suspended solids of sewage. PhD Thesis, Thesis of Philosophy of Doctorate: Universiti Teknologi Malaysia.
- Kalisinska, E., Bosiacka-Baranowska, I., Lanocha, N., Kosik-Bogacka, D., Krolaczyk, K., Wilk, A., Kavetska, K., Budis, H., Gutowska, I., and Chlubek, D. (2014). Fluoride concentrations in the pineal gland, brain and bone of goosander (*Mergus merganser*) and its prey in Odra River estuary in Poland. *Environ. Geochem. Health* **36**, 1063–1077.
- Kallman, E. N., Oyanedel-Craver, V. A., and Smith, J. A. (2010). Ceramic filters impregnated with silver nanoparticles for point-of-use water treatment in rural Guatemala. *J. Environ. Eng.* **137**, 407–415.
- Kang, S.-J. L. (2005). “Sintering: densification, grain growth, and microstructure.” Elsevier, Amsterdam.
- Karkush, M. O., Ahmed, M. D., and Al-Ani, S. M. (2019). Effects of Magnetic Fields on the Properties of Water Treated by Reversed Osmosis.
- Kauffman, J. M. (2005). Water fluoridation: A review of recent research and actions. *J. Am. Physicians Surg.* **10**, 38.
- Ketelaars, A. A. J., Kaasschieter, E. F., Coumans, W. J., and Kerkhof, P. J. A. M. (1994). The Influence of Shrinkage on Drying Behaviour of Clays. *Dry. Technol.* **12**, 1561–1574.
- Kilara, A. and Van Buren, J. P. (1989). Clarification of apple juice. In “Processed apple products,” pp83–96. Springer.
- Kimura, S. and Sourirajan, S. (1967). Analysis of data in reverse osmosis with porous cellulose acetate membranes used. *AIChE J.* **13**, 497–503.
- Kingery, W. D., Bowen, H. K., and Uhlmann, D. R. (1976). “Introduction to Ceramics,” Second ed. John Wiley & Sons Inc, New York.
- Kitazawa, K., Ikezoe, Y., Uetake, H., and Hirota, N. (2001). Magnetic field effects on water, air and powders. *Phys. B Condens. Matter* **294**, 709–714.
- Kittel, C. (2005). “Introduction to solid state physics.” Wiley.
- Knez, S. and Pohar, C. (2005). The magnetic field influence on the polymorph composition of CaCO₃ precipitated from carbonized aqueous solutions. *J. Colloid Interface Sci.* **281**, 377–388.

- Kobe, S., Dražić, G., McGuinness, P. J., Meden, T., Sarantopoulou, E., Kollia, Z., and Cefalas, A. C. (2003). Control over nanocrystalization in turbulent flow in the presence of magnetic fields. *Mater. Sci. Eng. C* **23**, 811–815.
- Kobe, S., Dražić, G., McGuinness, P. J., and Stražičar, J. (2001). The influence of the magnetic field on the crystallisation form of calcium carbonate and the testing of a magnetic water-treatment device. *J. Magn. Magn. Mater.* **236**, 71–76.
- Kováčik, J. (2006). Correlation between Poisson's ratio and porosity in porous materials. *J. Mater. Sci.* **41**, 1247–1249.
- Krishna, B. S., Murty, D. S. R., and Prakash, B. J. (2000). Thermodynamics of chromium (VI) anionic species sorption onto surfactant-modified montmorillonite clay. *J. Colloid Interface Sci.* **229**, 230–236.
- Kronenberg, K. (1985). Experimental evidence for effects of magnetic fields on moving water. *IEEE Trans. Magn.* **21**, 2059–2061.
- Krook, L. and Maylin, G. A. (1979). Industrial fluoride pollution. Chronic fluoride poisoning in Cornwall Island cattle. *Cornell Vet.* **69**, suppl-1.
- Krook, L. P. and Justus, C. (2006). Fluoride poisoning of horses from artificially fluoridated drinking water. *Fluoride* **39**, 3–10.
- Krüger, R., Vial, D., Arifin, D., Weber, M., and Heijnen, M. (2016). Novel ultrafiltration membranes from low-fouling copolymers for RO pretreatment applications. *Desalination Water Treat.* **57**, 23185–23195.
- Kurzeja, E., Synowiec-Wojtarowicz, A., Stec, M., Glinka, M., Gawron, S., and Pawłowska-Góral, K. (2013). Effect of a Static Magnetic Fields and Fluoride Ions on the Antioxidant Defense System of Mice Fibroblasts. *Int. J. Mol. Sci.* **14**, 15017–15028.
- Kwon, S. and Messing, G. L. (1998). Constrained densification in boehmite–alumina mixtures for the fabrication of porous alumina ceramics. *J. Mater. Sci.* **33**, 913–921.
- Laan, H. van der, Halem, D. van, Smeets, P. W. M. H., Soppe, A. I. A., Kroesbergen, J., Wubbels, G., Nederstigt, J., Gensburger, I., and Heijman, S. G. J. (2014). Bacteria and virus removal effectiveness of ceramic pot filters with different silver applications in a long term experiment. *Water Res.* **51**, 47–54.
- Lantagne, D., Klarman, M., Mayer, A., Preston, K., Napotnik, J., and Jellison, K. (2010). Effect of production variables on microbiological removal in locally-produced ceramic filters for household water treatment. *Int. J. Environ. Health Res.* **20**, 171–187.
- Lantagne, D. S., Blount, B. C., Cardinali, F., and Quick, R. (2008). Disinfection by-product formation and mitigation strategies in point-of-use chlorination of turbid and non-turbid waters in western Kenya. *J. Water Health* **6**, 67–82.
- Le Huec, J. C., Schaevebeke, T., Clement, D., Faber, J., and Le Rebeller, A. (1995). Influence of porosity on the mechanical resistance of hydroxyapatite ceramics under compressive stress. *Biomaterials* **16**, 113–118.

- Lebkowska, M., Rutkowska-Narożniak, A., Pajor, E., and Pochanke, Z. (2011). Effect of a static magnetic field on formaldehyde biodegradation in wastewater by activated sludge. *Bioresour. Technol.* **102**, 8777–8782.
- LeChevallier, M. W., Evans, T. M., Seidler, R. J., Daily, O. P., Merrell, B. R., Rollins, D. M., and Joseph, S. W. (1982). *Aeromonas sobria* in chlorinated drinking water supplies. *Microb. Ecol.* **8**, 325–333.
- Leclerc, H., Schwartzbrod, L., and Dei-Cas, E. (2002). Microbial agents associated with waterborne diseases. *Crit. Rev. Microbiol.* **28**, 371–409.
- Lee, D. J. (1997). Filter medium clogging during cake filtration. *AIChE J.* **43**, 273–276.
- Lee, K.-Y. and Santmartí, A. (2018). Crystallinity and Thermal Stability of Nanocellulose. In “Nanocellulose and Sustainability,” pp67–86. CRC Press.
- Lee, S.-H., Takeda, M., and Nishigaki, K. (2003). Gas–Liquid Interface Deformation of Flowing Water in Gradient Magnetic Field–Influence of Flow Velocity and NaCl Concentration. *Jpn. J. Appl. Phys.* **42**, 1828.
- Lima Leite, A. de, Ferreira Santiago Junior, J., Mauad Levy, F., Gutierrez Maria, A., Silva Fernandes, M. da, Favero Salvadori, D. M., Araki Ribeiro, D., and Afonso Rabelo Buzalaf, M. (2007). Absence of DNA damage in multiple organs (blood, liver, kidney, thyroid gland and urinary bladder) after acute fluoride exposure in rats. *Hum. Exp. Toxicol.* **26**, 435–440.
- Lima, R. B., Santos, T. B. dos, Vieira, L. G. E., Ferrarese, M. de L. L., Ferrarese-Filho, O., Donatti, L., Boeger, M. R. T., and Oliveira Petkowicz, C. L. de (2013). Heat stress causes alterations in the cell-wall polymers and anatomy of coffee leaves (*Coffea arabica* L.). *Carbohydr. Polym.* **93**, 135–143.
- Lin, S.-H. and Juang, R.-S. (2002). Heavy metal removal from water by sorption using surfactant-modified montmorillonite. *J. Hazard. Mater.* **92**, 315–326.
- Liu, D.-M. (1997). Influence of porosity and pore size on the compressive strength of porous hydroxyapatite ceramic. *Ceram. Int.* **23**, 135–139.
- Liu, G., Han, K., Ye, H., Zhu, C., Gao, Y., Liu, Y., and Zhou, Y. (2017). Graphene oxide/triethanolamine modified titanate nanowires as photocatalytic membrane for water treatment. *Chem. Eng. J.* **320**, 74–80.
- Lucier, K. J., Dickson-Anderson, S. E., and Schuster-Wallace, C. J. (2017). Effectiveness of silver and copper infused ceramic drinking water filters in reducing microbiological contaminants. *J. Water Supply Res. Technol. - Aqua*, jws2017028.
- Luke, J. A. (1997). The effect of fluoride on the physiology of the pineal gland. PhD Thesis, University of Surrey.
- Lychagin, N. I. (1974). Changing properties of magnetized water. *Sov. Phys. J.* **17**, 229–233.
- Lyckfeldt, O. and Ferreira, J. M. F. (1998). Processing of porous ceramics by ‘starch consolidation.’ *J. Eur. Ceram. Soc.* **18**, 131–140.

- Lynch, M., Painter, J., Woodruff, R., Braden, C., and others (2006). “Surveillance for Foodborne-disease Outbreaks: United States, 1998–2002.” US Department of Health and Human Services, Centers for Disease Control and Prevention (CD).
- Ma, J. F. and Yamaji, N. (2006). Silicon uptake and accumulation in higher plants. *Trends Plant Sci.* **11**, 392–397.
- Mackenzie, J. K. (1950). The Elastic Constants of a Solid containing Spherical Holes. *Proc. Phys. Soc. Sect. B* **63**, 2–11.
- Madsen, H. L. (1995). Influence of magnetic field on the precipitation of some inorganic salts. *J. Cryst. Growth* **152**, 94–100.
- Majewska-Nowak, K., Kabsch-Korbutowicz, M., Dodź, M., and Winnicki, T. (2002). The influence of organic carbon concentration on atrazine removal by UF membranes. *Desalination* **147**, 117–122.
- Mäser, P., Gierth, M., and Schroeder, J. I. (2002). Molecular mechanisms of potassium and sodium uptake in plants. In “Progress in Plant Nutrition: Plenary Lectures of the XIV International Plant Nutrition Colloquium,” pp43–54. Springer.
- Matijevic, E., Giesche, H., and Her, Y. S. (1996). Effects of particle uniformity on the sinterability of powders. *Sci Sinter* **28**, 3–17.
- Maylin, G. A. and Krook, L. (1982). Milk production of cows exposed to industrial fluoride pollution. *J. Toxicol. Environ. Health Part Curr. Issues* **10**, 473–478.
- Meenakshi, S., Sundaram, C. S., and Sukumar, R. (2008). Enhanced fluoride sorption by mechanochemically activated kaolinites. *J. Hazard. Mater.* **153**, 164–172.
- Michen, B., Diatta, A., Fritsch, J., Aneziris, C., and Graule, T. (2011). Removal of colloidal particles in ceramic depth filters based on diatomaceous earth. *Sep. Purif. Technol.* **81**, 77–87.
- Michen, B., Meder, F., Rust, A., Fritsch, J., Aneziris, C., and Graule, T. (2012). Virus removal in ceramic depth filters based on diatomaceous earth. *Environ. Sci. Technol.* **46**, 1170–1177.
- Mitchell, R. S. and Gluskoter, H. J. (1976). Mineralogy of ash of some American coals: variations with temperature and source. *Fuel* **55**, 90–96.
- Mocanu, A., Rusen, E., Diacon, A., Damian, C., Dinescu, A., and Sucheai, M. (2017). Electrochemical deposition of zinc oxide on the surface of composite membrane polysulfone-graphene-polystyrene in the presence of water soluble polymers. *J. Nanomater.* **2017**.
- Momberg, D. J., Ngandu, B. C., Voth-Gaeddert, L. E., Ribeiro, K. C., May, J., Norris, S. A., and Said-Mohamed, R. (2021). Water, sanitation and hygiene (WASH) in sub-Saharan Africa and associations with undernutrition, and governance in children under five years of age: a systematic review. *J. Dev. Orig. Health Dis.* **12**, 6–33.
- Montgomery, M. A. and Elimelech, M. (2007). Water and sanitation in developing countries: including health in the equation. *Env. Sci Technol* **41**, 17–24.

- Morimitsu, M., Shiomi, K., and Matsunaga, M. (2000). Magnetic effects on alkylammonium chloride solutions investigated by interfacial tension measurements at the mercury/solution interface. *J. Colloid Interface Sci.* **229**, 641–643.
- Morton, S. G. (1997). Method and apparatus for detecting and classifying contaminants in water.
- Mourouzidis-Mourouzis, S. A. and Karabelas, A. J. (2006). Whey protein fouling of microfiltration ceramic membranes—pressure effects. *J. Membr. Sci.* **282**, 124–132.
- Mukhopadhyay, A. K. and Phani, K. K. (1998). Young’s modulus—porosity relations: an analysis based on a minimum contact area model. *J. Mater. Sci.* **33**, 69–72.
- Muncaster, B. W., Hebert, P. D. N., and Lazar, R. (1990). Biological and physical factors affecting the body burden of organic contaminants in freshwater mussels. *Arch. Environ. Contam. Toxicol.* **19**, 25–34.
- Murad, S. (2006). The role of magnetic fields on the membrane-based separation of aqueous electrolyte solutions. *Chem. Phys. Lett.* **417**, 465–470.
- Murray, J. J. and Organization, W. H. (1986). “Appropriate use of fluorides for human health.” World Health Organization.
- Nakagawa, J., Hirota, N., Kitazawa, K., and Shoda, M. (1999). Magnetic field enhancement of water vaporization. *J. Appl. Phys.* **86**, 2923–2925.
- Ncube, E. J. and Schutte, C. F. (2005). The occurrence of fluoride in South African groundwater: A water quality and health problem. *Water SA* **31**, 35–40.
- Ncube, E. J. and Schutte, C. F. (2004). Relation of dental fluorosis to ground water fluoride in South Africa. In “Thailand: 4th international workshop on fluorosis prevention and defluoridation of water.”
- Nigay, P.-M., Salifu, A. A., Obayemi, J. D., White, C. E., Nzihou, A., and Soboyejo, W. O. (2019). Ceramic Water Filters for the Removal of Bacterial, Chemical, and Viral Contaminants. *J. Environ. Eng.* **145**, 04019066.
- Njogu, M. S., Nyongesa, F. W., and Aduda, B. O. (2008). Effect of plant-derived organic binders on fracture toughness and fatigue of kaolin-based refractories. *J. Mater. Sci.* **43**, 4107–4111.
- Nopakun, J., Messer, H. H., and Voller, V. (1989). Fluoride absorption from the gastrointestinal tract of rats. *J. Nutr.* **119**, 1411–1417.
- Nyongesa, F. W. and Aduda, B. O. (2004). Fracture strength of porous ceramics: stress concentration vs. minimum solid area models. *AJST* **5**.
- Ochoa-Villarreal, M., Aispuro-Hernández, E., Vargas-Arispuro, I., and Martínez-Téllez, M. Á. (2012). “Plant Cell Wall Polymers:Function, Structure and Biological Activity of Their Derivatives | IntechOpen.” IntechOpen.
- Ogacho, A. A., Aduda, B. O., and Nyongesa, F. W. (2006). Thermal shock behaviour of a kaolinite refractory prepared using a natural organic binder. *J. Mater. Sci.* **41**, 8276–8283.

- Ong, C. S., Al-Anzi, B., Lau, W. J., Goh, P. S., Lai, G. S., Ismail, A. F., and Ong, Y. S. (2017). Anti-fouling double-skinned forward osmosis membrane with zwitterionic brush for oily wastewater treatment. *Sci. Rep.* **7**, 1–11.
- Organization, W. H. (2004). “Guidelines for drinking-water quality.” World Health Organization.
- Oshitani, J., Yamada, D., Miyahara, M., and Higashitani, K. (1999). Magnetic effect on ion-exchange kinetics. *J. Colloid Interface Sci.* **210**, 1–7.
- Otero, J. A., Mazarrasa, O., Villasante, J., Silva, V., Prádanos, P., Calvo, J. I., and Hernández, A. (2008). Three independent ways to obtain information on pore size distributions of nanofiltration membranes. *J. Membr. Sci.* **309**, 17–27.
- Oummadi, S. (2019). Drying behaviour of ceramic green bodies: experimental characterization and numerical modelling. PhD Thesis, Université de Limoges.
- Oyanedel-Craver, V. A. and Smith, J. A. (2008). Sustainable colloidal-silver-impregnated ceramic filter for point-of-use water treatment. *Environ. Sci. Technol.* **42**, 927–933.
- Pang, X. and Deng, B. (2008). Investigation of changes in properties of water under the action of a magnetic field. *Sci. China Ser. G Phys. Mech. Astron.* **51**, 1621–1632.
- Pappas, J. L. (2005). Geometry and topology of diatom shape and surface morphogenesis for use in applications of nanotechnology. *J. Nanosci. Nanotechnol.* **5**, 120–130.
- Park, S.-J. and Jin, S.-Y. (2005). Effect of ozone treatment on ammonia removal of activated carbons. *J. Colloid Interface Sci.* **286**, 417–419.
- Paton, J. C. and Paton, A. W. (1998). Pathogenesis and diagnosis of Shiga toxin-producing *Escherichia coli* infections. *Clin. Microbiol. Rev.* **11**, 450–479.
- Patterson, A. L. (1939). Phys. Rev. 56, 978 (1939) - The Scherrer Formula for X-Ray Particle Size Determination. *Am. Phys. Soc.* **56**, 978.
- Pereira, M. F. R., Soares, S. F., Órfão, J. J., and Figueiredo, J. L. (2003). Adsorption of dyes on activated carbons: influence of surface chemical groups. *Carbon* **41**, 811–821.
- Peterson, J., MacDonell, M., Haroun, L., Monette, F., Hildebrand, R. D., and Taboas, A. (2007). Radiological and chemical fact sheets to support health risk analyses for contaminated areas. *Argonne Natl. Lab. Environ. Sci. Div.* **133**.
- Phani, K. K. and Niyogi, S. K. (1987). Young’s Modulus of Porous Brittle Solids. *J. Mater. Sci.* **22**, 257.
- Puri, R. K. and Babbar, V. (2010). “Solid State Physics.” S Chand, Ram Nagar, New Delhi.
- Purkait, M., Bhattacharya, P., and De, S. (2005). Membrane filtration of leather plant effluent: Flux decline mechanism. *J. Membr. Sci.* **258**, 85–96.
- Pype, M.-L., Lawrence, M. G., Keller, J., and Gernjak, W. (2016). Reverse osmosis integrity monitoring in water reuse: The challenge to verify virus removal—A review. *Water Res.* **98**, 384–395.

- Qu, F., Liang, H., Zhou, J., Nan, J., Shao, S., Zhang, J., and Li, G. (2014). Ultrafiltration membrane fouling caused by extracellular organic matter (EOM) from *Microcystis aeruginosa*: effects of membrane pore size and surface hydrophobicity. *J. Membr. Sci.* **449**, 58–66.
- Rafique, T., Naseem, S., Usmani, T. H., Bashir, E., Khan, F. A., and Bhangar, M. I. (2009). Geochemical factors controlling the occurrence of high fluoride groundwater in the Nagar Parkar area, Sindh, Pakistan. *J. Hazard. Mater.* **171**, 424–430.
- Rahimian, M., Ehsani, N., Parvin, N., and Baharvandi, H. reza (2009). The effect of particle size, sintering temperature and sintering time on the properties of Al–Al₂O₃ composites, made by powder metallurgy. *J. Mater. Process. Technol.* **209**, 5387–5393.
- Raisien, E. (1984). The control of scale and corrosion in water systems using magnetic fields. *Corrosion* **84**, 1984.
- Rayner, J., Luo, X., Schubert, J., Lennon, P., Jellison, K., and Lantagne, D. (2017). The effects of input materials on ceramic water filter efficacy for household drinking water treatment. *Water Supply* **17**, 859–869.
- Rayner, J., Zhang, H., Schubert, J., Lennon, P., Lantagne, D., and Oyanedel-Craver, V. (2013). Laboratory investigation into the effect of silver application on the bacterial removal efficacy of filter material for use on locally produced ceramic water filters for household drinking water treatment. *ACS Sustain. Chem. Eng.* **1**, 737–745.
- Reddy, C. R., Bhat, Y. S., Nagendrappa, G., and Prakash, B. J. (2009). Brønsted and Lewis acidity of modified montmorillonite clay catalysts determined by FT-IR spectroscopy. *Catal. Today* **141**, 157–160.
- Reihanian, H., Robertson, C. R., and Michaels, A. S. (1983). Mechanisms of polarization and fouling of ultrafiltration membranes by proteins. *J. Membr. Sci.* **16**, 237–258.
- Rice, R. W. (1996). Evaluation and extension of physical property-porosity models based on minimum solid area. *J. Mater. Sci.* **31**, 102–118.
- Rice, R. W. (1989). Relation of tensile strength-porosity effects in ceramics to porosity dependence of Young's modulus and fracture energy, porosity character and grain size. *Mater. Sci. Eng. A* **112**, 215–224.
- Rich, C. and Ensinnck, J. (1961). Effect of sodium fluoride on calcium metabolism of human beings. *Nature* **191**, 184–185.
- Rich, C., Ensinnck, J., and Ivanovich, P. (1964). The effects of sodium fluoride on calcium metabolism of subjects with metabolic bone diseases. *J. Clin. Invest.* **43**, 545–556.
- Ripa, L. W. (1993). A half-century of community water fluoridation in the United States: review and commentary. *J. Public Health Dent.* **53**, 17–44.
- Rivera-Utrilla, J. and Sánchez-Polo, M. (2002). The role of dispersive and electrostatic interactions in the aqueous phase adsorption of naphthalenesulphonic acids on ozone-treated activated carbons. *Carbon* **40**, 2685–2691.

- Rivera-Utrilla, J., Sánchez-Polo, M., Gómez-Serrano, V., Alvarez, P. M., Alvim-Ferraz, M. C. M., and Dias, J. M. (2011). Activated carbon modifications to enhance its water treatment applications. An overview. *J. Hazard. Mater.* **187**, 1–23.
- Roberts, A. P. and Garboczi, E. J. (2000). Elastic Properties of Model Porous Ceramics. *J. Am. Ceram. Soc.* **83**, 3041–3048.
- Rosen, A. D. (1993). Membrane response to static magnetic fields: effect of exposure duration. *Biochim. Biophys. Acta BBA - Biomembr.* **1148**, 317–320.
- Ruiping, L., Lihua, S., Jiuhui, Q., and Guibai, L. (2009). Arsenic removal through adsorption, sand filtration and ultrafiltration: In situ precipitated ferric and manganese binary oxides as adsorbents. *Desalination* **249**, 1233–1237.
- Ruth, B. F. (1946). Correlating filtration theory with industrial practice. *Ind. Eng. Chem.* **38**, 564–571.
- Ruth, B. F. (1935). Studies in filtration III. Derivation of general filtration equations. *Ind. Eng. Chem.* **27**, 708–723.
- Saadaldin, S. A. and Rizkalla, A. S. (2014). Synthesis and characterization of wollastonite glass–ceramics for dental implant applications. *Dent. Mater.* **30**, 364–371.
- Sacks, M. D. and TSENG, T.-Y. (1984a). Preparation of SiO₂ glass from model powder compacts: I, formation and characterization of powders, suspensions, and green compacts. *J. Am. Ceram. Soc.* **67**, 526–532.
- Sacks, M. D. and TSENG, T.-Y. (1984b). Preparation of SiO₂ glass from model powder compacts: II, sintering. *J. Am. Ceram. Soc.* **67**, 532–537.
- Safarzadeh-Amiri, A., Fowlie, P., Kazi, A. I., Siraj, S., Ahmed, S., and Akbor, A. (2011). Validation of analysis of arsenic in water samples using Wagtech Digital Arsenator. *Sci. Total Environ.* **409**, 2662–2667.
- Sakizci, M., Erdoğan Alver, B., and Yörükoğullari, E. (2009). Thermal behavior and immersion heats of selected clays from Turkey. *J. Therm. Anal. Calorim.* **98**, 429.
- Salinas-Rodriguez, S. G., Amy, G. L., Schippers, J. C., and Kennedy, M. D. (2015). The Modified Fouling Index Ultrafiltration constant flux for assessing particulate/colloidal fouling of RO systems. *Desalination* **365**, 79–91.
- Şan, O. and Özgür, C. (2009). Investigation of a high stable β -cristobalite ceramic powder from CaO–Al₂O₃–SiO₂ system. *J. Eur. Ceram. Soc.* **29**, 2945–2949.
- Sanchis, J. M., Merrell, J. C., and Kiker, J. E. (1951). Studies on Diatomaceous Earth Filtration [with Discussion]. *J. Am. Water Works Assoc.* **43**, 475–495.
- Saxena, V. and Ahmed, S. (2001). Dissolution of fluoride in groundwater: a water-rock interaction study. *Environ. Geol.* **40**, 1084–1087.
- Scannell, L. W. (2016). An analysis of performance criteria of porous ceramic water filter production methods. PhD Thesis, State University of New York at Buffalo.

- Scherer, G. W. (1990). Theory of Drying. *J. Am. Ceram. Soc.* **73**, 3–14.
- Schweitzer, R. W., Cunningham, J. A., and Mihelcic, J. R. (2013). Hydraulic modeling of clay ceramic water filters for point-of-use water treatment. *Environ. Sci. Technol.* **47**, 429–435.
- Seckler, D., Barker, R., and Amarasinghe, U. (1999). Water scarcity in the twenty-first century. *Int. J. Water Resour. Dev.* **15**, 29–42.
- Servi, A. T., Kang, P. K., Frey, D., and Murcott, S. (2013). A holistic optimization framework for improving ceramic pot filter performance. In “2013 IEEE Global Humanitarian Technology Conference (GHTC),” pp355–360. IEEE.
- She, J., Ohji, T., and Deng, Z.-Y. (2002). Thermal shock behavior of porous silicon carbide ceramics. *J. Am. Ceram. Soc.* **85**, 2125–2127.
- Sila, O. N. (2019). Physico-chemical and bacteriological quality of water sources in rural settings, a case study of Kenya, Africa. *Sci. Afr.* **2**, e00018.
- Silva, D. T. G. da, Ebdon, J., Okotto-Okotto, J., Ade, F., Mito, O., Wanza, P., Kwoba, E., Mwangi, T., Yu, W., and Wright, J. A. (2020). A longitudinal study of the association between domestic contact with livestock and contamination of household point-of-use stored drinking water in rural Siaya County (Kenya). *Int. J. Hyg. Environ. Health* **230**, 113602.
- Silva, I. B., Neto, J. C. Q., and Petri, D. F. (2015). The effect of magnetic field on ion hydration and sulfate scale formation. *Colloids Surf. Physicochem. Eng. Asp.* **465**, 175–183.
- Silvestri, L. S., Taraporewala, Z. F., and Patton, J. T. (2004). Rotavirus Replication: Plus-Sense Templates for Double-Stranded RNA Synthesis Are Made in Viroplasm. *J. Virol.* **78**, 7763–7774.
- Sobsey, M. D., Stauber, C. E., Casanova, L. M., Brown, J. M., and Elliott, M. A. (2008). Point of use household drinking water filtration: a practical, effective solution for providing sustained access to safe drinking water in the developing world. *Environ. Sci. Technol.* **42**, 4261–4267.
- Sondhi, H., Gupta, M. L., and Gupta, G. L. (1995). Intestinal effects of sodium fluoride in Swiss albino mice. *Fluoride* **28**, 21–24.
- Soppe, A. I. A., Heijman, S. G. J., Gensburger, I., Shantz, A., Van Halem, D., Kroesbergen, J., Wubbels, G. H., and Smeets, P. (2015). Critical parameters in the production of ceramic pot filters for household water treatment in developing countries. *J. Water Health* **13**, 587–599.
- Sorber, C. A., Malina Jr, J. F., and Sagik, B. P. (1971). “Virus rejection by the reverse osmosis-ultrafiltration processes.” Texas Univ at Austin Center for Research in Water Resources.
- Spiegel, M. S. (1998). Method and apparatus for applying magnetic fields to fluids. Google Patents.
- Srinivasan, R. (2011). Advances in Application of Natural Clay and Its Composites in Removal of Biological, Organic, and Inorganic Contaminants from Drinking Water. In “Advances in Materials Science and Engineering,” Vol. 2011, ppe872531. Hindawi.
- Szostak, R. J. and Toy, D. A. (1985). Magnetic fluid conditioning system allows 3000 ppm hardness without cooling tower scale buildup. *Chem. Process. Chic.* **48**, 44–45.

- Taitt, C. R., Shubin, Y. S., Angel, R., and Ligler, F. S. (2004). Detection of *Salmonella enterica* Serovar Typhimurium by Using a Rapid, Array-Based Immunosensor. *Appl. Environ. Microbiol.* **70**, 152–158.
- Tarr, P. I., Gordon, C. A., and Chandler, W. L. (2005). Shiga-toxin-producing *Escherichia coli* and haemolytic uraemic syndrome. *The lancet* **365**, 1073–1086.
- Templeton, M. R., Graham, N., and Voulvoulis, N. (2009). “Emerging chemical contaminants in water and wastewater.” The Royal Society Publishing.
- Thorat, D. D., Tripathi, B. M., and Sathiyamoorthy, D. (2011). Extraction of beryllium from Indian beryl by ammonium hydrofluoride. *Hydrometallurgy* **109**, 18–22.
- Ting, J.-M. and Lin, R. Y. (1994a). Effect of particle-size distribution on sintering. *J. Mater. Sci.* **29**, 1867–1872.
- Ting, J.-M. and Lin, R. Y. (1994b). Effect of particle-size distribution on sintering. *J. Mater. Sci.* **29**, 1867–1872.
- Toledo, E. J., Ramalho, T. C., and Magriotis, Z. M. (2008). Influence of magnetic field on physical–chemical properties of the liquid water: Insights from experimental and theoretical models. *J. Mol. Struct.* **888**, 409–415.
- Tombacz, E., Ma, C., Busch, K. W., and Busch, M. A. (1991). Effect of a weak magnetic field on hematite sol in stationary and flowing systems. *Colloid Polym. Sci.* **269**, 278–289.
- Trueba, F. J. and Koppes, L. J. H. (1998). Exponential growth of *Escherichia coli* B/r during its division cycle is demonstrated by the size distribution in liquid culture. *Arch. Microbiol.* **169**, 491–496.
- Uddin, M. K. (2017). A review on the adsorption of heavy metals by clay minerals, with special focus on the past decade. *Chem. Eng. J.* **308**, 438–462.
- Van der Bruggen, B. and Vandecasteele, C. (2003). Removal of pollutants from surface water and groundwater by nanofiltration: overview of possible applications in the drinking water industry. *Environ. Pollut.* **122**, 435–445.
- Van Halem, D. (2006). Ceramic silver impregnated pot filters for household drinking water treatment in developing countries.
- Varkey, A. J. and Dlamini, M. D. (2012). Point-of-use water purification using clay pot water filters and copper mesh. *Water SA* **38**, 721–726.
- Velde, B. (1995). Composition and mineralogy of clay minerals. In “Origin and mineralogy of clays,” pp8–42. Springer.
- Velde, B. and Druc, I. C. (1999). Origin of Clay Resources. In “Archaeological Ceramic Materials: Origin and Utilization” (B. Velde, I.C. Druc, Eds.), pp59–74. Springer, Berlin, Heidelberg.
- Venis, R. A. and Basu, O. D. (2020). Mechanisms and efficacy of disinfection in ceramic water filters: A critical review. *Crit. Rev. Environ. Sci. Technol.*, 1–41.

- Verwilghen, C., Rio, S., Nzihou, A., Gauthier, D., Flamant, G., and Sharrock, P. J. (2007). Preparation of high specific surface area hydroxyapatite for environmental applications. *J. Mater. Sci.* **42**, 6062–6066.
- Vick, W. S. (1991). Magnetic fluid conditioning. In “Environmental Engineering,” pp567–573. ASCE.
- Wada, K. and Harward, M. E. (1974). Amorphous Clay Constituents of Soils. In “Advances in Agronomy” (N.C. Brady, Ed.), Vol. 26, pp211–260. Academic Press.
- Wambu, E. W., Onindo, C. O., Ambusso, W. J., and Muthakia, G. K. (2011). Fluoride adsorption onto acid-treated diatomaceous mineral from Kenya. *Mater. Sci. Appl.* **2**, 1654.
- Wang, N., Liu, T., Shen, H., Ji, S., Li, J.-R., and Zhang, R. (2016). Ceramic tubular MOF hybrid membrane fabricated through in situ layer-by-layer self-assembly for nanofiltration. *AIChE J.* **62**, 538–546.
- Wang, S. S., Chang, M.-C., Chang, H.-C., Chang, M.-H., and Tai, C. Y. (2012). Growth behavior of aragonite under the influence of magnetic field, temperature, and impurity. *Ind. Eng. Chem. Res.* **51**, 1041–1049.
- Wang, Y., Wei, H., and Li, Z. (2018). Effect of magnetic field on the physical properties of water. *Results Phys.* **8**, 262–267.
- Wegmann, M., Michen, B., and Graule, T. (2008a). Nanostructured surface modification of microporous ceramics for efficient virus filtration. *J. Eur. Ceram. Soc.* **28**, 1603–1612.
- Wegmann, M., Michen, B., Luxbacher, T., Fritsch, J., and Graule, T. (2008b). Modification of ceramic microfilters with colloidal zirconia to promote the adsorption of viruses from water. *Water Res.* **42**, 1726–1734.
- White, D. A. (1996). The interpretation of the SDI for water solids content using the filtration equation. *Process Saf. Environ. Prot.* **74**, 137–140.
- White, P. J. and Broadley, M. R. (2003). Calcium in plants. *Ann. Bot.* **92**, 487–511.
- Wood, A. R., Justus, K., Parigoris, E., Russell, A., and LeDuc, P. (2017). Biological Inspiration of Salt Exclusion Membranes in Mangroves toward Fouling-Resistant Reverse Osmosis Membranes. *FASEB J.* **31**, 949–2.
- Xiong, X., Liu, J., He, W., Xia, T., He, P., Chen, X., Yang, K., and Wang, A. (2007). Dose–effect relationship between drinking water fluoride levels and damage to liver and kidney functions in children. *Environ. Res.* **103**, 112–116.
- Xu, H., Li, G., Cheng, J., and Liu, W. (2014). Recovery of high specific area silica and sodium fluoride from sodium hexafluorosilicate. *J. Cent. South Univ.* **21**, 4084–4090.
- Xu, L., Gao, X., Li, Z., and Gao, C. (2015). Removal of fluoride by nature diatomite from high-fluorine water: an appropriate pretreatment for nanofiltration process. *Desalination* **369**, 97–104.

- Yahya, M. T., Cluff, C. B., and Gerba, C. P. (1993). Virus removal by slow sand filtration and nanofiltration. *Water Sci. Technol.* **27**, 445–448.
- Yakub, I. (2012). Micro-and nano-porous adsorptive materials for removal of contaminants from water at point-of-use.
- Yakub, I., Du, J., and Soboyejo, W. O. (2012). Mechanical properties, modeling and design of porous clay ceramics. *Mater. Sci. Eng. A* **558**, 21–29.
- Yakub, I., Plappally, A., Leftwich, M., Malatesta, K., Friedman, K. C., Obwoya, S., Nyongesa, F., Maiga, A. H., Soboyejo, A. B. O., Logothetis, S., and Soboyejo, W. (2013). Porosity, Flow, and Filtration Characteristics of Frustum-Shaped Ceramic Water Filters. *J. Environ. Eng.* **139**, 986–994.
- Yakub, I. and Soboyejo, W. (2013). Adsorption of fluoride from water using sintered clay-hydroxyapatite composites. *J. Environ. Eng.* **139**, 995–1003.
- Yan, H., Cao, C., Bai, G., and Bai, W. (2016). Seawater desalination technology route and analysis of production capacity for large commercial nuclear power plant. In “International Conference Pacific Basin Nuclear Conference,” pp865–872. Springer.
- Yang, M., Zhao, C., Zhang, S., Li, P., and Hou, D. (2017). Preparation of graphene oxide modified poly (m-phenylene isophthalamide) nanofiltration membrane with improved water flux and antifouling property. *Appl. Surf. Sci.* **394**, 149–159.
- Yao, K.-M., Habibian, M. T., and O’Melia, C. R. (1971). Water and waste water filtration. Concepts and applications. *Environ. Sci. Technol.* **5**, 1105–1112.
- Ysart, G., Miller, P., Croasdale, M., Crews, H., Robb, P., Baxter, M., De L’Argy, C., and Harrison, N. (2000). 1997 UK Total Diet Study dietary exposures to aluminium, arsenic, cadmium, chromium, copper, lead, mercury, nickel, selenium, tin and zinc. *Food Addit. Contam.* **17**, 775–786.
- Zaidi, N. S. (2016). Application of magnetic field for reduction of sludge bulking in activated sludge system. *Univ. Teknol. Malays.*
- Zaidi, N. S., Sohaili, J., Muda, K., and Sillanpää, M. (2014). Magnetic Field Application and its Potential in Water and Wastewater Treatment Systems. *Sep. Purif. Rev.* **43**, 206–240.
- Zhang, D., Zhou, C.-H., Lin, C.-X., Tong, D.-S., and Yu, W.-H. (2010). Synthesis of clay minerals. *Appl. Clay Sci.* **50**, 1–11.
- Zhang, L., Zhang, P., Wang, M., Yang, K., and Liu, J. (2016). Research on the experiment of reservoir water treatment applying ultrafiltration membrane technology of different processes. *J. Environ. Biol.* **37**, 1007.
- Zhao, N., Wei, N., Li, J., Qiao, Z., Cui, J., and He, F. (2005). Surface properties of chemically modified activated carbons for adsorption rate of Cr (VI). *Chem. Eng. J.* **115**, 133–138.
- Zhou, G., Yang, L., Luo, C., Liu, H., Li, P., Cui, Y., Liu, L., Yu, X., Zeng, Q., and Chen, J. (2019). Low-to-moderate fluoride exposure, relative mitochondrial DNA levels, and dental fluorosis in Chinese children. *Environ. Int.* **127**, 70–77.